

HEAT AND FLUID FLOW IN AN INTEGRATED RECTANGULAR MICROCHANNEL: A COMBINED NUMERICAL-EXPERIMENTAL STUDY

Thesis

Submitted in partial fulfillment of the requirement for the degree of

DOCTOR OF PHILOSOPHY

By

G. NARENDRAN

(155138ME15F08)



**DEPARTMENT OF MECHANICAL ENGINEERING
NATIONAL INSTITUTE OF TECHNOLOGY KARNATAKA
SURATHKAL, MANGALORE – 575025**

JUNE, 2022

DECLARATION

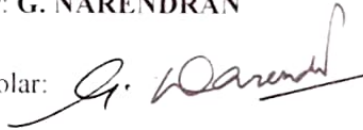
By the Ph.D research scholar

I hereby *declare* that the Research Synopsis entitled "**HEAT AND FLUID FLOW IN AN INTEGRATED RECTANGULAR MICROCHANNEL: A COMBINED NUMERICAL-EXPERIMENTAL STUDY**" which is being submitted to the **National Institute of Technology Karnataka, Surathkal** in partial fulfillment of the requirements for the award of the Degree of **Doctor of Philosophy in Mechanical Engineering** is a *bonafide report of the research work carried out by me*. The material contained in this Research Thesis has not been submitted to any University or Institution for the award of any degree.

Register Number: **155138ME15F08**

Name of the Research Scholar: **G. NARENDRAN**

Signature of the Research Scholar:



Department of Mechanical Engineering

Place: NITK, Surathkal

Date: *09.06.2022*

CERTIFICATE

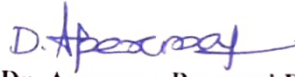
This is to certify that the Research Thesis entitled “**HEAT AND FLUID FLOW IN AN INTEGRATED RECTANGULAR MICROCHANNEL: A COMBINED NUMERICAL-EXPERIMENTAL STUDY**” submitted by **G. NARENDRAN (Register Number: 155138ME15F08)** as the record of the research work carried out by him, is *accepted as the Research Thesis submission* in partial fulfillment of the requirements for the award of degree of **Doctor of Philosophy**.



Dr. N. Gnanasekaran

Research Guide

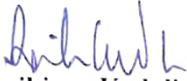
Date: 06/06/2022



Dr. Arumuga Perumal D

Research Guide

Date: 06/06/2022



Dr. Ravikiran Kadoli

Chairman-DRPC

Date: 6.6.2022



ACKNOWLEDGEMENT

I wish to convey my deep sense of gratitude and profound appreciation to my research guides **Dr. N. Gnanasekaran** and **Dr. D. Arumuga Perumal** for giving me this opportunity and support throughout my doctoral journey. Their constant encouragement during all stages of my work pushed me to bring this thesis into fulfilment.

I am very thankful to my RPAC committee members **Dr. M. Arun** and **Dr. K. Vadivuchezhian** for their valuable support.

I remain highly indebted to **Dr. Ravikiran Kadoli**, Head of the department for providing facilities during the course of the investigation. I would like to express my sincere gratitude to my previous heads of the department **Dr. S. M. Kulkarni**, **Dr. Shrikantha.S. Rao**, **Dr. S. Narendranath** and **Dr. K. V. Gangadharan** for their enduring support. I am extremely grateful to **Dr. Kumar G N** and **Dr. Ravikiran Kadoli** for supporting my numerical study with their CFD laboratory facility.

My heartfelt thanks to all the fabricators and industrial suppliers for their smooth cooperation to bring up my various experimental test setup in a grandeur. From bottom of my heart, I express my sincere thanks to all my friends with whomsoever i have shared my research failures, progress and success during this work. Especially, to my beloved colleagues **Dr. Viru**, **Dr. Avadooth**, **Dr. Vishwa** and **Dr. Kiran**.

I take this opportunity to acknowledge my respectful seniors **Dr. Harsha Kumar**, **Dr. Kotresha**, **Dr. Anil Kadam** and **Dr. Venkatesh** for their continuous support and insight.

I am also fortunate for having amazing and talented associates **Dr. Sreejesh**, **Dr. Shreyas Hedge** and **Amit Kumar** with whom I had extremely great time working with.

Finally, I cordially thank my family members for their love, sacrifice, patience and understanding; which still thrives me to travel towards my purpose.

Dedication

My works and efforts can only be dwarfed by the monumental dedication and hard work of my beloved father M. Ganesan and I thank him for his constant support and guidance throughout my life.

I dedicate this thesis to the two most beloved people whom I cherish and continue to mean so much to me, my wonderful mother S. Rani, and my loving wife Dr. L. Nakkiya for her endless support, patience, and encouragement.

Finally a special dedication to my amazing brother G. Krishnakumar, my best friend and my confidant.



ABSTRACT

This thesis work presents numerical and experimental investigations on flow maldistribution based conjugate axial conduction problems in parallel type channels for high density electronic cooling applications. Majorly, three issues relating to the practicality of the integrated parallel channel heat sinks are explored in the thesis: (a) The effect of integrated heat spreaders in mitigating the flow induced high temperature zones using parallel type heat sink, (b) The study of axial conduction and entrance effects of heterogeneous integrated heat sink and (c) the use of inertial channels to reduce flow maldistribution induced axial conduction in parallel flow type configuration heat sink.

In the first part, heat transfer investigations are performed to reduce hotspots with heat spreader integrated microchannel using nanofluid. The results of Nusselt number are compared with the benchmark literatures. Numerical simulations on microchannel heat sink are performed to understand the temperature distribution in the spreader and an elaborate discussion is provided for the deviations observed between numerical and experimental data. Critical effects like response time and bulk diffusion are discussed by varying hotspot, aspect ratio and processor cores. Reduction in flow induced hotspot has been observed by providing graphene oxide nanofluid with very low volume fraction. In the second part, both the numerical and experimental analyses are performed to investigate axial conduction in heterogeneous integrated microchannel using TiO_2 nanofluid. The inlet flow rate, volume fraction and power rating are varied to check the effects of axial conduction on heterogeneously integrated substrates. The thermo physical properties of the TiO_2 nanofluid are measured and characterized. Significant effect of axial conduction is seen for nanofluid at higher concentration at reduced flow rates. On the other hand, it has been observed that the effect of conjugate heat transfer decreases at higher flow rates.

The last part of the work presents the investigation on the special type of inertial channels to reduce the maldistribution induced axial conduction. The study is carried out on ribbed channels with three different geometrical configurations i.e. normal, inclined and lifted channels. The average temperature of the sink reduces for ribbed channels than normal straight channels. The effect of axial conduction is observed less for ribbed inclined channel due to the obstruction in flow, flow separation and increased fluid momentum in extreme channels.

Keywords: microchannel, nanofluid, axial conduction, maldistribution, hotspot.

TABLE OF CONTENTS

ACKNOWLEDGEMENT

ABSTRACT

TABLE OF CONTENTS **i**

LIST OF FIGURES **vii**

LIST OF TABLES **xiii**

NOMENCLATURE **xv**

CHAPTER 1	INTRODUCTION	1
	1.1 INTRODUCTION	1
	1.2 TRADE-OFFS IN MICROCHANNEL	2
	1.3 INTEGRATED COOLING DEVICE	3
	1.4 MALDISTRIBUTION FLOW	4
	1.4.1 Maldistribution flow induced hotspot	4
	1.4.2 Maldistribution induced axial conduction	5
	1.5 EFFECT OF FLOW STRUCTURES	6
	1.6 OVERVIEW OF THE THESIS	7
	1.7 ORGANIZATION OF THE THESIS	8
CHAPTER 2	LITERATURE REVIEW	11
	2.1 INTRODUCTION	11
	2.2 NUMERICAL STUDY IN MICROCHANNEL	11
	2.3 EXPERIMENTAL STUDIES ON MICROCHANNEL HEAT SINK	16
	2.4 ELECTRONIC COOLING USING MICROCHANNEL HEAT SINK	20
	2.5 MICROCHANNEL WITH STRUCTURES	23
	2.6 IRREVERSIBILITY	27
	2.7 NON- FOURIER HEAT CONDUCTION	31
	2.8 MOTIVATION AND SCOPE FOR THE PRESENT WORK	35

	2.9 OBJECTIVES OF THE PRESENT WORK	36
	2.10 CLOSURE	37
CHAPTER 3	EXPERIMENTAL TEST SETUP	39
	3.1 INTRODUCTION	39
	3.2 PARALLEL I-TYPE CHANNEL CONFIGURATION TEST SETUP	39
	3.2.1 Heat spreader integrated microchannel setup	39
	3.2.2 Heterogeneous integrated microchannel setup	43
	3.2.3 Minichannel heat sink setup	46
	3.3 TEMPERATURE MEASUREMENTS	51
	3.4 CLOSURE	54
CHAPTER 4	NANOFLUID SYNTHESIS AND CHARACTERIZATION	55
	4.1 INTRODUCTION	55
	4.2 METHODS FOR PREPARATION OF NANOFLUIDS	55
	4.3 SYNTHESIS OF GRAPHENE OXIDE (GO) NANOPLATELLETS	56
	4.4 PREPARATION OF GO NANOFLUID	57
	4.4.1 Thermo physical properties of nanofluid	59
	4.5 SYNTHESIS AND CHARACTERIZATION OF TiO ₂ NANOFLUID	61
	4.6 CLOSURE	64
CHAPTER 5	EXPERIMENTAL INVESTIGATION ON HEAT SPREADER INTEGRATED MICROCHANNEL USING GRAPHENE OXIDE NANOFLUID	65
	5.1 INTRODUCTION	65
	5.2 INTEGRATED HEAT SPREADER APPROACH	65
	5.3 EXPERIMENTAL SETUP	67
	5.3.1 Heat spreader assisted microchannel	67
	5.3.2 Description of the experimental study	67

	5.3.3 Uncertainty parameters	68
	5.4 RESULTS AND DISCUSSION	69
	5.4.1 Temperature distribution on heat spreader	69
	5.4.2 Heat transfer studies	77
	5.4.3 Friction factor	83
	5.4.4 Hotspot migration	87
	5.5 CONCLUSIONS	92
	5.6 CLOSURE	92
CHAPTER 6	INVESTIGATION ON TEMPERATURE RESPONSE EFFECTS IN MICROCHANNEL	93
	6.1 INTRODUCTION	93
	6.2 NON FOURIER HEAT TRANSFER	93
	6.3 BACKGROUND OF THE STUDY	95
	6.4 EXPERIMENTAL DETAILS	96
	6.5 THEORY AND ANALYSIS	98
	6.6 NUMERICAL METHODOLOGY	102
	6.6.1 Boundary conditions	102
	6.6.2 Governing equations	103
	6.6.3 Grid independence study	104
	6.7 RESULTS AND DISCUSSION	105
	6.7.1 Temperature study	105
	6.7.2 Response time study	112
	6.7.3 Bulk diffusion study	117
	6.8 CONCLUSIONS	120
	6.9 CLOSURE	122
CHAPTER 7	THERMODYNAMIC IRREVERSIBILITY AND CONJUGATE EFFECTS OF INTEGRATED MICROCHANNEL COOLING DEVICE USING TiO₂ NANOFLUID	123
	7.1 INTRODUCTION	123
	7.2 IRREVERSIBILITY STUDY	123

7.3 MOTIVATION	125
7.4 DATA REDUCTION	127
7.5 NUMERICAL SCHEME	129
7.5.1 Governing equations	129
7.5.2 Boundary conditions	130
7.6 RESULTS AND DISCUSSION	132
7.6.1 Validation study	132
7.6.2 Temperature study	134
7.6.3 Exergy analysis	136
7.6.4 Entropy generation study	137
7.7 CONCLUSIONS	143
7.8 CLOSURE	144
CHAPTER 8	145
INVESTIGATION ON INERTIAL MINICHANNELS TO MITIGATE FLOW MALDISTRIBUTION INDUCED HIGH TEMPERATURE ZONES	
8.1 INTRODUCTION	145
8.2 EXPERIMENTAL SETUP	145
8.3 NUMERICAL MODELLING	147
8.3.1 Boundary conditions	147
8.3.2 Governing equations	147
8.3.3 Grid independence study	148
8.4 HEAT SINK MODULES COMPARISON	149
8.5 TEMPERATURE DISTRIBUTION OF THE SOURCE AND MODULE	150
8.6 RESULTS AND DISCUSSION	151
8.6.1 Validation study	151
8.6.2 Thermo hydrodynamics study	153
8.6.3 Velocity study	159
8.6.4 Temperature distribution study	162

	8.7 CONCLUSIONS	165
	8.8 CLOSURE	166
CHAPTER 9	CONCLUSIONS	167
	9.1 SCOPE FOR FUTURE WORK	171
	REFERENCES	173
	LIST OF PUBLICATIONS	185
	BIO-DATA	187

LIST OF FIGURES

FIG. No.	TITLE	PAGE No.
Figure 1.1	Schematics of the flow configuration (a) I-type, (b) C-type and Z-type.	5
Figure 1.2	Overview of the thesis	7
Figure 3.1	Schematic diagram of microchannel integrated heat spreader with dimensions (a) section view of the assembly, (b) fluid handling unit, and (c) heat spreader dimensions.	40
Figure 3.2	Photographs of experimental microchannel module with FHU (a) microchannel with thermocouple locations, (b) FHU with pressure tapping, and (c) microchannel heat sink	41
Figure 3.3	Experimental setup of microchannel with heat spreader (a) heat sink, (b) heat sink with FHU, (c) heat sink with sensors, and (d) complete module.	42
Figure 3.4	Flow diagram of the experimental setup	42
Figure 3.5	Exploded view of the diagram of microchannel experimental setup	43
Figure 3.6	Schematics of the microchannel with dimensions	44
Figure 3.7	Actual photographs of the microchannel and aluminium block with sensor locations	45
Figure 3.8	Photograph of the microchannel experimental setup	45
Figure 3.9	Schematic diagram of the experimental flow line	46
Figure 3.10	Actual diagram of minichannel module. (a) channel dimensions, and (b) minichannel module.	47
Figure 3.11	Minichannel module with sensor locations and fixtures	47
Figure 3.12	Actual photograph of the complete minichannel experimental setup	48
Figure 3.13	Flow line of the experimental setup	49
Figure 4.1	FTIR of GO	56
Figure 4.2	Characterization images (a) XRD-GO, and (b) TEM- GO	57
Figure 4.3	Nanofluid stability test (a) Particle size, and (b) Zeta potential	58

Figure 4.4	Thermal conductivity of GO/water nanofluid	60
Figure 4.5	Viscosity of GO/water nanofluid	60
Figure 4.6	TiO ₂ characterization (a) SEM image, (b) particle size measurement of 0.25% vf using dynamic light scattering	61
Figure 4.7	Effect of particle concentration on effective thermal conductivity of TiO ₂ nanofluid	62
Figure 4.8	Effective viscosity of nanofluid on effect of particle concentration	63
Figure 5.1	Conceptual diagram of microchannel integrated heat spreader approach	66
Figure 5.2	Infrared photographs of the processor (a) 8 s, (b) 12 s, and (c) 16 s	67
Figure 5.3	Schematic of thermocouple locations in different temperature zones	68
Figure 5.4	Infrared photographs of the module during heating for two time periods (a) 25 s, and (b) 50 s	69
Figure 5.5	Infrared photographs of the module at progressive cooling at three time periods (a) 10 s, (b) 20 s, and (c) 30 s	70
Figure 5.6	Temperature distribution with water as working fluid for different flow rates (a) 0.21 L/min, (b) 0.26 L/min, and (c) 0.31 L/min	72
Figure 5.7	Temperature distribution with GO-0.02% as working fluid for different flow rates (a) 0.21 L/min, (b) 0.26 L/min, and (c) 0.31 L/min	74
Figure 5.8	Figure 5.8 Temperature distribution with GO-0.12% as working fluid for different flow rates (a) 0.21 L/min, (b) 0.26 L/min, and (c) 0.31 L/min.	76
Figure 5.9	Comparison of temperature data for microchannel heat sink and heat spreader integrated microchannel heat sink with different fluids	77
Figure 5.10	Heat transfer coefficient as a function of flow rate for different volume fractions	78
Figure 5.11	Nusselt number as a function of flow rate for different volume fraction. (a) water, (b) GO-0.02%, (c) GO-0.07, and (d) GO-0.12%.	81

Figure 5.12	Pressure drop as a function of flow rate for different fluids	84
Figure 5.13	Friction factor as a function of Reynolds number for different fluids	85
Figure 5.14	Pumping power as a function of flow rate for different fluids	86
Figure 5.15	Heat spreader temperature distribution for different flow rates (Direction of arrow indicates the increase in mass flow rate) a) HSEZ-water, (b) HSMZ-water, (c) HSEZ-GO-0.07%, (d) HSMZ-GO-0.07%, (e) HSEZ-GO-0.12%, (f) HSMZ-GO-0.12%.	90
Figure 6.1	Schematics of heat spreader integrated microchannel with details of the interface materials	96
Figure 6.2	Schematic of heat spreader integrated microchannel (a) details of temperature sensors, and (b) location of the temperature sensors	97
Figure 6.3	Schematic of free body model of the heat conduction from the processor to the heat sink and to the bottom substrate, where T_C is the core temperature, T_S is the heat sink temperature and T_P is the substrate temperature	100
Figure 6.4	Schematic of the computational domain with boundary conditions	103
Figure 6.5	Grid independence study	104
Figure 6.6	Temperature of the heat spreader (T_{hs}) on heating condition	105
Figure 6.7	Temperature of the heat spreader (T_{hs}) on cooling condition for different fluids, (a) water, (b) GO-0.02%, (c) GO-0.07%, (d) GO-0.12%	107
Figure 6.8	Temperature of the heat sink along the flow length (T_{HS}), (a) $Re=100$, and (b) $Re=350$	109
Figure 6.9	Temperature distribution for different Reynolds number, (a) Temperature along the axial length of the extreme microchannel wall (T_{EC}), and (b) Temperature distribution below the channel bed (T_{Y1})	111
Figure 6.10	Temperature contour in the microchannel bottom floor for different flow rate and working fluid, (a) water at $Re=100$, (b) water at $Re=350$, (c) GO-0.12% at $Re=100$, and (d) GO-0.12% at $Re=350$	112

Figure 6.11	Response of lagged diffusion heat conduction in the heat spreader	113
Figure 6.12	Comparison of temperature at different locations, (a) heating the heatsink till 85°C under room temperature and (b) cooling heat sink using water at Re=150 when the temperature of the heat sink is at 85°C	114
Figure 6.13	Temperature comparison for different nanofluid, (a) heating room temperature heatsink till 85°C, (b) cooling the 85°C heat sink using water at Re=150, and (c) using GO-0.12% nanofluid.	116
Figure 6.14	Combined temperature distribution of the heat sink	118
Figure 6.15	Bulk fluid diffusion for different nanofluid, (a) water, (b) GO-0.07%, and (c) GO-0.12%	120
Figure 7.1	Schematics of the numerical model (a) Computational domain, and (b) boundary conditions	130
Figure 7.2	Mesh structure of the computational domain	131
Figure 7.3	Grid independence study of outlet temperature for different nanofluids	132
Figure 7.4	Nusselt number variation along the channel length	133
Figure 7.5	Friction factor comparison for increased flow rate	133
Figure 7.6	Comparative study on temperature variation along the length of the channel for a flow rate of 200 mL/min	134
Figure 7.7	Comparative study on transient temperature decrement as a function of time	135
Figure 7.8	Temperature reduction in channel for different power with constant flow rate using water	135
Figure 7.9	Outlet exergy for different nanofluid concentrations as a function of flow rate	136
Figure 7.10	Exergy gain for different nanofluid concentrations as a function of flow rate	137
Figure 7.11	Thermal entropy generation rate for different nanofluid concentrations	138
Figure 7.12	Frictional entropy generation rate for different nanofluid concentrations	138

Figure 7.13	Bejan number variations as a function of flow rate for different TiO ₂ nanofluid concentrations.	139
Figure 7.14	Temperature contours for different volume fractions, flow rate and power factor. 12 W power (a-d); 18 W power (e-h), (a) water at 200 mL/min, (b) TiO ₂ -0.25% at 200 mL/min, (c) water at 460 mL/min, (d) TiO ₂ -0.25% at 460 mL/min, (e) water at 200 mL/min, (f) TiO ₂ -0.25% at 200 mL/min, (g) water at 460 mL/min, (h) TiO ₂ -0.25% at 460 mL/min	141
Figure 7.15	Temperature iso-surfaces for outlet fluid and aluminium block for different TiO ₂ nanofluid at a constant flow rate of 460 mL/min with power factor of 18W. (a) Water, (b) 0.1%, (c) 0.15%, (d) 0.20%, and (e) 0.25%.	142
Figure 8.1	Exploded view of the experimental setup and channel flow structures used for the investigation	146
Figure 8.2	Schematics of the different channel configuration. (a) straight channel, (b) ribbed channel, (c) ribbed inclined and (d) ribbed lifted	146
Figure 8.3	Schematics of the computational domain with boundary condition	147
Figure 8.4	Grid independence study of the outlet temperature of fluid	148
Figure 8.5	Temperature distributions of the core under different cooling module conditions	148
Figure 8.6	IR images of the processor core at two different loading. (a) 40% loading, and 100% loading condition	150
Figure 8.7	IR images of the processor core at progressive cooling at different time periods. (a) Time, t=0 s, (b) t=20 s, (c) t=30 s, (d) t=50 s, and (f) t=60 s.	151
Figure 8.8	Experimental and numerical study comparison of temperature as a function of time	152
Figure 8.9	Experimental and numerical study comparison of pressure drop	152
Figure 8.10	Temperature variation along the length of the channel for different channels	153
Figure 8.11	Velocity along the length of the channel for different channels	154
Figure 8.12	Pressure drop along the length of the channel for different channels	155

Figure 8.13	Temperature contours of minichannel for different channels, (a) Normal channel, (b) ribbed channel, (c) ribbed inclined, and (d) ribbed lifted.	156
Figure 8.14	Y-Z plane temperature contours near the exit of the, minichannel (a) Normal channel, (b) ribbed channel, (c) ribbed inclined, and (d) ribbed lifted	157
Figure 8.15	X-Z plane temperature contours for the entire length of minichannel, (a) Normal channel, (b) ribbed channel, (c) ribbed inclined, and (d) ribbed lifted	158
Figure 8.16	velocity in minichannel for increased flow rate, minichannel (a) Normal channel, (b) ribbed channel, (c) ribbed inclined, and (d) ribbed lifted	161
Figure 8.17	Temperature distribution in minichannel for different channel design near exit, (a) 210 mL/min, (b) 260 mL/min, (c) 310 mL/min, and (d) 360 mL/min	163
Figure 8.18	Temperature distribution along the width of the channel for different flow configurations	164
Figure 8.19	Maximum base temperature of the heat sink as a function of flow rate for different flow configuration	165

LIST OF TABLES

TABLE. No.	TITLE	PAGE No.
Table 2.1	Summary of the heat spreader investigations integrated with microchannel heat sink	19
Table 2.2	Summary of investigations on hotspot management for electronic cooling with different techniques	22
Table 3.1	Instruments utilized for experimental investigation	49
Table 3.2	Calibration chart of thermocouples at room temperature	52
Table 3.3	Calibration chart at different thermostatic temperatures	53
Table 5.1	List of uncertainty parameters	68

NOMENCLATURE

IoT	internet of things
3D	three dimension
M	axial conduction number
TiO ₂	titanium dioxide
Re	Reynolds number
V _f	volume fraction
FVM	finite volume method
SMAC	simplified marker cell
Cu-Be	Copper beryllium alloy
FHU	fluid handling unit
T ₁ , T ₂ , T ₃	microchannel temperature without heat spreader, °C
F _{in}	fluid in
F _{out}	fluid out
P _{in}	pressure in, Pa
P _{out}	pressure out, Pa
T _{HS1} , T _{HS2}	temperature of the heat spreader near the microchannel outlet, °C
T _{HS3}	temperature of the heat spreader at its edge, °C
T _{C1} , T _{C2} , T _{C3}	temperature of the microchannel with heat spreader, °C
Al	Aluminum
Cu	Copper
NI	National instruments
T _{A11} - T _{A16}	temperature of the aluminum block, °C
W ₁	width of the microchannel wall, mm
W ₂	width of the microchannel, mm
H	height of the microchannel, mm
D	diameter of the cartridge heater, mm
T _w	total width of the microchannel, mm
L	total length of the channel, mm
T _{sink}	temperature of the minichannel heat sink, °C

IR	infra-red
TEM	tunneling electron microscope
FTIR	Fourier- transform infrared spectroscopy
$C_{p_{nf}}$	specific heat of nanofluid
C_{p_p}	specific heat of the particle
k_{nf}	thermal conductivity of the nanofluid
k_p	thermal conductivity of the particle
n	shape factor
R_i	interfacial thermal resistance
GO	graphene oxide
DLS	dynamic light scattering
T_{con}	conduction temperature due to heat flux, °C
T_{conv}	convection temperature due to the working fluid, °C
T_{hs}	temperature of the hotspot, °C
T_{Ihs}	temperature of the induced hotspot, °C
HSEZ	heat spreader end zone
HSMZ	heat spreader mid zone
PCB	printed circuit board
h_x	local heat transfer coefficient
q''	heat flux, W/cm ²
T_w	temperature measured along the length of the channel, °C
T_f	average fluid temperature, °C
Nu_x	local nusselt number
D_h	hydraulic diameter
k_f	thermal conductivity of the fluid
h_{avg}	average heat transfer coefficient, W/m ² K
A	heat transfer area
Pr	Prandtl number
f	friction factor

\dot{m}	mass flow rate, kg/s
P_p	pumping power, W
T_{HS1}	temperature of the heat spreader, °C
T_{HS}	temperature of the heat sink, °C
T_{EC}	temperature of the end channel, °C
R	real part
\bar{q}	wave vector
T_{Y1}	temperature plane location below the microchannel, °C
X_1	distance between the thermocouple locations in the heat spreader from the hotspot
X_2	distance between the thermocouple locations in the heat spreader
T_{X2}	temperature plane locations in heat spreader edge
T_{X1}	temperature plane location in the heat spreader near the microchannel outlet
T_c	temperature of the core, °C
U	velocity of the thermal wave, (X/t_p)
T_p	temperature penetration time
h_k	coefficient of kapista resistance
g_p	volume power density of the substrate layer
J_1, J_2	temperature jump locations
h	height of the channel, mm
S^\bullet	total entropy generation
$S_{g,HT}^\bullet$	thermal entropy generation
$S_{g,FF}^\bullet$	frictional entropy generation
EX_{out}	exergy out
EX_{gain}	exergy gain
Be	Bejan number

Greek symbols

α_c	channel aspect ratio
θ	non dimensional time, $(T-T_i/T_{ref}-T_i)$
ζ	non dimensional temperature, (t/τ)
τ	thermal relaxation time, (α/v^2)
α	thermal diffusivity, $(k/\rho C_p)$
μ_{nf}	viscosity of the nanofluid
μ_{bf}	viscosity of the base fluid
ϕ	nanoparticle volume fraction
ρ_{nf}	density of the nanofluid
ρ_{bf}	density of the nanofluid
ρ_p	density of the particle
ρ_f	density of the fluid
Δp	pressure drop

Subscripts

nf	nanofluid
bf	base fluid
p	particle
f	fluid
c	channel
HT	heat transfer
FF	friction factor
X1	distance between the thermocouple locations
P	power
HS	heat sink
X	thermocouple locations in the microchannel
Ihs	induced hotspot
hs	hotspot
HS1	heat spreader thermocouple location

i	initial
ref	reference

CHAPTER 1

INTRODUCTION

1.1 INTRODUCTION

The rapid advancement in the field of consumer electronics has drastically reduced the size of the solid state devices and exponentially increased the computational efficiency. Advances in 3D transistor technology further allowed the electronic packaging density to reach the range less than 22nm. As a result, these miniaturized electronic components have occupied a vast application and redefined our working space that has reached a tremendous level where its future growth is highly diversified. Nowadays, it has morphed into flexible electronics, wearable technology, optoelectronics, electronic bio-implants and IoT. However, these devices face bottleneck due to enormous heat dissipation from its increased power density in the transistors. Moreover, lack of concurrent evolution in cooling technologies let the present cooling systems inadequate to meet the new paradigm of these latest compact electronic devices, which will be a challenging and an active field among researchers in coming years. In order to meet the cooling demands of latest high power devices, it is necessary to look for novel and ingenious cooling solutions.

Recently, remarkable works have been reported on microscale heat transfer devices to dissipate heat flux more than $1\text{kW}/\text{cm}^2$ (Faulkner and Shekarriz (2003), Zhang et al. 2015). In particular, microchannel heat sinks have been investigated to a great extent for the application of high density electronic cooling, Singh et al. (2009) and Singh et al. (2011). However, in the case of latest multicore processors the use of microchannel heat sink developed limitations and does not meet the progressive cooling demands of the integrated circuit due to the hotspots. Subsequently, Choi et al. (1995) reported the enhancement in heat transfer based on high thermal conductive fluids with highly dispersed nanosize metallic or oxide in the base fluid. Implementing nanofluid in microscale devices delivered superior heat transfer enhancement for a huge price of pressure drop thereby developing lower device performance. Additionally, the issue on reliability and stability of nanofluid is highly debatable. A substantial amount of studies by Kandlikar (2005) and Han et al. (2016) on microchannels have also put forth a

necessity of novel microscale devices for advanced heat dissipation due to integration issues in the case of two-phase flow. Currently, we are in the golden age of micro fabrication, it further appeals for an innovation in microchannel heat sink design or a hybrid methodology to push the present cooling capability of the microchannel to the next level. However, it is pertinent to note that the importance of novel technologies in microchannels is not only the hour of demand for high density electronic components but also to cool data centers, workstation computers, nozzle cooling for 3D printers, super capacitors thermal management etc. Therefore, the requirement of new sink design to enhance the existing cooling is persuasive by many factors and might provide new insight into many interdisciplinary fields Duryodhan et al. (2017). The above requirements can be approached by methods such as: Designing novel microscale devices (Kewalramani et al. (2019)) for electronic cooling, microscale hybrid cooling devices (involves a combination of two or more cooling technologies), design modifications in existing microchannels etc.

1.2 TRADE-OFFS IN MICROCHANNEL

The current electronic cooling systems majorly employ heat pipes, fins and a combination of both. The use of the fin and heat pipe based cooling system manages to occupy large volume and appeals a huge setback from the perspective of compactness of the device. For example, a normal heat pipe combined with a fan can dissipate ($300\text{W}/\text{cm}^2$) energy and at lower magnitude with only fins ($80\text{W}/\text{cm}^2$) (Tullius et al. 2011). These systems cannot dissipate the latest range of $2000\text{W}/\text{cm}^2$, due to this, the above devices have limitations for recent electronic devices. However, by considering the increased surface area and working fluid one can have better options to move further. Tuckerman and Pease (1981) first coined the concept of microchannel heat sink for high heat flux cooling applications. This path breaking work initiated many other researchers to compare their numerical and experimental works with other microchannel shapes using different fluids in different application domains. Its reduced channel size increases the surface area density; as a result, heat transfer surface area per unit volume increases. This develops a dominant advantage of increasing the volumetric heat transfer of the compact cooling device with decreased thermal

resistance. Besides the above well-established benefits of the microchannel, it also has its own operational limitations as follows:

- Due to the increased surface area, friction factor increases in microchannels leading to higher pressure drop and it further intensifies while introducing high viscous fluids.
- The use of nanofluid or two-phase fluid develops corrosion in the channels and causes a decrement in heat transfer due to fouling effects.
- The mass flow rate in the channels is not evenly distributed, due to this localized high-temperature zone is developed.
- Identifying effective manufacturing process for microchannel that provides near zero surface roughness is very difficult.
- If the above point is reality then the concern about early turbulence and higher pressure drop can be solved. Most importantly, the primary responsible factor that influences heat transfer in the microchannel can be cornered.
- Robust cooling of multicores which are subjected to the various loading heat flux is quite challenging.

However, most of the studies highlight the effects of heat transfer enhancement; but very rare attention is paid on multi-physics effect on the use of integrated microchannel in compact electronic devices. Upcoming new types of designs must facilitate to solve the fundamental problems on heat transfer characteristics and flow phenomenon in micro-meso scale level which eventually bridge the gap to work with an optimized liquid cooling system for the future generation. Thus, there is a thrust for further research in the cooling of electronic devices using microchannel; therefore, it is worth progressing for further designs, techniques and their applications.

1.3 INTEGRATED COOLING DEVICE

In general, the effect of heat conduction in the heat sink for a standalone microchannel is almost different from the case of densely integrated cooling system. Here, the systems are closely integrated such that the neighboring component experiences thermal load. Moreover, packaging heat sinks are integrated to the materials which are not homogenous in all cases. It has several layered structures with different thermal conductivity materials packed as a single module. This allows us to study the additional

aspect of understanding the influence of conjugate nature of microchannel in an integrated domain. From the repeated investigations, nanofluid has emerged as a potential working fluid for microscale cooling systems with better heat transfer characteristics. In such cases, it is equally important to look into the conduction effects of the heat sink in both microchannel and its integrated system. In real time situation with integrated system the effect of increased thermal conductivity in nanofluid can increase the fluid diffusion. As a result, for lower Reynolds number this may develop reliability issues in densely packed components, so it is essential to determine the operating conditions of microscale devices in an integrated setup.

1.4 MALDISTRIBUTION FLOW

Among the different methods of electronic cooling, micro and minichannel heat sinks are highly attractive technique to dissipate high heat flux. In which parallel type channels are studied intensively for their heat transfer effectiveness. However, the smaller hydraulic diameter of the channels develop a low mass flux that results in flow maldistribution. This phenomenon is highly common in parallel type channels with common inlet and outlet. This includes uneven fluid velocity in all channels with reduced effectiveness in heat sink, Datta et al. (2017) and Siddique et al. (2017). Actually, there exist two different types of maldistributions; one associated with improper header design and next one is passage to passage maldistribution due to manufacturing defects. Furthermore, the basic differentiation in manifold types are mainly constructive and bifurcation types in which constructive type is widely used due to lower pressure drop than the bifurcated type.

1.4.1 Maldistribution flow induced hotspot

The flow induced hotspot maldistribution is defined in accordance with the sink design and flow configuration. The most standard flow configuration types are I-type, C-type, and Z-type, refer Figure 1.1. Maldistribution happens due to the non-uniform fluid flow in the microchannels. In the case of I-type parallel microchannels as shown in Figure 1.1(a) the flow rate in the central channels is comparatively higher than the extreme channels. Due to this, the outlet temperature of the extreme channels are higher and there is minimal heat transfer near the outlet region of the microchannels. This gives

raise to two symmetric flow maldistribution induced hotspot region near the outlet which is unavoidable in the case of I-type flow. These effects were observed on several other varied configurations of I-type such as rectangular double layer and I-type with pin fins. Similar, results were observed for C-type and Z-type, shown in Figures 1.1(b) and (c), at different locations of the heat sinks.

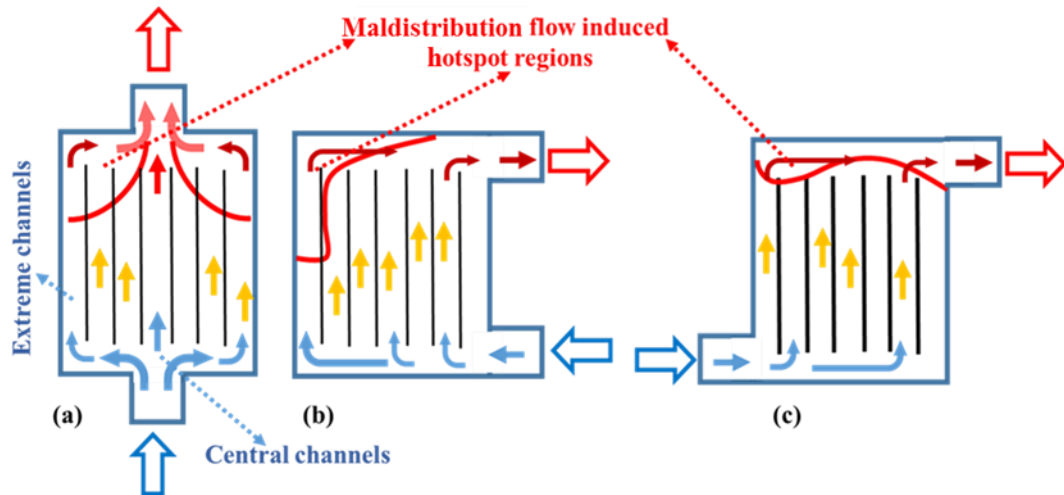


Figure 1.1 schematics of the flow configuration (a) I-type, (b) C-type and Z-type.

Maganti et al. (2018) investigated parallel microchannels to mitigate hotspot using different nanofluid. They noticed that the heat sink undergoes two different hotspot types one which developed due to flow maldistribution and other formed by the localized heat flux developed by the device. Most importantly from all the three flow configuration cases, maldistribution flow induced hotspots are formed at the outlet region of the heat sink irrespective of the sink design and working fluid.

1.4.2 Maldistribution induced axial conduction

In addition, maldistribution increases the axial conduction of the channels and develop localized high temperature region in the heat sink. This is further intensified in the case of nanofluid due to the enhanced diffusion effect of the bulk nanofluid. It was reported that the axial conduction effect approaches the inlet of the channel as a result of enhanced nanofluid bulk conduction effect. Due to this the nanofluid temperature gets increased before it reaches the target heat transfer zones. This effect is noticed for both low and high Reynolds number ranges. In the investigation of Moharana et al. (2011), this phenomenon is highlighted as axial back conduction by using a non-dimensional

axial conduction number (M). They also observed reduced axial back conduction at elevated Reynolds number with decreased conjugate effects. Some studies have neglected the effect of axial conduction by maintaining very low maldistribution ratio and others by reducing the model to one dimensional system. Analytically, perturbation techniques were used in parallel plate with pressure based pulsating flow to investigate the possibility of eliminating axial conduction but it was not successful. Similarly, Metha and Khandekar, (2015) performed investigations on sinusoidal flow at channel inlet and reported null effect on the axial conduction of the channel. Several, researchers reported better numerical and experimental results, but still deviation in temperature is observed due to neglecting the axial conduction in minichannel. Alfaraui et al. (2017) performed investigations by including the axial conduction losses in a minichannel heat exchanger. Maranzana et al. (2004) experimentally found the influence of the axial conduction and its importance in heat transfer investigations.

1.5 EFFECT OF FLOW STRUCTURES

From the perspective of fluid hydrodynamics, the periodic obstructions develop flow redevelopments and flattens the thermal boundary layer which potentially reduces the axial conduction. From several recent investigations, optimization based on channel flow structures generated phenomenal impact in minimizing axial conduction. Novel innovations like fins in corrugated channels and chevron type fins as the flow structures improved the heat sink effectiveness to a great extent. These investigations concluded that in all ways the flow configuration combined with structures increases the effectiveness of the sink. These fins develop localized swirl flow which enhances the localized heat transfer rate with increased outlet temperature due to the drastic mixing. Recently, Hekmatipour et al. (2019) investigated the inclined micro fin structures experimentally. They reported 28% increase in mixed convection as a result of inclined structures and also observed increase in pressure drop for all the cases of flow configurations. By including ribs in wavy channel, pressure drop increased by 185 % more than the straight channel. Besides the structures, investigations were carried with spherical and tear drop dimple configuration. It was found that tear drop structure increases the heat transfer by 17% by enhancing the flow patterns. The complete overview of the present thesis is shown in Figure 1.2.

1.6 OVERVIEW OF THE THESIS

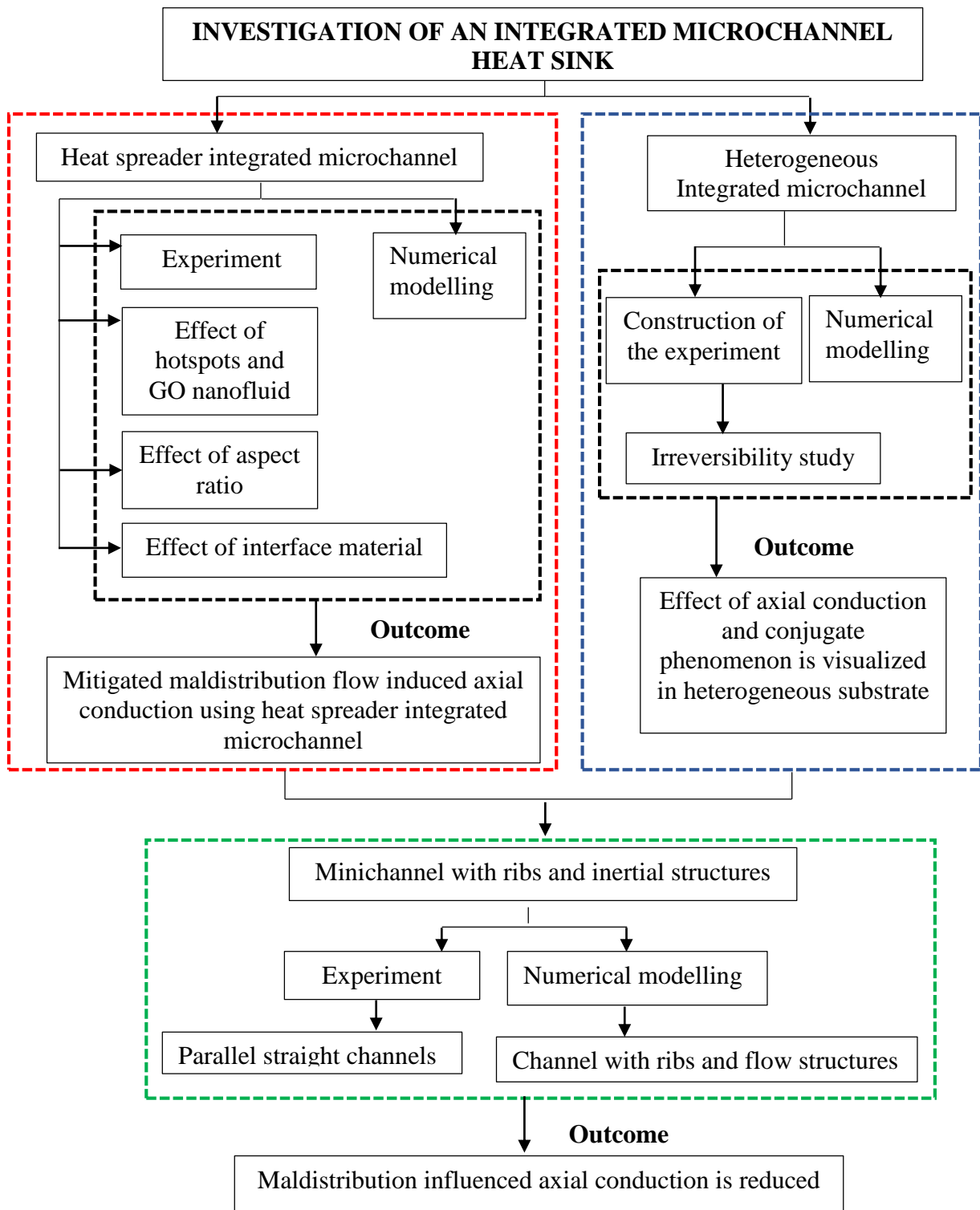


Figure 1.2 Overview of the thesis

1.7 ORGANIZATION OF THE THESIS

Chapter 1 provides a brief introduction on the conjugate heat transfer effects involving an integrated microchannel and nanofluid.

Chapter 2 reports an extensive literature review about different numerical and experimental investigations carried out on microchannel heat sink. The recent investigations relate microchannel heat sink specifically for electronic cooling applications. The effect of heat and flow characteristics in flow structures is additionally captured from the recent literature.

Chapter 3 gives complete constructional details of the experimental setups used in each problem of the current investigations. Also, separate details on different instruments used in the experimentation are discussed.

Chapter 4 presents the thermo physical properties and characterization of different nanofluids. Experimental analysis was carried out to measure the thermal conductivity, viscosity, zeta potential and particle size.

Chapter 5 provides complete details of the investigation on heat spreader integrated microchannel subjected to hotspot. Heat transfer analysis in conjunction with the influence of the heat spreader using nanofluid has been reported. The use of nanofluid to mitigate maldistribution flow induced high temperature zones is also discussed in detail. The effect of high concentration GO nanofluid along with flow rate and nanoparticle concentration is extensively dealt with in this chapter.

Chapter 6 explains the response time phenomenon behind the temperature distribution in the heat spreader. The temperature responses were captured from various locations of the microchannel heat sink and heat spreader which helped understand the bulk diffusion characteristics of nanofluid. Transient experiments were considered to interpret the underlying superposition effects. Nanofluid influenced axial conduction has also been presented elaborately.

Chapter 7 provides the details of the conjugate heat transfer phenomenon for heterogenous substrate. The copper microchannel heat sink has been integrated with aluminium block. Both pure fluid and TiO₂ nanofluid have been used as working fluids.

Experimental studies were performed to investigate the simultaneous conjugate cooling effects under various heat flux conditions. Experimental data is used to perform the irreversibility study. Information such as temperature distribution, entrance effect and power factor has been simulated using 3D computational model.

Chapter 8 presents the experimental and numerical investigations on parallel minichannel implemented with ribs and flow structures to reduce the axial conduction and maldistribution simultaneously. Experimental study for straight parallel channels with I-type flow configuration is carried out. The maldistribution effects with rib and flow structures were numerically attempted. Effect of rib length, height and spacing for different flow rates were considered.

The last chapter highlights the specific contribution made in the work along with the summary of the work. Also a special mention on scope for the future work is presented.

CHAPTER 2

LITRATURE REVIEW

2.1 INTRODUCTION

The latest high performance computers are equipped with multicore processors capable of functioning in time varying loads with extreme clocking. These operating conditions push the workability of the conventional cooling modules to reach threshold degree with extreme compromise in efficiency. Under these circumstances, it is very crucial to employ a robust cooling system for smooth and reliable functioning of the device. To accomplish this, several novel and hybrid cooling solutions were proposed in recent past. One among them is the highly established microchannel heat sink with better techno-economical solutions under high heat flux conditions.

2.2 NUMERICAL STUDY IN MICROCHANNEL

Kalteha et al. (2011) numerically investigated forced convection of nanofluid in a microchannel using a two-phase method by implementing Finite Volume Method (FVM). They coupled both the phases of copper water nanofluid to simulate the Eulerian two fluid model. Cosine weighting function is used to refine the grids of the wall and entrance length of the channel. Line by line method is used in numerical scheme and power law for discretizing the convection and diffusion terms. Mass conservation of the particle and fluid was obtained for pressure correction equation in order to use SIMPLE algorithm. They state that the two-phase model provides the uniform distribution of nanoparticles throughout the flow region. They numerically depicted that the nanoparticles inclusion increases the thermal boundary layer significantly.

Izadi et al. (2009) numerically studied the performance of Alumina nanofluid in an annulus. Single phase model has been implemented to study the hydrodynamics and thermal characteristics of nanofluid. According to their study, there is no change in dimensionless velocity due to the increase in volume fraction but the temperature distribution is highly influenced by the volume fraction. Single phase model assumes the use of ultra-fine nanoparticles which is in the range less than 50 nm. The numerical

computation was carried out for various Reynolds number ($Re = 100-900$) and volume fraction ($V_f = 0-5\%$) for a particle diameter of 25 nm.

Nimmagadda and venkatasubbaiah (2015) discussed the numerical studies on conjugate heat transfer analysis using hybrid nanofluid (Al_2O_3 and Ag/Water). The studies reported the effect of various Reynolds number, volume fraction and particle size with water as base fluid. The governing equations were computed by Simplified Marker and Cell (SMAC) procedure with a non-staggered grid using FVM. Further, the interface temperatures between solid and fluid regions for different nanofluid were also analyzed. Results provide 148% increase in heat transfer coefficient for the use of (0.6vol% Al_2O_3 + 2.4vol% Ag) than the pure water.

Li and Kleinstreuer (2008) presented a numerical investigation with trapezoidal microchannel using CuO/water nanofluid. The analysis was performed for the particle diameter of 28.6 nm for the range of 1-4% of volume fractions. The computations were carried out to compare KKL (Koo- Kleinstreuer-Li) model with Brownian- motion model. For a maximum volume fraction of 4%, pressure drop was found to increase by 15%.

Akbarina et al. (2011) performed an investigation on rectangular microchannel with alumina nanofluid using FVM. The analyses were intended to study on slip and non-slip flows regimes in microchannel. Their results state that the increase in volume fraction does not enhance the Nusselt number, on contrary; the inlet velocity augments the heat transfer. The particle concentration does not have considerable effect in Poiseuille number for examined Reynolds number.

Tsai and Chein (2007) analytically reported the investigation of microchannel heat sinks using copper-CNT/Water nanofluid. The results were obtained for thermal resistance and performance characteristics of nanofluid. They found reduction in conductive thermal resistance and thermal capacity of the sinks by using nanofluid. This analysis was performed by including the porous medium model for nanofluid used in the microchannel and the result suggests that better performance was obtained for optimum porosity and aspect ratio. They used a channel height of 364 μm with 88 channels for 4% volume fraction.

Abbassi and Aghanajafi (2006) investigated conjugate heat transfer in a microchannel heat sink using a combined analytical and numerical approach. The governing equations were based on porous medium model accompanied with Darcy equation. The study involved assuming the ultrafine copper nanoparticles dispersed in a base fluid. The thermal dispersion model is adopted for heat transfer analysis and it is also integrated with the effect involving interfacial shells between nanoparticles and base fluid. They also investigated the influence of particle concentration, Reynolds number and thermal dispersion coefficient. Work is extended to find the effect of heat transfer in a turbulent region. It also reveals that nanofluid does not influence the temperature distribution of the channel wall.

Zhou et al. (2005) conducted a numerical study on silicon microchannel within a trapezoidal and triangular cross section using water as cooling fluid. The governing equations were discretized using FVM. Field synergy principle was discussed on the effect of varying Reynolds number and its influence on channel geometry. From their studies it was found that, velocity and temperature gradient are in better synergy when the Reynolds number is less than 100. Their study suggests that trapezoidal geometry provide better heat transfer. Their investigation concluded that the Nusselt number was found to increase in fully developed region which is contradictory for the case of conventional ducts.

Li et al. (2019) performed optimization study by using field synergy principle. They particularly analyzed synergy field angle, flow and temperature field. They used inclined cavities to develop heat and fluid flow relations between cavities and synergy field. They used 3D computational domain and conjugate heat transfer model to solve the problem. They have neglected the effects of viscous dissipation and thermal effects. They reported that increase in cavities increases the heat transfer intensity. They also observed that the increase in number of cavities increases the fluid compression and expansion effects which led to increased frictional resistance with reduced overall performance. The numerical heat transfer performance and synergy field effect have great effect on axial conduction, entrance effects and redevelopments in boundary layer and perturbation effects.

Kumar (2019) investigated the trapezoidal microchannel with groove structures numerically. They used finite volume method and investigated with Reynolds number ranging from 96 to 720. They observed that nearly 12% increase in heat transfer on comparison with straight and trapezoidal channels. They observed 28% increment in heat transfer on using groove structures and concluded that the enhancement is due to the flow redevelopments and thermal boundary layers. They reported that the semicircular grooves have 16% more heat transfer than the rectangular grooves with higher pressure drop. They have specifically highlighted that for a constant channel groove area, the groove width is more influential than channel height to enhance heat transfer.

Shen et al. (2019) performed numerical investigation to improve the thermal performance in microchannel by using flow arrangements such as concurrent flow and counter concurrent flow on the double layer. The best condition was observed for novel staggered flow alteration structure. Double layer microchannel was found good for multi flow directions. Also, changing the location of the staggered alteration structure does not result in increased pressure drop for the case of double layer microchannel. The upper inlet counter concurrent arrangement significantly improved the thermal performance by providing the staggered flow arrangement at the center of the microchannel. They reported that the use of lower inlet counter flow arrangement is less efficient than all the counter flow arrangement. Since the energy is transferred predominantly to the upper deck of the microchannel. They highlighted that by using staggered flow counter microchannel, two high temperature locations were developed in the microchannel double layer.

Snoussi et al. (2018) performed numerical simulation to enhance the heat transfer of microchannel heat sink. They reported that under increased heat flux more than the pure fluid the effect of nanofluid is highly dominant. They observed decrease in heat sink temperature on higher volume fraction nanofluid. They reported a pressure drop increment of 24% by increasing the particle fraction from 0-2%. On using pure fluid they observed that the heat transfer coefficient has no effect on the subjected heat flux.

Sabaghan et al. (2016) performed numerical simulation using two phase Eulerian approach for microchannel using vortex generators. They used TiO₂ nanofluid with

different base fluids where particle concentration varying as 2-3%. They observed enhanced heat transfer rate on implementing the vortex generators. They highlighted that the efficiency of the nanofluid degrades at higher Reynolds number and increase in nanoparticle diameter also degrades the heat transfer enhancement. On the other hand, at higher volume fraction nanofluid, the local heat transfer coefficient gets enhanced on using longitudinal vortex generators.

Wang et al. (2018) performed numerical investigation on inclined rectangular ribs in a microchannel heat sink. They reported that the crucial factors of flow distribution enhance the heat transfer of microchannel. According to them this enhancement is due to the factor such as chaotic advection, enhanced heat transfer due to increase in area of the fins and due to the thermal boundary layer disturbance. Having investigated both single ribbed channel and double ribbed channel both encourage chaotic advection. But in the case of developed vortexes more stable vortexes are developed for the case of double ribbed channel. But the scenario was different for the ribs with lesser angle of attack and at lower Reynolds number.

Vinothan and Rajan (2014) numerically investigated microchannel heat sink with different flow configurations. They reported that the use of new multi flow type configuration decreases the thermal resistance by 50% than the conventional microchannel heat sink. They reported that the maximum heat transfer was observed near the bends of the microchannels. They extended that the presence of the bends increases the vortexes and reduces the thermal gradient and remaining places are developed with hotspots. Also, they observed higher Nusselt number at the entrance of the microchannels with increased number of entrance than their channels with higher bends.

Akbari et al. (2019) numerically investigated a novel cavity based microchannel using nanofluid. They reported that the addition of cavity structures alters the velocity component with enhanced fluid mixing. As a result, the nanofluid develops better thermal equilibrium with the microchannel floor due to the increased heat absorption. The use of dimples increases the secondary flow with elevated fluid temperatures.

2.3 EXPERIMENTAL STUDIES ON MICROCHANNEL HEAT SINK

Manay and Sain (2017) conducted experiments to study the influence of channel height on heat transfer and pressure drop characteristics. TiO₂ with the particle diameter of 25 nm dispersed nanofluid with volume fraction ranging from 0.25 to 2% was considered. The work was carried out with four different channel heights ranging from 200 to 500µm for a constant flux. Their results provide that increase in channel height increases the pressure drop and reduces the heat transfer rate. However, the TiO₂ nanofluid enhanced heat transfer than pure fluid.

Rimbault et al. (2014) performed an experimental study on copper oxide nanofluid in a microchannel heat sink with a particle diameter of 29 nm. Tests were conducted with different volume fractions ranging from 0.24 to 4.5% for both laminar and turbulent regimes. The conditions of isothermal and varying temperatures were analyzed for *Re* 2500 and 5000. Additionally, 70% increase in friction factor is noted for a volume fraction of 4.5%. From the results of suspended fluid, they observed that the transition from laminar to turbulent at *Re* = 1000 was seen similar to that of water. Also, behavior of nanoparticles does not have an impact when we include pumping power to our analysis and further decrease when volume fraction is increased.

Zhang et al. (2013) experimented with Alumina nanofluid in a circular microchannel with the diameter of 500µm with the particle volume fraction ranging from 0.25 to 0.77%. Tests were focused to determine the effect of nanoparticles over the Nusselt number and particle concentration. Increase in heat transfer was observed for maximum volume fraction with the increment of 10.6%. A correlation was also proposed for the Nusselt number with the experimental results with a deviation of -4% and +5%.

Peyghambarzadeh et al. (2014) performed an experimental investigation on rectangular Cu-Be alloy microchannel with CuO and Al₂O₃ nanofluid. The study was performed for a constant heat flux of 19W/cm² with the Reynolds number ranging from 500 to 2000. The study performed in a channel dimension of 400 x 560µm with 17 channels to analyses heat transfer coefficient, Nusselt number and pressure drop. Maximum enhancement was provided by alumina nanofluid of 49% with 1% volume fraction

compared to that of copper oxide of 27% with 0.2% volume fraction. According to them, CuO has better enhancement than alumina; they also registered that increment is not due to volume fraction but due to increased Reynolds number.

Ahmed et al. (2016) conducted an experimental study on double layered microchannel with triangular and rectangular cross sections. The experimental series was carried out by suspending alumina and silicon nanoparticles. According to their study, double layered channels provide better performance compared to conventional single layered. Their results showed that triangular double layer provided wall temperature reduction by 27.4% than double rectangular layered and it also provides better uniformity of temperature. The triangular double layer has 16.6% less thermal resistance; moreover, there were no significant changes in pressure drop for both the cross-sections.

Xia et al. (2016) conducted an experimental study on microchannel heat exchangers using oxide nanofluid like alumina and TiO₂. The nanofluid was prepared by a two-step process with the volume fraction ranging from 0 to 1%. They used PVP (Poly Vinyl Pyrrolidone) for the stability of particle and also to reduce aggregation. They have used IR imaging to investigate the temperature distribution over heat sink. This reveals that thermal motion of nanoparticles would influence the early breakage of laminar flow and enhance the fluid and channel wall heat transfer.

Anoop et al. (2012) performed experimental studies on microchannel with the suspensions containing silica nanoparticles for constant wall temperature conditions. Their results showed that an increase in flow rate enhanced heat transfer for both pure fluid and nanofluid. However, comparatively higher enhancement is seen for lower flow rates using nanofluid. They also performed a fouling test on microchannel by performing electron microscope examination due to nanoparticles precipitation.

Yang et al. (2016) performed numerical and experimental studies on different sets of pin fin arrangements. The objective of the study is to maximize the heat transfer rate by analyzing the hydraulic performance of the heat sink.

Lin et al. (2019) performed critical investigation on thermal management using integrated microchannel for the application of cooling light emitting diodes. The study highlighted different combination of the heat dissipation modules including heat sinks

and thermoelectric cooler. Based on the Taguchi method the orthogonal experiments predicted most influential parameters such as: thermoelectric cooler current, working fluid inlet temperature, fluid velocity and room temperature. They observed a very poor performance for the combination of thermoelectric cooler and conventional heat sink. On other hand, superior results were observed by integrating microchannel with light emitting diode and the thermoelectric cooler. From Taguchi analysis, it was found that among all the four factors the thermoelectric cooler current played a major deciding factor on the heat sinks effectiveness.

Hadad et al. (2019) conducted a combined numerical and experimental investigation on a multi die processor using a rectangular microchannel. The effect of the interfacial material in the processor die and the heat spreader temperature distribution is effectively presented with numerical simulations. Further optimization studies were conducted to reduce the maximum processor die temperature with a minimal pressure drop. They reported that the performance of the microchannel heat sink is highly dependent on the width of the channel. It was also suggested to use shorter fins for maximum thermal enhancement with lower pressure drop.

Ozguc et al. (2019) demonstrated a novel heat spreader containing vapor chambers for the application of electronic cooling subjected to hotspots. Their experimental results reported a successful reduction in overall thermal resistance of the device by effectively spreading the heat from the hotspot. They added that a better uniformity in surface temperature was observed in the condenser at the charged condition than the empty chamber. Similar investigation on heat spreader based thermal management devices are summarized in Table 2.1.

Table 2.1 Summary of heat spreader investigations integrated with microchannel heat sink.

Authors	Study type	Performed Investigation	Outcomes
Soliman and Hassan (2018)	Numerical	Heat spreader is added with microchannel to enhance the solar cell performance and it uses microchannel beneath the heat spreader.	Adding heat spreader, microchannel developed lowest temperature in the solar cell with improved solar cell efficiency and electrical output.
Soliman et al. (2018)	Analytical and Numerical	Mathematical approach dedicated to analyze the effects of heat spreader with microchannel at the bottom of the heat spreader.	The presented model showed 15°C lower temperature in photovoltaic solar cell module with increment in efficiency up to 19%.
Lee et al. (2018)	Experimental	It uses 3D printed heat spreader with dedicated channels through which the fluid is flown to cool laser driven head lamp.	With the use of heat spreader the generated performance was comparatively better than thermoelectric cooling.
Kelly et al. (2018)	Experimental	Use of fractal pulsating heat pipe in heat spreader to perform thermal management for hotspots in electronic components. In this case the radial pulsating pipe is provided in the heat spreader itself.	Result showed effective thermal spreading of hotspot. The study presented decrease in temperature by 23°C for the case of 30W heater power using heat spreader.
Tian et al. (2019)	Experimental	Investigated on embedded pulsating microchannel on alumina heat spreaders.	It resulted in lower thermal resistance as same as that of metals which is about 0.3 K/W. They reported an optimal binder of 2.5 wt% to reduce cracking.

2.4 ELECTRONIC COOLING USING MICROCHANNEL HEAT SINK

Localized high-temperature regions in processors are referred to as hotspots, these are developed due to high speed circuits, due to which lower transistor threshold voltage develops a higher source to drain leakage. This leakage current in the transistor is a limiting factor on the development of lower power processors since this generates hotspots. However, comparatively lower temperature is witnessed by cache zones of microprocessor this produces a non-uniform power and temperature distribution in the processor. Due to this, the temperature difference in the processors tries to reach up to 5 to 30K. This hotspot is an acute issue for the latest highly integrated compact devices and has the potential to reduce the effectiveness of the cooling system. Several critical studies to mitigate hotspot are performed using various methods some of which are listed in Table 2.2.

Sharma et al. (2016) performed numerical approach on hotspot targeted conjugate heat transfer studies and additional investigation on optimization on the power maps in multicore by providing a non-uniform heat flux at different regions ranging from 20 to 300W/cm². They used response surface model (RSM) to optimize the system by majorly concentrating to develop an optimal channel structure combined with a better flow rate. By optimizing the system non-uniform temperature distribution got reduced by 54% for a steady heat flux of 300W/cm².

Maganti et al. (2017) performed an investigation on selecting an optimal parallel microchannel to target hotspots in multicore processor. They have used Intel i7-4770 processor for their study. Additionally, investigation of fluid maldistribution accompanied with induced temperature maldistribution is captured by both numerically and experimentally. Eulerian- Lagrangian models were considered for modeling the nanofluid flow in the system. They concluded that the increase in flow maldistribution concurrently increases the thermal maldistribution.

Drummond et al. (2016) investigated the intra chip hotspot cooling using hierarchical manifold based microchannel cooling. They investigated the hotspot fluxes greater than 2500W/cm² and maintained 30°C as the average temperature of the chip with a pressure drop generated up to 75 kPa. Inlet and outlet are provided perpendicular to the chip.

Lee et al. (2015) conducted an experimental investigation on the obliquely finned microchannel heatsink. Here, they investigated the effectiveness of the oblique fin by varying the fin pitch for cooling hotspot regions. They reported that more than two hotspot condition the performance of the oblique enhanced microchannel developed more uniform temperature in the microchannel.

Han et al. (2015) performed an experimental investigation on hotspots cooling using diamond heat spreader accompanied with microchannel Gallium nitride (GaN) heat sink. Additionally, numerical investigation was performed using COMSOL software considering temperature dependent material properties. The hotspot was developed by 8 micro heaters with power varying from 10 to 50W. They observed that by providing diamond heat spreader the maximum heater temperature reduces up to 22.9%.

Narayanan et al. (2010) developed a thin film based evaporating cooling to target hotspots which are implemented by impinging dry air over the capillary assisted porous membrane with a thickness of 15 μ m. Here, they have demonstrated for higher heat flux range which is more than 600W/cm² where heat transfer coefficient reached up to 0.1MW/m²K.

Sharma et al. (2019) performed numerical investigation on thermal hydraulic performance of microchannel with different textures. On comparison between square, triangle and herringbone configurations better thermo hydraulic performance was generated for herringbone texture. It was found that the effect of fluid inertia and friction factor is profound for the microchannel with larger flow constrictions.

Moraveji et al. (2019) performed investigation on thermo hydraulic effectiveness of microchannel using CuO nanofluid for laminar regime. The major objective of this study is to distinguish a modest model for nanofluid study in microchannel. They used very low volume fraction nanofluid ranging from 0.005 to 0.01%. It was critically found that for the case of higher volume fraction nanofluid single phase method predicted exact results.

Table 2.2 Summary of investigations on hotspot management for electronic cooling with different techniques.

Authors	Study type	Performed Investigations	Outcomes
Wang et al. (2009)	Experimental and Numerical	Investigation of hotspots in densely packed component using thermoelectric cooling.	The results showed that hotspot of 1250 W/cm ² heat flux can be reduced to 17°C with 20µm thermoelectric mini contacts.
B-Cohen and Wang (2012)	Experimental and Numerical	On chip thermal management of hotspot using thermoelectric micro coolers and two- phase micro gap coolers.	Their results shows that effect of heat spreader is dominant in reducing the hotspot and for better cooling effect micro cooler must be larger than that of hotspot.
Ansari and Kim (2018)	Numerical	A hybrid rectangular microchannel combined with cylindrical micro fins to cool hotspots.	The hybrid sink maintains 30.6% lower hotspot temperatures with 11.7% higher pumping power.
Pi et al. (2018)	Experimental	Presented an effective method to estimate the hotspot temperature on multiple hotspots.	Results showed that cooling performance of the device decreased with decrease in hotspot size.
Lorenzini et al. (2016)	Numerical	Investigated embedded microfluidic cooling by implementing micro gaps between pin fin structures for mitigating hotspot.	Results showed that the embedded cooling design effectively maintains the device temperature below 65°C with a marginal increase in pressure drop.
Green et al. (2009)	Analytical and Experimental	Presented a chip level thermal management by a compact fluid -to -fluid spot-to -spreader hybrid heat sink.	Results showed effective cooling of hotspot heat flux near 1000 W/cm ² .

2.5 MICROCHANNEL WITH STRUCTURES

Yang et al. (2017) performed experimental and numerical studies on microchannel with different pin fin shaped like a rhombus, hydrofoil and sine with a top area of 0.0625 mm^2 and the entire surface area of 1061119 mm^2 . From their numerical simulation, they found that sine type pin fins develop comparatively better results than the remaining at the flow rate of 100 ml/min with a heat flux of 144 W/cm^2 . Similarly, the lower pressure drop of 15 kPa is obtained by using sine type pin fins for maximum velocity of 4.46 m/s .

Ghani et al. (2017) conducted a numerical investigation on microchannel containing sinusoidal cavity with rectangular ribs for Reynolds number ranging between 100 and 800. The studies were performed by considering the parameters like Nusselt number and friction factor. According to them, the combined output of sinusoidal cavities with rectangular ribs is superior to cavities and ribs of the other designs due to the increased surface area but interestingly with reduced friction factor. The best heat transfer results were found for the Reynolds number of 800.

Tokit et al. (2012) performed a numerical investigation on interpreted channels with nanofluid as cooling fluid. They have studied Al_2O_3 , CuO and SiO_2 nanofluid with a volume fraction ranging from 1 to 4% under the Reynolds number ranging from 140 to 1034 with a particle diameter of 30 to 60nm. According to them, the augmentation in heat transfer is due to an increase in volume fraction with decreased particle size and maximum enhancement was reported for Al_2O_3 nanofluid. Interpreted channels developed higher heat transfer than the conventional straight channels with comparatively higher pressure drop.

Chai et al. (2016) conducted numerical simulation on different types of interpreted ribs in a micro chamber. They have showed that with the use of ribs, local heat transfer coefficient can be incremented. They have used rectangular, triangular, diamond and ellipsoidal rib types in which ellipsoidal design developed a better heat transfer than other types of ribs. The maximum Nusselt number was seen for the Reynolds number 75 with an increment of 57% with an increased friction factor of 70% compared to conventional channels.

Chen et al. (2017) conducted an investigation on entropy generation due to pin fin cylindrical structures. Their study includes developing an optimal system with inlet velocity, heat load and finning material. They found that the generation of entropy increases with increasing aspect ratio of the sink and concluded that by opting reduced fluid velocity

with less aspect ratio accompanied with increased material fraction can provide minimum entropy condition.

Wong and Lee (2015) studied microchannels with triangular ribs in micro chambers to develop an optimal design by varying its design parameters. They studied parameters like friction factor, Nusselt number and thermal enhancement factor. They observed that the heat transfer increases with the increase in design parameters like width and height but reduces with increasing length. They registered a highest Nusselt number for Reynolds number of 500 with width, length and height of 100, 400 and 120 μm , respectively, up to 56% enhancement with conventional channels.

Abdoli et al. (2015) conducted numerical studies on pin fin structures for the application of cooling high heat flux in electronic devices. Their investigation on shapes includes circular, hydrofoil, convex and altered hydrofoil with staggered fin arrangement. They have used a hotspot value of $2\text{KW}/\text{cm}^2$ for an area of 0.25mm^2 but remaining zones with $1\text{KW}/\text{cm}^2$. According to them, hydrofoil pin shape found better than the other designs with a reduced pumping power of 30.4% and 3.2% more effective than circular pin fins. They found that the altered hydrofoil fin decreases the maximum temperature by 6.4°C than circular design.

Shahabeddin et al. (2014) investigated the effect of nanofluid on micro fins based heat exchangers. According to them, providing lower nanoparticle volume fraction can develop better Coefficient of Performance (COP) with reduced entropy generation. Additionally, under lower Reynolds number, the effect of nanoparticle has negligible effect with increased COP when alumina nanofluid was used as the cooling fluid. The study was performed by providing heat exchanger on both sides of the thermoelectric generator by switching cooling fluid on both hot and cold end. Recently, a cooling system dedicated to micro fins with hydrophilic/hydrophobic surfaces involving under higher heat flux was developed for higher heat flux condition that resulted in better performance.

Zhao et al. (2016) optimized micro pin fin arrangement for the application of electronic cooling with porous media. Here, the investigations were carried out by allowing the porosity values with altered pin fin locations. They have registered an equal importance of the above two parameters for heat transfer enhancement and an optimal porosity of 0.75 with a square rib angle of 30° was recommended. In the case of porous based pin fin cooling under a velocity of 1.44 m/s a maximum Nusselt number of 24 was developed with a

pressure drop of 4.6 kPa. With the flow velocity of 1.44 m/s, Nusselt number increases with increased pressure drop up to 15% for porosity of 0.56.

Vinoth and Senthilkumar (2017) performed experimental studies on microchannel with oblique fins, alumina nanofluid along with 0.25% volume fraction. Three different cross sections were used like square, semicircle and trapezoidal. Here, the study is majorly intended to investigate flow hydrodynamics on these different designs with varied mass flux. Trapezoidal fin develops a 5.878% increased heat transfer with nanofluid as working fluid, this is comparatively higher than other cross sections. They suggested the use of trapezoidal fin configuration for the application of electronic cooling than other fin types.

Adeyemi et al. (2013) observed that addition of pin fin increases the global thermal conductance. Better results were obtained for limited three fin configuration but six rows above that the effect of heat transfer is negligible. They found that increase in Bejan number reduces the peak temperature of the microchannel. They concluded that microchannels with few rows having less aspect ratio provide the best results. The pin fins with integrated domain performed better for decreased fin length for all the cases.

Shafeie et al. (2013) observed that the performance of microchannel is enhanced by increasing the height of the fin. Optimal fin height of 300 μ m is recommended which provided better thermal performance. Performance of higher aspect ratio pin fins is better in smaller channels. They reported that for a constant pumping power oblique fin pattern provides better heat removal than staggered fin. It was also observed that finned heat sink had better performance than optimal microchannel for the case of lower pumping power.

Xie et al. (2014) observed that with the increase in bifurcation stages develops higher pressure drop. Additionally the local velocity in the microchannel with bifurcations is higher than the smooth channels and it is also a function of plate length. Addition of bifurcation increases the thermal enhancement factor by 1.78 times more than normal channels. On comparison with bifurcation configurations, it was observed that single stage bifurcation has better performance than multistage microchannel. In the case of multistage bifurcation the microchannel overall thermal resistance decreases with uniform temperature throughout the sink.

Li et al. (2014) obtained thermal enhancement by varying angle of Y arms and inlet velocity. Result shows that when the angle between Y arms increases pressure drop also

increases. Additionally, the Y shaped bifurcations reduced the thermal resistance compared to conventional microchannel. The comparison with five different Y- shaped bifurcation plate configuration showed that the thermal performance of the microchannel with bifurcation is better than the straight channels. They reported that the Y-shaped arm with 90° angle provided better performance.

Lee et al. (2012) investigated oblique microchannel performance is better than normal microchannels by minimizing the total thermal resistance under increased Reynolds number. By introducing oblique fin in microchannels provides uniform heat removal capacity throughout the sink. Boundary layer thickness is reduced along the flow direction and supports secondary flows with frequent redevelopment. Nusselt number increments 47% more than conventional microchannels. The heat transfer augmentation is better for fin angle 27°. The increased pressure drop was marginally compensated by the diffuser effect found in the diverging section, where the pressure is recovered.

Brinda et al. (2012) reported three stage ladder microchannel generates that 3.85 kPa which is 162% more than the conventional channels. Implementing 10 stage ladder substrate temperature is decreased by 7.3°C for $Re = 400$ and for $Re = 2000$ it reached up to 4.4°C. By extending till 10 links microchannel thermal resistance drops by 20%. From numerical investigation it was observed that increase in ladder number elevates the pressure drop to a great extent with better heat transfer. On the other hand, by using higher ladder stages decrement in thermal resistance was reached up to 20%. In case of rigidity of the microchannel a marginal decrement in mechanical strength was observed by crossing three ladder links.

Chai et al. (2013) reported that the introduction of the ribs increases the fluid mixing and develops recirculation and vortex generation beside the channel wall. Stagnation zone is developed behind the rectangular rib where the maximum pressure is seen in the microchannel. They suggested that for $Re < 600$ microchannel with rib is beneficial and more than $Re > 600$ ribs with interrupted microchannel is better. Further thermal enhancement factor is reduced if Reynolds number is more than 0.1mm of rib length.

Liu et al. (2011) observed that both heat transfer and friction factor increase with an increase in Reynolds number using staggered square pin fins. Transition of friction factor

is observed at $Re = 300$. They proposed a new correlation for Nusselt number and used 625 square fins in a staggered arrangement.

Aliabadi et al. (2017) used alumina nanofluid as the working fluid with 0.1 and 0.4% volume concentration. Implementation of the ribs enhances heat transfer by chaotic advection of working fluid. For the observed Re of 100-900, the maximum heat transfer coefficient of 128% with maximum pressure drop of 185% is observed. Oblique positioning of the ribs is the best for wavy microchannel. Volume fraction of 0.4% nanofluid developed maximum heat transfer of 19.3% with 15.6% pressure drop.

Chai et al. (2016) observed with increase in rib length and its spacing between them develops a decrease in average friction factor but along the length it increases. By increasing the height of the rib and lowering the ratio of the rib length to its spacing also increases the friction factor. But for the microchannels having offset rib placement has developed lesser friction factor.

2.6 IRREVERSIBILITY

Xie et al. (2016) performed analytical investigation on entropy generation of Al_2O_3 -water and Al_2O_3 -ethylene glycol nanofluid using a circular pipe. They observed increase in frictional entropy generation for nanofluid at higher particle fraction. Furthermore, optimal working condition was suggested for nanofluid based on entropy generation. The use of nanoparticle in the base fluid is positive when thermal irreversibility is dominant. The use of 1% nanoparticle volume fraction reduced the entropy generation by 3.6% and the maximum decrease in entropy generation was found in case of 5% volume fraction for both the base fluids. It was found that for flow rate lesser than $Re = 40,000$ the use of nanoparticle was significant.

Li and Kleinstreuer (2010) performed irreversibility studies in trapezoidal microchannel using water and CuO water nanofluid. It was suggested that the micro heating systems requires special attention for frictional entropy generation at higher velocity situations. Frictional entropy generation is higher near the walls for higher aspect ratio and its location get shifted in case of channel with lower aspect ratio. For all the investigated channel configurations the channel center and corners does not have frictional entropy generation. In case of increased fluid inlet temperature the decrease in total entropy generation was

observed due to the increased bulk fluid temperatures. They recommended lower volume fraction nanofluid for increased thermal performance with better entropy minimization.

Sohel et al. (2013) performed entropy generation analysis with different nanoparticle and basefluid for a varied particle volume fraction ranging from 2% to 6%. In which Cu-H₂O nanofluid delivered the maximum reduction in entropy generation of 38% at 6% of nanoparticle volume fraction. They also reported that smaller particle diameter develops lower entropy generation. Alumina nanofluids developed entropy generation greater than unity but in case of CuO the entropy generation was lower than unity. The total entropy generation was found identical for both the case of CuO and Al₂O₃ nanofluid, but found different in the case of different basefluid.

Manay et al. (2018) investigated the irreversibility effects using TiO₂ nanofluid. The TiO₂ is suspended in from the range of 0.25% to 2.0% under different channel heights ranging from 200 μm to 500 μm. They observed increase in total entropy generation due to friction than thermal irreversibility at higher particle volume fraction. Further, increasing the channel heights yields higher thermal entropy generation from 30% to 52% on other hand decrease in channel height increased frictional entropy generation from 66% to 78%.

Singh et al. (2010) performed theoretical investigation on entropy generation using Al₂O₃ nanofluid. Their investigation suggested to use high viscous nanofluid in microchannels for the case of turbulent flow in conventional channels. They observed higher frictional entropy generation at lower tube diameters for both laminar and turbulent regimes. Results predicted that the frictional entropy generation is twofold higher for turbulent regimes than laminar flow. In turbulent regime the thermal entropy generation is not dependent only on conductivity of the fluid but also viscosity plays a major role. They found that the thermal entropy generation of minichannel is almost similar to that of microchannel.

Bahiraei et al. (2017) investigated irreversibility characteristics of water-Boehmite alumina nanofluid with different nanoparticle shapes in microchannel heat sink. The study was conducted for five different shapes for Reynolds number ranging from 300 to 1800 with a fixed particle concentration of 1%. Irrespective to the nanoparticle shape the thermal entropy generation is decreased with the increase in Reynolds number and highest entropy generation was developed for spheroid nanoparticle. The variation in thermal entropy generation is minimal due change in Reynolds number but increase in frictional entropy

generation is very significant. At elevated Reynolds number the most optimized nanoparticle shape is platelet shaped with a lower irreversibility.

Li et al. (2020) investigated bio inspired shark skin flow controls to augment thermal performance of microchannel heat sink. They developed four different models to improve the temperature uniformity in the device in a laminar flow regime. Temperature performance steadily improved for all models at increased Reynolds number range. At lower Reynolds number the maximum thermal performance was developed for the model with smaller entropy generation. In case of increased Reynolds number of 500 both thermal performance and entropy generation was higher for the model with least flow area. These bio inspired structure along the flow length redirects the primary flow towards the channel wall but the secondary flow developed is not sufficient enough to develop uniform temperature on the side walls.

Rashed et al. (2019) performed numerical investigation on irreversibility studies in wavy walled microchannel using silver nanofluids. The parameters such as particle fraction, Reynolds number, wave amplitude and wavelength of the channels are studied focusing heat transfer coefficient. Increase in Reynolds number and nano additives enhances the heat transfer coefficient and significantly decreases the processors surface temperature. But on other hand, adverse effects were observed with elevated frictional entropy generation for higher Reynolds number and particle concentration. Total entropy generation rate was decreased with increase in channel wavelength but it increases the microchannel heat sinks hydrodynamic performance. Further, increase in the channel amplitude above 138 μm decreases the performance evaluation criterion and in case of higher wavelength it increases the performance evaluation criterion.

Khosravi et al. (2019) performed irreversibility studies on cylindrical microchannel liquid block using graphene-platinum nanoparticles. The microchannel used has a hydraulic diameter of 564 μm with thirty six individual channels. Increase in particle concentration augmented the heat transfer and frictional entropy generation but thermal entropy generation was reduced. They pointed out that the influence of Reynolds number is more significant on entropy production rate than particle fraction. Further, in both the cases reduction in Bejan number was observed. Additionally, artificial neural network with 10 neurons employed with single hidden layer to predict entropy generation rates.

Li et al. (2020) performed numerical study for Ag-MgO/water hybrid nanofluid in sinusoidal hairpin heat exchanger. The factors such as Reynolds number, particle concentration and amplitude of sinusoidal waves are studied with the heat exchanger performance from first and second law perspective. They found that increasing volume fraction and Reynolds number augments the heat transfer but it directly degrades the heat sink performance. Additionally, their results revealed that the irreversibility due to heat transfer is dominant for the use of hybrid nanofluid and with increase in amplitude of the sinusoidal hairpin.

Shen et al. (2020) proposed x-structural double layer microchannel heat sink to augment the heat transfer of conventional double layer microchannel. It was reported that the new configuration developed higher entropy generation number with better thermal uniformity. They observed that the structure was able to maintain significantly lower temperature gradient with negligible increase in pressure drop. By increasing the overlap ratio of the x-structure, the increase in pressure drop was observed with a minor enhancement in overall thermal performance.

Sindhu and Gireesha (2020) performed analytical investigation for entropy generation studies using AA705 and Ti₆Al₄V alloy nanoparticles in microchannel. Analysis were performed for influential factors such as nanoparticle shape factor, magnetism, viscous heating and joules heating parameters. The entropy generation rate of Ti₆Al₄V alloy nanoparticle is higher than AA7075 particle. Similarly, investigation within several different shape factors, let the sphere shape with higher entropy generation rate. The impact of Biot number, Reynolds number and thermal conductivity parameter has very less impact on Bejan number. The maximum Bejan number was found for spherical particle.

Heshmation et al. (2019) modelled and evaluated entropy generation rates for TiO₂ water nanofluid for frictional and heat transfer involving nanoparticle migration. The factors such as viscosity gradient, non-uniform shear and Brownian diffusion in minichannel and conventional channels are studied. They observed significant effects of particle migration in minichannel and its thermal entropy generation rate increased by 5% for 200 μm channel but only 16% in the case of 1000 μm channel. On comparison with conventional channel total entropy generation increases for minichannel at higher nanoparticle concentration.

Cheng et al. (2020) performed entropy generation study using slit pillar array in microchannel. The numerical study analyzed the effects of slit angle height over diameter and also thermal performance index. In particular, height to diameter ratio 0.3 was demonstrated for better performance index. Moreover, Nusselt number increased up to 37% and with reduction in pressure drop from 12 to 9%. They observed reduction in entropy generation for all the microchannel cases with slit pillar array. The maximum thermal performance index was generated for the split angle of 15°.

Samal et al. (2020) performed entropy generation analysis of recharging microchannel using graphene-silver hybrid nanofluid. For the case of hybrid nanofluid, increase in fluid velocity and nanoparticle concentration reduced the peak temperature and thermal resistance of the sink with increase in heat transfer coefficient. On other hand use of hybrid nanofluid increased the pressure drop and increased the pumping power. The performance factor of recharging microchannel was 1.72 which is better than the conventional microchannel. Recharging microchannel was found beneficial at high heat flux conditions with respect to 1st and 2nd law of thermodynamics.

2.7 NON-FOURIER HEAT CONDUCTION

Rubin (1992) proposed an alternative for heat conduction equation with modification in internal energy. The developed equation included temperature rate for rigid conductors. Initially, they discussed the difficulties associated with second law and deduced Cattaneo's model for hyperbolic heat conduction. Even though, the Cattaneo's equation predicts the thermal propagation of the unrealistic heat wave from cold to hot regions, this new alternate formulation modifies the specific internal energy and specific Helmholtz free energy but still assumes Fourier heat conduction. In particular, the equation is included with temperature rate which is a monotonically increasing quantity.

Conti et al. (2012) performed numerical investigation to examine the time dependent heat flux input in rectangular microchannel for electronic cooling applications. The effects of heat flux amplitude, fluid velocity and heat sink thickness are investigated. The smaller width channels are observed to be more sensitive for higher heat flux conditions. For increased channel width, the fluid velocity is considered to be an influencing factor using time varying sources. Increase in heat flux amplitude increases the outlet temperature and also the interface temperatures. Moreover, the increase in velocity develops deviation in

thermal equilibrium between the heat sink and the working fluid by developing temperature mismatch between outlet and heat sink temperatures. This is due to the fact that the interface heat transfer coefficient is increased because of the elevated thermal gradient. This increases the advection from the solid sink region to the fluids. They reported that larger microchannels with increased velocities are recommended at higher heat flux conditions. Their response time is highly influenced by viscous dissipation in case of microchannels.

Liu et al. (2016) proposed a dual-phase-lag model based on Cattaneo-Christov model to study heat transfer characteristics in the moving media. The formulated equation constitutes relaxation parameters and time fractional derivative to inhibit both relaxation and memory characteristics. By using numerical differences method, the solutions are obtained using L_1 scheme. They observed for smaller gap between x locations the transport of the temperature was faster while in the case of larger x the transport was slower for larger thermal diffusion in materials with higher relaxation parameter. Two scenarios were discussed. In the first case, temporal evolution of temperature and convection velocity effects are studied, in which the temperature transport attains slower for higher positive convection velocity. In the second case, the temperature transport at different conditions is studied with spatial evolution of temperature.

Kundu et al. (2018) investigated Fourier and non-Fourier effects with dual primary fin surfaces for the application of dehumidification. The investigation discusses the non-Fourier effect with design modification of the wet fin under different surface conditions. The maximum fin efficiency was found for lower values of Fourier number at higher Vernote number. They reported a strong dependency on Fourier number for both Fourier and non-Fourier heat conduction. Also in case of steady state, there were no much difference in Fourier number. When Fourier number increases, the spatial temperature in the fin approaches the respective base temperature to reach a steady temperature. But at lower Fourier number, the curve shows a significant dominance in non-Fourier heat conduction which shows a reduced heat conduction rate with increased surface heat transfer.

Xu and Wang (2004) performed numerical investigation on non-Fourier heat transport using transient laser heating. Lattice Boltzmann method was used to simulate the femtosecond laser heating of silver substrate. The temperature fields developed by LBM are compared with parabolic heat conduction and hyperbolic heat conduction equation.

They presented this method as an alternative to the conventional method and solved to answer regarding the different behavior of the thermal wave. Additionally, they found that at ballistic limit the speed of thermal wave is equivalent to speed of sound but in case of hyperbolic equation it was limited only to the diffuse limit. They reported that the energy near the boundary condition is predominantly transported due to ballistic conduction rather than diffusion. Both the parabolic and hyperbolic equations fail in this situation since they operate by equilibrium hypothesis. They also achieved by using LBM to recapitulate the wave like thermal transport in the substrate.

Roetzel et al. (2003) discussed the Fourier and non-Fourier conductions by examining investigations to solve the controversy of different groups. The work also proposed a combined experiment to determine the thermal diffusivity and relaxation time using temperature oscillations in semi-infinite medium. Their experiments reveal that the existence of the hyperbolic effect was found comparatively less than that reported by others. For all the materials considered with non-homogenous inner structure, hyperbolic behavior was observed with lesser magnitude of relaxation time. In case of investigations performed on processed meat their results matched almost similar to that of metals. They pointed out that the controversy is majorly due to the inconsistency of the experimental practices of the respective researchers. The authors added that their investigations still require various levels of micro and macro effects to comprehend more realistic effects of bulk heat propagation.

Zhang et al. (2014) performed a combined experimental and numerical study to characterize the transient response of the microchannel heat sink. For these purpose, three different heat sinks have been tested to study the transient behavior for different heat flux conditions. They observed that the heat sink showed higher response time than the heater. At increased flow rate the response time was found decreasing for all configurations. The lowest response time was reported for U-type channel compared to straight serpentine channel. Due to this the U-type channels reached steady state in shorter time. Further, the response time is significantly influenced by the thermal capacity and thermal resistance of the heat sink.

Antaki (2005) reported dual phase lag model of heat conduction to present experimental evidence for non-Fourier conduction in processed meat. The used model effectively combines wave features of hyperbolic conduction with diffusion feature to solve hyperbolic

equation. The current model accounts for the heterogeneous property of the meat which was not possible by Fourier conductivity. By using dual phase lag model initial increase in temperature was noticed at larger non-dimensional time which cannot be explained using Fourier theory based penetration time.

Herwig and Beckert (2000) presented experimental observation to clear the controversy by presenting a Fourier behavior in non-homogenous inner structure. Finally, they reported no such evidence of non-Fourier effects of heat conduction in non-homogenous materials. They highlighted the work of Tzou and Cheu (1998) where they mentioned, that the time constants for the non-Fourier effects are in the range of micro to picoseconds, which is lower in magnitude than the questions reported by other investigators.

Mitra et al. (1995) presented an experimental evidence for the heat propagation in a processed meat as wave in nature. Their results showed a significant difference from Fourier heat conduction model. Further, they proved the superposition nature of heat waves inside the processed meat representing the hyperbolic heat conduction. The processed meat was experimented with different boundary conditions in which meat is tested to show that the heat waves take finite time to reach a particular point rather than instantaneous propagation predicted by Fourier law. To demonstrate the wave superposition addition when two similar sample temperature sample brought into contact. At last, superposition subtraction with dissimilar temperatures. They clearly observed temperature jumps associated with two waves and non-Fourier behavior in all their experiments.

Rowlette and Goodson (2008) reported a detailed review on heat generation and transport phenomena of electrons and thermal vibrations in transistor devices. They reported that ballistic nature of conduction was observed in nanoscale devices, where sudden temperature increase in device increases the proton population and generates impact to the reliability of the device. These effects are potential enough to significantly impact the electrical transport and delay thermal conduction factor near the hotspot.

Chen et al. (2018) reported the development of complete method and technique for thermal simulation of transition eddy sensor circuits. The performed simulation delivered different thermal conduction mechanisms in the sensor circuit. The thermal conductance in the substrate is ballistic and by changing the continuous temperature channel distribution to radiative power law they have represented ballistic phonon transport. The joule heating

developed by the source is transferred to different substrates by phonons. Initially, at lower temperature less noticeable electron-proton thermal conduction generate discrepancies in estimating electron- phonon temperatures.

Sverdrup et al. (2001) provided the experimental evidence for the failure of Fourier law in the case of small heat source. They observed the conduction by Fourier law is of 60% when phonon mean path is in a factor 30 higher than the resistor thickness. Additionally, their work provides experimental information regarding the additional thermal resistance near the hotspot. From two fluid phonon conduction theory it is confined that the results deviate from conventional Fourier theory.

Both et al. (2016) studied heat pulse experiments to study the discrepancies developed using Fourier law. Guyer-Krumhansel equation is modelled for the experimental data and compared with the conventional diffusion theory. The heat pulse experiment delivered comparatively higher faster propagation speed than the estimated using Fourier theory. The investigation proceeded with a comparable size of characteristic length and sample size but the relaxation time was found to be larger than pulse length which requires further experimental investigations.

Kovacs and Van (2018) discussed the thermodynamic consistency of dual-phase-lag heat conduction equation. They pointed out that at lower temperature deviations in Fourier law was noticed. They also pointed out that with other investigations where heterogeneous media is used the propagation was not like wave, instead its over-diffusive propagation. They used both Guyer-Krumhansl and Jeffreys type equations which consider Boltzmann equation with the double relaxation time of Callaway collation integral and Fourier law with memory integral. They observed deviation in both type of equations from Fourier law used for uniform thermodynamic principle extending to local equilibrium.

2.8 MOTIVATION AND SCOPE FOR THE PRESENT WORK

Based on the understanding from the available literature, it is identified that the hotspots are predominately developed in multicore processor that are potentially capable of developing thermal imbalance in the heat sink which in turn reduces the reliability of the miniaturized electronic components. In the past few decades diverse works have been carried out to address an efficient compact microchannel based electronic cooling device. Apart from the heat transfer augmentation due to microchannel, the embedded integration

of the cooling system develops multiphysics effects which have slightly different behavior. The coalescence characteristics developed in microchannel involving hotspot, nanofluid and heterogeneous substrates are highly elusive. Few essential reasons behind this investigation are,

1. Irrespective of the optimized flow configuration, the parallel type channels develops maldistribution induced hotspot zones.
2. Change in header design solves the uneven mass flux near the entrance of the channels to some extent. But, the inherent axial conduction along the channel length poses threat to the heat sink effectiveness.
3. In the case of densely integrated microchannel with heterogeneous substrates, the effect of parasitic thermal loads must also be considered.
4. In addition to the microchannel heat and fluid phenomenon, the behavior of the nanofluid is highly diffusive and it is predominately influenced by nanofluid volume fraction and flow rate.
5. Availability of the high precision manufacturing techniques and computational resources provide sophisticated channel design to solve the concurrent problem involved in the parallel heat sink.

With this insight, the primary investigation of thesis is to present better channel configuration to solve flow maldistribution induced hotspot associated with axial conduction involving several numerical and experimental investigations. In consideration of the above listed scope, the objectives of the present study are as follows,

2.9 OBJECTIVES OF THE PRESENT WORK

1. Experimental and numerical investigation of heat spreader integrated microchannel using graphene oxide nanofluid by varying volume fraction, aspect ratio, processor cores and mass flow rate.
2. Experimental investigation on response time effects in heat spreader integrated microchannel using high thermal conductive nanofluid.
3. To perform critical analysis of irreversibility effects in microchannel integrated heterogeneous heat sink for compact cooling application using TiO₂ nanofluid.
4. To design and perform experiments on inertial based parallel channels to reduce the maldistribution induced high temperature zones of heat sink.

2.10 CLOSURE

A detailed discussion on the literature review apropos to the problems considered in this study was presented. The objectives of the present work listed in this chapter. In the next chapter, the experimental set up and the instruments used for experimentation is elaborated.

CHAPTER 3

EXPERIMENTAL TEST SETUP

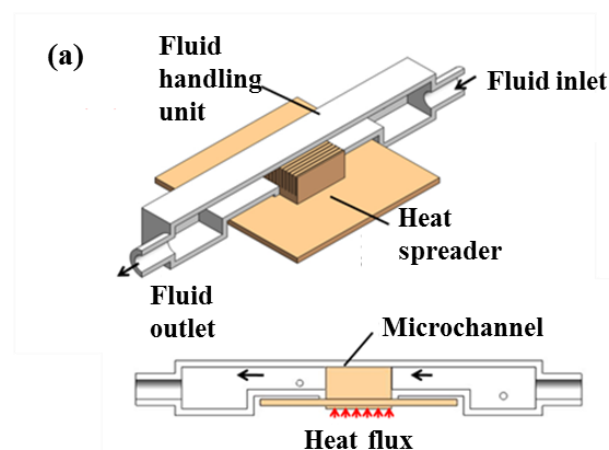
3.1 INTRODUCTION

This chapter presents the details of the constructed experimental setups used to perform heat and fluid flow experiments. Here, three different experimental test rigs are fabricated to investigate the conjugate heat transfer phenomenon for the case of integrated microchannel. In all the cases, the heat sink is fabricated using copper material and transient experiments were conducted for different flow rate and nanofluid.

3.2 PARALLEL I-TYPE CHANNEL CONFIGURATION TEST SETUP

3.2.1 Heat spreader integrated microchannel setup

A highly compact in-house microchannel device has been developed as a thermal management device to facilitate laminar forced convection for an active multicore processor. For this, a conventional heat pipe based cooling system is removed from the mother board of a working laptop. In order to maintain the level of compactness the developed thermal management device has only two parts; heat sink and fluid handling unit. The heat sink is manufactured by wire cut electro discharge machining from solid copper, while the compact fluid handling unit is manufactured using 3D printing. Additionally, a thin heat spreader is attached beneath the microchannel. Figure 3.1 represents the schematic diagram of a microchannel integrated heat spreader with dimensions.



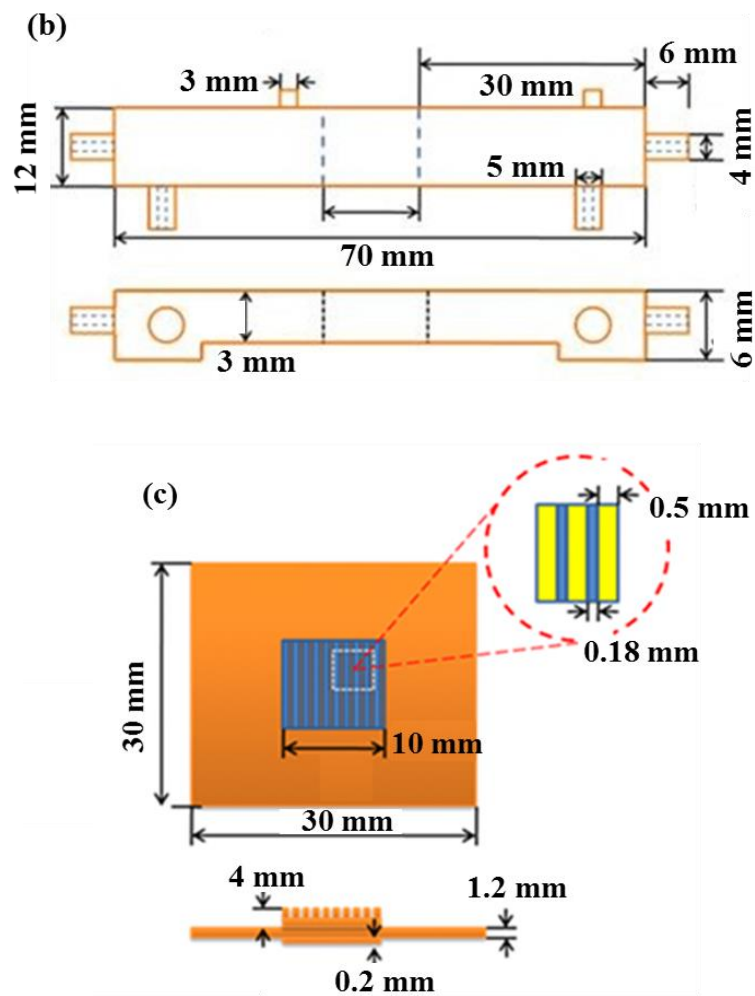


Figure 3.1 Schematic diagram of microchannel integrated heat spreader with dimensions (a) section view of the assembly, (b) fluid handling unit, and (c) heat spreader dimensions.

Figure 3.2 presents the actual photograph of experimental microchannel module with FHU. The complete microchannel integrated heat spreader is directly mounted upright over the electronic component. The experimental module of the test setup is shown in Figure 3.3. The FHU is made up of three dimensional printed high-density acrylonitrile butadiene styrene plastic having fill density of 90% with dedicated orifices for fluid transport and sensing probes. Parallel microchannel with 1 cm length having 14 channels with the height of 2 mm is used to manage the hotspot developed in the processor.

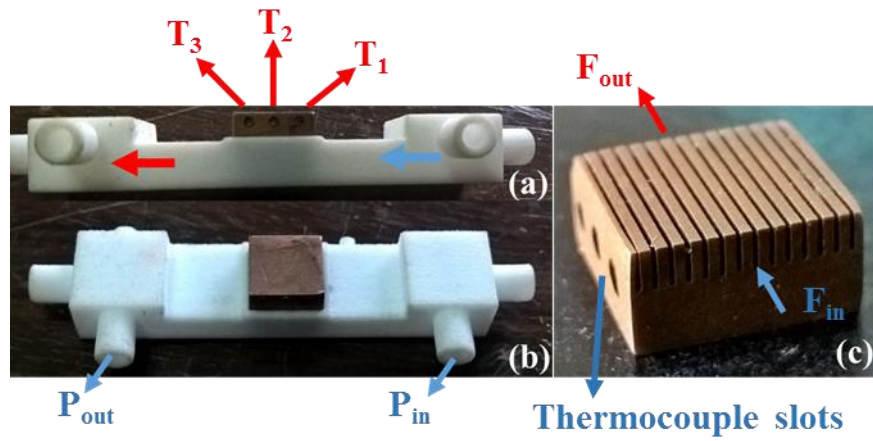


Figure 3.2 Photographs of experimental microchannel module with FHU (a) microchannel with thermocouple locations, (b) FHU with pressure tapping, and (c) microchannel heat sink.

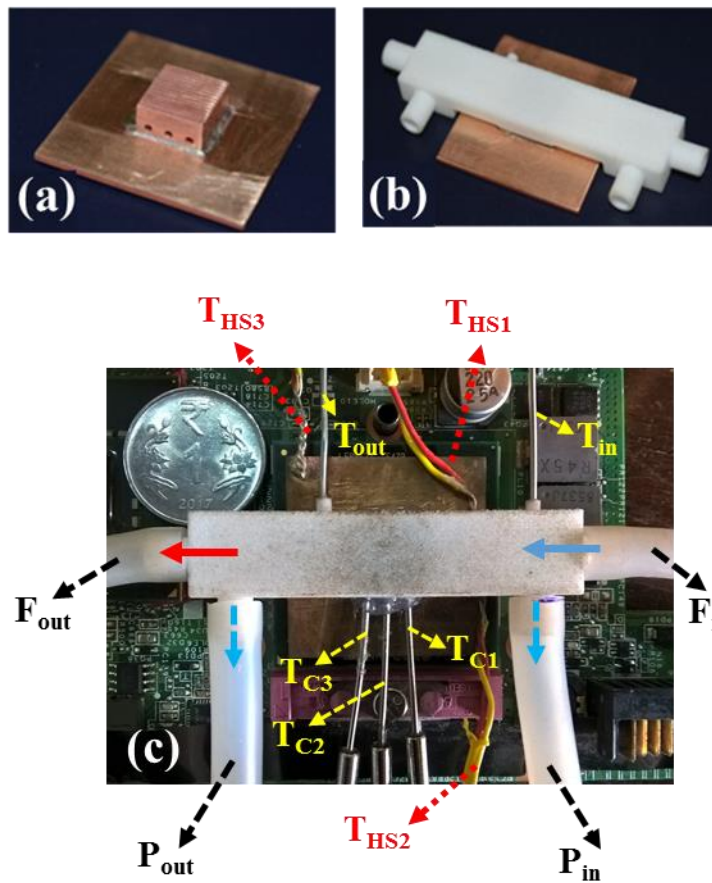




Figure 3.3 Experimental setup of microchannel with heat spreader (a) heat sink, (b) heat sink with FHU, (c) heat sink with sensors, and (d) complete module.

The study was carried out on a two core processor (Intel core 2 duo-T7700) with a thermal dissipation power of 35 W. The flow diagram of the experimental test module is shown in Figure 3.4. The processor and the motherboard are externally controlled and operated at the rated thermal dissipation power. The microchannel setup is integrated with heat spreader and FHU.

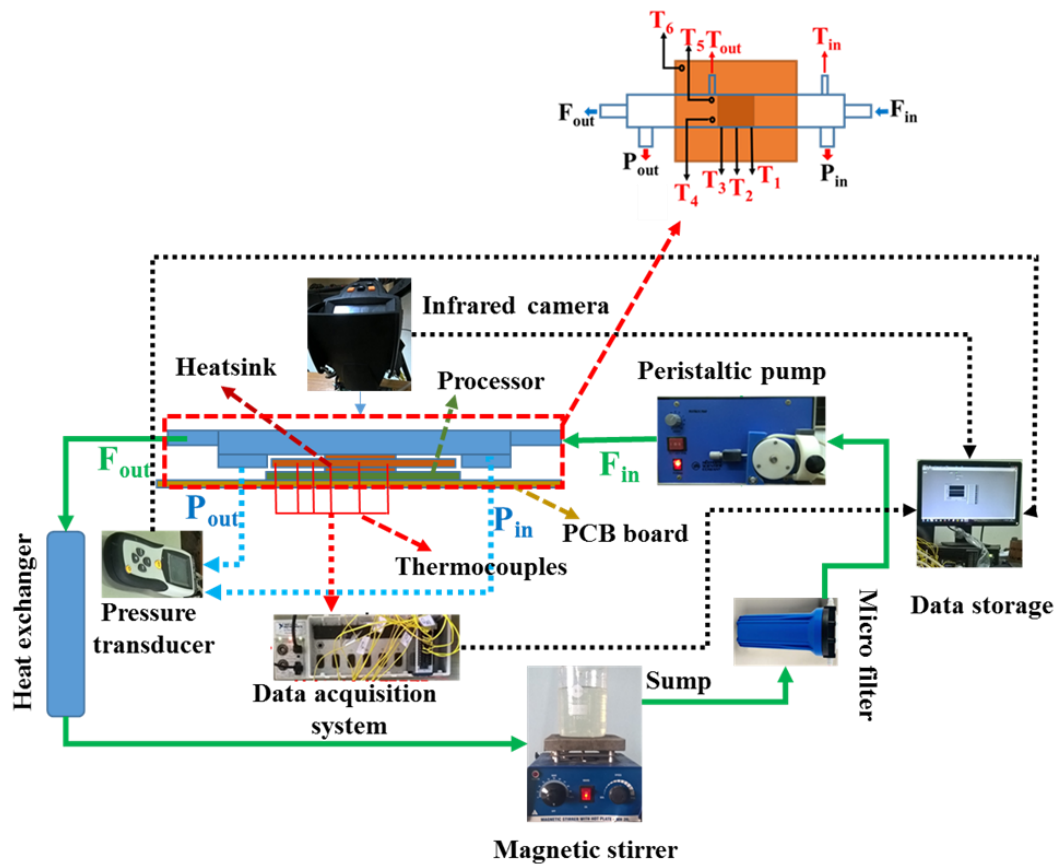


Figure 3.4 Flow diagram of the experimental setup.

A peristaltic pump (Murhopye scientific, India) is connected to the FHU to provide a pulsating flow. The outlet is connected to a secondary heat exchanger to reduce the outlet temperature of the working fluid to the room temperature before it is let to the sump that stores the fluid. The fluid is actively stirred in low RPM for the case of nanofluid to stabilize the dispersion of the working fluid. The heat sink is connected with the thermocouples to record the necessary change in temperatures at the inlet and the outlet of the channel.

3.2.2 Heterogeneous integrated microchannel setup

In addition to the compact integrated microchannel setup, the investigation of the axial conduction is also extended to heterogeneous integrated microchannel domain. To accommodate this, an experimental setup is developed by integrating aluminium block with copper microchannel. Figure 3.5 depicts the exploded view of the integrated microchannel heat sink module. It mainly consists of two parts: copper microchannel and aluminium block section. The copper channel is shrink fitted in to the aluminium block and the provision for the fluid to flow is machined in the aluminium block. The complete flow path in the aluminium block is insulated with Teflon to avoid the fluid getting preheated before entering the copper channel. The microchannel is covered with transparent acrylic sheet of 8 mm thickness.

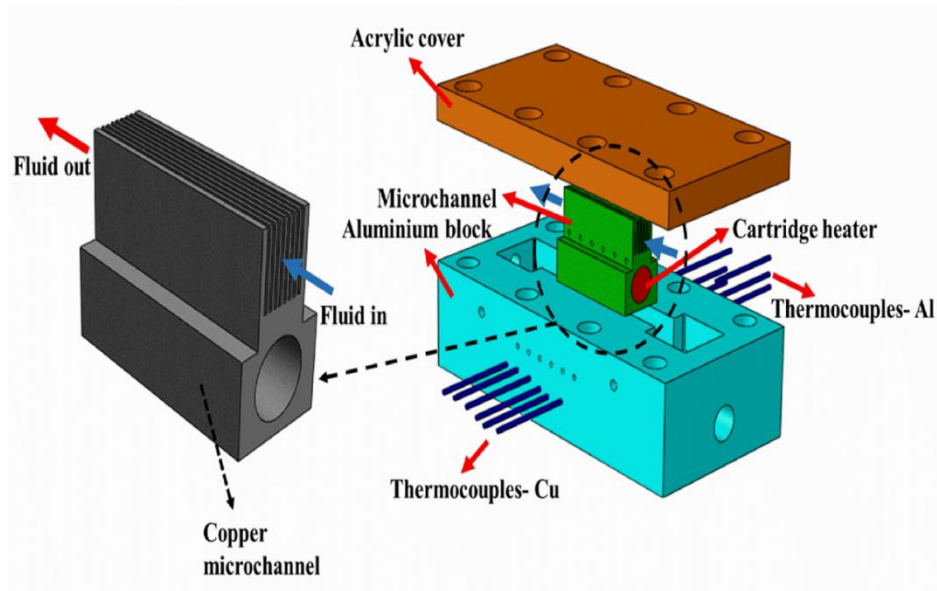


Figure 3.5 Exploded view of the diagram of microchannel experimental setup.

The rectangular microchannel was fabricated with nine channels by wire cut electrode discharge machining process. The length of the channel is 36 mm with the channel height of 9 mm, as shown in Figure 3.6.

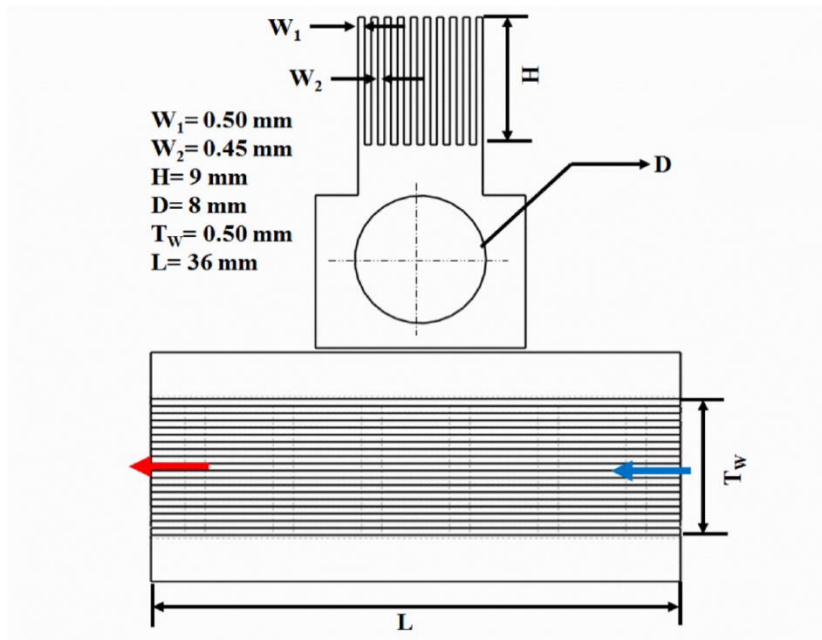


Figure 3.6 Schematics of the microchannel with dimensions.

Calibrated sheathed thermocouples were used to measure the temperatures of both microchannels and aluminium block which are shown in Figure 3.7. The side walls of the microchannel and inner wall of the aluminium are milled with minimum surface roughness to reduce the contact resistance. A gasket groove, milled with 6 mm length and 2 mm depth, is maintained throughout the flow path to provide rigid bolting between the acrylic glass cover and the aluminium block. The copper channel is fitted with cartridge heater of 8 mm diameter and 36 mm length to deliver a maximum temperature of 150°C using flux controller. The pressure drop is measured using pressure transducer (MSE-5200, USA) placed near the inlet and outlet of the channel. 1mm diameter holes are drilled to insert thermocouples in microchannel. The photograph of the complete integrated module assembly is shown in Figure 3.8.

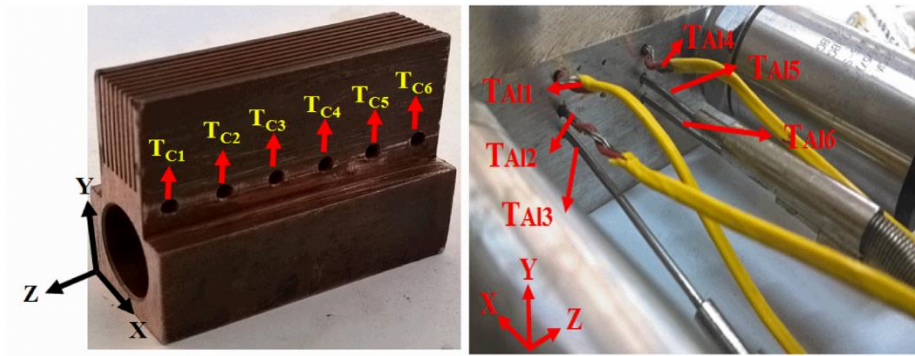


Figure 3.7 Actual photographs of the microchannel and aluminium block with sensor locations.

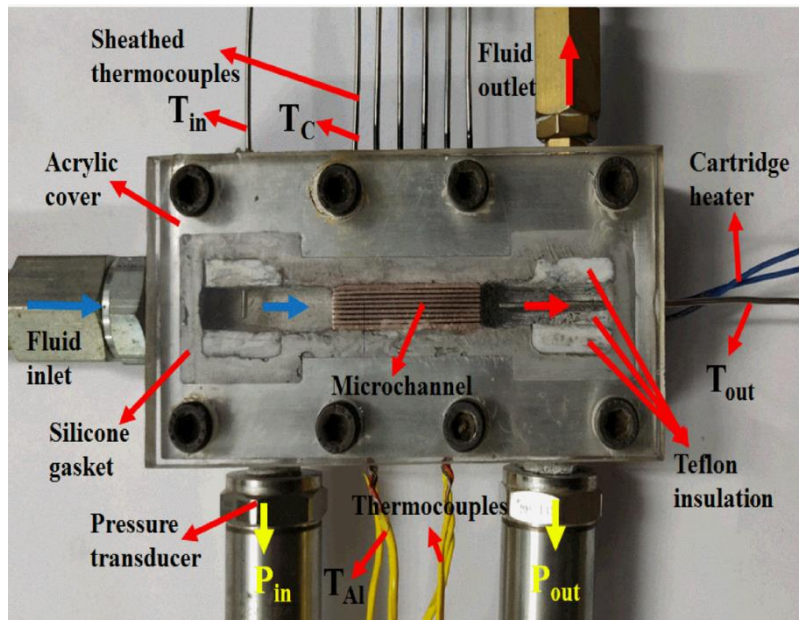


Figure 3.8 Photograph of the microchannel experimental setup.

The schematic diagram of the experimental flow line is shown in Figure 3.9. The fully stabilized nanofluid is passed through the flow line by a peristaltic pump. The fluid flows subsequently to the microchannel channel inlet section; the outlet fluid is circulated in the heat exchanger for temperature regulation and returns to sump. The temperature of the integrated microchannel module is controlled by the cartridge heater using varying flux controller. The temperature variations in both copper and aluminium are acquired by NI data acquisition module and monitored by a standalone system. The current investigation employs deionized water and TiO_2 nanofluid as working fluids.

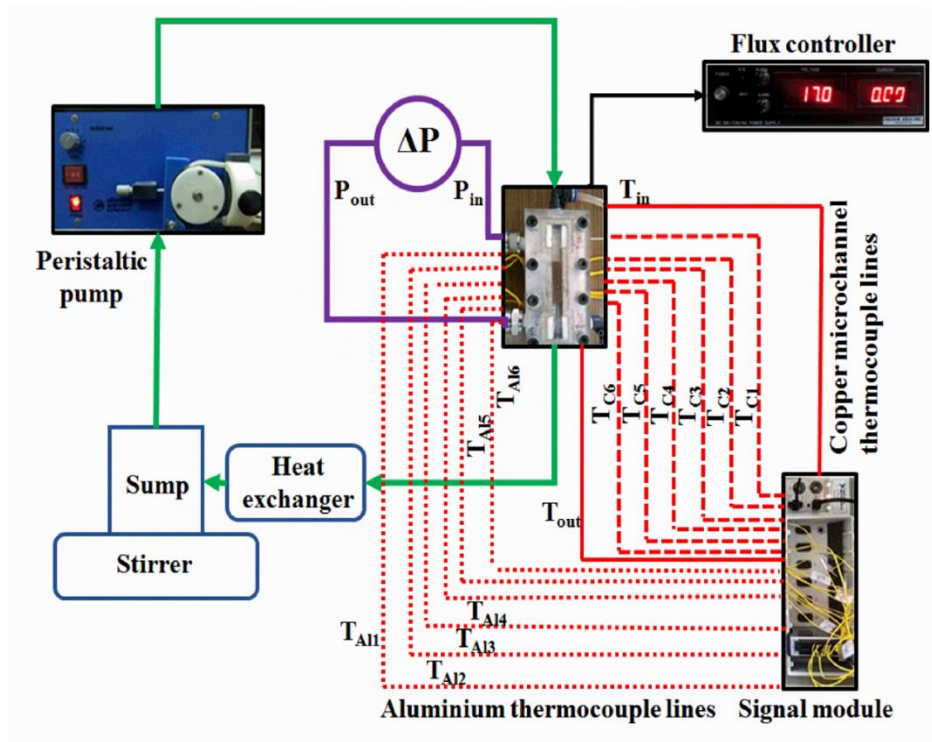


Figure 3.9 Schematic diagram of the experimental flow line.

The nanofluid filled in the sump is subjected to continuous stabilization using magnetic stirrer at very low rpm. The flux controller is operated gradually to increase the temperature of microchannel by varying the voltage supply. The microchannel is allowed to reach a preset temperature of 60°C above which peristaltic pump is operated. The data from the thermocouples is recorded at higher rates of 70 Hz to measure the instantaneous temperature distribution along the flow. The pressure and temperatures are recorded at inlet and outlet of the microchannel. After 120 s of run time, a difference in temperature of 4°C was found between inlet and outlet. This procedure is followed for all other working fluids and power ratings.

3.2.3 Minichannel heat sink setup

Additionally, the effects of flow maldistribution and axial conduction under the influence of channel structures are investigated using common inlet and outlet headers. Specifically, I-type minichannel is fabricated to visualize the heat and flow distribution associated with maldistribution. Figure 3.10 shows the actual minichannel setup fixed in the on-board system. Figure 3.10(a) represents dimension of the heat sink and individual minichannel. Figure 3.10(b) shows the minichannel module. The top part of the sink is covered with

acrylic sheet to visualize the flow of cooling fluid. The inlet and outlet to the sink are provided at the ends of sink. An extension of small blocks fabricated from hylam- bakelite is used so as to provide the necessary insulation for the sides of the heat sink. The connections for thermocouples and differential pressure transducer for pressure measurement are accommodated in the sink shown in Figure 3.11.

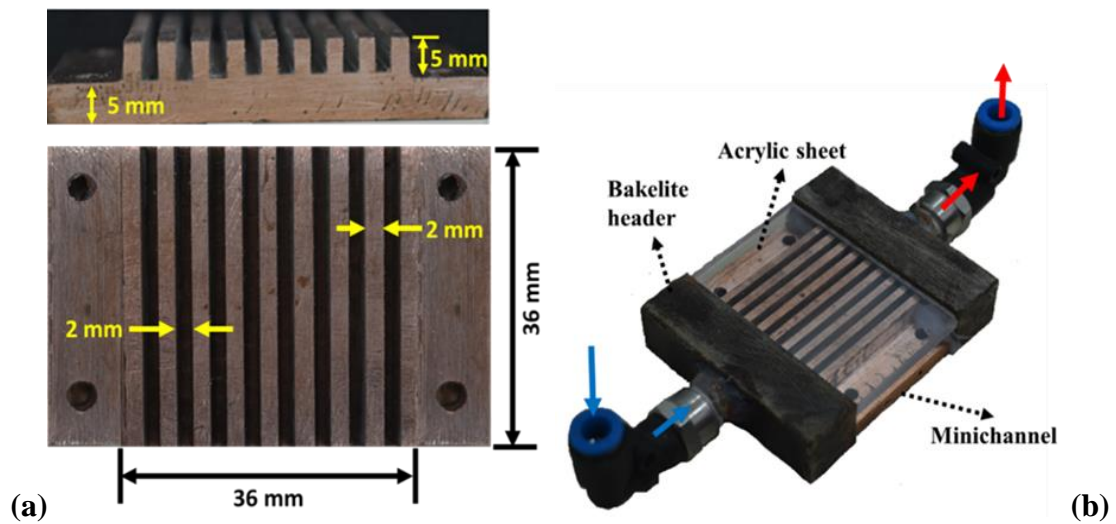


Figure 3.10 Actual diagram of minichannel module. (a) channel dimensions, and (b) minichannel module.

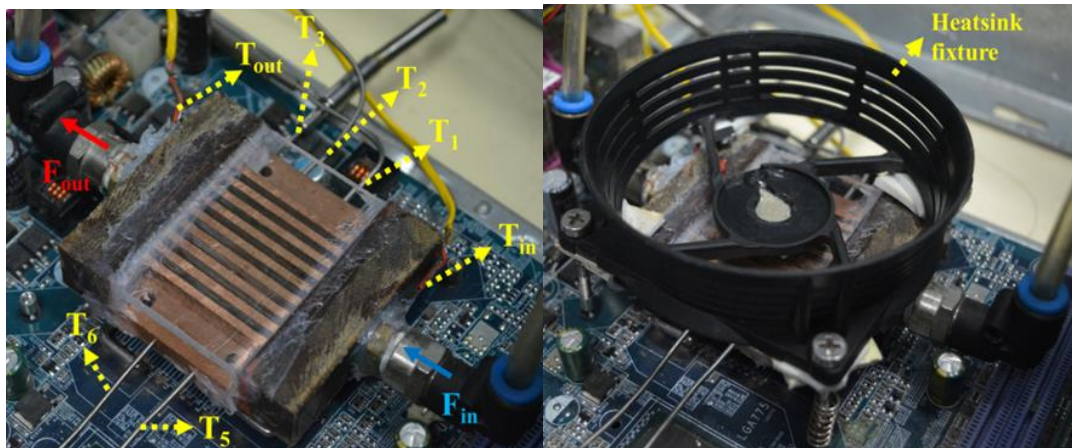


Figure 3.11 Minichannel module with sensor locations and fixtures.

The complete experimental setup is shown in Figure 3.12. It consists of the minichannel module, sump, stirrer, pressure transducers, thermocouples and data-acquisition system. A peristaltic pump is used to pump the cooling fluid from the sump, to the sink and the coolant is collected back in the sump. A practical working processor (Pentium Dual Core) is used for the heat generation. The minichannel is located just above the processor chip. A paste

of Silver is applied between the bottom faces of the sink and the processor to avoid contact resistance between them. A total of five K-type thermocouples is used with a diameter of 1 mm in which three of these were used to calculate the temperature drop along the flow length and the remaining thermocouples were used to calculate the inlet and outlet working fluid temperature. The outlet of the minichannel is connected to a secondary cooling loop where its temperature is reduced to room temperature for recirculation. The thermocouple and pressure transducers are connected to the data acquisition system and saved in a standalone system. The fabricated length and the width of the heat sink is about 36 mm x 36 mm, and it is selected in accordance to the size of the processor. The width of each channel is 2 mm, followed by a gap of 2 mm. The channel bottom is polished to maximum extent to reduce surface roughness.

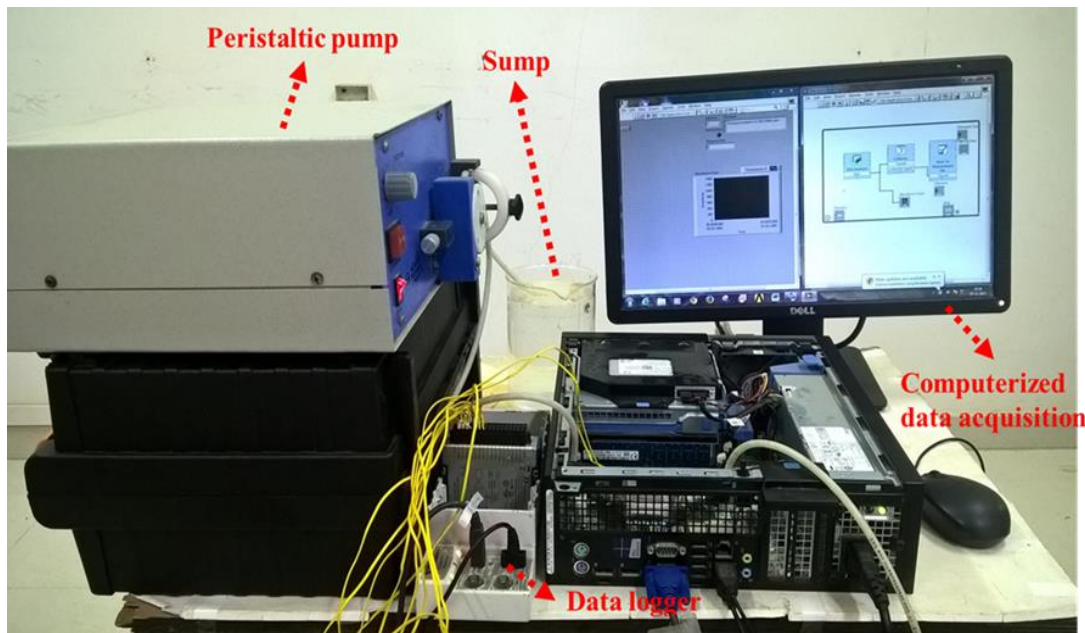


Figure 3.12 Actual photograph of the complete minichannel experimental setup.

The CPU is initially kept in a horizontal position such that the minichannel is parallel to the processor then the CPU is initialized. When the average minichannel temperature reaches the target temperature i.e. (45°C), the pump is started and is allowed to run until the temperature of the minichannel decreases near room temperature. Further similar procedure is performed for higher flow rates. Figure 3.13 presents the flow line of the experimental setup. Table 3.1 presents the list of experimental instruments used in the investigation.

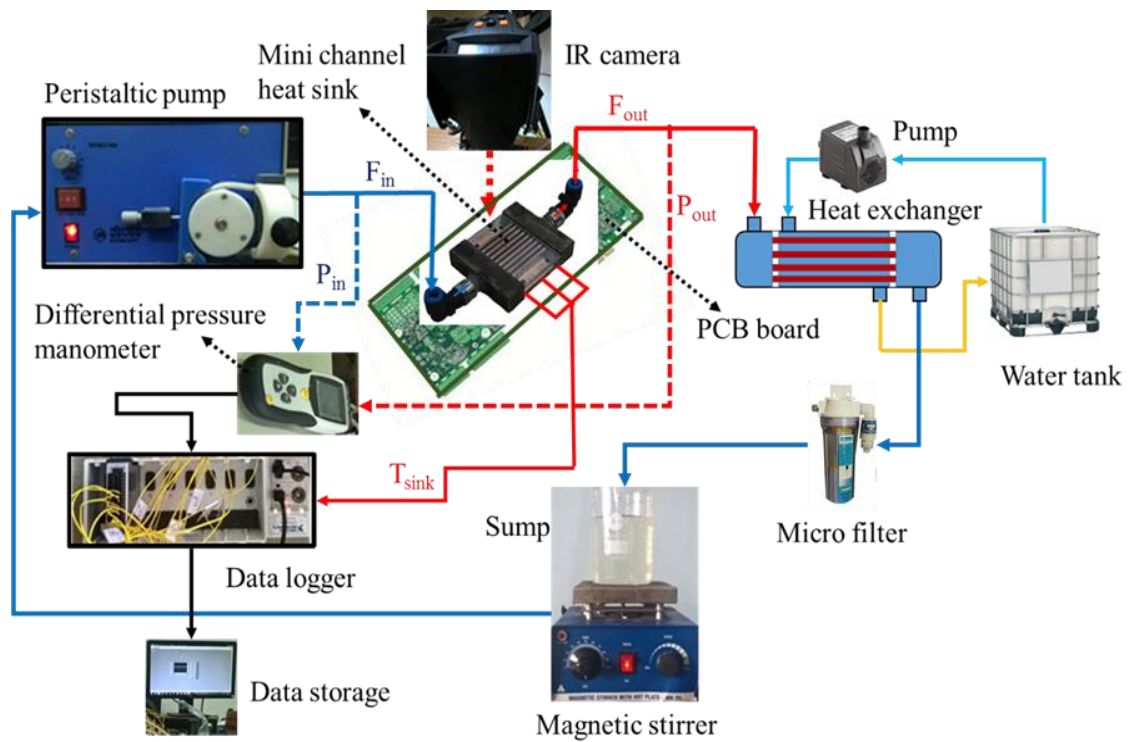










Figure 3.13 Flow line of the experimental setup.

Table 3.1 Instruments utilized for experimental investigation.

Component	Description	Properties
	Pressure transducer MEAS-5300	Pressure range: 0-10000 psi Output span: 0.5 to 4.5 V Accuracy: $\pm 0.1\%$ total error band: $\pm 0.5\%$ operating condition: -40°C to 125°C
	Data acquisition chassis NI-cDAQ-9178	Output frequency: 0 -20 MHz Time resolution: 12.5 ns Base clock accuracy: 50 ppm Output: -15V to 20V

	<p>High density thermocouple module NI-9213</p>	<p>Noise rejection: 50Hz/60 Hz Sensitivity: 0.02°C Voltage measurement range: ±78.125 mV Sample rate: 75 S/s</p>
	<p>Magnetic stirrer</p>	<p>RPM: 250- 3600 Hot plate temperature:30-90°C</p>
	<p>Peristaltic pump Murhopye scientific, India</p>	<p>Tube diameter: 5 mm Pulsating levels: 5 Maximum discharge: 100 – 450 mL/min</p>
	<p>Heat flux controller Proxim Asia Inc.</p>	<p>Output Voltage: 0-150 V Output Current: 0-2 A AC input: 1 phase AC 220 V Frequency: 50/60 Hz</p>
	<p>Infrared camera Testo 875-1i</p>	<p>Sensitivity: ±2°C Temperature range: -20 to 1200°C Thermal sensitivity <50 mK Display resolution: 640 x 480 pixel</p>
	<p>Motherboard Intel core 2 duo T7700</p>	<p>TDP: 35 W Core voltage: 1.25 V Packaging: 65 nm</p>

	Sheathed K-type Thermocouple Heatron Industrial Heaters	Thermocouple diameter: 1 mm K-type: Chromel/Alumel
	Beaded K-type Thermocouple Heatron Industrial Heaters	Thermocouple bead diameter: 1.3 mm K-type: Chromel/Alumel
	Bead welded K-type Thermocouple Heatron Industrial Heaters	Thermocouple bead diameter: 1.2mm Bead depth: 0.6 mm K-type: Chromel/Alumel
	Bead making machine Dyna weld	Voltage rating: 100- 120 V Storage energy output: 0-175 Joules Charging time: 10 s Wire gauge: 0.3-0.5 mm
	Differential pressure manometer HTC PM 6202	Accuracy: $\pm 0.3\%$ Hysteresis: $\pm 0.29\%$ Pressure range: 0-2 psi Ratability: $\pm 0.2\%$

3.3 TEMPERATURE MEASUREMENTS

The temperatures along the length of the heat sink and the inlet and outlet fluid are measured using thermocouples. Eight sheathed thermocouples, six beaded thermocouples and three bead welded K-type thermocouples were used for the temperature measurements. Thermocouples with 1 mm diameter are inserted into the holes in the microchannel. The beaded thermocouples with 1.3 mm are used to measure the aluminium block temperatures. The heat spreader temperatures are measured by bead welding 1.2 mm diameter

thermocouple in the spreader plate. Other end of these thermocouples is connected to data acquisition system for measuring temperature data. Before using the thermocouple for measurements it is subjected to standard thermostatic bath calibration supplied by Thermo Scientific with 0.01°C accuracy. Initially all the thermocouples are calibrated with respect to controlled room temperature by using a reference mercury bulb thermometer listed in Table 3.2. Further, thermostatic bath is used with different temperature settings for thermocouple calibration. Table 3.3 shows the details of the calibration of thermocouples at different constant temperature settings.

Table 3.2 Calibration chart of thermocouples at room temperature.

Thermocouple type	Bulb thermometer temperature, °C							
	30°C							
	Number of thermocouples							
Sheathed K-type	(1)	(2)	(3)	(4)	(5)	(6)	(7)	(8)
Set-1	29.78	29.85	30.12	29.79	30.07	29.81	29.83	29.88
Set-2	29.75	29.88	30.07	29.76	30.02	29.85	29.78	29.81
Set-3	29.68	29.76	30.17	29.67	30.05	29.73	29.85	29.82
Error (%)	0.88	0.57	0.44	0.87	0.15	0.68	0.60	0.54
Beaded K-type								
	(1)	(2)	(3)	(4)	(5)	(6)	-	-
Set-1	29.72	29.68	29.68	29.68	29.65	29.71	-	-
Set-2	29.63	29.61	29.67	29.71	29.72	29.68	-	-
Set-3	29.64	29.63	29.75	29.67	29.62	29.72	-	-
Error (%)	1.07	1.21	1.07	1.05	1.06	1.04	-	-
Bead welded								
	(1)	(2)	(3)	-	-	-	-	-
Set-1	29.87	29.70	29.77	-	-	-	-	-
Set-2	29.71	29.74	29.78	-	-	-	-	-
Set-3	29.70	29.79	29.72	-	-	-	-	-
Error (%)	0.80	0.86	0.81	-	-	-	-	-

Table 3.3 Calibration chart at different thermostatic temperatures.

Thermocouple type	Thermostatic bath temperature, °C		
	40.5	60.00	80.05
	Thermocouple reading, °C		
Sheathed K-type			
1	40.02	59.44	79.31
2	40.04	59.55	79.41
3	40.10	59.59	79.40
4	40.13	59.66	79.44
5	40.20	59.68	79.48
6	40.18	59.55	79.35
7	40.24	59.59	79.38
8	40.07	59.23	79.42
Error (%)	0.94	0.86	0.83
Beaded K-type			
1	40.11	59.6	79.57
2	40.08	59.46	79.41
3	40.14	59.54	79.45
4	40.12	59.51	79.27
5	40.01	59.48	79.57
6	40.20	59.53	79.52
Error (%)	0.97	0.89	0.65

3.4 CLOSURE

This chapter provided the details about the experimental setup, equipment and sensors required for the operation of the experiment along with its specification. The next chapter explains about the synthesis and characterization of the nanofluid used in the present work.

CHAPTER 4

NANOFLUID SYNTHESIS AND CHARACTERIZATION

4.1 INTRODUCTION

The first step in the analysis of nanofluid for various applications is the preparation of nanofluid. Preparation of nanofluid is not simply mixing the nanoparticles in the base fluid. Uniform dispersion and stability of nanoparticles in the fluid are most important concerns for the experimental investigation of nanofluid. Unless the nanoparticles are dispersed uniformly, the nanoparticles cannot be stable and agglomerate easily. The agglomeration affects the thermo physical properties of nanofluid. There are different techniques available to prepare stable and uniformly distributed nanofluid. This chapter presents an outline of the various preparation methods of nanofluid used in this study.

4.2 METHODS FOR THE PREPARATION OF NANOFLUID

Generally, there are two major methods used for the preparation of nanofluid;

- a) One-step process
- b) Two-step process

The one step method is a process of simultaneously making and dispersing the particles in the fluid. In this method the process of drying, storage, transportation, and dispersion of nanoparticles are avoided, so the agglomeration of nanoparticles is minimized and stability of fluid is increased. Several techniques have been used to prepare the nanofluid in one step method such as chemical reduction method, vacuum based submerged arc method, microwave irradiation method etc. The major advantages of this method are (i) nanoparticle agglomeration is minimized; (ii) well-dispersed and stable nanofluid. However, there are some disadvantages for one step method: (i) This method cannot synthesize nanofluid in large scale, (ii) The residual reactants are left in the nanofluid due to incomplete reaction or stabilization. It is difficult to elucidate the nanoparticle effect without eliminating the impurity; (iii) The cost is high; and (iv) It can be preferred only to produce certain type of fluids where vaporization of precursors of the nanoparticles is possible, and where the base fluid has a low vapor pressure.

In two step method, the nanoparticle may be nanosphere, nanofibers, nanotubes or other nanomaterial are first produced as dry powders by chemical or physical methods. Then, the

nanosize power dispersed into a base fluid in the next processing step with the help of intensive magnetic force agitation, high shear mixing, homogenizing and ball milling. Two step method is considered as the most economic method to produce nanofluid in large scale, since the nanopowder synthesis technique has already been scaled up to industrial production levels. Hence, two step method is employed in the present investigation considering this method as economical method for large scale production especially for heat transfer applications.

4.3 SYNTHESIS OF GRAPHENE OXIDE (GO) NANOPLETTELS

The procedure for synthesis of GO is followed from Hummers and Offeman's method (Hummers and Offeman, 1958). On preparation of 1g of graphite flakes, an equivalent amount of sodium nitrate (NaNO_3) is mixed with 46 mL of H_2SO_4 solution. It is kept in the ice bath and stirred until it forms a thick paste. 46 mL of deionized water is added to the paste gradually. Then the step is preceded with 140 mL of deionized water after 30 min and 10 mL of H_2O_2 is introduced. This generates a golden yellow precipitate which is then washed with 3% of HCl mixture to remove the impurities. It is then dried to get GO powder. The GO powder is characterized with tunneling electron microscope (TEM) to observe the morphology of the GO nanoparticles (Sreejesh et al. 2017). Fourier transfer infrared spectroscopy (FTIR) is used to characterize the functional group of GO which is shown in Figure 4.1.

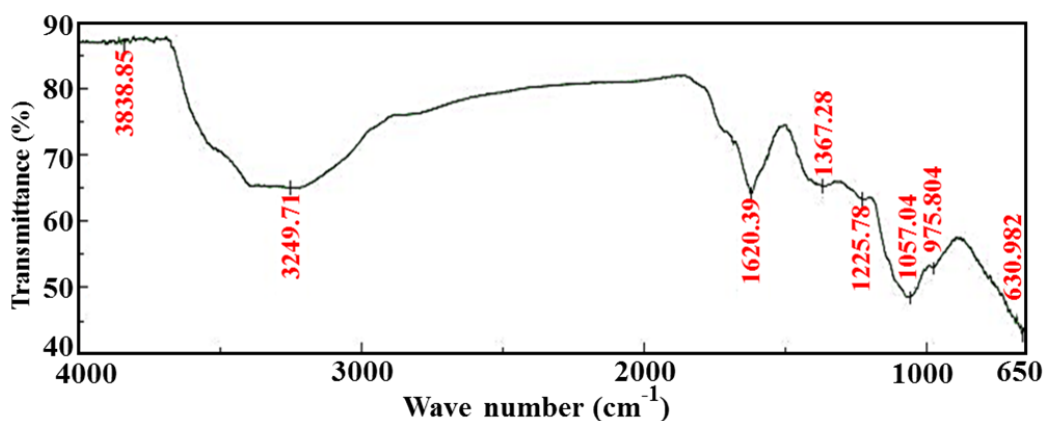


Figure 4.1 FTIR of GO.

The recorded pattern is from 650 to 4000cm^{-1} . The peaks are developed at 1057.04cm^{-1} and 1367cm^{-1} are by formation of $\text{O}=\text{C}-\text{O}$ and $\text{C}=\text{O}$ functional groups. The peaks at 1620cm^{-1} corresponds to stretching vibrations of $\text{C}=\text{O}$ bonds. The peak at 3249cm^{-1} conforms the

presence of GO. Figure 4.2 presents the X-ray diffraction and TEM images of produced GO.

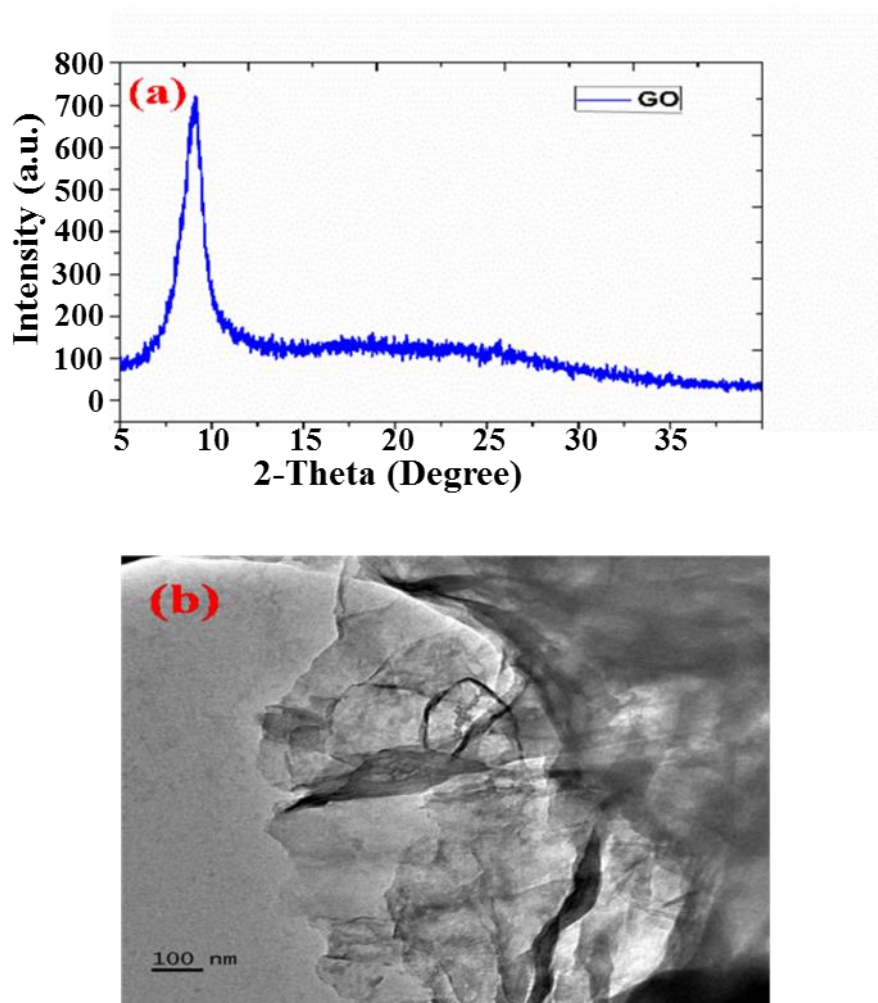


Figure 4.2 Characterization images (a) XRD-GO, and (b) TEM- GO.

4.4 PREPERATION OF GO NANOFLUID

In the present study, the nanofluid was prepared by varying volume concentration of the GO nanoparticle in the distilled water without any addition of surfactants. The mass of the GO nanoparticles required for the preparation of required quantity of nanofluid for a particular volume concentration was estimated initially. The mass of the GO nanoparticle is measured accurately using electronic balance with 0.1mg resolution. The pre-weighed quantities of silver nanoparticles were dispersed in the known volume of distilled water to make sample nanofluid. The required quantity of surfactant was added with them. Initially, it was mixed in a magnetic stirrer for 30 minutes. Then the nanofluid was taken to ultrasonic cleaning bath for ultrasonication process. The process of ultrasonication was carried out

continuously for 3 hours. The use of mechanical stirring and ultrasonication is to break down the agglomeration of nanoparticles and to keep the suspension stable for long period. The duration for magnetic stirring and ultrasonication was fixed by conducting the experiments for different time durations and observing these by keeping the minimum 10 ml capacity glass containers for 24 hours to one week. Figure 4.3 shows the average particle size and zeta potential of GO/water nanofluid. Dynamic light scattering technique is used to determine the average particle size which was about 200 nm as shown in Figure 4.3(a) and zeta potential is about -45mV as shown in Figure 4.3(b).

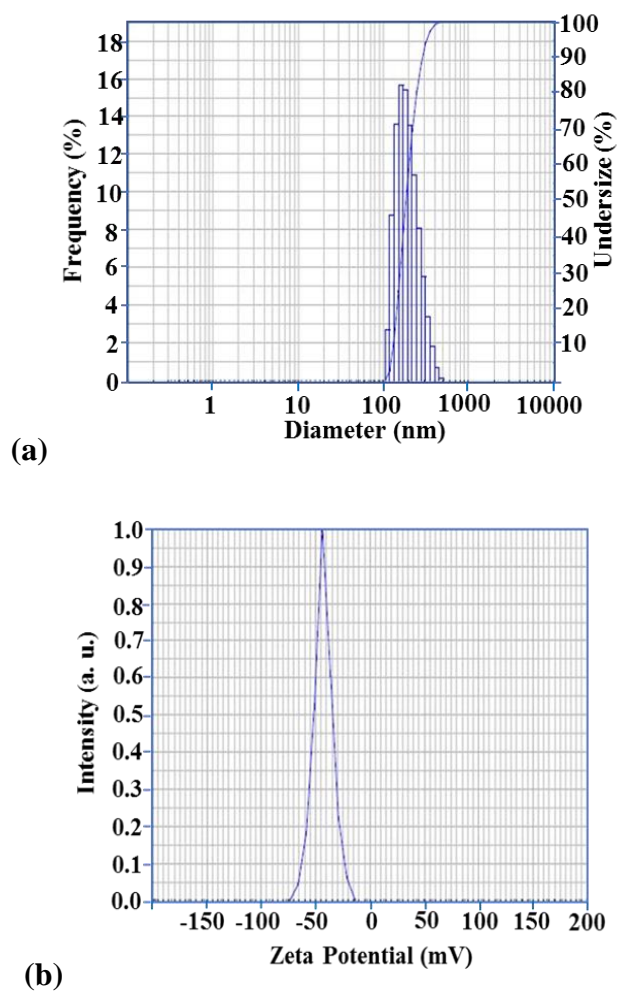


Figure 4.3 Nanofluid stability test (a) Particle size, and (b) Zeta potential.

4.4.1 Thermophysical properties of nanofluid

The thermophysical properties of the nanofluid have been calculated using the following equations. The density and specific heat of the nanofluid Equations 4.1 and 4.2 are determined using (Pak and Cho, 1998) and (Xuan and Roetzel, 2000).

$$\rho_{nf} = \rho_{bf}(1 - \phi) + \rho_p \phi \quad (4.1)$$

$$C_{p,nf} = \frac{(\rho_f C_{pf}(1 - \phi)) + \rho_p (C_{pp} \phi)}{\rho_f (1 - \phi) + \rho_p \phi} \quad (4.2)$$

The effective viscosity of the nanofluid Equation 4.3 is calculated using (Brinkman, 1952) equation.

$$\mu_{nf} = \frac{\mu_{bf}}{(1 - \phi)^{2.5}} \quad (4.3)$$

Thermal conductivity of the nanofluid Equation 4.4 is given by (Hamilton and Crosser, 1962) model considering shape factor of the nanoparticle

$$k_{nf} = \frac{k_p + (n - 1)k_f - (n - 1)\phi(k_f - k_p)}{k_p + (n - 1)k_f + \phi(k_f - k_p)} k_f \quad (4.4)$$

Baby and Ramaprabhu, (2011) relation is implemented for the calculation of thermal conductivity of synthesized GO nanofluid

$$k_{nf} = \frac{k_p(1 - 2\alpha) + 2k_f + 2[k_p(1 - \alpha) - k_f]\phi}{k_p(1 - 2\alpha) + 2k_f - [k_p(1 - \alpha) - k_f]\phi} k_f \quad (4.5)$$

Here $\alpha = \frac{2R_i k_f}{d}$ is the Kapitza constant, d corresponds to average particle diameter and

R_i is denoted as interfacial thermal resistance. The thermophysical properties of water and GO nanofluid for different volume fractions are experimentally found. The properties obtained based on experiments are then compared with Equations 4.3 and 4.4 and also with the experimental results provided by (Mirzaei and Azimi 2016). Such results are provided in Figures 4.4 and 4.5. Figure 4.4 shows the maximum enhancement in thermal

conductivity for GO-0.12% which is 23% more than the base fluid. This augmentation is due to the increased surface area of the GO nanoplatelets and enhanced stability of the nanofluid.

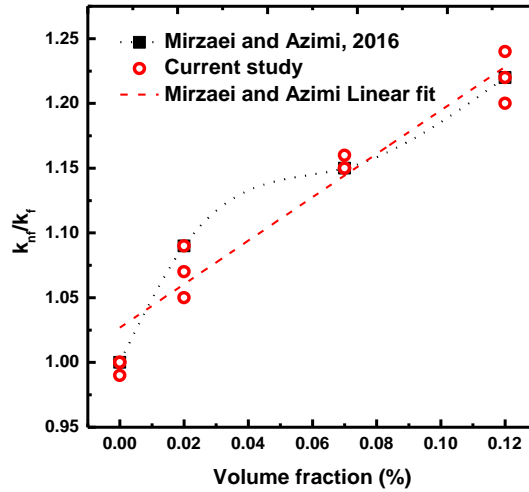


Figure 4.4 Thermal conductivity of GO/water nanofluid.

The increment in viscosity of GO nanofluid as a function of volume fraction is given in Figure 4.5. The increment in viscosity by 30% is observed for the GO-0.12% nanofluid than water.

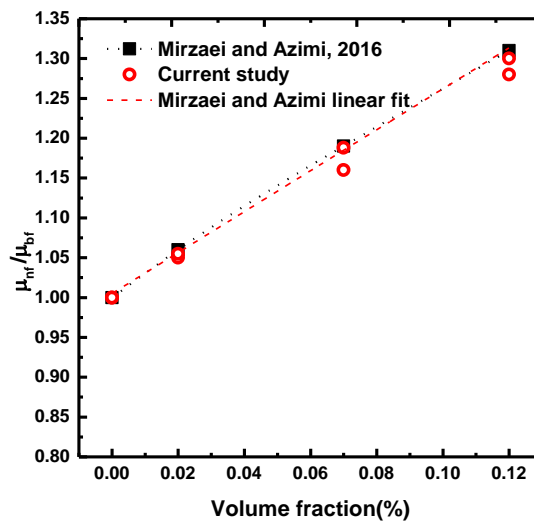


Figure 4.5 Viscosity of GO/water nanofluid.

4.5 SYNTHESIS AND CHARACTERIZATION OF TiO₂ NANOFLUID

The nanofluid is synthesized by two stage process and the rutile form of TiO₂ purchased from Merck chemical is dispersed in DI water. Stabilization of the nanofluid is performed by altering the PH and probe sonication. The morphology of the TiO₂ is spherical and reported to have an average diameter of 100 nm mentioned by manufacturer. Figure 4.6(a) shows the TiO₂ SEM (JEOL) image at magnification of X 25,000. Figure 4.6(b) shows the average particle size measurement of TiO₂ nanofluid using DLS (HORIBA).

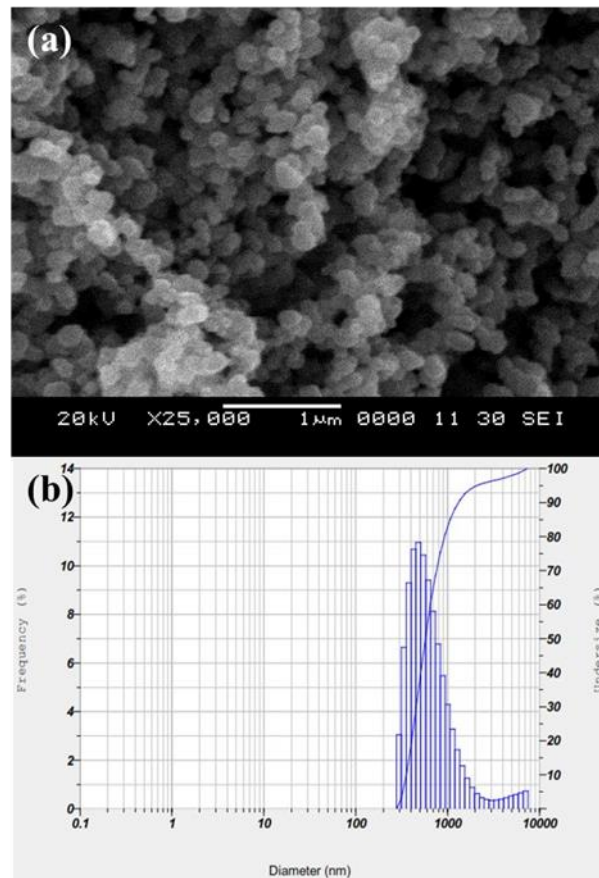


Figure 4.6 TiO₂ characterization (a) SEM image, (b) particle size measurement of 0.25% vf using dynamic light scattering.

The experimental study is conducted using the nanofluid consisting of TiO₂ nanoparticles with water as the base fluid. The nanofluid is ensured for its homogeneity before proceeding to experiments and finding out its thermophysical properties are of high importance in order to study its heat transfer performance. The nanofluid is subjected to sonication for 40 min to develop highly dispersed mixture with base fluid. The thermal conductivity of the TiO₂ nanofluid is measured using thermal conductivity analyser (ABB, Swiss) which provides

the values in the form of thermal conductance ($1/\mu\Omega$). These values are substituted to the correlation to generate the effective thermal conductivity as shown in Figure 4.7.

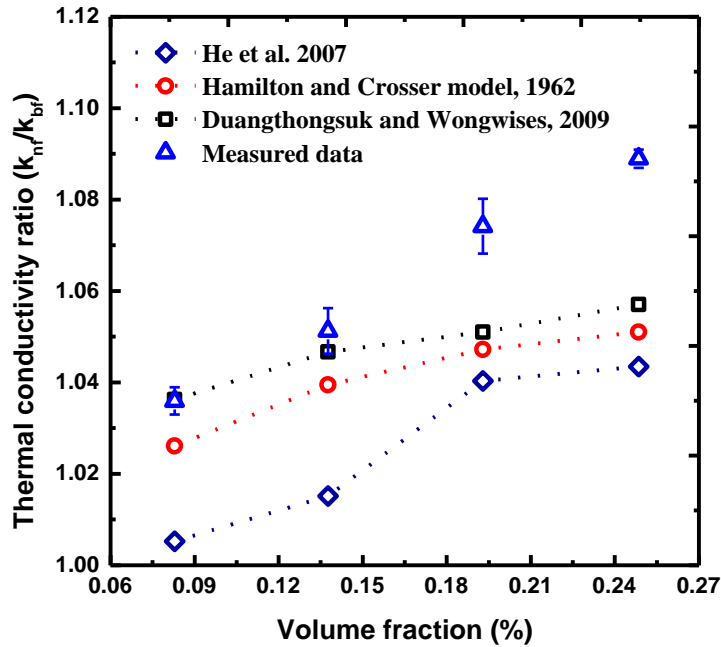


Figure 4.7 Effect of particle concentration on effective thermal conductivity of TiO₂ nanofluid.

The viscosity of the nanofluid is determined using rotary type viscometer presented in Figure 4.8. The density and specific heat of the nanofluid (Equations 4.1 and 4.2) are determined using models of (Pak and Cho, 1998 and Xuan and Roetzel, 2000) respectively. Additionally, several models on thermal conductivity (Hamilton and Crosser, (1962), He et al. (2007) and Duangthongsuk and Wongwises, 2009) and viscosity (Einstein, (1906), Brinkman, (1952), Batchelor, (1977), Duangthongsuk and Wongwises, (2009), and Said et al. 2015) were also compared with the present results. The obtained thermal conductive value of 1.10 W/m.K of TiO₂ nanoparticle was close to that of Duangthongsuk and Wongwises, 2009. However, according to the theoretical models of Hamilton and Crosser, (1962), calculations of the particle shape factor are introduced in the equation so the results were more precise than He et al. (2007). Recently, Mamand (2021) performed studies with very low nanoparticle volume fraction ranging from 0.005 to 0.05%. It was found that most

of the existing models under predicted the thermal conductivity and viscosity by not considering the interfacial layer and aggregation of the nanoparticle.

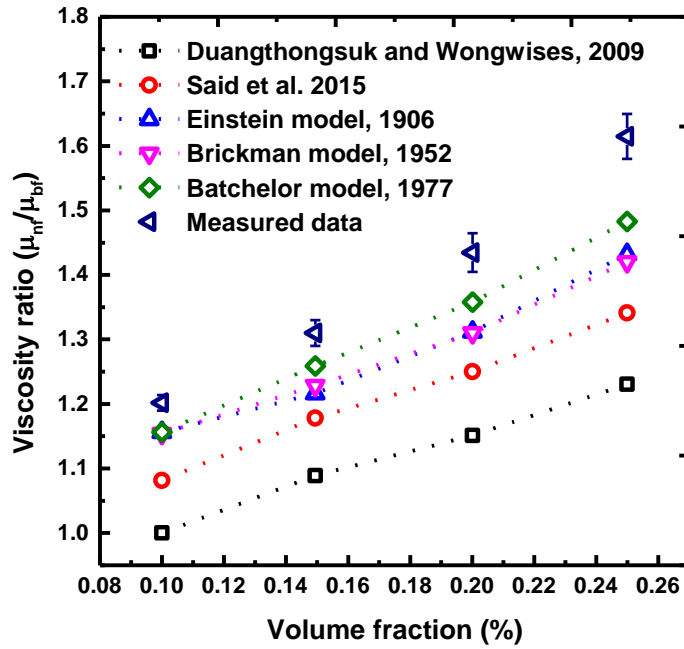


Figure 4.8 Effective viscosity of nanofluid on effect of particle concentration.

4.6 CLOSURE

The synthesis and characterization of GO and TiO₂ nanofluid are presented. The nanofluid is developed by two step process. The morphology of the GO nanoparticle is flake type platelets and TiO₂ nanoparticle is spherical type. The next chapter presents the details about the experimental heat transfer performance of GO nanofluid in a heat spreader integrated microchannel.

CHAPTER 5

EXPERIMENTAL INVESTIGATION ON HEAT SPREADER INTEGRATED MICROCHANNEL USING GRAPHENE OXIDE NANOFLUID

5.1 INTRODUCTION

Thermal design consideration is highly essential for efficient heat dissipation in advanced microprocessors which are subjected to conjugate heat transfer under high heat flux with a minimal area of cooling. Generally, these multicore processors develop a localized high density heat flux referred to as hotspot. The effective use of microchannel in order to mitigate the hotspot is found in literature; however, the flow induced hotspot still exist due to maldistribution of flow inside the microchannel. Henceforth, the present chapter provides an experimental insight on laminar forced convection in a parallel microchannel heat sink accompanied with 1.2 mm thin copper heat spreader with a surface area of 30 mm² to effectively migrate the maldistribution flow induced hot spot. The experimental study provides a profound insight into the hotspot and migration of hotspot to safe zones; as a result, not only the performance of the multi core microprocessor is highly improved but also the reliability of neighboring components is well secured.

5.2 INTEGRATED HEAT SPREADER APPROACH

A high thermal conductivity plate is attached beneath the microchannel shown in conceptual diagram of Figure 5.1. Figure 5.1(a) shows the heat spreader integrated microchannel heat sink. The fluid flow is normal to the microchannel through fluid handling unit (FHU) and exits the channel. The heat flux from electronic processor is directly applied to the heat sink base, the thermal energy splits evenly on both directions of the heat spreader and majority of the energy is conducted towards the microchannel. Figure 5.1(b) shows the initiation of the flow, where maximum cooling is observed at the entrance region of the microchannel. Due to this very less conduction happens in the spreader plate near the entrance region. On the other hand, same amount of flux is conducted and get distributed to microchannel and spreader near the exit of the channel. The continuous flow in the microchannel generates an accumulation of flow maldistribution induced hotspot highlighted near the channel exit. The heat capacity of working fluid transports majority of the heat flux conducted from microchannel denoted as $T_{con} = T_{conv}$ as shown in Figure 5.1(c). The temperature of the heat spreader is reduced and the peak temperature is at the

maldistribution accumulated microchannel exit region. This temperature difference from microchannel to heat spreader allows the thermal energy to migrate in heat spreader which is highlighted as $T_{hs} < T_{ths}$.

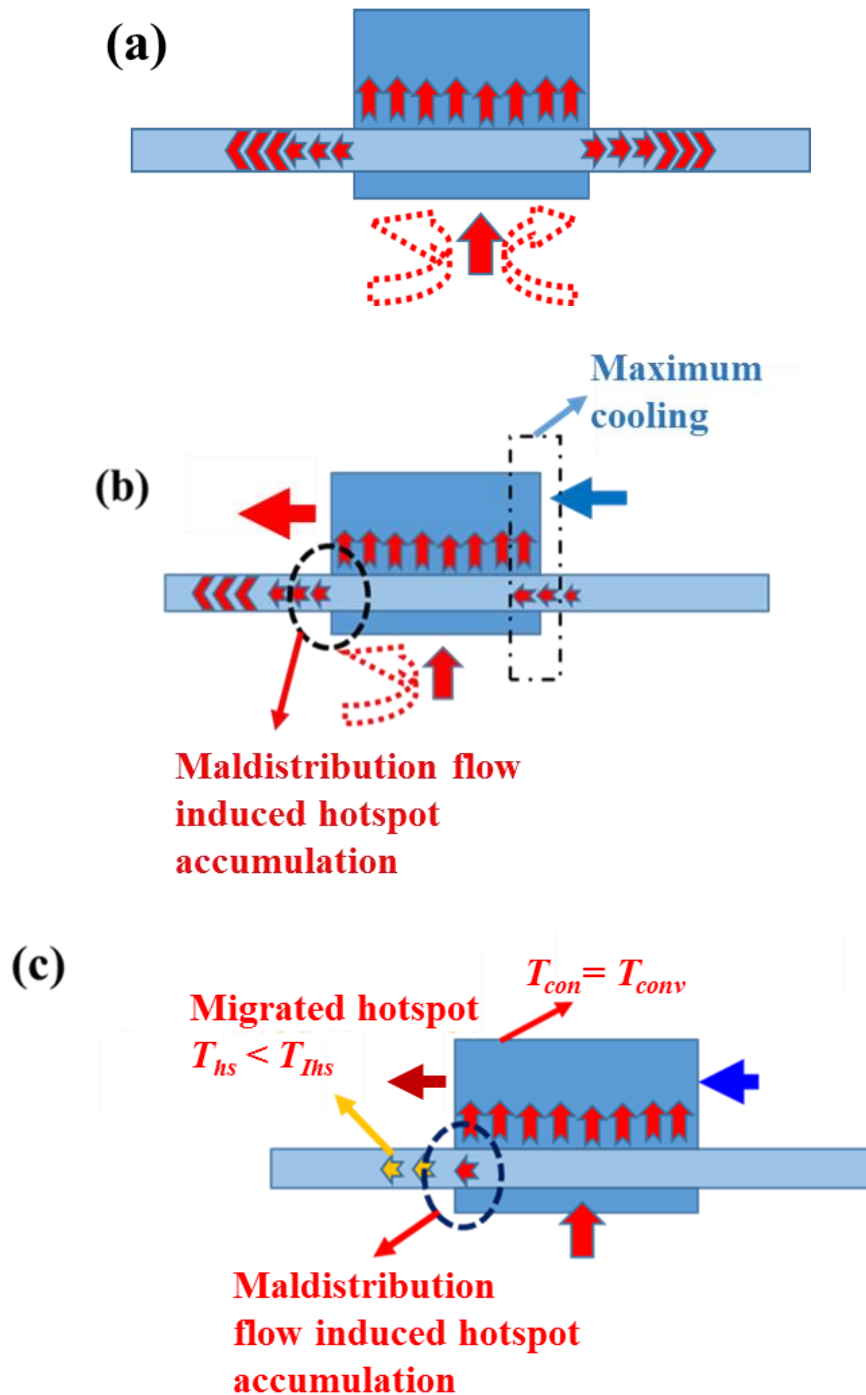


Figure 5.1 Conceptual diagram of the heat spreader integrated microchannel.

5.3 EXPERIMENTAL SETUP

5.3.1 Heat spreader assisted microchannel

The major concern of the present heat sink is to mitigate hotspot using heat spreader with the help of compact FHU, so that effective packaging can be implemented. The experimental setup was elaborately discussed in Chapter 3. Figure 5.2 shows the Infrared photographs of the processor for 8 s, 12 s and 16 s.

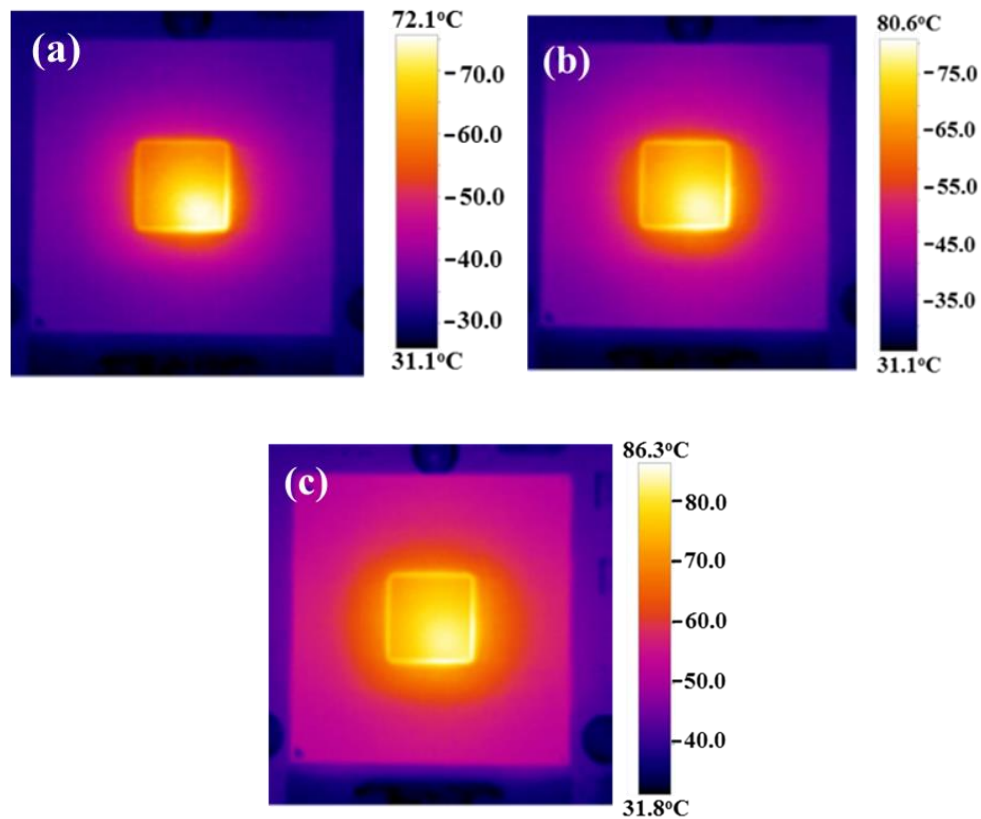


Figure 5.2 Infrared photographs of the processor (a) 8 s, (b) 12 s, and (c) 16 s.

5.3.2 Description of the experimental study

Figure 5.3 shows the locations of thermocouples in different temperature zones of the heat sink. The arrangement is to obtain the temperature distribution of the heat spreader integrated microchannel under different mass flow rates and GO volume fraction. The spreader is mainly divided into trailing and leading edges. This corresponds to temperature distribution developed in the spreader plate in accordance to the fluid flow direction. This region is additionally divided into heat spreader end zone (HSEZ) and heat spreader middle

zone (HSMZ) to specifically quantify the temperature responses near the outlet of the microchannel (T_4 and T_5) and at end of the heat spreader (T_6).

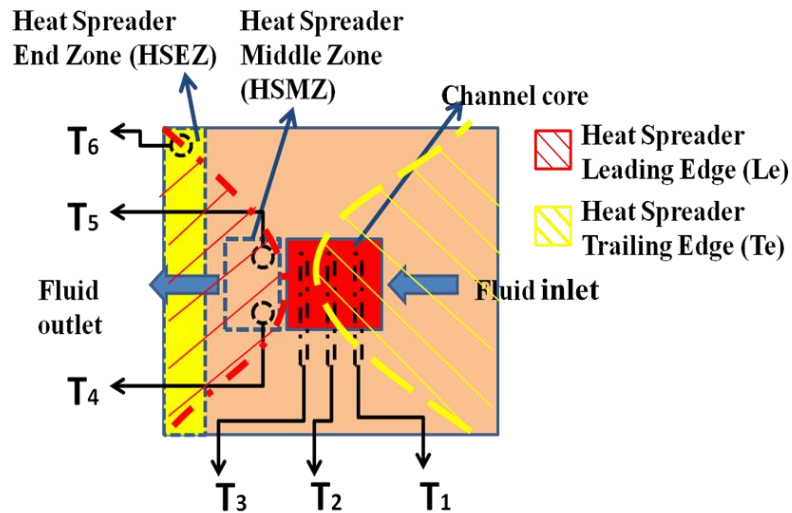


Figure 5.3 Schematic of thermocouple locations in different temperature zones.

5.3.3 Uncertainty parameters

The uncertainties involved in the measurements of various quantities are shown in Table 5.1.

Table 5.1 List of uncertainty in parameters.

Parameter	Uncertainty
Voltage, (V)	± 2.0 %
Current, (A)	± 2.0 %
Flow rate (L/min)	± 2.2 %
Temperature of copper sink	± 0.10 °C
Temperature of heat spreader	± 0.50 °C
Thermal camera	± 2.0 °C
Pressure transducer (kPa)	± 3 %

5.4 RESULTS AND DISCUSSION

5.4.1 Temperature distribution on heat spreader

Figures 5.4-5.9 show the temperature distribution prevailed in the heat sink and FHU for three different flow rates using water, GO-0.02% and GO-0.12% nanofluids. Additionally, the temperature distribution on different zones of heat spreader is also discussed. Figure 5.4 shows infrared-thermal images for heating cycle of the heat sink for a flux of 35 W/cm^2 . Figure 5.4(a) depicts the increase in temperature of the heat sink up to 50°C within 25 s.

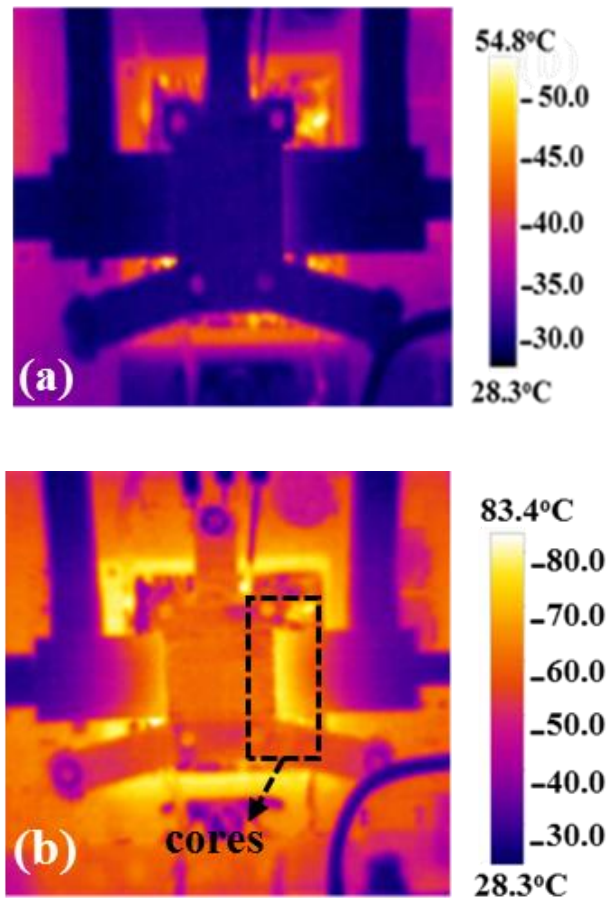


Figure 5.4 Infrared photographs of the module during heating for two time periods (a) 25 s, and (b) 50 s.

The temperature of the FHU region, which is very near to the channel, increases by 7°C . In this case, the hotspot is at the right edge of the channel where increase in temperature is more compared to the left side of the channel core. The surrounding temperature of the heat spreader in the PCB increases by 5°C and a negligible temperature increment is observed

at extreme ends of the FHU. But increase in 10°C was observed after 50 s, shown in Figure 5.4(b) and the area near the heat sink reaches 60°C . As noticed, the intensity of the temperature above the processor cores is more than 70°C . This shows the significance of hotspot penetration over the microchannel heat sink which is generated from the processor core.

Figure 5.5 shows the Infrared photographs of the microchannel module for three time periods using water as working fluid. After the run time of 10 s the temperature prevailed in heat sink is about 33°C and the entire FHU is maintained less than 30°C which is seen in Figure 5.5(a). The difference in 4°C is maintained from inlet to outlet fluids measured from the thermocouples placed within the FHU. The temperature of the surrounding regions in PCB reduces from 65°C to 40°C . Further progress in time above 20 s there was no much difference in the inlet and the outlet temperatures as shown in Figures 5.5(b) and (c). Moreover, a steady temperature of 42°C prevailed throughout the cooling period in area surrounding the heat sink.

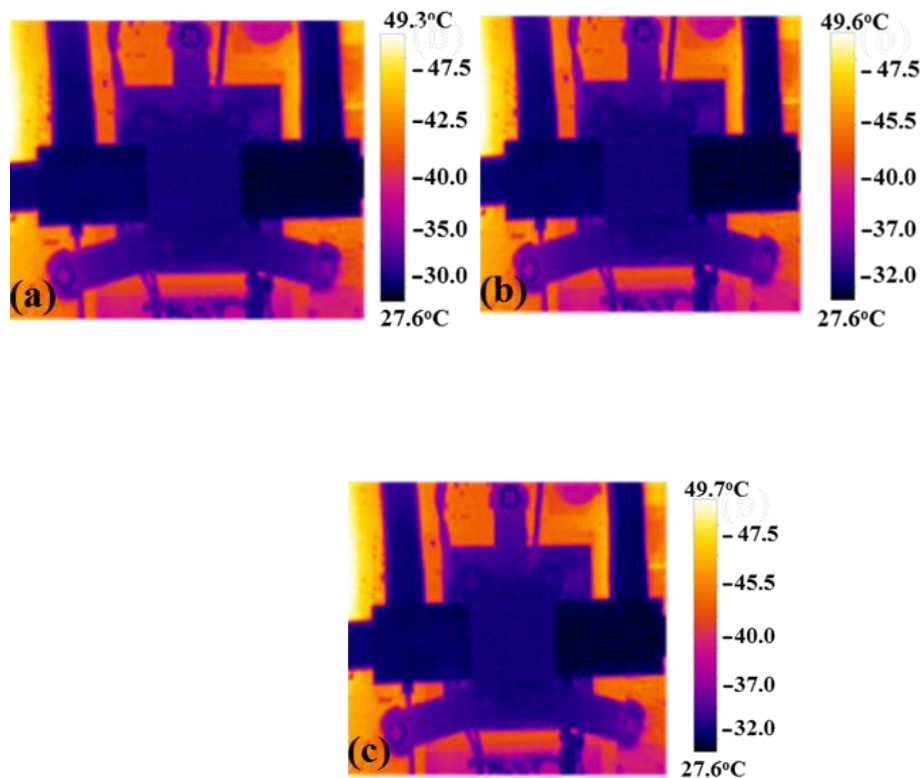
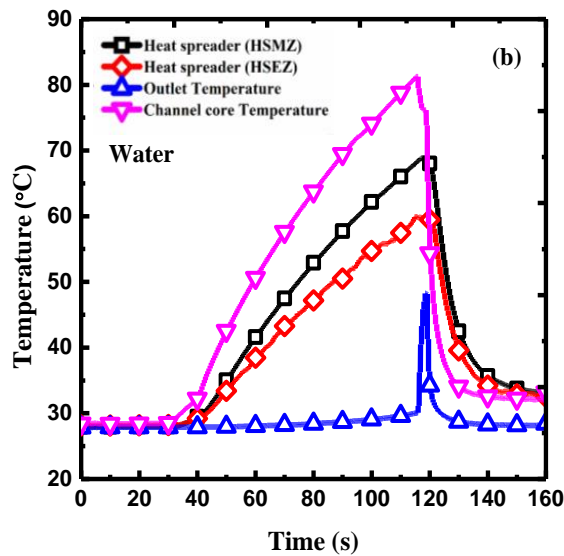
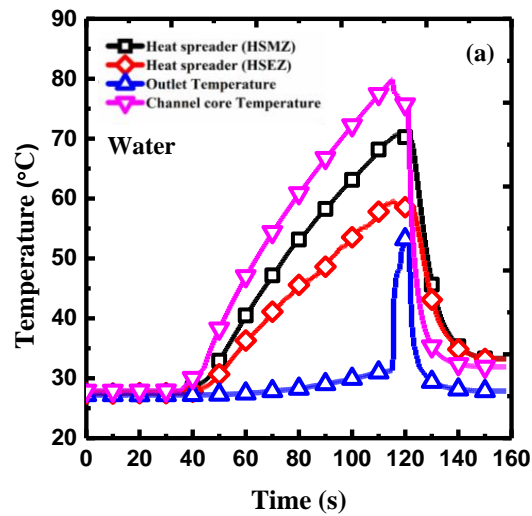


Figure 5.5 Infrared photographs of the module at progressive cooling at three time periods (a) 10 s, (b) 20 s, and (c) 30 s.

Figure 5.6 depicts the heating and cooling curves for various locations of heat sink and for three different flow rates with water as working fluid. Figure 5.6(a) shows the temperature distribution for lowest flow rate of 0.21 L/min as a function of time. On initializing the processor, the maximum temperature reached by microchannel core was 80°C. The corresponding HSMZ and spreader tip temperatures are 70°C and 60°C, respectively. As observed, once the flow is initiated, the outlet temperature of the microchannel increases and temperature of the channel core reduces rapidly.



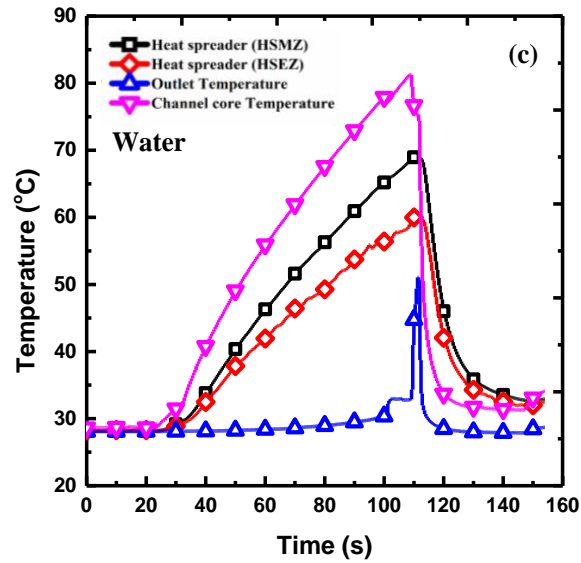
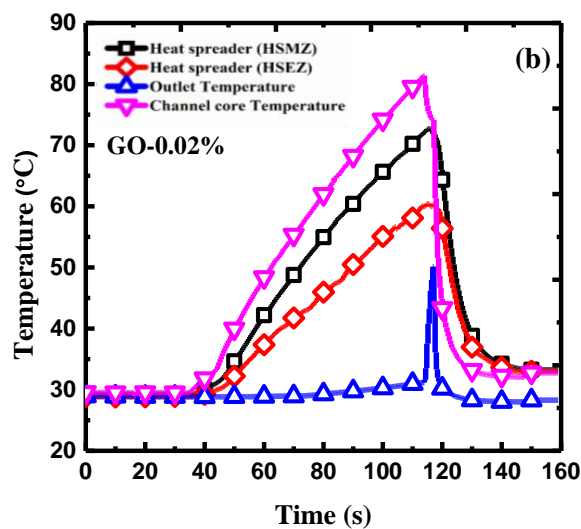
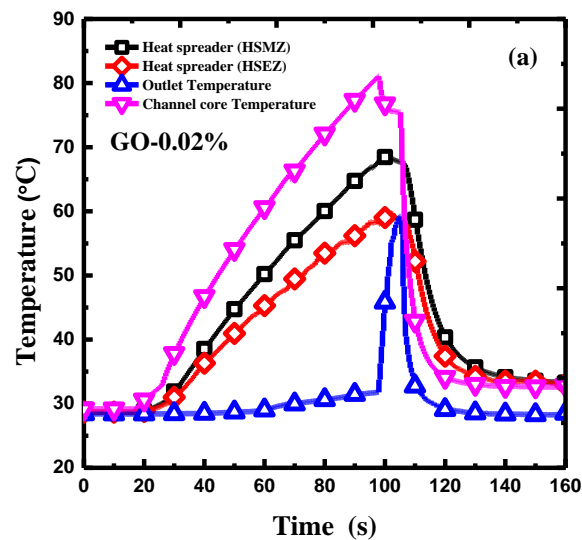


Figure 5.6 Temperature distribution with water as working fluid for different flow rates (a) 0.21 L/min, (b) 0.26 L/min, and (c) 0.31 L/min.

The working fluid takes 5 s to reach the maximum temperature of 55°C and the HSEZ temperature is still in the range of 60°C. After the run time of 60 s, the heat sink and core temperature settled down to 38°C. This instant drop in core temperature is due to the enhanced surface area of parallel microchannel combined with the pulsating flow. Figure 5.6(b) shows the temperature distribution for 0.26 L/min. In this case, the maximum outlet temperature is decreased by 6°C and all the cooling curves have become comparatively steep. The area under the cooling curve is reduced by 50% and the time taken for the working fluid to attain T_f is minimized. But still HSMZ correspondingly takes longer time for cooling than other zones in the heat sink. The maximum steep curve is developed for higher flow rate of 0.310 L/min which is shown in Figure 5.6(c).

On close observation, the response time of cooling microchannel core is reduced at increased flow rates. Furthermore, at lower flow rates the effect of fluid diffusion increases and dominates the axial heat conduction in microchannel heat sink which eventually leads to higher temperature in HSMZ. On the other hand, increased flow rates accompanied with nanofluid generates higher temperature due to flow maldistribution in parallel channels. Figure 5.7 presents the temperature distribution in the heat sink for GO-0.02% nanofluid. At lower flow rate of 0.21 L/min the outlet temperature reaches nearly 60°C which is higher

than the outlet temperature developed for water as shown in Figure 5.7(a). This temperature is equivalent to the temperature noticed in HSEZ of heat spreader in the heat sink. This is majorly due to the increased thermal conductivity of nanofluid combined with reduced flow rate. As observed, the core temperature reduces from 80°C and maintains 75°C for 5 s before it experiences steep decrease in temperature. This clearly shows that there is an effect of bulk fluid conduction in the heat sink especially for nanofluid; but, in case of water similar effect was noticed for less than 5 s under different flow rates. With the increased flow rate of 0.26 L/min, there is sudden decrease in temperature in all zones of the heat sink as observed in Figure 5.7(b).



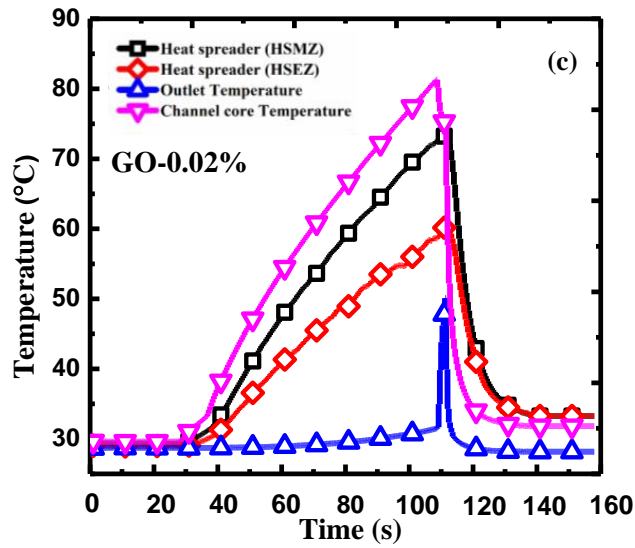
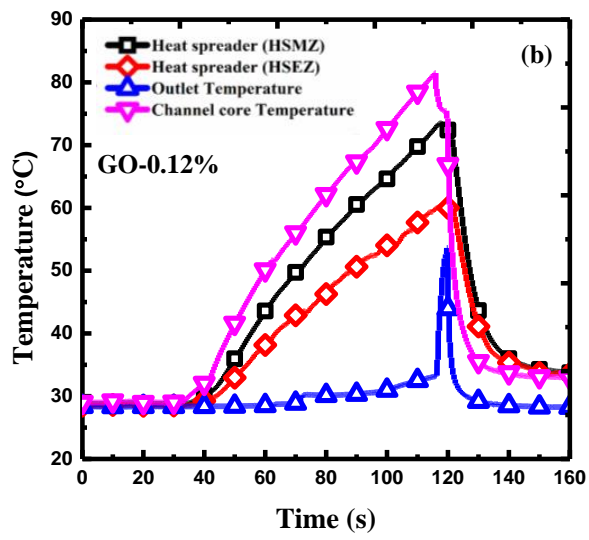
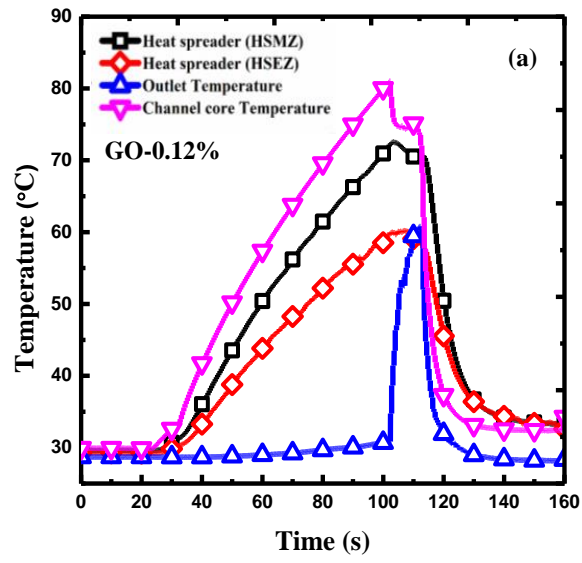


Figure 5.7 Temperature distribution with GO-0.02% as working fluid for different flow rates (a) 0.21 L/min, (b) 0.26 L/min, and (c) 0.31 L/min.

The decrease in temperature is steep and the peak of the outlet temperature is comparatively sharp. Further increase in the flow rate reduces the response time and there is no significant effect of fluid bulk diffusion over the heat sink for the flow rate of 0.31 L/min as shown in Figure 5.7(c).

Figure 5.8 presents the results for GO-0.12% nanofluid at different flow rates. At lower flow rate of 0.21 L/min the outlet temperature reaches maximum of 60°C which is higher than the HSEZ temperature as shown in Figure 5.8(a). Compared to the other two working fluids, the effect of bulk fluid diffusion and axial conduction effects are seen distinctly for the case of GO-0.12% nanofluid. Further increment in flow rate reduces peak outlet temperature by 5-6°C but not below 50°C which is shown in Figure 5.8(b). For 0.31 L/min the cooling in HSMZ and HSEZ is more or less similar to the 0.26 L/min flow rate but temperature drop at core reached maximum refer Figure 5.8(c). In all the cases the temperature of HSMZ and HSEZ is about 3-4°C more than the core temperature.



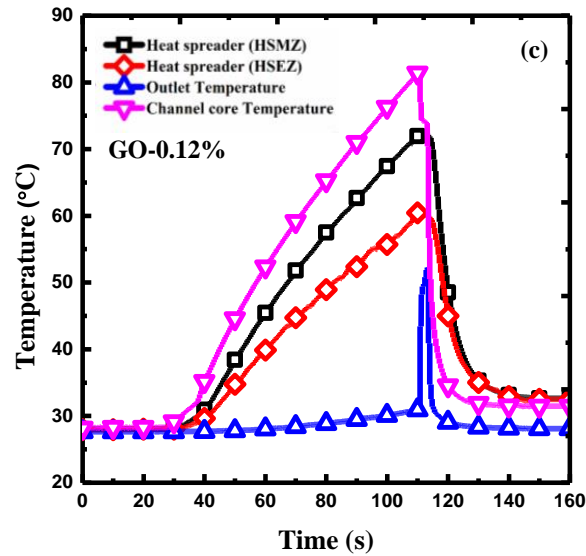


Figure 5.8 Temperature distribution with GO-0.12% as working fluid for different flow rates (a) 0.21 L/min, (b) 0.26 L/min, and (c) 0.31 L/min.

From the above observations the axial conduction effects combined with flow maldistribution in parallel microchannel develop higher temperature at outlet region of the microchannel. This effect further intensifies for high thermal conductivity nanofluid at lower flow rates. The core temperature reduces by 6°C due to the increased thermal conductivity but at the same time the heat sink is subjected to fluid diffusion based conduction effects. In the case of higher flow rates for all subjected fluids the channel core and HSMZ temperatures have less marginal gap for the first time. Overall the increase in HSMZ temperature is majorly due to the migrated temperature from the sink core.

The comparison of temperature between microchannel heat sink and microchannel integrated heat spreader module with different fluids is shown in Figure 5.9. The temperature variations are taken using thermocouple T₃ for both the heatsinks which represent the location of flow maldistribution hotspot region. The microchannel heat sink shows higher temperature than the microchannel with spreader for all the flow rates and working fluids. More than 6°C decrease in temperature was observed by implementing heat spreader. For all the flow rates and working fluids considered, an average increase of 7°C is observed for the case of only microchannel heat sink module. Apparently, for microchannel heat sink case the maldistribution flow induced hotspot accumulates near the

exit of the microchannel. Subsequently, there is increase in temperature T_3 not only due to maldistribution but also the effect of axial conduction. As noticed, when the heat spreader is integrated with the microchannel heat sink the temperature T_3 reduces significantly.

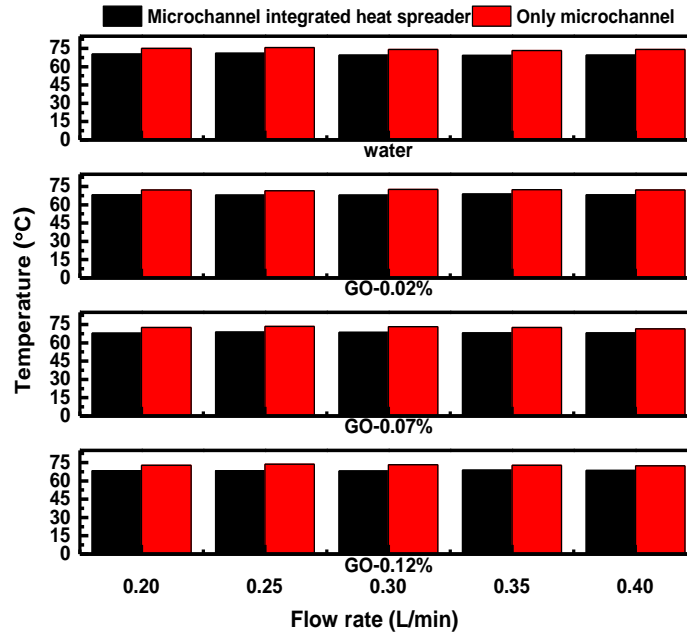


Figure 5.9 Comparison of temperature data for microchannel heat sink and heat spreader integrated microchannel heat sink with different fluids.

5.4.2 Heat transfer studies

The experimental observations were made for five different flows rates ranging from 0.21 to 0.45 L/min. The local heat transfer coefficient is obtained from the following equation

$$h_x = q'' / (T_w - T_f) \quad (5.1)$$

Where q'' is the heat flux subjected to the walls of the electronic chip. T_w is the microchannel wall temperature. T_f is defined as the local bulk fluid temperature. Local

Nusselt number in the study is defined as

$$Nu_x = h_x D_h / k_f \quad (5.2)$$

Where D_h is the hydraulic diameter of the microchannel which is given as

$$D_h = 4ab/a + b, \quad a \text{ and } b \text{ are the corresponding length and breadth of the microchannel.}$$

The average Nusselt number for the present study is reported by calculating the average heat transfer coefficient along the channel length which is given by

$$h_{avg} = \frac{1}{L} \int_0^L h_x dx \quad (5.3)$$

$$Nu_{avg} = \frac{h_{avg} D_h}{k} \quad (5.4)$$

Figure 5.10 shows the increase in heat transfer coefficient with respect to GO/water nanofluid for different volume fractions and increased flow rates. It can be seen that the average heat transfer coefficient calculated using Equation 5.3 increases with increasing flow rate. Similarly, higher volume fraction of nanoparticles results in enhancement of heat transfer coefficient. The maximum heat transfer coefficient was achieved for volume fraction of GO-0.12 %.

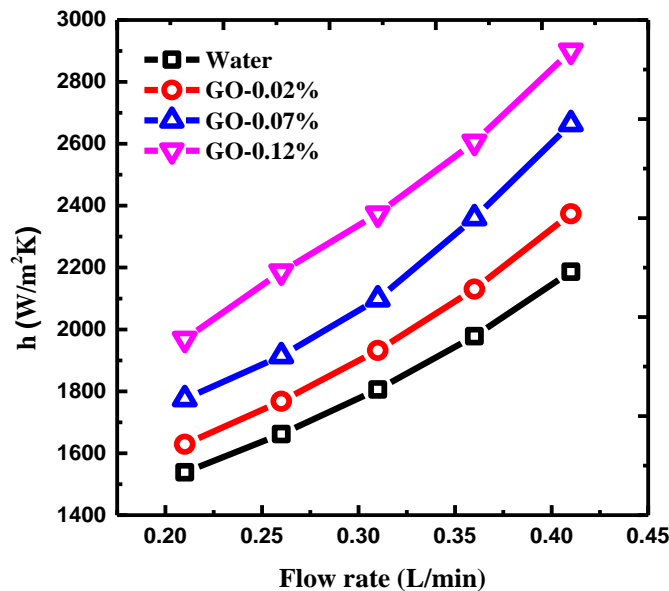


Figure 5.10 Heat transfer coefficient as a function of flow rate for different volume fractions.

Figure 5.11 depicts the experimental comparison of Nusselt number for three different nanofluids for the Reynolds number ranging from 100 to 320. It was observed that the Nusselt number was found to be maximum at the higher flow rates. This trend was also seen in other three GO nanofluid. The maximum Nusselt number was obtained for GO-0.12 % nanofluid which is 17% higher than water. Additionally, the Nusselt number obtained using the present experimental data is compared with the existing benchmark correlations proposed by other researchers (Choi et al. (1991), Wang and Peng (1994), Peng and Peterson (1996), and Jung et al. 2009).

Choi et al. (1991) presented a correlation for the Nusselt number for micro tubes and water as working fluid for $Re < 2200$ and is given in Equation 5.5

$$Nu = 0.000972Re^{1.17} Pr^{1/3} \quad (5.5)$$

Where Re is the Reynolds number calculated as $\rho_f u D / \mu_f$ and Pr is the Prandtl number given as $C_p \cdot \mu_f / k_f$. (Peng and Peterson, 1996) proposed a correlation for Nusselt number correlation for the Reynolds number ranging between 200 and 4000 for $Pr=1.69$. The proposed correlation with a deviation approximately $\pm 30\%$ as follows

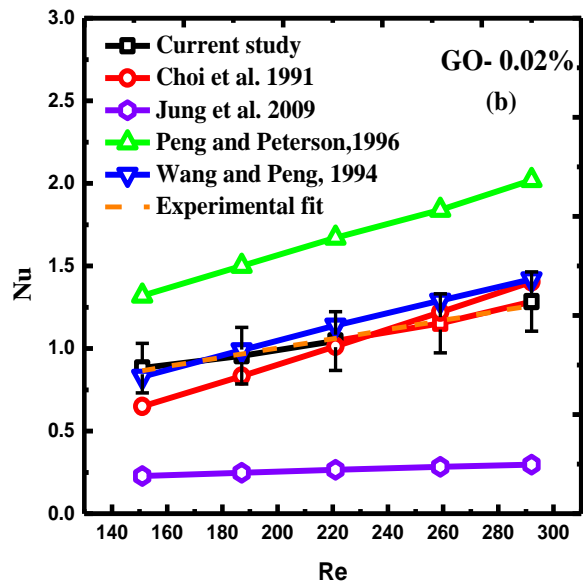
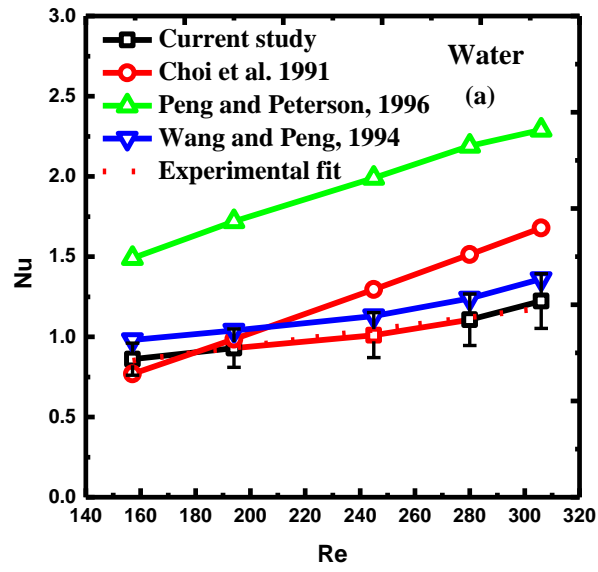
$$Nu = 0.1165(D_h / W_c)^{0.81} (H / W)^{-0.79} Re^{0.62} Pr^{1/3} \quad (5.6)$$

Wang and Peng, (1994) presented Nusselt number correlation on rectangular channels for Reynolds number ($70 < Re < 1500$) for Pr ranging between 2.69 and 7.56. Equation 5.7 represents a correlation developed from experimental data for all the tested channels with a maximum deviation of $\pm 25\%$.

$$Nu = 0.0080Re^{4/5} Pr^{1/3} \quad (5.7)$$

Jung et al. (2009) proposed a modified form of Dittus-Boelter equation for microchannels which includes a volume fraction for the nanoparticle for a range of Pr ($0.6 < Pr < 160$) and Reynolds number ($0 < Re < 350$).

$$Nu = 0.014\phi^{0.095} Re^{0.4} Pr^{0.6} \quad (5.8)$$



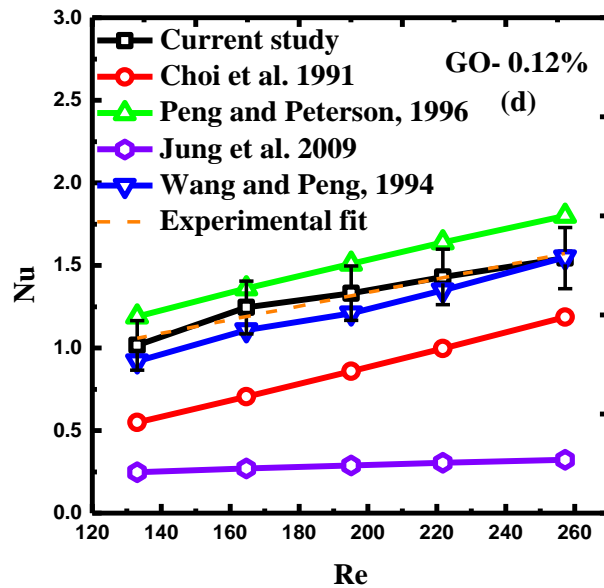
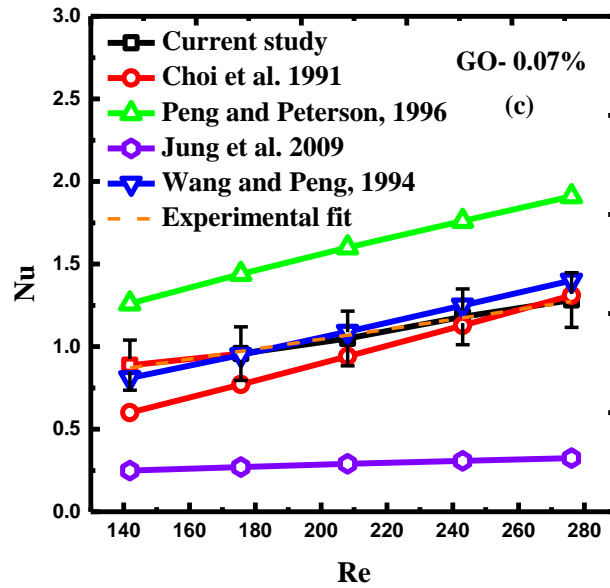


Figure 5.11 Nusselt number as a function of flow rate for different volume fractions.

(a) water, (b) GO-0.02%, (c) GO-0.07% and (d) GO-0.12%.

Figure 5.11(a) depicts the variation of experimental Nusselt number for increased Reynolds number with water as working fluid in the rectangular microchannel. The Nusselt number is calculated using Equation 5.4 for which the required wall temperature and bulk fluid temperature for the applied heat flux are acquired from thermocouple data. As seen in

Figure 5.11(a) the experimental results having a deviation of $\pm 2\%$ is compared with correlation proposed by Choi et al. (1991) and Wang and Peng (1994) for water and found to have a deviation of 6%. But a maximum deviation of 30% was observed for Peng and Peterson (1996) and the predicted Nusselt number was higher than that of experimental results. Similar discrepancies were noted for the results presented by Peng et al. (1995) and Qu et al. (2000). Peng and Peterson (1996) suggested a correlation that takes in to account the height and width of microchannel which may be one of the reasons for the deviation. Since the aspect ratio of the channel considerably affects the thermal and flow characteristics; the current study has high temperature core at the entrance of the microchannel, that results in temperature difference at inlet and outlet sections of the microchannel. The thermal gradient in the microchannel heat sink resulted by hotspot could conceivably be reduced with the use of nanofluid. Nevertheless, use of nanofluid in parallel microchannel undergoes flow maldistribution and axial conduction effects there by increasing the temperature of the outlet section of the microchannel. Comparatively the thermal gradient developed by flow maldistribution induced hotspots is relatively lower than the hotspot cores.

In order to show the enhancement of heat transfer due to GO nanofluid, the experimental results were demonstrated with other established Nusselt number correlation. Moreover, Nusselt number correlation for nanoplatelets based nanofluid using microchannel is not yet established clearly. On the other hand, the performance of microchannels with very low volume fraction nanofluid for heat transfer augmentation has been focused much by the researchers recent times. As a result, the GO nanofluid used in the present study is added with nanoparticle ϕ less than 1% and the correlations available for pure fluid are then used to study the effect of GO nanoparticle. Figure 5.11(b) shows the Nusselt number for GO-0.02% as a function of Reynolds number. The results demonstrated that GO-0.02% nanofluid provided improved heat transfer performance than water. The experimental results evidently show the influence of lower ϕ GO-0.02% nanofluid in augmentation of Nusselt number. However, the influence of nanoparticle is not substantially noticed at increased ϕ of GO-0.07% as shown in Figure 5.11(c). The reason might be attributed to the increased conduction effects of the heat sink due to the increased bulk fluid temperature for higher thermal conductivity nanofluid at lower Reynolds number. This increases the thermal gradient of microchannel heat sink, as discussed in temperature study section, refer

Figures 5.6-5.8. Furthermore, increase in ν_f to GO-0.12% reduced the deviation from the predictions of Peng and Peterson (1996) as shown in Figure 5.11(d).

From the observation it is clear that the improved performance of microchannel heat transfer at higher Reynolds number is predominantly due to the augmented thermal conductivity of GO nanofluid and enhanced stability of the GO nanoparticles in the base fluid. Additionally, the shape factor of the GO nanoparticles enhances the contact of nanoparticle with base fluid. This progressively increases the particle collision and escalates heat transfer mechanisms according to Brownian motion, Thermophoresis and Ballistic transport. The above mentioned GO nanoparticle characteristics and mechanisms eventually intensifies the thermal energy transport owing to diffusion and thereby increasing the bulk cooling fluid temperature. Concurrently, the increased GO volume fraction contributes higher particle interaction with microchannel wall with increased momentum which results in effective thermal transport. It was observed that the effect of Reynolds number is highly sensitive for higher volume fraction nanofluid. As observed, for lower Reynolds number the bulk fluid temperature of the nanofluid is higher and increases the heat sink temperature with highly stable and directional temperature gradients. This increase in bulk fluid conduction in heat sink was predominant at lower Reynolds number and the effects are profoundly seen for higher ν_f nanofluid and similar effect was observed by Ebrahimi et al. (2016).

5.4.3 Friction factor

Figure 5.12 shows the increase in pressure drop as a function of flow rate for different working fluids. It is clearly seen that the addition of GO nanoparticles increases the pressure drop and amplifies even further at higher flow rate. A maximum pressure drop of 6 kPa was developed for water at 0.36 L/min. For the same flow rate GO-0.12% nanofluid developed pressure drop of 10 kPa. On comparison with water the use of nanofluid in microchannel heat sink augments the pressure drop by 45% for GO-0.02% and 60% in the case of GO-0.12%.

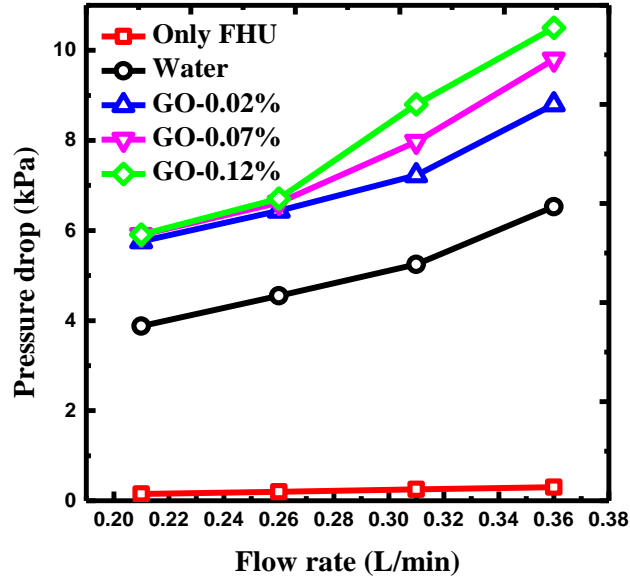


Figure 5.12 Pressure drop as a function of flow rate for different fluids.

Moreover, the difference in pressure drop among GO nanofluid is minimal at lower flow rates but a very low concentration GO-0.02% nanofluid generates significant pressure drop than water. It is evident that at lower flow rate the nanoplatelets are marginally assisted by gravity and at higher flow rate channel surface and entrance effects amplifies the pressure drop to a maximum limit.

The experimentally measured pressure drop across the microchannel in FHU is used to calculate experimental friction factor by the following equation given in Equation 5.9

$$f = \frac{\Delta P D_h}{1/2 \rho \bar{u}^2 L} \quad (5.9)$$

In Figure 5.13 the experimental friction factor is compared with the theoretical friction factor predicted using Hagen- Poiseuille equation given by Equation 5.10 as function of Reynolds number ranging from 150 to 350 with error less than $\pm 2\%$.

$$f = \frac{64}{Re} \quad (5.10)$$

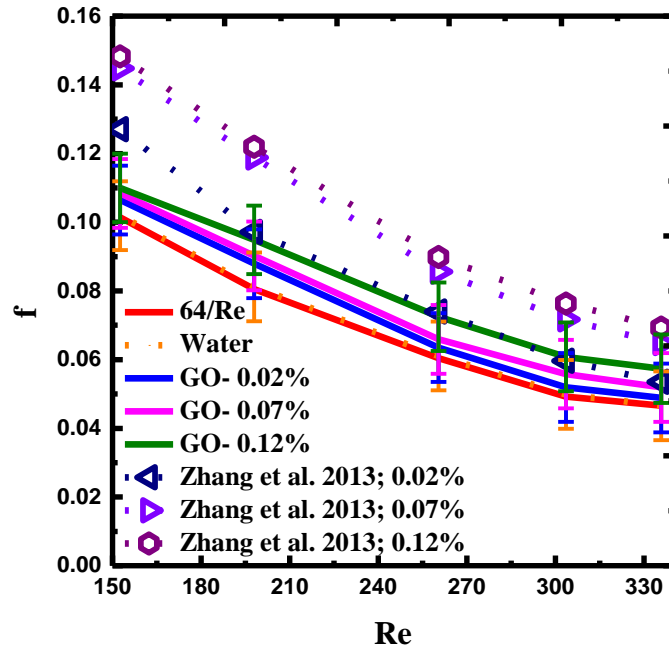


Figure 5.13 Friction factor as a function of Reynolds number for different fluids.

A considerable agreement with a deviation of 3% was found between the theoretical and experimental friction factors. For low volume fraction of 0.02%, typical friction factor result was observed, in which the friction factor decreases as Reynolds number increases. In the case of higher volume concentration of GO-0.12%, the friction factor increased by 20% due to the increased viscosity developed for higher mass fraction; consequently, the use of lower volume fraction of 0.02% resulted in increase of friction factor by 6% than water. This certainly shows that even for very low volume fraction of GO nanoplatelets a considerable increase in friction factor is unavoidable. This penalty in friction factor is highly attributed to substantial increment in surface area of GO nanoplatelets based nanofluid.

Additionally, the experimental results were compared with the friction factor correlations obtained by Zhang et al. (2013) given by Equation 5.11.

$$f = 6.3265Re^{-0.656}(1 + \phi)^{4.835} \quad (5.11)$$

The error developed by using 0.02, 0.07 and 0.12 vf% in this correlation for examined Reynolds number were 34%, 41% and 48%, respectively. As observed in Figure 5.13, the

experimental results when compared with (Zhang et al. 2013) resulted in higher friction factor than the current study. But still at higher Reynolds number the predicted friction factor of GO nanofluid agrees well with the experimental results. This is due to the proposed correlation that was investigated for a Reynolds number range of 600-2000. Moreover, they used circular cross section with comparatively denser Al_2O_3 nanofluid.

Figure 5.14 shows the results of pumping power, refer Equation 5.12, with respect to the flow rate for water and GO nanoplatelets based nanofluid.

$$P_p = Q \cdot \Delta P = \frac{\dot{m} \Delta P}{\rho} \quad (5.12)$$

Here Q is volumetric flow rate and ΔP is experimentally obtained pressure difference from microchannels.

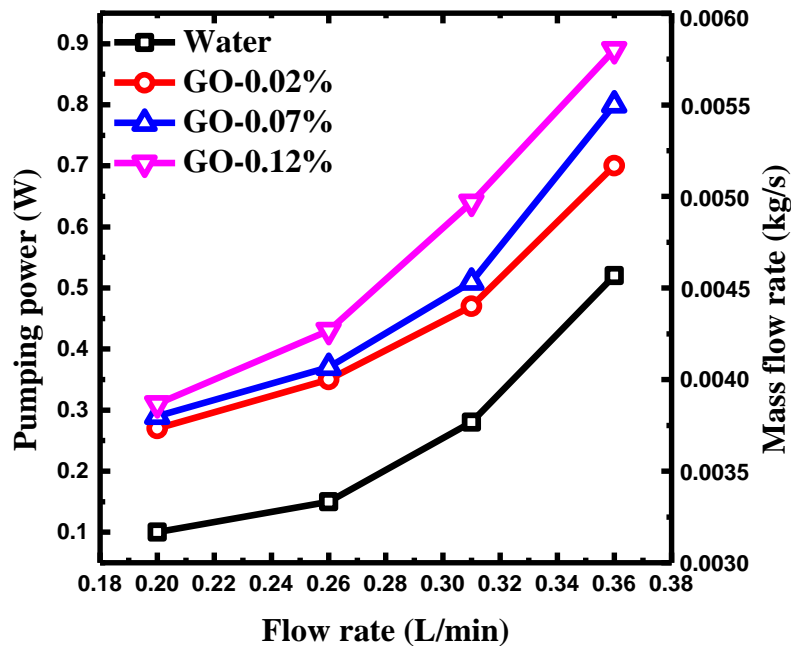


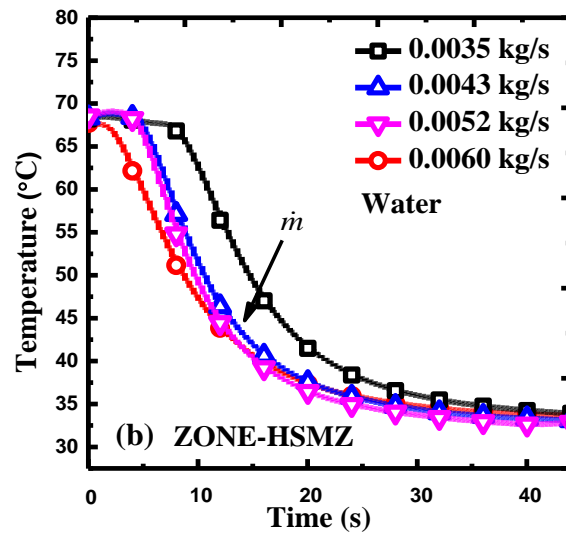
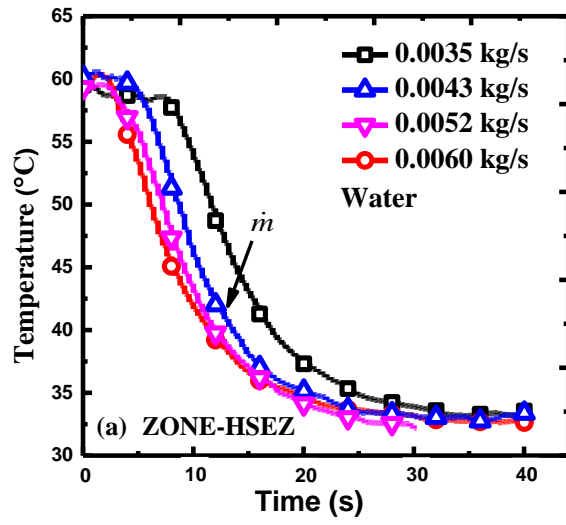
Figure 5.14 Pumping power as a function of flow rate for different fluids.

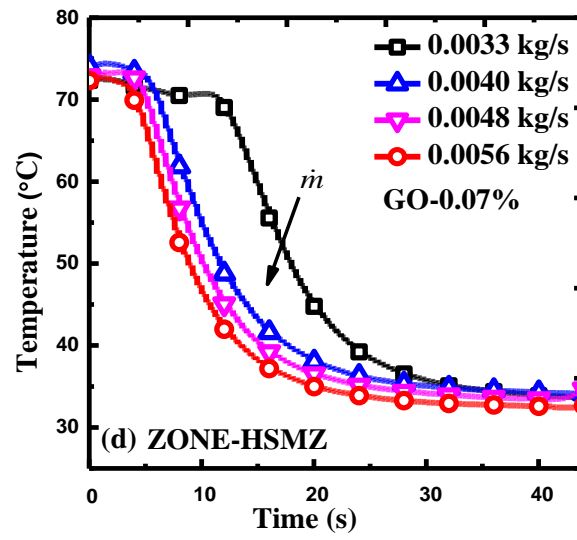
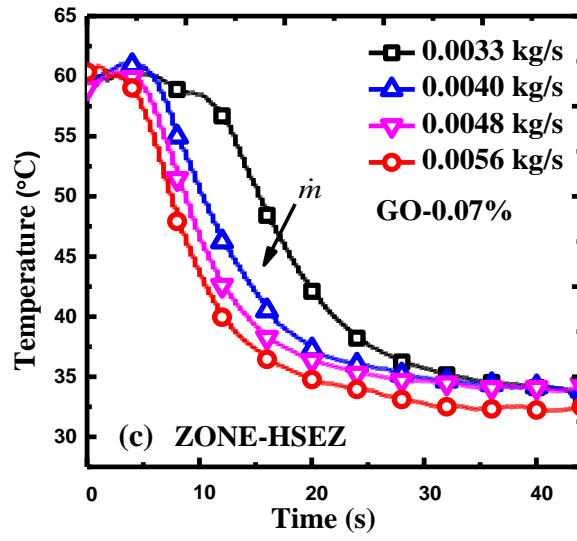
As noticed, the pumping power increases as the flow rate increases for all the fluids. Furthermore, the increase in particle concentration additionally increases the pumping power. This implies pumping power majorly relies on factors such as flow rate and volume fraction of nanofluid. The maximum pumping power of 0.87 W was generated by GO-

0.12% which is 74% higher than water for the same flow rate of 0.36 L/min. But the deviation of pumping power between GO-0.02% and GO-0.12% is comparatively lower by about 25%.

5.4.4 Hotspot migration

The use of the heat spreader with the microchannel allows for the study of thermal energy migration from the channel core to various regions of the large surface area heat spreader under different flow rates. Depending on the flow rates the movement of temperature distribution in heat spreader is parallel to the flow and along the direction of the fluid. Thus the heat spreader facilitates to extract high density thermal loads developed by multicore processor. This migration of higher temperature in heat spreader is qualitatively captured by experimentation which is shown in Figures 5.15(a-f). Figure 5.15(a) shows the temperature in HSEZ for varying mass flow rate of 0.0035 to 0.0060 kg/s for water with a constant heat flux of 35 W/cm². For the case of mass flow rate 0.0035 kg/s, the temperature at HSEZ slightly decreased by 2°C and maintains 58°C till 10 s and then the temperature of HSEZ decreases rapidly to 35°C. This is majorly attributed to the lower flow rate, but the effect of cooling wave is experienced in HSEZ due to the initial decrease in temperature of 2°C. In the case of 0.0043 kg/s, there is no effect of initial decrease in temperature at HSEZ, but rapid decrease in temperature is noticed within 5 s. In this consideration, with the increased mass flow rate the effect of thermal migration is reduced by 50% and relative cooling performance of the heat sink is doubled. For the cases of 0.0052 and 0.0060 kg/s similar decrease in HSEZ temperature is observed. The results of temperature for HSMZ are shown in Figure 5.15(b). The effect of initial decrease in temperature in HSMZ is not observed and the temperature decrement is comparatively more gradual than HSEZ. The decrease in temperature for higher mass flow rates developed identical curves after 10 s, but did not reduce the spreader temperature less than 35°C. These combined effects in HSEZ and HSMZ reveal that once the flow is initiated within the heat spreader there exhibits a decrease in transfer of thermal energy from the heat sink core. Note that at this point the cooling wave has propagated throughout the heat spreader except HSMZ, since it is in the vicinity of high temperature region generated by flow maldistribution induced hotspot at the exit of the microchannel.





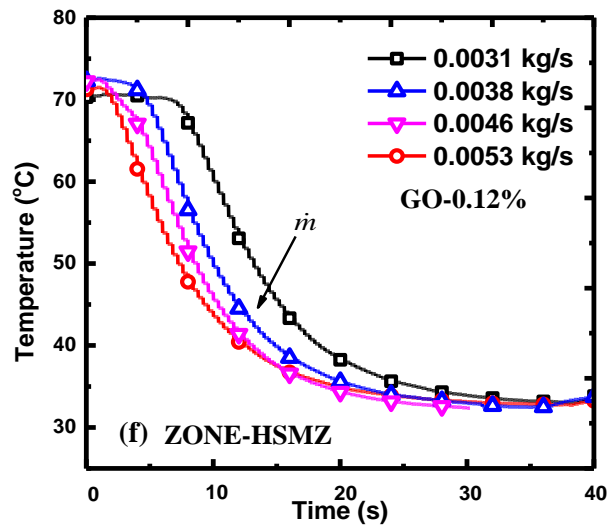
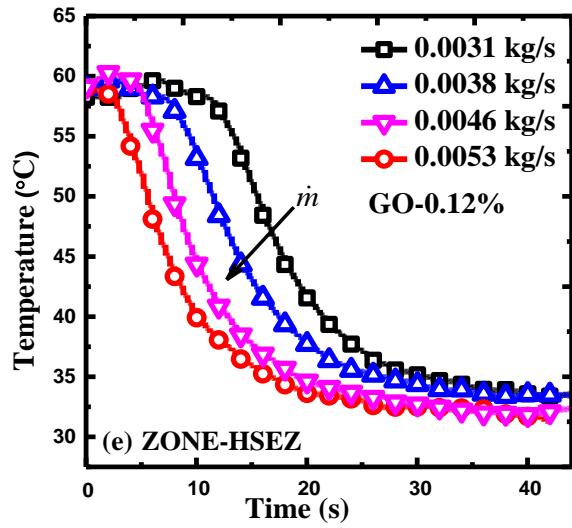


Figure 5.15 Heat spreader temperature distribution for different flow rates (Direction of arrow indicates the increase in mass flow rate). (a) HSEZ-water, (b) HSMZ-water, (c) HSEZ-GO-0.07%, (d) HSMZ-GO-0.07%, (e) HSEZ-GO-0.12%, and (f) HSMZ-GO-0.12%.

Figures 5.15(c) and (d) represent the temperature distribution for GO-0.07% nanofluid with different mass flow rates. For the lower mass flow rate of 0.0033 kg/s the temperature of HSEZ decreased with comparatively higher time period than HSEZ of water as shown in

Figure 5.15(c). The explanation for this higher time period is due to the increased thermal conductivity of the GO-0.07% nanofluid. This in turn causes the nanofluid to carry more heat towards the HSEZ region. More appropriately the conduction effects in the heat sink influenced by bulk fluid diffusion potentially ceases the drastic transmit of cooling to HSEZ region. As demonstrated, the decrease in HSEZ temperature is very drastic for increased mass flow rate of 0.0040 kg/s with the reduced time period of 30%. On the other hand, the corresponding differences in time period between mass flow rates of 0.0048 and 0.0056 kg/s are comparatively lower. Due to the combined impact of increased mass flow rate and thermal conductivity, the temperature of the HSEZ region reaches 33°C which is more or less near to room temperature. Figure 5.15(d) shows the temperature decrement at HSMZ as a function of time for different mass flow rates. It is observed that the maximum temperature of HSMZ region increases to 76°C and is higher compared to water. Most importantly, the temperatures of the heat spreader are at two different temperatures with the difference of 16°C at the same time period. This large increment in HSMZ temperature is attributed to increased thermal conductivity and lower flow rate which increases the outlet fluid temperature more than 60°C as seen in temperature study section. Besides the increment in HSMZ temperature, the higher thermal energy migration from the microchannel to the heat spreader has increased by using higher volume fraction nanofluid. Moreover, more stable temperature distribution in heat spreader has been developed by GO-0.12% nanofluid presented in Figure 5.15(e). As noticed before in GO-0.07%, the temperature of HSEZ increased gradually for more than 10 s and then it reduces. However, no significant temperature stability is seen in HSMZ as shown in Figure 5.15(f). Since the HSMZ is near the microchannel outlet, the temperature of 70°C is maintained nearly 10 s at lower mass flow rate of 0.0031 kg/s which was noticed only for GO nanofluid. But once the flow rate is increased the temperature of HSMZ drops drastically similar to all the other working fluids. Moreover, for all the fluids there exists an increase in temperature of 2°C in HSMZ even though the heat sink is subjected to cooling. This increase is due to thermal migration from outlet region of the sink to HSMZ.

5.5 CONCLUSIONS

Experimental investigations were performed on the rectangular microchannel accompanied with heat spreader for various flow rates using water and GO with three different volume fractions (GO-0.02%, GO-0.07% and GO-0.12%) as working fluid. For a constant heat flux of $35\text{W}/\text{cm}^2$, the heat removal rate of GO-0.12% nanofluid was found superior to pure fluid, GO-0.02% and GO-0.07%. The important key findings are

- Heat spreader effectively operates at a lower flow rate of 0.21-0.30 L/min, beyond that the presence of heat spreader is compromised.
- The Nusselt number was found to increase by 17% with the use of GO-0.12% nanofluid.
- The surrounding temperature prevailed near to the heat sink drops from 60°C to 42°C due to the supply of high thermal conductivity fluid in microchannel.
- Experimental characterization demonstrates that the contribution of very low concentration (GO-0.02 vf%) can alter the hydrodynamic and heat transfer phenomena.
- It has been found that the GO nanofluid as working fluid provides steady cooling and can effectively be suitable for handling high flux density components without compromising packaging for highly compact electronic devices.
- Due to low pumping cost and miniaturization of electronic equipment, the micro heat sink presented in this work provides a better and profitable solution as a compact electronic cooling device.

5.6 CLOSURE

This chapter provided the details about the experimental investigation of the heat spreader integrated microchannel. The effect of the nanofluid concentration and its dependence on flow rate were discussed in view of heat spreader temperature distribution. The next chapter provides an insight to the response time effects of heterogeneously integrated microchannel with heat spreader.

CHAPTER 6

INVESTIGATION ON TEMPERATURE RESPONSE EFFECTS IN MICROCHANNEL

6.1 INTRODUCTION

In any microchannel cooling device, the response time distinctively varies due to heterogeneous integration of the source and the sink. Due to local temperature gradients which is referred to as hot spots and maldistribution of the fluid flow in the microchannel, there is a considerable change in the response time which can be investigated using non-Fourier heat conduction. An in-house rectangular microchannel with heat spreader experimental setup is developed to investigate the thermo-hydrodynamics of the heat sink with GO-water nanofluid as the working fluid.

6.2 NON FOURIER HEAT TRANSFER

Most of the studies in the literature have considered integrating heat sink directly to the heat generating electronic chip. Moreover, the latest processors are subjected to multiple hotspots which are potentially capable of developing thermal imbalance in cooling system. Additionally, ineffective fluid handling can further intensify the effects of hotspot. These hotspots vary according to computational loads and mostly diffuse by fast transient heat conduction processes involving high temperature gradients. These cases are more prone to thermal lagging between the source and the developed temperature gradient in the substrate and expected to diffuse by non-Fourier conduction. In fact, non-Fourier heat conduction is profoundly seen in the studies of heterogeneous materials. More recently, Liu et al. (2016), Kovas and Van (2018) pointed out the dual phase lag based on the Cattaneo-Christov model. Even at room temperature, experiments with heterogeneous materials show that the conduction is due to diffusive propagation compared to wave propagation. Typically, Fourier conduction does not account for the time lag developed during the transient heat conduction process and predicts the temperature deviations throughout the solid with infinite propagation velocity. But in reality, local change in temperature develops temperature perturbations with dampened propagation at every location of the substrate due to thermal relaxation time. Thermal relaxation time for a heat sink can be defined as the time taken by a substrate to attain thermal equilibrium for a temperature gradient developed due to a given heat flux. It is decisive that the thermal relaxation time is a significant time

period to accumulate energy and transfer it to the substrates. Moreover, the Fourier model fails to predict the initial temperature jump on transient applications for which the applied heat flux is instantaneous. It is very crucial to note that, it is not just associated with micro scale devices but several works reported the behavior of non-Fourier conduction in macroscopic domain where operational time and size are comparatively large. The importance of relaxation time is very significant because it may exhibit non-Fourier behavior in many densely packed micro cooling devices. Although, several analytical studies have reported non-Fourier heat conduction and thermal wave behavior in heterogeneous materials, this still remains as a hot topic among researchers. Apart from materials and phenomenon of transient diffusion, the configuration of microchannel influences the response time of the heat sink. The response time can be defined as the ratio of temperature between the heating cycle and steady state condition. It is found that the heater source and microchannel heat sink have different response timings in which heat sink has higher response time than the heater. The response time of the heat sink with a constant flow rate is observed to be stable for different heat fluxes with increased outlet and interface temperature for higher amplitude of heat fluxes. Moreover, at increased flow rates temperature deviations in solid and fluid interfaces are observed in micro scale domain. At the same time, velocity of the temperature propagation is found to vary among different bonding materials to which the heat sink is interfaced. The effects of surface roughness of bonding surface analytically with heterogeneous substrates and suggested that the effect of surface roughness is very similar to that of flat surface except with reduced contact resistance due to increased surface area.

Some of the mentioned investigations were conducted in microchannel with different flow configurations and heat sink materials to determine the response time, but its influence due to hotspots and nanofluid has not been explored much experimentally. Besides, analytical studies predict negligible influence of propagation velocities for bonding different materials with surface roughness which has to be revisited with critical findings. Hence, the focus of this study is to present comprehensive experimental and numerical investigations on the effects of conduction in heat sink and response timing of Graphene oxide (GO) nanofluid in a heat spreader integrated microchannel with hotpot. Further, the present work emphasizes on two important findings: (a) the effects of heat conduction in heat sink at low Reynolds number with graphene oxide nanofluid and (b) the influence of hotspots and heterogeneous medium with nanofluid on response time.

6.3 BACKGROUND OF THE STUDY

Recently, the transistor scaling in electronic processors has reached greater extent with elevated power generation and has increased the packaging density that caused new challenges for thermal management of compact systems. This demanded researchers to critically analyze the cognitive effects of heat conduction and its dependence on semiconductor nanostructures, in particular the physics of heat conduction of the material for better thermal management. The basic phenomenon for heat conduction is interactions of phonon and its average distance travelled between two consecutive phonon scatterings that are described as phonon mean free path. This phenomenon is differentiated based on physical conditions and operational parameters of high-power systems. It is highly influenced by type of material used for device integration and its size which decides the mean free path of the phonons. When the size of the device is comparatively larger than mean free path, the heat conduction is by Fourier diffusion. On the other hand, if the device size is much smaller than the mean free path, the conduction is due to ballistic phonon transport. The latest three-dimensional transistors in processors are in the size range lower than 10 nm and it is near to the mean free path of phonons. This in turn develops difficulty in studying these applications with the conventional heat conduction equations. Further, these are installed with dense interconnecting solders like Zn-Al, Bi with CuAlMn on Mo heat sink. This intricate bonding structures makes the propagation velocity of the heat conduction complex. Moreover, the multicore processors have individual cores with different power rating corresponding to the computational load. These individual cores act as potential hotspot and dynamically vary local temperature of the substrate. This combined effect of heterogeneous materials with transient loading conditions generates different response time and develops bottleneck for thermal management. Furthermore, for effective thermal management these devices are mounted with macro scale cooling predominately copper or aluminum. In these cases, the local temperature in the substrate is not well defined and due to the transient hotspot, the thermal equilibrium is never achieved in the heat sink. This gives raise to localized high temperature zones in the heat sink which reduces the efficiency of the microchannel cooling system. Several studies have been performed to effectively mitigate the hotspot but effects like maldistribution and flow induced hotspots dominate the heat sink. Recent times, microchannel integrated with heat spreader have been investigated to reduce the dynamic loads; results showed an effective thermal spreading of heat flux with reduced heater temperature. However, thermal responses influenced by

dynamic hotspots and its conjugate effects are not studied much. In the present study, microchannel cooling device is integrated with heat spreader using silver soldering as shown in Figure 6. 1.

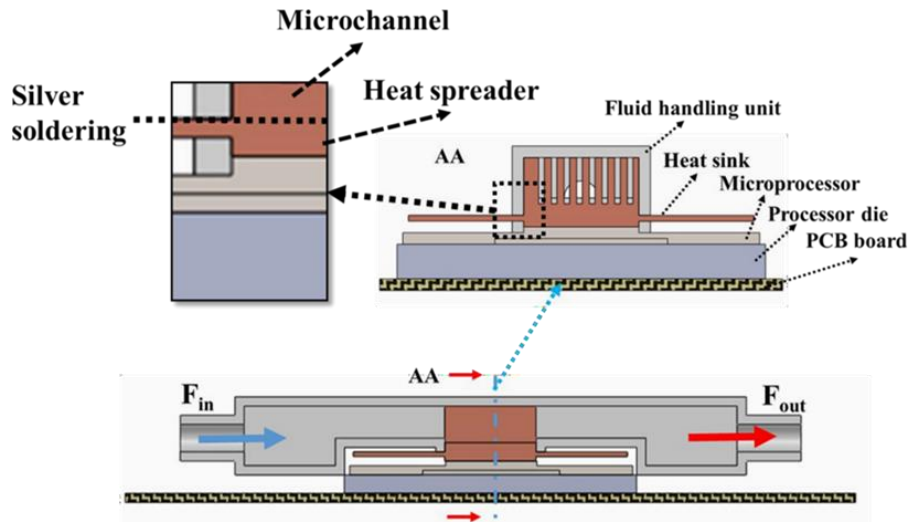


Figure 6.1 Schematic of heat spreader integrated microchannel with the details of the interface materials.

Experiments are conducted to present the time dependent thermal wave that propagates in microchannel core and the heat spreader. Initially, both the heat sink and the processor core are at room temperature. Once the processor is initialized, the heat sink is subjected to instantaneous two hotspots. Thermocouples are fixed in both the microchannel core and the heat spreader; 2 mm near the core and 15 mm at the edge of the heat sink in the spreader. The same setup is used to obtain response time of conduction thermal wave upon cooling.

6.4 EXPERIMENTAL DETAILS

Experiments are performed for three different cases to capture the transient superposition characteristics of the heat spreader integrated microchannel. Initially, the heatsink is allowed to get heated up to 85°C and then water is passed and the corresponding temperature distribution is measured. Similarly, the heat sink is tested with different concentrations of the nanofluid. The temperature distribution thus obtained contains the information of the microchannel temperature, hotspot temperature, heat spreader temperature and the fluid outlet temperature. The total duration of the experiment is approximately 180 s. This procedure is followed with different flow rate and nanofluid concentration.

Figure 6.2(a) shows the details of the locations and temperature sensors installed in the microchannel and heat spreader. Figure 6.2(b) shows the details of the thermocouple locations used to determine the response time.

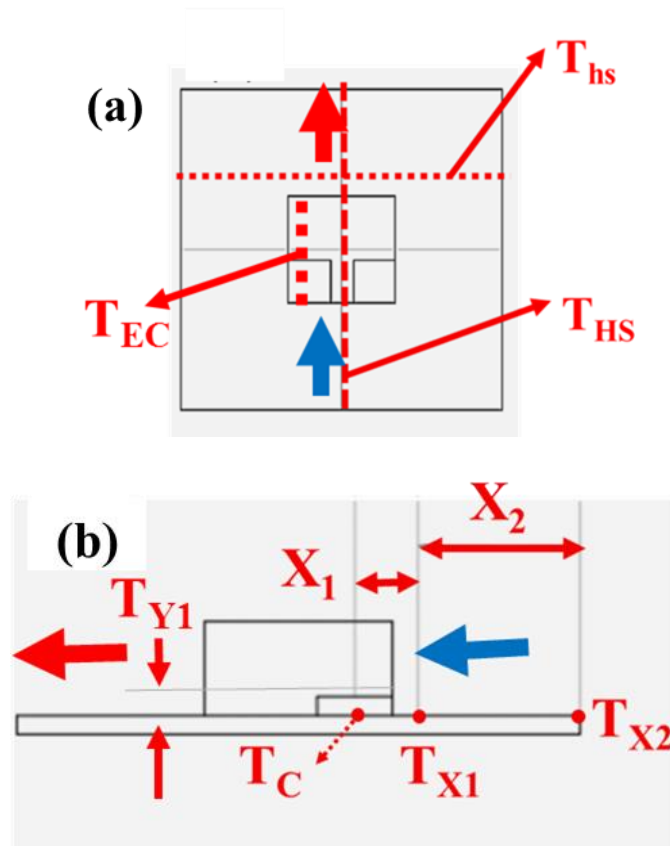


Figure 6.2 Schematic of heat spreader integrated microchannel (a) details of temperature sensors, and (b) location of the temperature sensors.

High thermal conductive silver paste is used as interface material between the processor and the heat sink to reduce the contact resistance. Inlet and outlet temperatures are measured using two K-type thermocouples in the direct fluid flow with temperature accuracy of 0.1°C . The pressure drop in the microchannel is measured by differential digital manometer. These temperature and pressure sensor sets are attached to NI Data logger and connected to the computer for monitoring the experiments. The data acquisition (NI 9213) is set to a range of 0-0.78 mV with 8 digit resolution, implying a sensitivity of 0.02°C . The wave form generator is additionally used to calibrate the acquired signals from the thermocouples with different pulses. The entire study utilizes Chromel-Alumel type thermocouples having diameter of 0.15 mm and the bead diameter of 0.6 mm. Each

thermocouple is calibrated against standard thermometer in an oil bath ranging from room temperature to 120°C.

6.5 THEORY AND ANALYSIS

The term thermal wave commonly indicates the temperature field in a wave like propagation caused by heat flux. These propagations have been under investigations to determine thermal diffusivity of the materials for decades. But, due to its remarkable importance and scope in the study of transient heat conduction process it is renamed into thermal waves. Still the discussion on true nature of thermal waves is highly debatable among the scientific community, Chen et al. (2018). But relatively, it is widely accepted to present the temperature field in the periodical system. The major concern is to know how the heat conduction exhibit wave like behavior. It starts by understanding the fundamentals of Fourier heat conduction equation by linearly equating the heat flux and the temperature gradient, given as

$$q = -k\nabla T \quad (6.1)$$

In which k is thermal conductivity of the material and assumed to be independent of temperature perturbations. In several thermal wave investigations, the variation of induced temperature is within 10°C; so, k is essentially a constant. Further, thermal wave propagation by energy conversation in a differential form is given in Equation 6.2

$$\nabla \cdot q + \frac{\partial(\rho CT)}{\partial t} = f(r, z)Q(t) \quad (6.2)$$

Where ρ and C are the density and specific heat of the material respectively. The right side of the Equation 6.2 presents the heat input rate per unit volume in a spatial distribution, $f(r, z)$ and $Q(t)$ denotes the time dependent factor. Sinusoidal time dependent form of $Q(t)$ is assumed to form thermal wave equation, given as

$$Q(t) = Qe^{-i\omega t} \quad (6.3)$$

The thermal wave equation can be generated by combining Equations 6.1 to 6.3 with a boundary condition which relates temperature $T(x, t)$ distribution within the solid, given as

$$-k \frac{\partial T}{\partial x}(x,t) \Big|_{x=0} = R \frac{I_0}{2} e^{i\omega t} \quad (6.4)$$

By combining Equations 6.1 to 6.4, we get

$$\nabla \cdot \left(R \frac{I_0}{2} e^{i\omega t} \right) + \frac{\partial}{\partial t} \rho C T = f(r,z) Q e^{-i\omega t}$$

$$\int \rho C \frac{\partial T}{\partial t} = \int \left[f(r,z) Q e^{-i\omega t} - R \left[\frac{I_0}{2} e^{i\omega t} \right] \right] \partial t$$

$$\nabla^2 T + q^2 T = -f(r,z) Q / k \quad (6.5)$$

Equation 6.5 presents the fundamental form of thermal wave physics used to describe the wave propagation. Here \bar{q} denotes with wave vector given as

$$\bar{q} = (1+i) \left(\frac{\omega \rho c}{2k} \right)^{\frac{1}{2}} \quad (6.6)$$

$$\bar{q} = \frac{(1+i)}{\mu} \quad (6.7)$$

From Equation 6.6 it is clear that the thermal wave becomes extraneous after certain diffusive length from the point of heat flux. One cannot find thermal diffusion length directly by experiments; it can be found by including other factors such as thermal characteristic time and penetration time (t_p). The penetration time can be identified from a definite location (X_p) within the sink from the source. This is to determine the time period required for the thermal waves to reach the respective location. The velocity of the thermal wave can be given as

$$v = \frac{x_p}{t_p} \quad (6.8)$$

From the wave velocity the value of the relaxation time (τ) can be determined

$$\tau = \frac{\alpha}{\nu^2} \quad (6.9)$$

Where α is the thermal diffusivity of the material. In this current problem the heat flux from the core is diffused through the heat sink and the substrate as shown in Figure 6.3. Since the understanding of the diffusion is very essential for the thermal wave propagation and its superposition characteristics, it is good to exemplify the physical model in a brief.

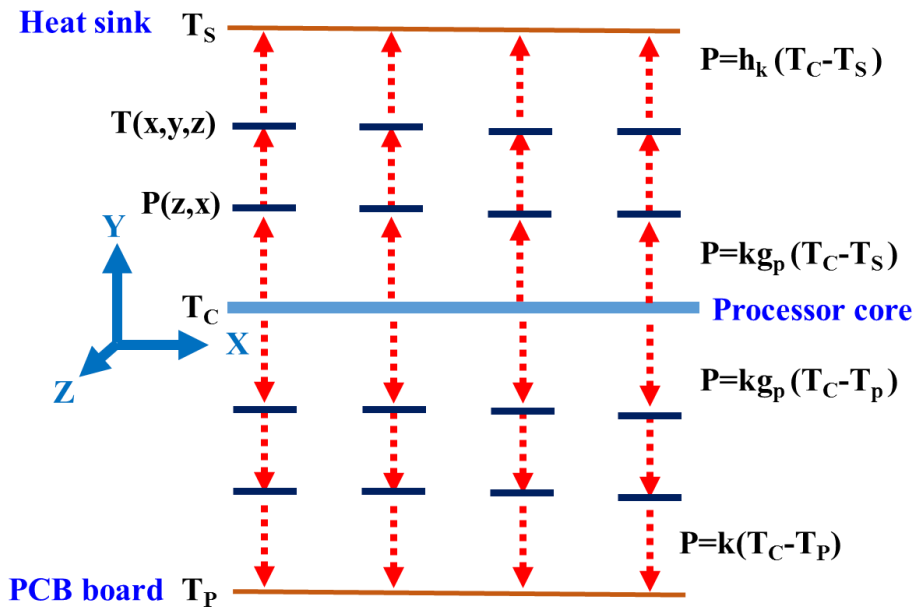


Figure 6.3 Schematic of free body model of the heat conduction from the processor to the heat sink and to the bottom substrate, where T_C is the core temperature, T_S is the heat sink temperature and T_P is the substrate temperature.

Fourier's law states that the applied heat flux \vec{q} is equivalent to the temperature gradient developed, that is

$$\vec{q} = -k\vec{\nabla}T(x, y, z) \quad (6.10)$$

Where $T(x,y,z)$ is the temperature distribution in the core substrate and k is the thermal conductivity of the material. By energy conservation principle, we can deduce the material layer temperature distribution

$$\rho c \frac{\partial T(x, y, z, t)}{\partial t} = \bar{\nabla} \cdot (k \bar{\nabla} T(x, y, z, t) + g(x, y, z, t)) \quad (6.11)$$

Here ρ denotes the material density, specific heat is denoted by C and g is the volume power density. In this current problem the total heat is generated by the core and no other heat source is present; it makes $g=0$, so the equation becomes

$$\rho c \frac{\partial T(x, y, z, t)}{\partial t} = \bar{\nabla} \cdot (k \bar{\nabla} T(x, y, z, t)) \quad (6.12)$$

For the case of homogenous heat sink the thermal conductivity is constant, in the case of only microchannel heat sink the above equation can be given as

$$\rho c \frac{\partial T(x, y, z, t)}{\partial t} = \nabla^2 T(x, y, z, t) \quad (6.13)$$

From the core surface, the heat is transferred to the microchannel heat sink by the thermal contact. In case of good thermal contact, the condition of both heat sink and source approach more or less similar temperature and it can be represented as

$$T(x, y, z, t) \Big|_{y=d} = 0 \quad (6.14)$$

On the bottom side, significant amount of power density is balanced by heat conduction along $-y$ direction under non-homogenous substrates under multiple thermal conductive substrates. But on together the Fourier conduction can be considered as

$$\frac{k \partial T(x, y, z, t)}{\partial y} \Big|_{y=0} = P(x, z) \quad (6.15)$$

In the case of sides of heat sink, it is covered with FHU; hence, it can be represented as adiabatic boundary condition

$$\frac{\partial T(x, y, z)}{\partial x} \Big|_{x=0,a} = 0 \quad (6.16)$$

$$\frac{\partial T(x, y, z)}{\partial z} \Big|_{z=0,b} = 0 \quad (6.17)$$

Here a and b are the length and breadth of the rectangular heat sink, respectively. In the case of heat spreader integrated heat sink, more area is available for convection.

$$\frac{\partial T(x, y, z)}{\partial x} \Big|_{-a \leq x \leq a} = h_{conv} (T - T_{\infty}) \quad (6.18)$$

$$\frac{\partial T(x, y, z)}{\partial z} \Big|_{-b \leq z \leq b} = h_{conv} (T - T_{\infty}) \quad (6.19)$$

6.6 NUMERICAL METHODOLOGY

A single phase model has been adopted for the numerical studies of laminar forced convection heat transfer of the rectangular microchannel. This model involves conduction and convection heat transfer simultaneously. The single phase mass, momentum equation and energy equations are solved for nanofluid. The heat conduction equation is solved for the solid copper region and the discretization for solid and fluid regions are made using finite volume method. The entire microchannel is considered for the purpose of computations. SIMPLE (Semi-Implicit method for pressure linked equations) method is chosen for pressure and velocity couplings. The resulting algebraic system of equations is solved by using Gauss Seidal iterative method with successive over relaxation (SOR) to improve the convergence time. The numerical model is verified with grid independence study and validated with standard experimental result to ensure the fidelity of the mathematical model and the approach of the methodology. The numerical simulations are performed until the residuals of the governing equations are less than 10^{-6} .

6.6.1 Boundary conditions

The following conditions have been imposed in the current study, refer Figure 6.4

- a) Both the fluid and solid domain have been modeled as three dimensional for the analysis of transient heat transfer.
- b) Laminar based forced condition with working fluid modeled in single phase approach.
- c) The material properties of fluid and solid domain are independent of the effects of temperature.
- d) The solid and fluid domain surfaces are maintained in thermal equilibrium.

e) The surface of the heat spreader in the heat sink is exposed to the surroundings.

A uniform velocity is applied at the channel inlet and the flow is assumed to be fully developed at the outlet of the rectangular channel. The top surface of the channel is provided with the convection boundary condition. The front and side walls of the microchannel are applied with adiabatic boundary condition.

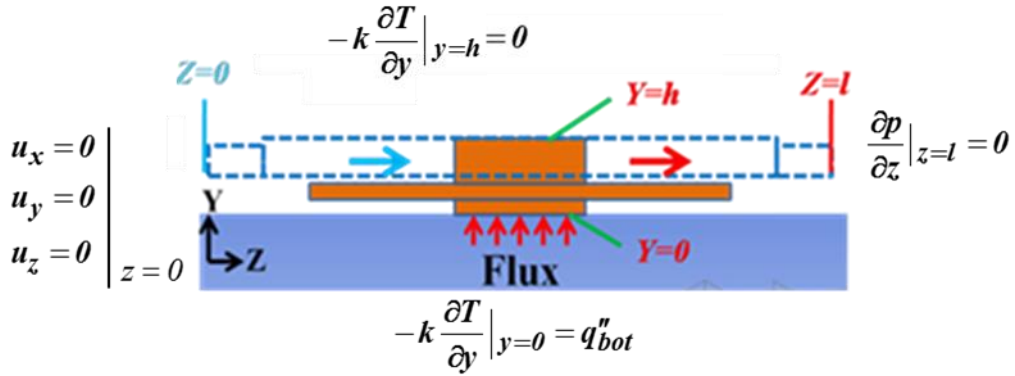


Figure 6.4 Schematic of the computational domain with boundary conditions.

6.6.2 Governing equations

A single phase model is adopted for the conjugate studies of laminar forced convection heat transfer in a rectangular microchannel. This model involves solving conduction and convection heat transfer simultaneously. The governing equations pertaining to the analysis are given in Equations

Continuity equation

$$\frac{\partial u}{\partial x} + \frac{\partial v}{\partial y} + \frac{\partial w}{\partial z} = 0 \quad (6.20)$$

X-momentum equation

$$u \frac{\partial u}{\partial x} + v \frac{\partial u}{\partial y} + w \frac{\partial u}{\partial z} = -\frac{1}{\rho} \frac{\partial p}{\partial x} + \nu \left(\frac{\partial^2 u}{\partial x^2} + \frac{\partial^2 u}{\partial y^2} + \frac{\partial^2 u}{\partial z^2} \right) \quad (6.21)$$

Y-momentum equation

$$u \frac{\partial v}{\partial x} + v \frac{\partial v}{\partial y} + w \frac{\partial v}{\partial z} = -\frac{1}{\rho} \frac{\partial p}{\partial y} + \nu \left(\frac{\partial^2 v}{\partial x^2} + \frac{\partial^2 v}{\partial y^2} + \frac{\partial^2 v}{\partial z^2} \right) \quad (6.22)$$

Z-momentum equation

$$u \frac{\partial w}{\partial x} + v \frac{\partial w}{\partial y} + w \frac{\partial w}{\partial z} = -\frac{1}{\rho} \frac{\partial p}{\partial z} + \nu \left(\frac{\partial^2 w}{\partial x^2} + \frac{\partial^2 w}{\partial y^2} + \frac{\partial^2 w}{\partial z^2} \right) \quad (6.23)$$

Energy equation of the fluid

$$\frac{\partial T}{\partial t} + u \frac{\partial T}{\partial x} + v \frac{\partial T}{\partial y} + w \frac{\partial T}{\partial z} = \alpha \left(\frac{\partial^2 T}{\partial x^2} + \frac{\partial^2 T}{\partial y^2} + \frac{\partial^2 T}{\partial z^2} \right) \quad (6.24)$$

Energy equation of the solid

$$\frac{\partial^2 T}{\partial x^2} + \frac{\partial^2 T}{\partial y^2} + \frac{\partial^2 T}{\partial z^2} = \frac{1}{\alpha} \frac{\partial T}{\partial t} \quad (6.25)$$

6.6.3 Grid independence study

The grid system employed in the numerical analysis has 227714 elements in the x, y and z directions. The sensitivity of the numerical results is checked with four different grids 150000, 227714, 515980 and 891604. The results of the last two grids are very close to each other as shown in Figure 6.5. Hence, the grid size of 227714 elements is considered for the numerical simulations.

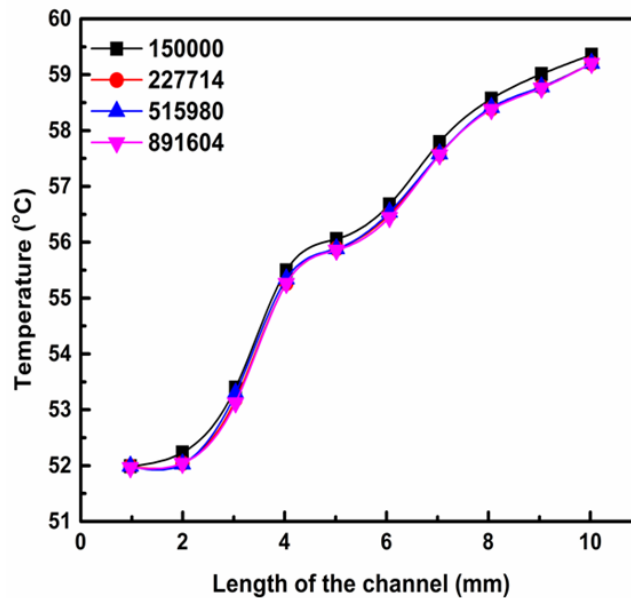


Figure 6.5 Grid independence study.

6.7 RESULTS AND DISCUSSION

6.7.1 Temperature study

In this part, parallel microchannels with heat spreader is first studied by 3D numerical analysis relating the effect of transient superposition on heat spreader influenced by flow rate and particle volume fraction. The temperature distribution in heat spreader (T_{hs}) near the core at heating condition is shown in Figure 6.6. The propagation of the temperature is smooth and periodic. The wave critically represents the time dependent superposition addition over the previous waves.

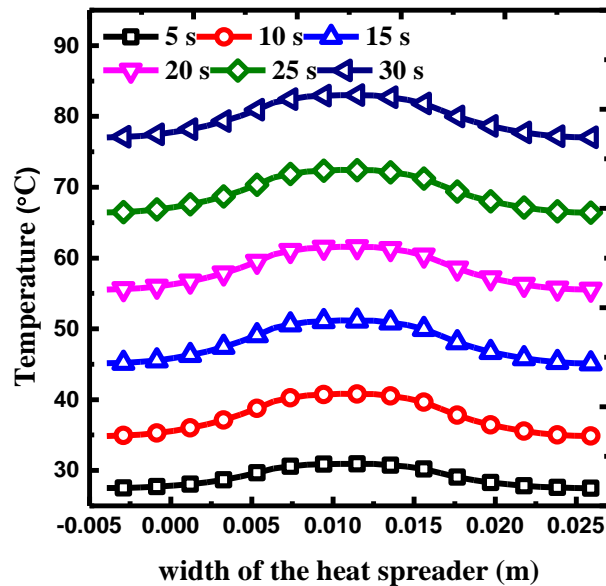
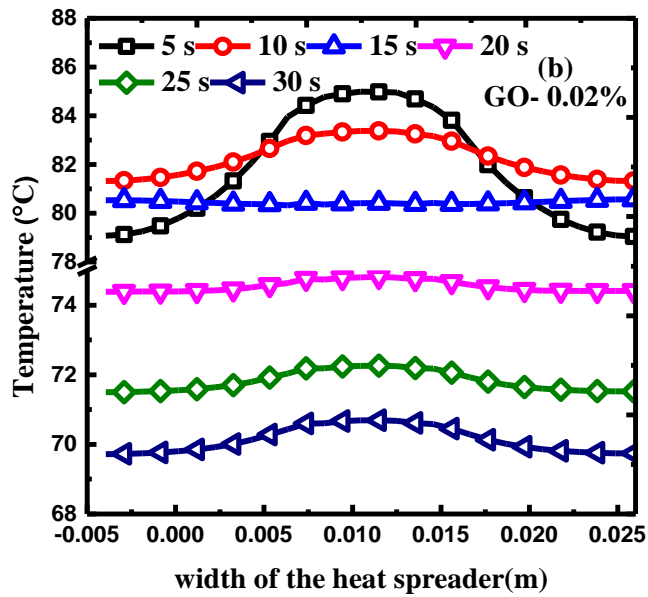
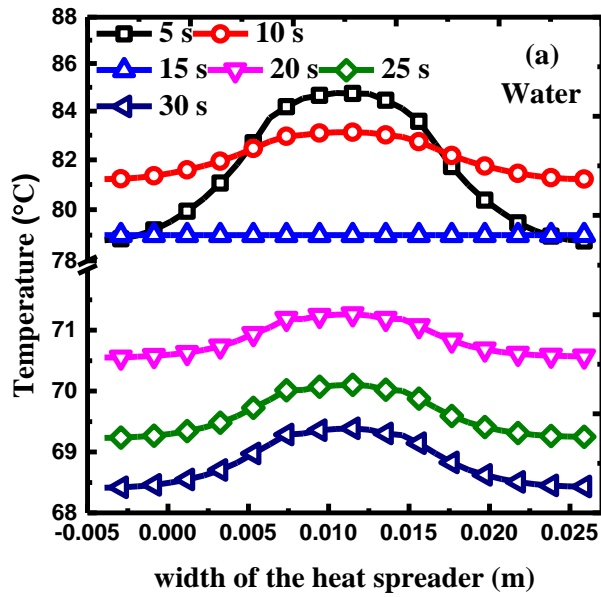


Figure 6.6 Temperature of the heat spreader (T_{hs}) on heating condition.

Figure 6.7 shows the transient temperature distribution in the heat sink using different working fluids. Figure 6.7(a) shows the cooling of heat sink for $Re=100$ using water. Initially the sink temperature is maintained at 80°C and inlet fluid temperature of 27°C is used for circulation. Due to low Reynolds number, the temperature of the sink increases to 84°C . In particular, increase in temperature of heat spreader near the microchannel outlet is more than other sections of heat spreader. Subsequently, due to continuous flow of working fluid, superposition waves are generated consecutively and at 15 s iso-thermal condition is observed at HSMZ of heat spreader. Thereafter, a decrease in temperature of 10°C is observed throughout the heat spreader. The underlying physics of the present

scenario is majorly attributed to the superposition of adjoining waves with decreased temperature. Moreover, the temperature increase in HSMZ during cooling of microprocessor core using water is considerably higher than the other sections of heat spreader. In case of nanofluid with all concentrations, the isothermal condition at 15 s seems to be more compared to water.



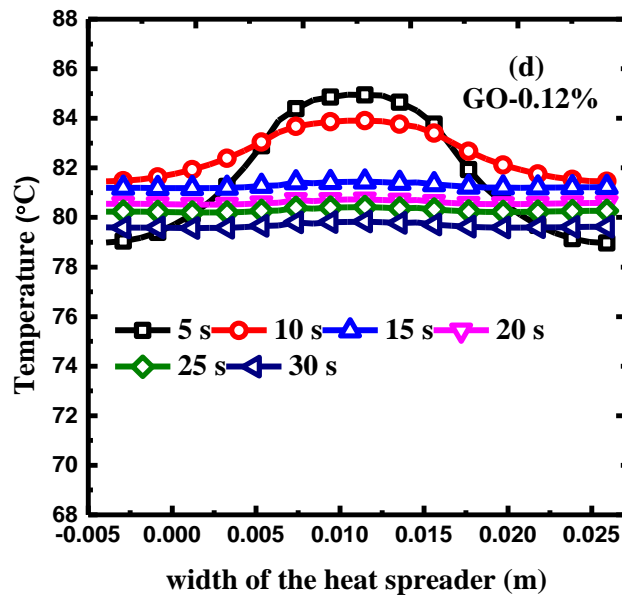
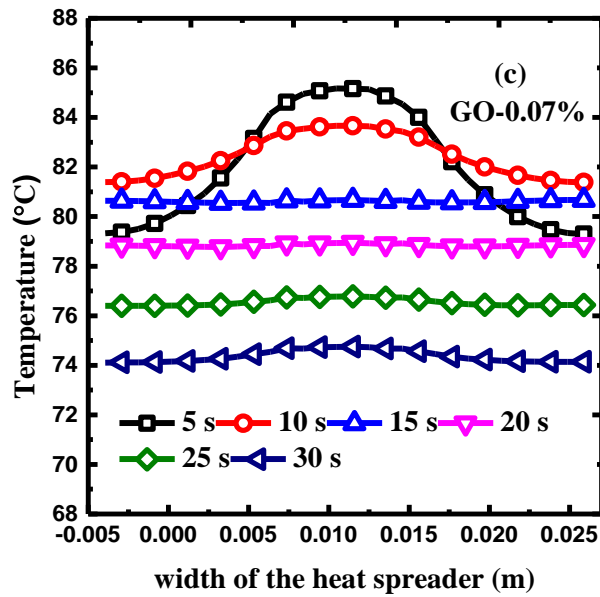


Figure 6.7 Temperature of the heat spreader (T_{hs}) on cooling condition for different fluids, (a) water, (b) GO-0.02%, (c) GO-0.07%, (d) GO-0.12%.

This is due to the effect of axial conduction in the heat sink at low Reynolds number as shown in Figure 6.7(b-d). For example, the use of GO-0.02% develops shift in isothermal condition towards the higher temperature zone. Further, a similar decrease in temperature was observed for GO-0.02% at 20 s i.e., the temperature decreases to 76°C which is 4°C

higher than the water as seen in Figure 6.7(b). The drastic decrease in heat spreader temperature at initial period when the fluid is water and GO-0.02% was not observed with the use of GO-0.07% and GO-0.12% nanofluid shown in Figure 6.7(c, d).

In the case of GO-0.07% the total sink temperature at 30s reached up to 74°C, shown in Figure 6.7(c). On the other hand, temperature of the heat sink with respect to the time increased by subsequent superposition which leads to accumulation of higher temperature at HSMZ zone and this trend was not seen with the use of pure fluid. These notable characteristics of higher temperature are due to the increased thermal conductivity of the nanofluid. This phenomenon is distinctively noticed for GO-0.12%, shown in Figure 6.7(d). This same trend is captured experimentally which will be discussed in detail in forthcoming section of response time study.

Figure 6.8 presents the temperature distribution of the heat sink along the flow length (THS) for different working fluid. For the case of low Reynolds number; $Re=100$, the increase in sink temperature is maximum for GO-0.12% as shown in Figure 6.8(a). Despite of using higher thermal conductivity nanofluid, one may observe increase in sink temperature considerably. It is pertinent to mention that a common Reynolds number is incorporated for all the working fluids despite the increase in viscosity of nanofluid. Moreover, to exactly determine reduced Reynolds number for higher nanoparticle concentrations is not well established; only the level of influences is investigated both analytically and numerically in the literature. This may further reduce the Reynolds number of nanofluid attributed due to the increased viscosity of GO-0.12%.

One important aspect is how vicious is this combined effect of increased volume fraction of nanoparticle; for instance, at increased Reynolds number the effect of volume fraction is negligible as shown in Figure 6.8(b). At higher Reynolds number, the bulk diffusion of the fluid decreases with the increased cooling waves that incident upon microchannel with lower temperature. However, the effect of nanofluid is found near the outlet of the microchannel due to the axial conduction.

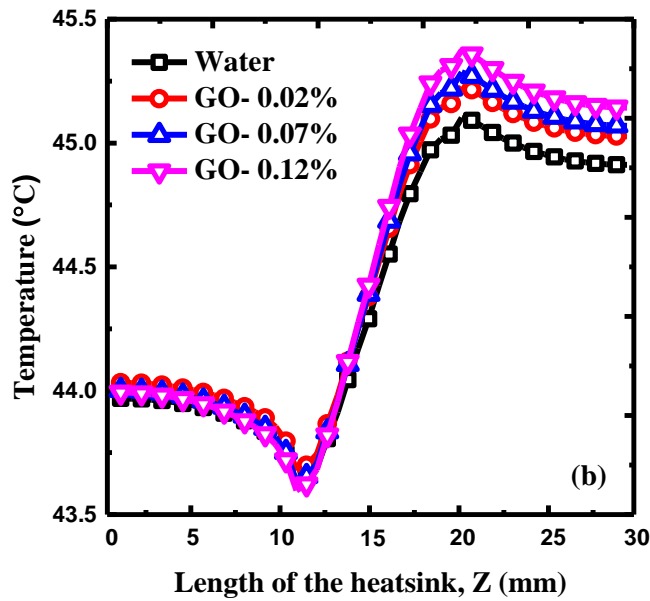
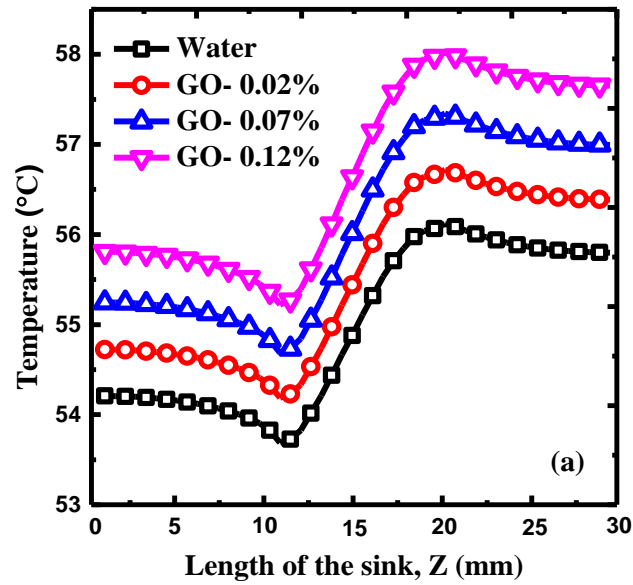
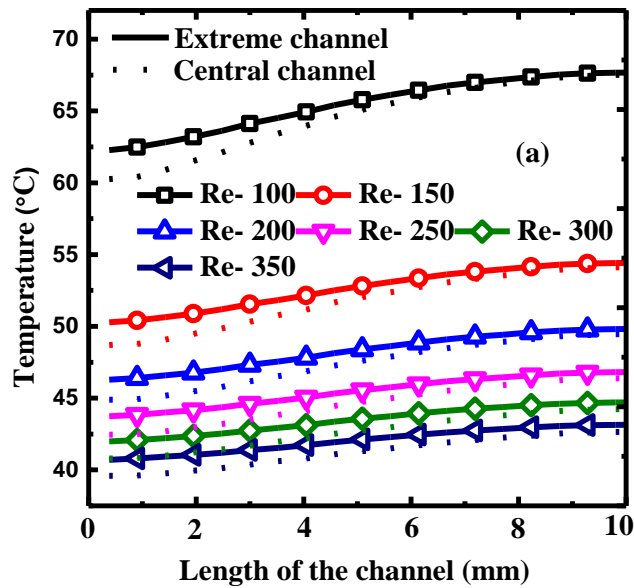


Figure 6.8 Temperature of the heat sink along the flow length (T_{HS}), (a) $Re=100$, and (b) $Re=350$.

Figure 6.9 shows the temperature of the microchannel at two different locations (only water): (i) at axial length of the extreme channel wall (TEC) and (ii) temperature of the microchannel slightly below the channel floor (TY1), as shown in Figure 6.10. For the case of extreme microchannel wall with Re as 100, a temperature gradient of 5°C is observed

along the axial length as shown in Figure 6.9(a). Further increase in Reynolds number there is no significant temperature variation along the length of the channel. Figure 6.9(b) presents the temperature along the width of the microchannel for different Reynolds number using water as working fluid. As shown, for a given Reynolds number difference in temperature is observed to be minimum across the channel width. On the other hand, there is no much effect on temperature due to maldistribution of flow at T_{Y1} . The location T_{Y1} is in the vicinity of bottom of the microchannel where the maximum bulk diffusion is expected to happen. From this it clear that the effect of temperature distribution is highly influenced by superposition directions of both the heat flux and the cooling fluid. Since in the current study, the superposition subtraction is established orthogonal to the flow, the heat sink temperature varies along the length of the channel. Stated explicitly, it is highly debatable that to what level the effectiveness of the microchannel is compromised due to superposition.



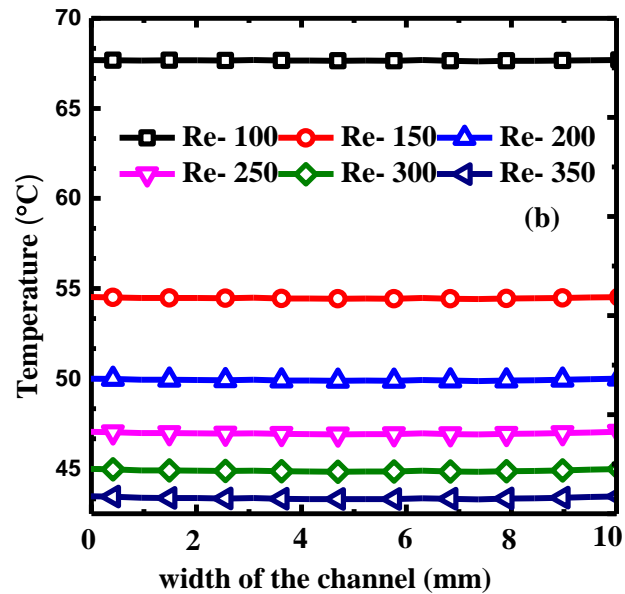


Figure 6.9 Temperature distribution for different Reynolds number, (a) Temperature along the axial length of the extreme microchannel wall (T_{EC}), and (b) Temperature distribution below the channel bed (T_{YI}).

But interestingly the effect of maldistribution is clearly noticed in the microchannel floor as presented in Figure 6.10. It shows the influence of the Reynolds number and volume fraction of the working fluid at channel bottom of the microchannel throughout the width and length of the microchannel. Figure 6.9(a) shows the maximum temperature at exit of the microchannel. Unlike the distribution developed in Figure 6.10(b), considerable variation in temperature was observed between the central and extreme channels along the width of the channel. For increased Reynolds number, the mass flow of the middle channels is higher than the extreme channels thereby allowing the floor bed temperature to reduce by 10°C as shown in Figure 6.10(b). Addition of higher nanoparticles at lower Reynolds number increases the channel floor temperature considerably. On comparison of GO-0.12% nanofluid with water the high temperature zone near the outlet of the microchannel increased by 15% shown in Figure 6.10(c). As highlighted in the previous discussion the effect of volume fraction has minimal effect, and had no difference than that of water at higher Reynolds number which is shown in Figure 6.10(d).

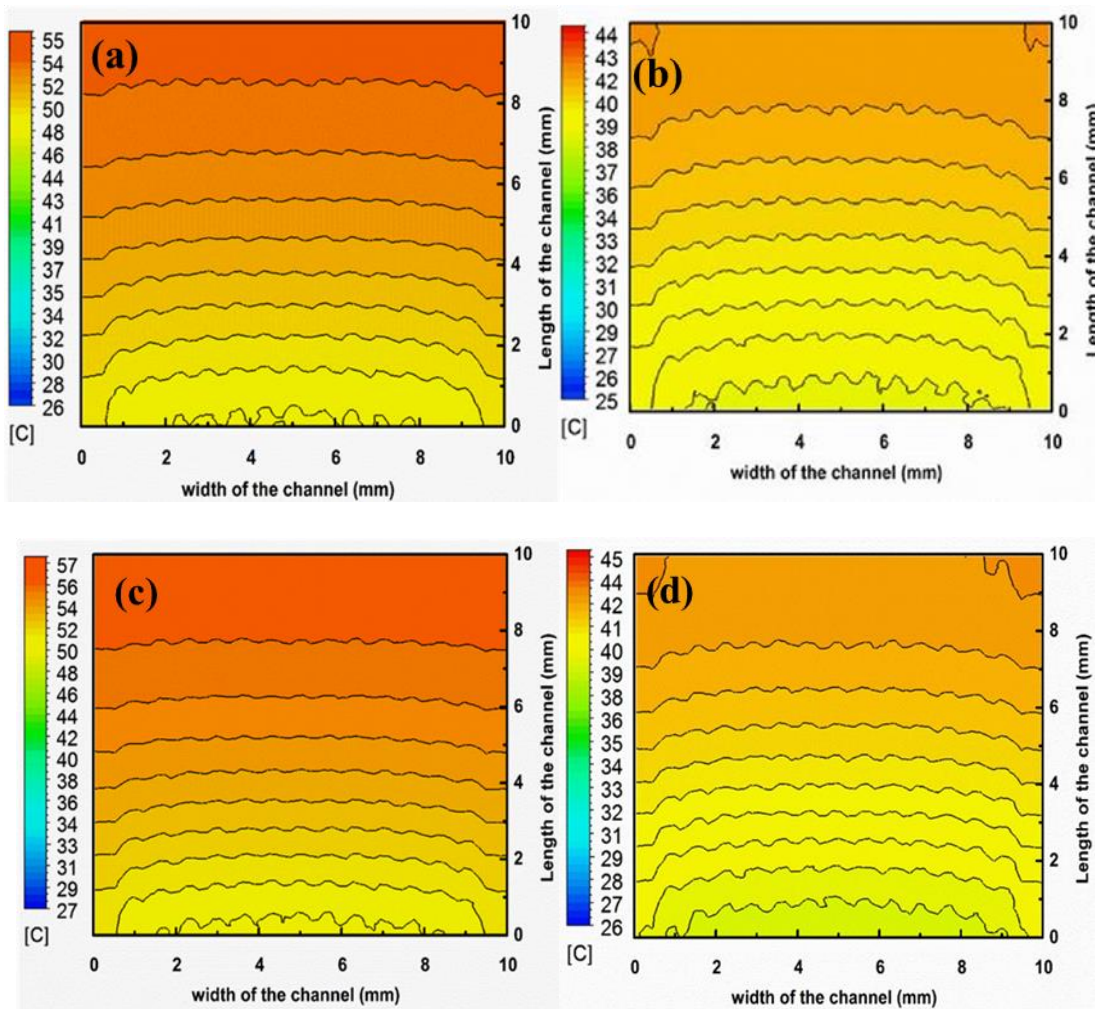


Figure 6.10 Temperature contour in the microchannel bottom floor for different flow rate and working fluid, (a) water at $Re=100$, (b) water at $Re=350$, (c) GO-0.12% at $Re=100$, and (d) GO-0.12% at $Re=350$.

6.7.2 Response time study

The results of the experiments convincingly exhibit the wave nature of the heat conduction in a silver soldered heterogeneous heat sink with hotspots. The fact is that a definite time is required for the thermocouples welded in heat spreader to indicate any temperature variations, and these temperature deviations are not instantaneous. This signifies a wavy behavior of lagged diffusion heat conduction in the heat spreader. This characteristics is distinctly observed from the experimental study as shown in Figure 6.11.

On contrast, the hotspot temperature in the microchannel core increases abruptly. This is due to the constructive superposition characteristics of heat waves in the microchannel core by the perpendicular heat flux nearing one another; this effect is substantiated

experimentally. Interestingly, the hotspot develops diffused heat conduction in lateral direction on heat spreader and direct penetration in the case of microchannel core.

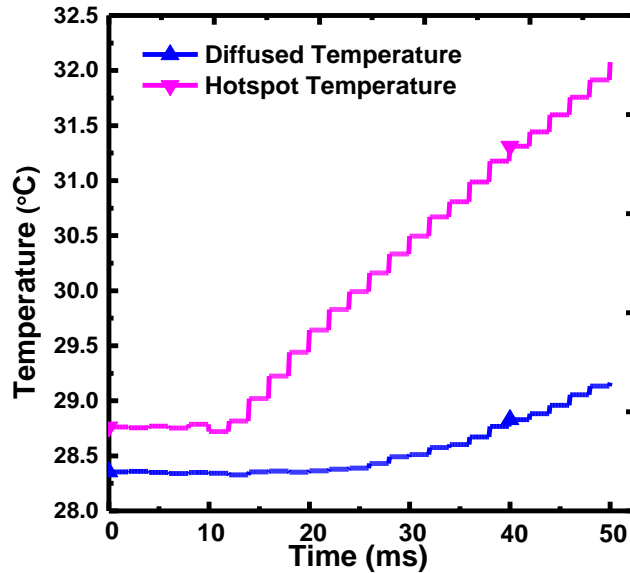


Figure 6.11 Response of lagged diffusion heat conduction in the heat spreader.

To show the effects of temperature lag in the heatsink at different locations, Figure 6.12 is plotted. Here thermocouples at microchannel core (T_3) and heat spreader (T_8 , T_4 and T_6) are chosen. It shows the non-dimensional temperature of the heat sink as function of time. Here, again the temperature jump is observed in microchannel core which clearly notifies the wave addition to the sample at room temperature as shown in Figure 6.12(a). The temperature jumps J_1 and J_2 are predominately due to the superposition addition in the microchannel core. Similar characteristics of temperature jump is not noticed in any other location of the heatsink. The notable design factor is the effect of wave interfaces that are diminished on heterogeneous condition, further it will be more appropriate to use the size of microchannel as same as that of the processor. On the other hand, no such temperature jump effects were noticed on cooling, shown in Figure 6.12(b). It shows that apart from channel core the temperature decrement in other three locations followed similar trend when water is used at Reynolds number 150.

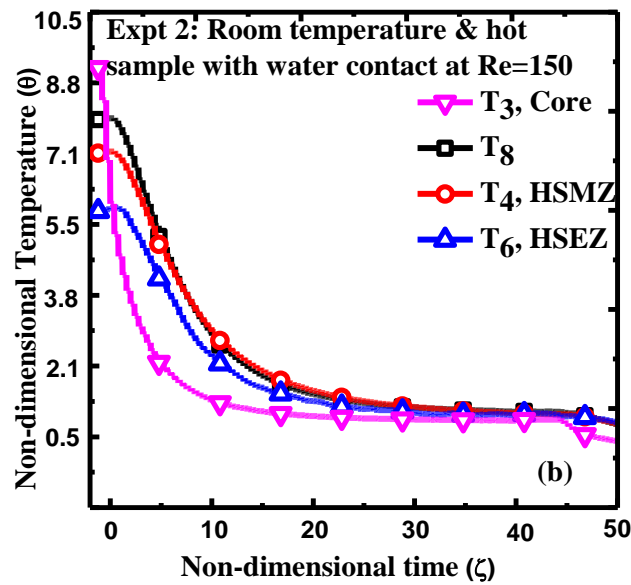
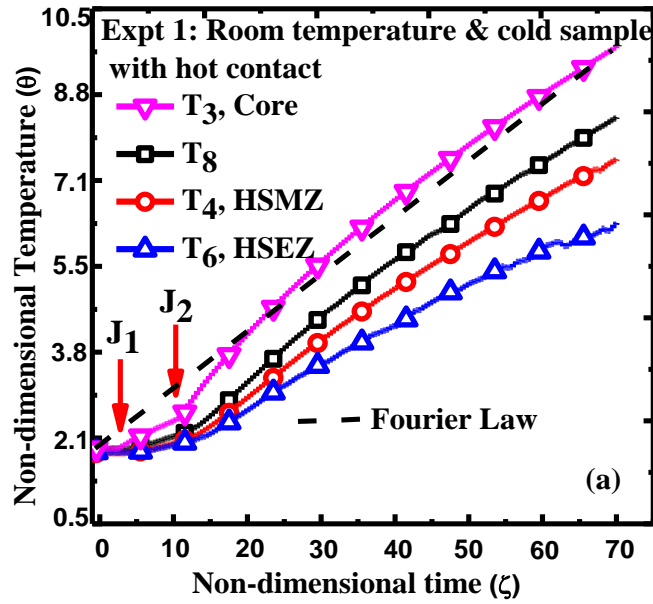
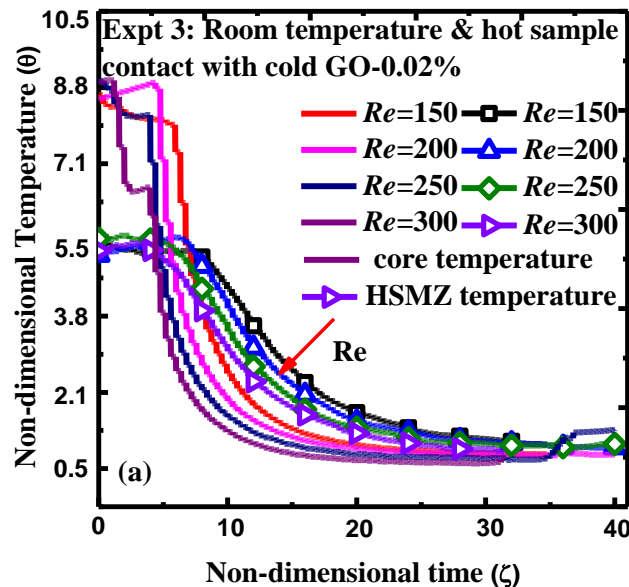


Figure 6.12 Comparison of temperature at different locations, (a) heating the heatsink till 85°C under room temperature and (b) cooling heat sink using water at $Re=150$ when the temperature of the heat sink is at 85°C.

Figure 6.13 depicts the effect of Reynolds number and volume fraction on temperature distribution in the heat sink. A direct dependence of decrease in temperature is observed at

both microchannel core and HSMZ at increased Reynolds number. It is understood that the use of higher thermal conductivity nanofluid and Reynolds number provide better cooling capability which is better than water at different locations of heat sink, shown in Figure 6.12(b). But in case of GO-0.02% shown in Figure 6.13(a), the decrease in temperature of the microchannel core is not rapid, rather temperature increases for a definite time and then decreases. Moreover, initial decrease in temperature is due to the initial wave superposition subtraction and then constant temperature prevails before complete decrease in the temperature for Reynolds number 150. This phenomenon is observed for all the subjected Reynolds number and similar trend is observed in HSMZ. It is because HSMZ conditionally witnesses an effectively diffused cooling wave in the heat spreader. Further, using GO-0.07% nanofluid, significantly increases the heatsink conduction effects to 10 s very much similar trend to that of GO-0.02% as shown in Figure 6.13(b). Interestingly, when compared with GO-0.02% the temperature profiles of GO-0.07% develop distinct smooth profiles. Further increase in volume fraction to GO-0.12% the conduction in heat sink intensifies, shown in Figure 6.13(c). For the case of Reynolds number 150; the superposition of the cooling wave is witnessed well above the 10 s, this effect is also seen in heat spreader HSMZ. It is found that for increased particle concentration heat sink conduction is highly sensitive for Reynolds number.



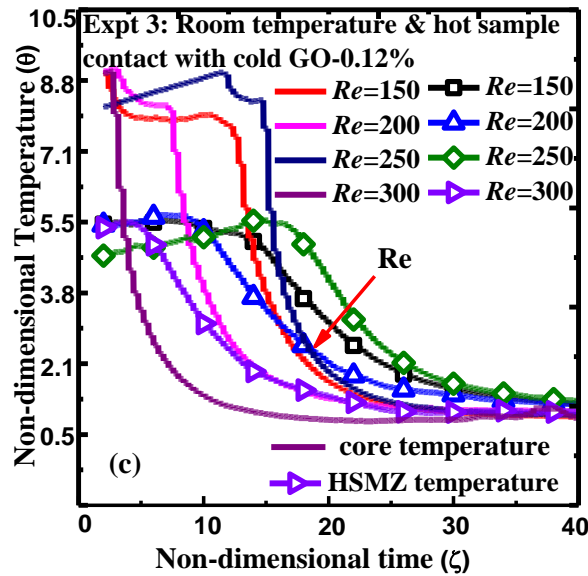
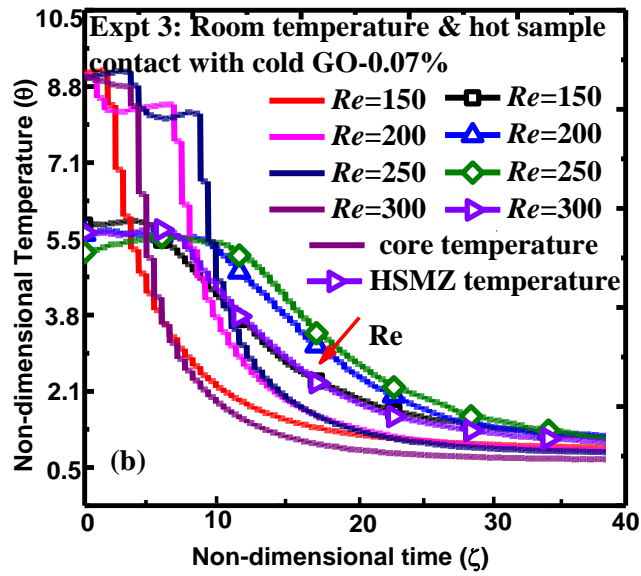


Figure 6.13 Temperature comparison for different nanofluid, (a) heating room temperature heatsink till 85°C, (b) cooling the 85°C heat sink using water at $Re=150$, and (c) using GO-0.12% nanofluid.

We argue that the increase in heat sink temperature on using nanofluid is profoundly due to axial conduction, especially at low Reynolds numbers and higher volume fraction nanofluid. Several experimental studies have been performed to investigate the effects of

axial conduction in microchannel and also some researchers have observed prejudicial effects of excluding axial conduction that has resulted in deviations of local Nusselt number values. Notably, the effect of axial conduction on heat sink with nanofluid can be established by analytical and numerical methods with limitations. But to a possible extent, it is analytically accepted that the introduction of nanoparticles raises the fluid temperature. Since, it is possible to analytically model the bulk fluid diffusion by implementing the specific heat and thermal conductivity of the fluid, but its heat transfer mechanism for fluid domain is neglected in many cases. One such is the Brownian motion in nanofluid highlighted by Koo and Kleintreurer (2004), by comparing the static and dynamic portions of the effective thermal conductivity. But, their investigation pointed out that the heat sink temperature distribution is independent to the used nanofluid which is highly contradictory to the current experimental results. To examine this further the effect of high conductive GO and its conduction is studied critically.

6.7.3 Bulk diffusion study

In Figure 6.14, a complete cycle of temperature distribution in heat sink for different working fluids is shown. Note that for the case of GO-0.12% nanofluid the initial flow develops a steep drop in the sink temperature due to superposition. But the presence of nanoparticle has a strong effect of increasing the fluid bulk temperature and maintains mean fluid temperature closer to the sink wall temperature. Moreover, the thermal characteristics of the heatsink in the case of nanofluid are significantly affected at reduced Reynolds number. Similar trends for water and GO-0.07% in the heat sink are observed but the initial decrement in temperature owing to superposition subtraction is less noticeable for water and GO-0.07% cases. Referring to the above observations, it can also be appreciated that the high conductive nanofluid reduces the thermal resistance between the bulk fluid and the channel wall. In particular, this significant difference in bulk fluid temperature caused by the presence of nanoparticle is observed in the solid heat sink. Based on the results, it is seen that the effect of nanofluid volume fraction has impact on increasing heat sink temperature at low Reynolds number.

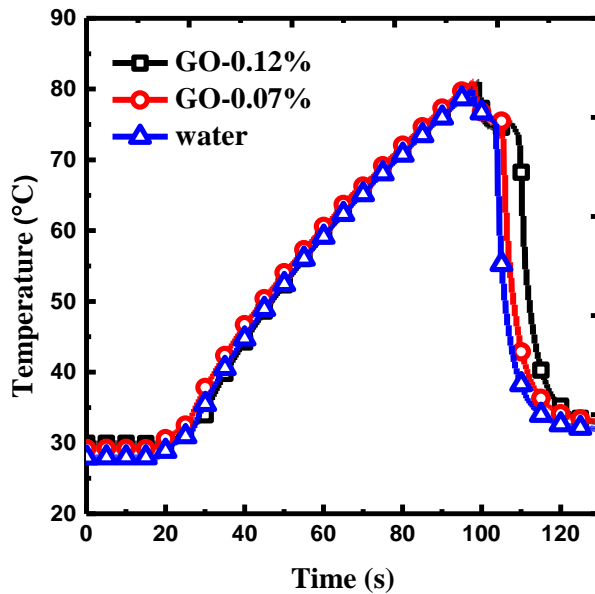
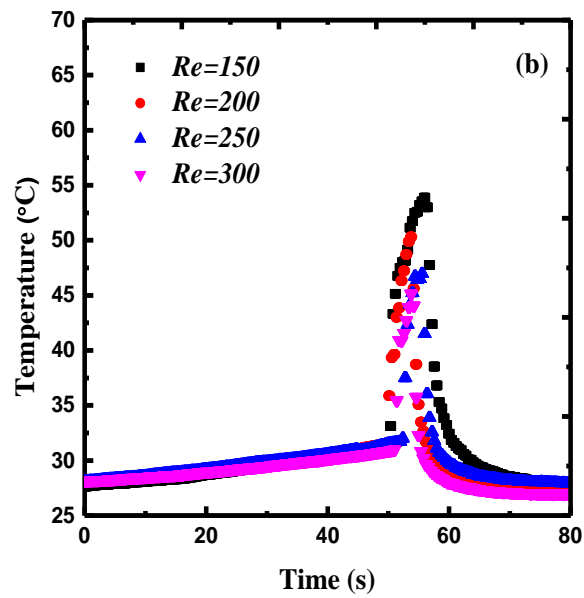
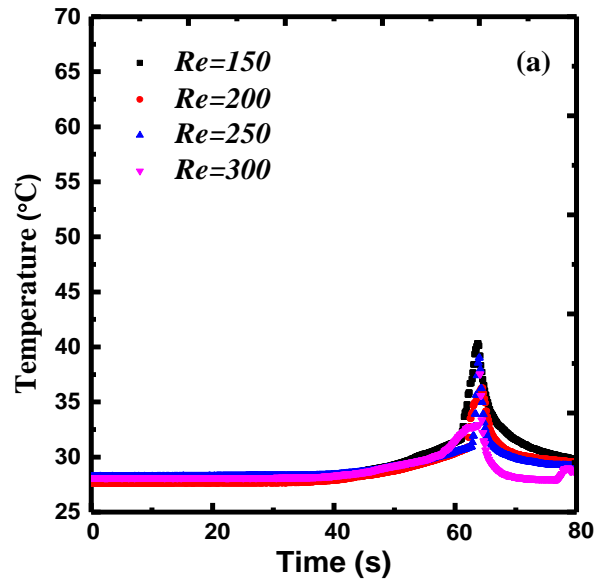


Figure 6.14 Combined temperature distribution of the heat sink.

In order to have more detailed analysis on effects of bulk fluid temperature, a comprehensive study on effects of nanofluid temperature is experimented for different nanofluid. Figure 6.15 shows the effect of nanoparticle volume fraction for the bulk fluid diffusion of GO nanofluid. It has been plotted for four Reynolds number with water, GO-0.07% and GO-0.12% nanofluid as working fluids. Figure 6.15(a) shows the transient bulk fluid temperature increase of water against time. The first characteristics which can be observed is that the response time and increase in peak temperature for different Reynolds number is more or less the same for water. It also suggests that the effect of bulk fluid conduction is low for water for all subjected Reynolds number. The highlighted region in the figure indicates a steady increase in fluid temperature as time progresses. The increase in Reynolds number comparatively reduces the peak temperature of the bulk fluid. For comparison, similar effect on GO-0.07% and GO-0.12% nanofluid is shown in Figure 6.15(b) and (c). In both the cases, the behavior of bulk fluid temperature is totally different from water. In the case of GO-0.07% the increase in temperature is very steep and reaches up to 55°C, shown in Figure 6.15(b). We could observe profound increase in bulk fluid temperature in the case of GO-0.12% which is highly contributed due to the effect of increased thermal conductivity of GO nanofluid as shown in Figure 6.15(c). Here a

foremost question arises, why the spontaneous increase in bulk fluid temperature of GO nanofluid is non-identical with that of water at lower Reynolds number.



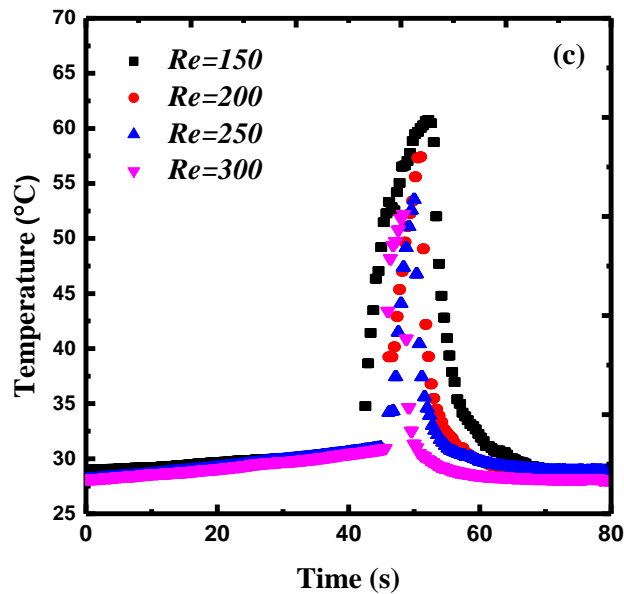


Figure 6.15 Bulk fluid diffusion for different nanofluid, (a) water, (b) GO-0.07%, and (c) GO-0.12%.

This characteristics can be explained that due to the presence of nanoparticle superior bulk conduction which increases the diffusion within the nanofluid. As the volume fraction increases the ballistic transport based diffusion increases along the length of the microchannel at reduced flow rates. Moreover, the subjected GO nanoplatellets based nanofluid inhabits increased thermal conductivity at higher temperatures. Thus ballistic diffusion in the fluid rapidly manages to develop thermal equilibrium with channel bottom walls. The major difference between water and nanofluid is the instant temperature responses generated when it interacts with the solid walls. On comparison, with water the responses of the nanofluid is spontaneous, particularly the bulk fluid temperature reach up more than 55°C within 3 s. Similar effect is seen for higher Reynolds number but the increased fluid momentum affects the thermal equilibrium and reduces the bulk fluid temperature sharply.

6.8 CONCLUSIONS

Microchannel heat transfer device provides a very high heat transfer rate under multiple heat flux conditions and therefore it is of great interest for compact electronic cooling applications. In this work, a real time high power processor has been experimentally and numerically studied through parallel microchannel heat sink integrated with heat spreader.

The microchannel consists of 14 channels machined in solid copper of 4 mm thick. The investigation on axial conduction, bulk diffusion of nanofluid and heat spreading of maldistribution induced high temperature are discussed; for this a thin heat spreader is attached below the microchannel using silver soldering. The heat sinks are subjected to two different experiments, one with transient heating with sink at initial room temperature (28°C) and transient cooling with sink temperature at 85°C and T_{in} at 27°C. Response time, bulk fluid temperature, temperature distribution for both microchannel and heat spreader were studied critically using pure fluid, GO-0.02%, GO-0.07% and GO-0.12% as working fluid, the main conclusions of the study are:

- For higher GO volume fraction a steep increase in bulk fluid temperature response was observed, the outcome for the effect may possibly comprehend the ballistic diffusion nature of GO nanoplatelets.
- The experimental setup was intended to investigate the temperature and response time due to the transient hotspot. The difference in response time was found between the microchannel core and heat spreader; the temperature jump was registered in the core; temperature jump in the core during heating is due to superposition effects were observed, but not much seen in heat spreader. It was found that the penetration of hotspot is very low in lateral direction of the heat sink.
- Results clearly show that, the overall temperature of the heat sink increased on using higher volume fraction GO nanofluid. During higher Reynolds number the effect of increased heat sink temperature due to higher volume fraction has no notable effect. Apart from the fact that both microchannel and heat spreader is interfaced with silver, its effects is found negligible in the case of hotspot heat source.
- It is shown that for a given Re , the temperature of HSMZ was subjected to continuous superposition of cooling waves from the microchannel to other locations of the heat sink. In the case of pure fluid the wave superposition subtraction leads to high temperature exactly near the microchannel output. But in the case of nanofluid, the subsequent superposition temperature were very close, due to that the entire heat spreader near the microchannel outlet was maintained with more or less similar temperature. Even though the sink temperature has reduced drastically.

- The experimental investigation on temperature wave propagation shows that the bulk fluid diffusion of GO- nanofluid increases the heat spreader temperature by 30%. In case of working fluid temperature, it gets increased by 35% for water and 52% for GO- 0.12%. More than that the use of pure fluids delivers a gradual increase in fluid temperature but for the cases of GO nanofluid it was drastic. This will be a critical parameter in the case of investigation dealing with highly conductive nanofluid and hotspots.
- On observing critically, lower response time was generated for GO-0.12% near the inlet but it increases the sink conduction with higher outlet temperature. From analysis, it can be recommended to design hot spot near the microchannel entrance for better heat transfer. In case of high thermal conductive GO nanofluid the effect of bulk diffusion and dynamic hotspot needs further investigation.

6.9 CLOSURE

This chapter dealt with investigating the transient phenomenon developed in the heat sink by employing nanofluid and hotspot. An extensive experimental observations were proposed for the different multiphysics effects involved in heterogeneous integration. Next chapter explains the irreversibility and conjugate effects of integrated microchannel using nanofluids.

CHAPTER 7

THERMODYNAMIC IRREVERSIBILITY AND CONJUGATE EFFECTS OF INTEGRATED MICROCHANNEL COOLING DEVICE USING TiO₂ NANOFLUID

7.1 INTRODUCTION

Thermal management is highly essential for the latest electronic devices to effectively dissipate heat in a densely packed environment. Usually, these high power devices are cooled by integrating micro scale cooling systems. Most of the works reported in the literature majorly concentrate on microchannel heat sink in which the characteristics of friction factor and enhancement of heat transfer are analyzed in detail. However, due to the advent of compact electronic devices a crucial investigation is required to facilitate an amicable environment for the neighboring components so as to improve the reliability of the electronic devices. Henceforth, in the present study a combined experimental and numerical analysis is performed to provide an insight to determine the performance of a copper microchannel integrated with Aluminum block using TiO₂ nanofluid for different particle configurations. Needless to say, the present study, which also focuses on entropy generation usually attributed to the thermodynamic irreversibility, is very much significant to design an optimum operating condition for better reliability and performance of the cooling devices

7.2 IRREVERSIBILITY STUDY

The recent advances in high end scaling of electronic components have developed more densely packed systems with ultra-speed computational performance. Under operating conditions these microelectronic chips generate high heat flux, which demands robust cooling solutions for thermal management in several electronic appliances. But inadequate heat dissipation delivered by the currently available cooling technologies results in the system thermal instability under peak computational loads. Hence, optimum thermal dissipation technique is crucial for several such high power systems. Most importantly, embedded microchannel heat sinks are integrated with highly conductive substrates which undergoes simultaneous conjugate cooling effects of the nanofluid and relatively loses heat at high rate due to parasitic heat loads. From thermodynamics perspective, the energy lost by the integrated devices is irreversible

processes termed as exergy and it is proportional to the entropy gained by the system combined with the surroundings. In the latest cooling devices, optimization studies based on irreversibility generated a phenomenal impact in quantifying and minimizing the entropy generation. It deals with the simultaneous assessment of thermal and frictional characteristics of the heat exchangers and its interaction with the surroundings. Previous studies showed numerous investigations in optimizing mechanical design parameters of the microchannel. But the operational effects of microchannel embedded cooling system for the application of the densely packed system have not been well established. However, minimization of entropy is essential to determine the suitable operating criteria for the system. Moghaddami et al. (2011) pointed out that the effects of irreversibility for both the laminar and the turbulent regime were found to reduce when nanofluid was used as a working fluid and at higher turbulent flow rates the effect was still more predominant due to increased viscous dissipation. It is due to the efficient attainment of thermal equilibrium of the nanofluid with the microchannel substrate; as a result, the local temperature gradients were found to get reduced. This results in reduction in entropy generation due to enhanced heat transfer of nanofluid.

The entropy generation studies considering nanofluid for electronic applications with integrated structures are less reported in the literature. Heshmatian and Bahiraei (2017) conducted numerical investigations on irreversibility developed in circular microchannels using TiO_2 nanofluid by incorporating particle migration and Brownian diffusion effects. It is observed that the particle migration influences the entropy generation. On comparison, nanofluid develops lower thermal entropy generation with increased heat transfer capacity than the pure fluids. Leong et al. (2012) performed entropy generation studies with TiO_2 and Al_2O_3 nanofluid at constant wall temperature under both laminar and turbulent regimes. It was found that the use of TiO_2 nanofluid is more efficient than Al_2O_3 nanofluid. However, reduction in entropy generation is not observed for all the investigated turbulent cases. Similar study by Karami et al. (2012), investigates entropy generation of Al_2O_3 in a circular tube under constant heat flux. They concluded that using higher volume fraction nanofluid is not appreciable due to its increased frictional entropy generation. For increased volume fractions of TiO_2 nanofluid, the outlet exergy increases at higher flow rates with reduced thermal entropy

generation. In many cases the use of nanofluid increases the total entropy generation and the increase is predominately attributed by frictional irreversibility. Sarkar et al. (2012) noticed no considerable difference between total entropy generation for both Al_2O_3 and TiO_2 nanofluid for the volume fraction ranging from 0 to 20%. Some of the other entropy generation minimization techniques like increasing fluid inlet temperature and reduction in aspect ratio of the channel were also performed.

7.3 MOTIVATION

Most of the work reported in the aforementioned literature is about the enhancement of heat transfer and associated irreversibility due to the use of nanofluid in microchannel. At the same time, the practical outcomes of integrating micro heat sinks in densely packed embedded systems have not been adequately dealt with until now. Also, it is quite challenging to analyze the conjugate effects of axial conduction in the microchannel in an integrated system. In general, the effects of axial heat conduction in a channel wall for a standalone microchannel are almost different from the case of densely integrated cooling system. Here, the systems are closely integrated such that the neighboring component experiences thermal load. Moreover, upon packaging heat sinks are integrated to the materials which are not homogenous in all cases, it has several layered structures with different thermal conductivity materials packed as a single module. This allows us to study the additional aspect of understanding the influence of conjugate nature of microchannel in an integrated domain. Besides, from the repeated investigations nanofluid has emerged as a potential working fluid for microscale cooling systems with better heat transfer characteristics. In such cases, it is equally important to look into the conduction effects of the heat sink in both microchannel and its integrated system. The first of these, Hang et al. (2014) used very low Reynolds number and experimentally reported the axial conduction effects in microchannel, but the microchannel system is constructed in Polydimethylsiloxane (PDMS) polymer which cannot be used in practical heat transfer application. Suppose, if the same operating condition is imposed in real time situation with integrated system the effect of nanofluid on axial conduction under lower Reynolds number may develop reliability issues in densely packed components, so it is essential to determine the operating conditions of microscale devices in an integrated setup. Ramiar et al. (2012) reported a considerable change in axial conduction for the channels of higher aspect

ratio in the case of nanofluid. Additional investigations on higher aspect ratio channels support parallel investigations for multi layered microchannels and staged core processors. This combined responses involving non-homogeneity in heat sink, lower Reynolds number and nanofluid coupled with transient time and temperature field has to be established experimentally. To qualitatively replicate the actual situation, the present study proposes integrated heat sink with two different materials. For which copper microchannel is completely integrated in aluminium block and made as a complete heat sink. Both copper and aluminium metals are chosen due to its high thermal conductivity and their excellent machining capabilities to develop better surfaces with less contact resistance for an integrate heat sink. In this process, apart from the experimentally measured temperature distributions, the temperature dependencies upon entrance and interface are extremely difficult and cumbersome to measure. Hence, numerical analysis is used to support the data for the present investigation. To proceed further, the repeated experimentations are compared with numerical results. The second point is that although several previous work established importance of irreversibility and heat transfer issues involving nanofluid in microchannel, necessary practicality issues are not addressed, e.g., the influence of entropy generation under non-homogenous heatsink, transient temperature distribution in integrated heat sink using nanofluid and the temperature responses due to normal and pulsating pumping.

In the current investigation, all these issues are addressed. A numerical model with integrated domain is presented and used to investigate the heat transfer and irreversibility in a microchannel heat sink for low Reynolds numbers. The numerical model is based on a simplified three-dimensional conjugate heat transfer approach using single phase approach. As a result, the current study focuses on the detailed study of irreversible effects in an integrated microchannel. Both experimental and numerical investigations are carried out using TiO₂ nanofluid in a rectangular microchannel. Particularly, TiO₂ is chosen due to highly established thermo physical model both by means of experimental and numerical. Moreover, TiO₂ nanofluid has higher stability compared to other oxide based nanofluid.

7.4 DATA REDUCTION

The present experimental result is validated by comparing with the Shah (1975) for Nusselt number which is given in Equation 7.1.

$$Nu = \begin{cases} 1.953 \left(\text{Re Pr} \frac{D_h}{x} \right)^{1/3} & \left(\text{Re Pr} \frac{D_h}{x} \right) \geq 33.3 \\ 4.364 + 0.0722 \left(\text{Re Pr} \frac{D_h}{x} \right) & \left(\text{Re Pr} \frac{D_h}{x} \right) < 33.3 \end{cases} \quad (7.1)$$

$$Nu = \frac{hD_h}{k_{nf}} \quad (7.2)$$

Where D_h is the hydraulic diameter of the channel and h is heat transfer coefficient and k_{nf} is the thermal conductivity of the nanofluid.

$$D_h = \frac{4W_{ch} H_{ch}}{2(W_{ch} + H_{ch})} \quad (7.3)$$

Here W_{ch} and H_{ch} are the width and height of the channel.

$$h_l = - \frac{Q_h}{A_c (T_w - T_f)} \quad (7.4)$$

Where h_l is the local heat transfer coefficient expressed by Equation 7.4, A_c is the area of the channel and Q_h is the amount of heat extracted for corresponding wall temperature T_w and inlet fluid temperature T_f . Darcy-Weisbach equation is used to determine the friction factor, expressed by Equation 7.5

$$f = \frac{2D_h \Delta P}{v_m^2 L \rho} \quad (7.5)$$

$$P_p = \frac{\dot{m}}{\rho} \Delta P \quad (7.6)$$

Here, the experimentally measured pressure difference values at the inlet and the outlet of plenum is used to calculate the pumping power as given in Equation 7.6.

$$v_m = \frac{\dot{m}}{\rho_{nf} (nA_{ch})} \quad (7.7)$$

Where n is number of channels, \dot{m} is the flow rate in the microchannel.

The outlet exergy of the microchannel heat sink is calculated by using the Equation (7.8)

$$Ex_{out} = C_{nf} \left((T_{nf,out} - T_e) - T_e \ln(T_{nf,out} / T_e) \right) \quad (7.8)$$

Where C_{nf} is heat capacity of the nanofluid which can be written as in Equation 7.9

$$C_{nf} = (C_p)_{nf} \dot{m} \quad (7.9)$$

Exergy gain acquired by the cooling fluid is calculated through Equation 7.10, where P_p represents the pumping power used in the system given by Equation 7.11.

$$Ex_{gain} = (Ex_{out} - Ex_{in}) - P_p \quad (7.10)$$

$$Ex_{gain} = C_{nf} \left((T_{nf,out} - T_{nf,in}) - T_e \ln(T_{nf,out} / T_{nf,in}) - P_p \right) \quad (7.11)$$

To determine the total irreversibility developed due to the nanofluid, the sum of entropy generated by heat transfer and fluid friction can be expressed by Ahammed et al. (2016) as follows

$$\dot{S} = \dot{S}_{g,HT} + \dot{S}_{g,FF} \quad (7.12)$$

$$\dot{S}_{g,HT} = \frac{q''^2 \pi D_h^2 L}{k T_{fin} T_{fout} Nu} \quad (7.13)$$

$$\dot{S}_{g,FF} = \frac{8 \dot{m}^3 L}{\pi^2 \rho^2 \left(\frac{T_{fin} + T_{fout}}{2} \right) D_h^5} f \quad (7.14)$$

Additionally the total irreversibility contributed by heat transfer and fluid friction can be represented by a non-dimensional number, Bejan number (Be), defined as in Equation 7.15.

$$Be = \frac{\dot{S}_{g,HT}}{\dot{S}_{g,HT} + \dot{S}_{g,FF}} \quad (7.15)$$

7.5 NUMERICAL SCHEME

7.5.1 Governing equations

A single phase model is adopted for the conjugate studies of laminar forced convection heat transfer in a rectangular microchannel. This model involves solving conduction and convection heat transfer simultaneously. The governing equations pertaining to the analysis are given in Equations 7.16-7.21.

Continuity equation

$$\frac{\partial u}{\partial x} + \frac{\partial v}{\partial y} + \frac{\partial w}{\partial z} = 0 \quad (7.16)$$

X-momentum equation

$$u \frac{\partial u}{\partial x} + v \frac{\partial u}{\partial y} + w \frac{\partial u}{\partial z} = -\frac{1}{\rho} \frac{\partial p}{\partial x} + \nu \left(\frac{\partial^2 u}{\partial x^2} + \frac{\partial^2 u}{\partial y^2} + \frac{\partial^2 u}{\partial z^2} \right) \quad (7.17)$$

Y-momentum equation

$$u \frac{\partial v}{\partial x} + v \frac{\partial v}{\partial y} + w \frac{\partial v}{\partial z} = -\frac{1}{\rho} \frac{\partial p}{\partial y} + \nu \left(\frac{\partial^2 v}{\partial x^2} + \frac{\partial^2 v}{\partial y^2} + \frac{\partial^2 v}{\partial z^2} \right) \quad (7.18)$$

Z-momentum equation

$$u \frac{\partial w}{\partial x} + v \frac{\partial w}{\partial y} + w \frac{\partial w}{\partial z} = -\frac{1}{\rho} \frac{\partial p}{\partial z} + \nu \left(\frac{\partial^2 w}{\partial x^2} + \frac{\partial^2 w}{\partial y^2} + \frac{\partial^2 w}{\partial z^2} \right) \quad (7.19)$$

Energy equation of the fluid

$$\frac{\partial T}{\partial t} + u \frac{\partial T}{\partial x} + v \frac{\partial T}{\partial y} + w \frac{\partial T}{\partial z} = \alpha \left(\frac{\partial^2 T}{\partial x^2} + \frac{\partial^2 T}{\partial y^2} + \frac{\partial^2 T}{\partial z^2} \right) \quad (7.20)$$

Energy equation of the solid

$$\frac{\partial^2 T}{\partial x^2} + \frac{\partial^2 T}{\partial y^2} + \frac{\partial^2 T}{\partial z^2} = \frac{1}{\alpha} \frac{\partial T}{\partial t} \quad (7.21)$$

7.5.2 Boundary conditions

The fluid is considered as single phase, incompressible laminar without viscous dissipation of energy. The inlet temperature of the fluid is about 28°C. Laminar fully developed flow and uniform zero pressure is assumed at the outlet, as shown in Figure 7.1. All the walls satisfy the slip condition and both fluid flow and heat transfer are three dimensional.

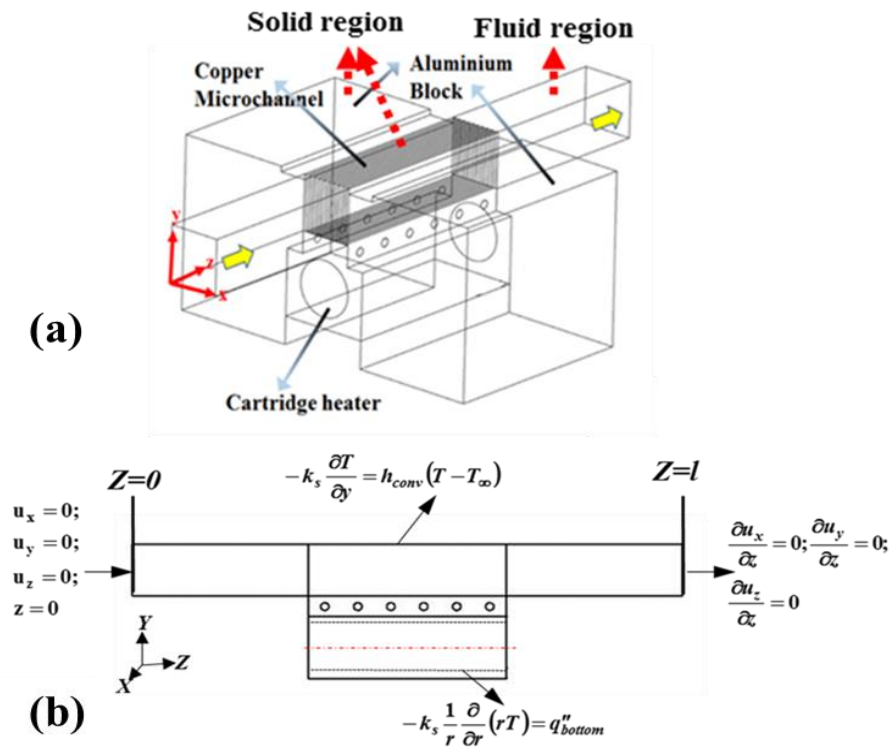


Figure 7.1 Schematics of the numerical model. (a) Computational domain, and (b) boundary conditions.

The solid and fluid regions are discretized using finite volume method. The entire microchannel is considered for computational domain. Unstructured grid is generated using prismatic elements. Mesh density is increased near the interface region between copper and aluminium by incrementing the mesh density from 2 cells per 0.2 mm^2 to 10 cells shown in Figure 7.2. The orthogonal and skewness mesh quality are in the order of 0.79 and 0.14. SIMPLE (Semi-Implicit Method for Pressure Linked Equation) method is chosen to couple pressure and velocity. The convective terms of all governing equations were discretized by a second-order upwind scheme.

The resulting algebraic system of equations is solved using Gauss Seidal iterative method with Successive Over Relaxation (SOR) to improve convergence time. The numerical model is verified with grid independence test and additionally validated with standard experimental results to ensure the fidelity of the computational model and its methodology. The convergence criterion is set to 10^{-6} for all corresponding continuity, momentum and energy terms. Since the model is time dependent the domain is solved for every time step of 0.0025 s with 100 individual iterations. Every time step the average temperature is obtained and compared with experimental results.

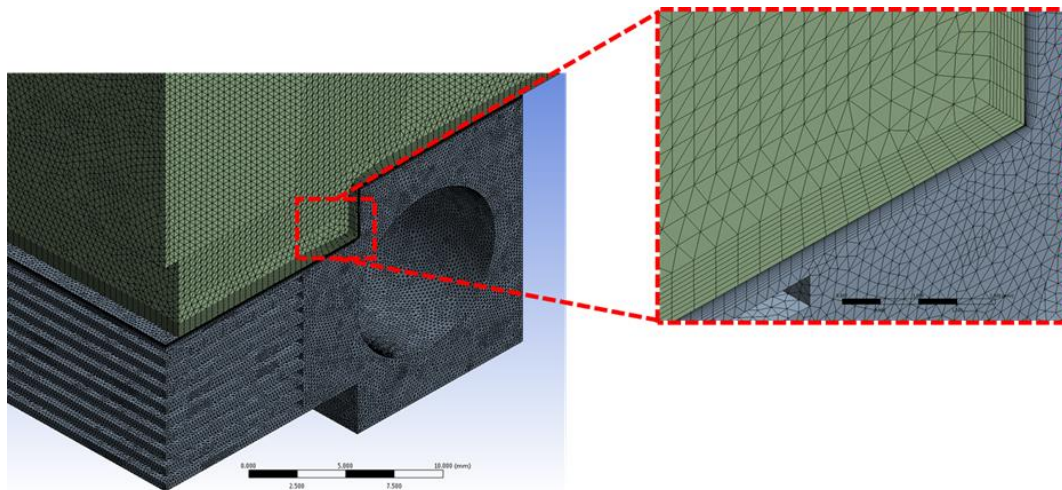


Figure 7.2 Mesh structure of the computational domain.

The grid system employed in the numerical analysis has 1660824 elements. The sensitivity of the numerical results is checked with different grid ranging from 297184 to 3727937 as presented in Figure 7.3. There is no considerable change in the results

beyond the grid size of 1660824. Hence, the grid size of 1660824 is used for further numerical simulations in order to minimize the computational time.

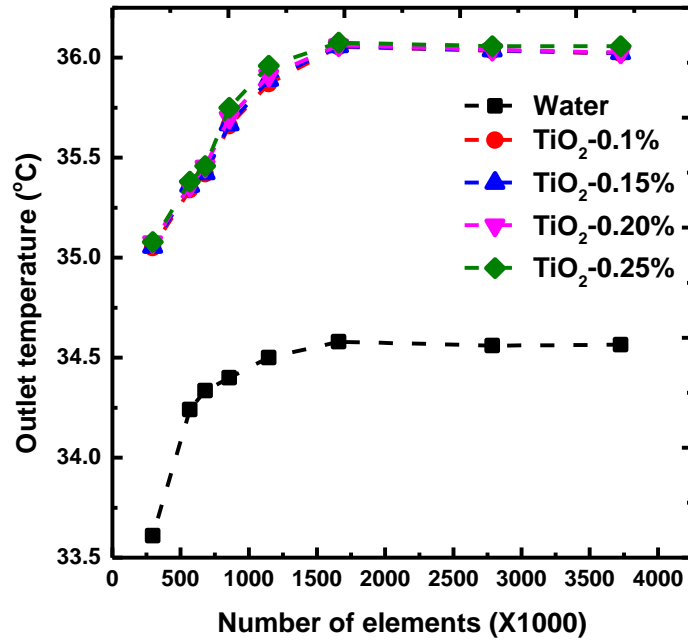


Figure 7.3 Grid independence study of outlet temperature for different nanofluids.

7.6 RESULTS AND DISCUSSION

7.6.1 Validation study

Laminar forced convection experiments are conducted under very low flow rate of 200 mL/min using DI-water with a constant heat flux condition. The obtained results provide considerable agreement with the benchmark Shah Equation. Figure 7.4 shows the comparison of Nusselt number results along the length of the flow. Figure 7.5 represents the comparison of friction factor with respect to the flow rate. With a maximum deviation of 5%, a good agreement between the experimental and analytical results was found.

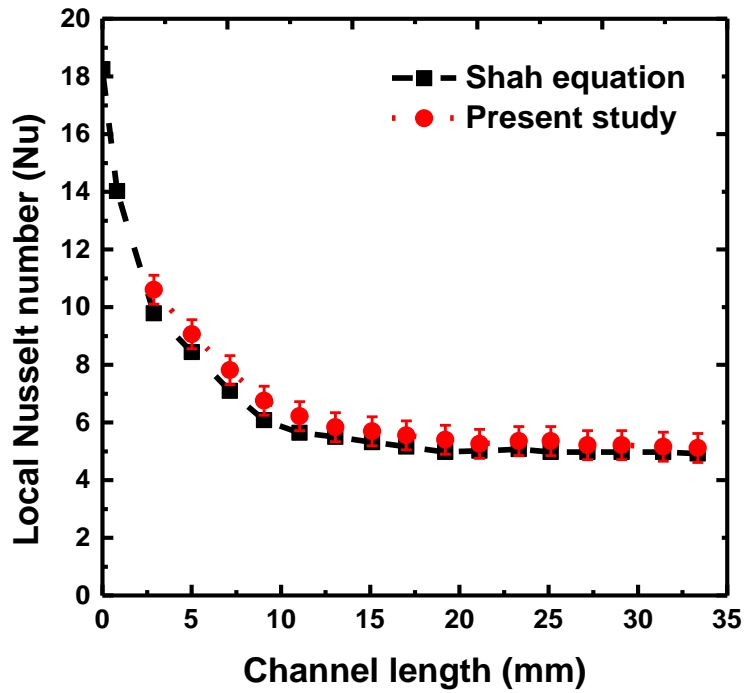


Figure 7.4 Nusselt number variation along the channel length.

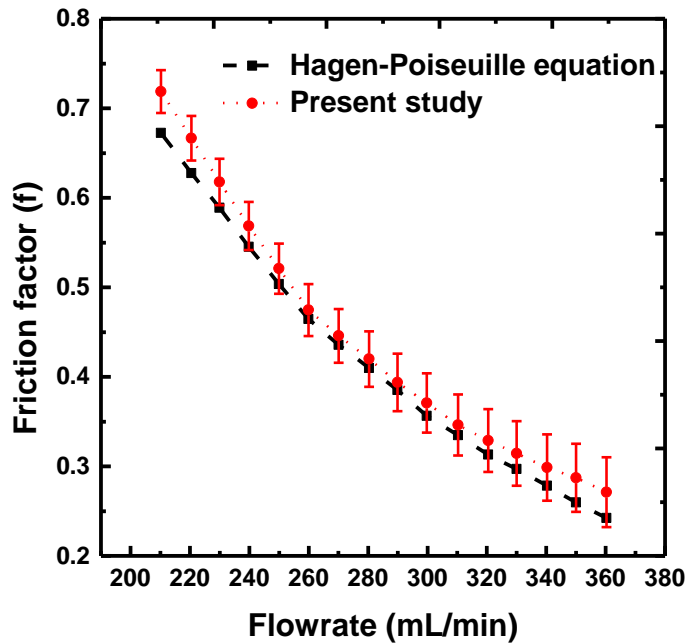


Figure 7.5 Friction factor comparison for increased flow rate.

7.6.2 Temperature study

Figure 7.6 shows the comparison between numerical and experimental studies of temperature along the length of the channel at a fixed flow rate of 200 mL/min. The presented temperature measurements were obtained from six thermocouples (TC1 to TC6). An appreciable agreement is obtained with minor deviations due to the use of multiple thermocouples.

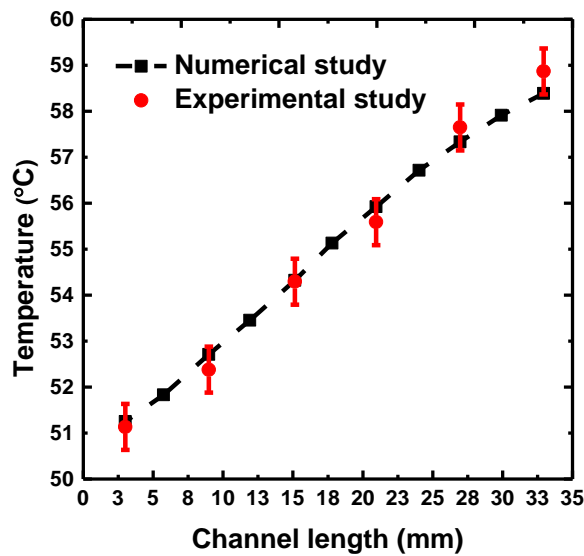


Figure 7.6 Comparative study on temperature variation along the length of the channel for a flow rate of 200 mL/min.

Transient temperature measurement comparison upon single thermocouple is presented in Figure 7.7 with qualitatively better agreement. It shows the decrease in temperature for a flow period of 120 s using pure fluid at a flow rate of 200 mL/min with normal and pulsating flow. Comparatively, slight decrease in temperature was observed for pulsating flow than normal flow in both microchannel and aluminium block section. As soon as the flow starts a steep decrease, a temperature drop of 12°C is observed within 3 s in copper channel. The reduction in temperature is observed as the flow progresses and remains nearly 7°C more than the inlet fluid. But the temperature decrease in the aluminium block is very gradual compared to the copper channel. Since the materials under investigations possess high thermal conductivity, the temperature difference measured between aluminium and copper channel core is more or less

similar when the flow is initiated. Due to the conjugate effect, the direct cooling of copper channel influences the aluminium block temperature.

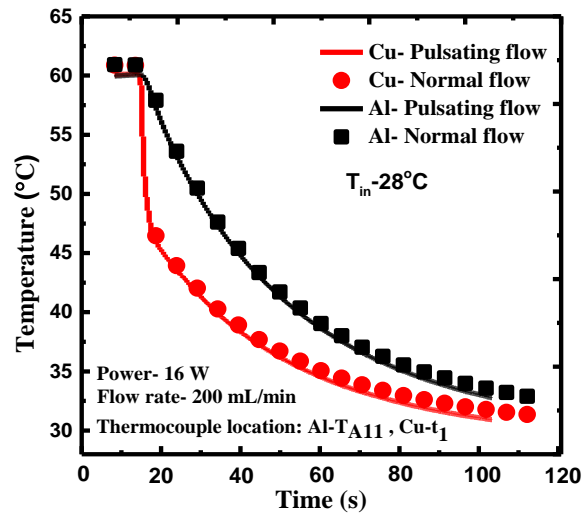


Figure 7.7 Comparative study on transient temperature decrement as function of time.

Figure 7.8 depicts the decrease in temperature for different power factors ranging from 14W to 20W. For a constant mass flow rate of 200 mL/min, 20 W power consumes more working fluid to attain the room temperature and in other hand 14W reaches room temperature within 75 s of runtime by using minimal working fluid.

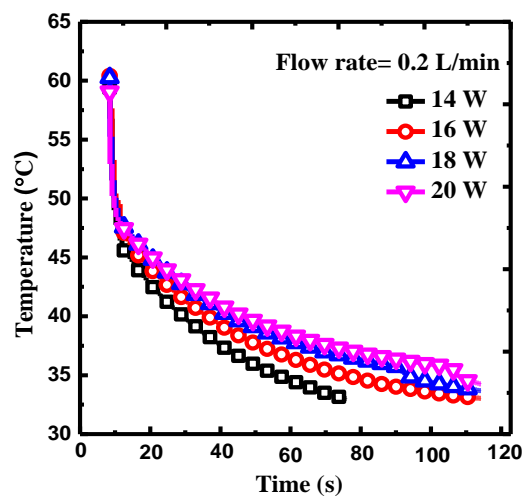


Figure 7.8 Temperature reduction in channel for different power with constant flow rate using water.

7.6.3 Exergy analysis

The outlet exergy for different volume fractions of TiO_2 for increase in flow rate is calculated and presented in Figure 7.9. It is observed that the maximum outlet exergy is developed by using TiO_2 nanofluid with 0.25% volume fraction generating outlet exergy of 150W which is 80% more than that of water for the same flow rate of 410 mL/min. This increase in outlet exergy is highly contributed to increased thermal conductivity of the working fluid at higher volume fractions. On the other hand, increase in flow decreases the exergy gain which is presented in Figure 7.10 and a maximum gain of 112 W is developed for 0.25% of TiO_2 at a lower flow rate of 210 mL/min but with the increase in flow rate the exergy gain started to reduce considerably. This decrease in exergy gain can be attributed to the increased flow rate. This effect is predominately found between water and TiO_2 nanofluid and deviation between TiO_2 volume fractions are very minimal. For the same flow rate condition, the pure fluid developed a reduction of exergy gain of 12 W. This trend is contributed to increase in sink temperature for increased flow rate.

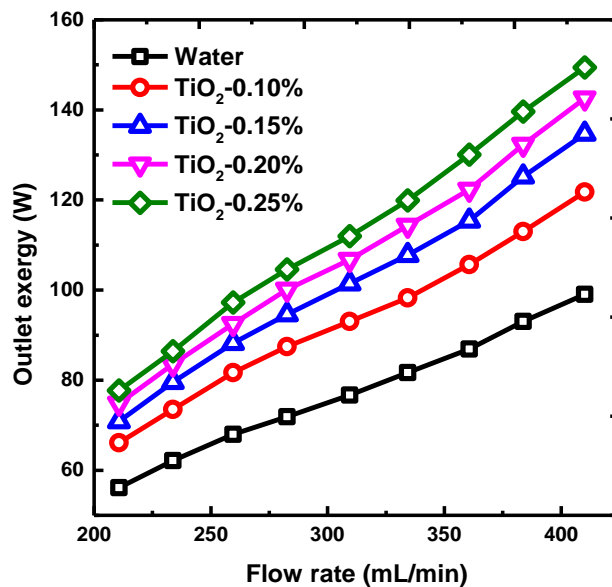


Figure 7.9 Outlet exergy for different nanofluid concentration as a function of flow rate.

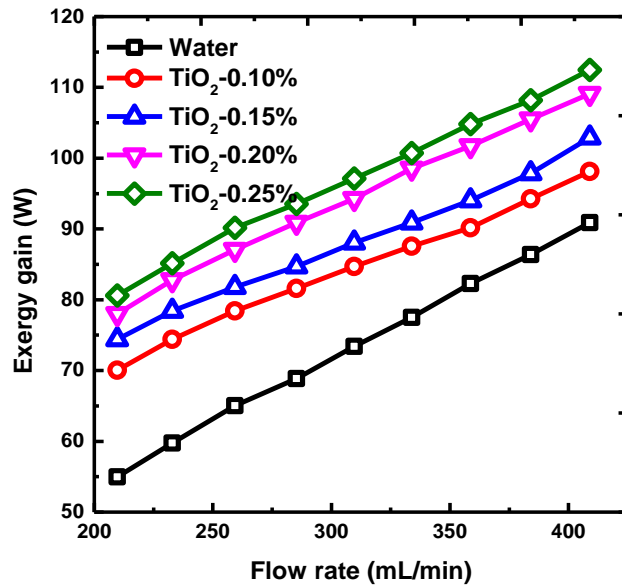


Figure 7.10 Exergy gain for different nanofluid concentrations as a function of flow rate.

7.6.4 Entropy generation study

The entropy generated for different TiO₂ nanofluid is discussed in Figures 7.11 and 7.12. Figure 7.11 depicts the thermal entropy generation and Figure 7.12 represents the entropy generated from fluid friction which is calculated from Equations 7.13 and 7.14. It is observed that increasing thermal conductivity of the fluid combined with increased flow tend to reduce the thermal entropy generation. The thermal entropy generated by TiO₂-0.25% is about 0.044 W/K and 0.02 W/K for flow rates of 210 mL/min and 410 mL/min respectively. In contrast, frictional entropy increases with the increased flow rate and the contribution of the frictional entropy is lower when compared with the thermal entropy generation. It majorly takes into account of increase in friction along the flow length. The maximum frictional entropy is developed for highest mass flow rate of 460 mL/min compared to the increment of TiO₂-0.25% which is 6% more than that of TiO₂-0.01% and 9% more than pure fluids. Frictional entropy generation is relatively lower than the thermal entropy which is primarily due to the increased aspect ratio of microchannels. Additionally, higher difference in frictional entropy is observed for higher volume fraction of TiO₂-0.25% and water at increased flow rate.

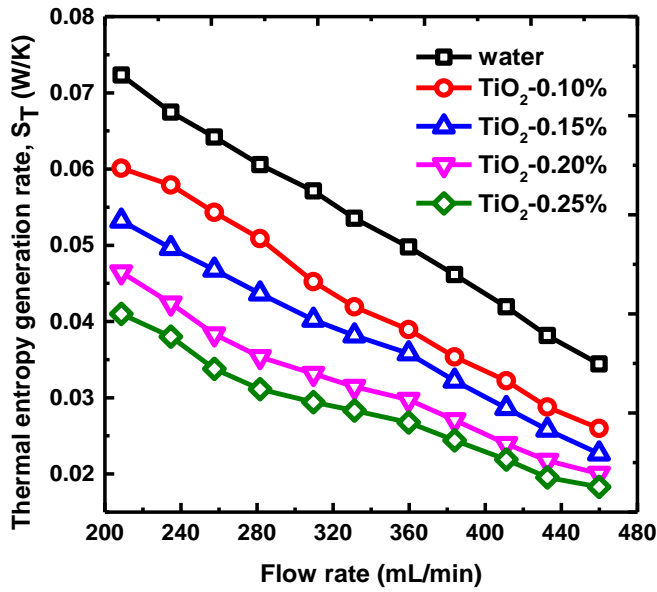


Figure 7.11 Thermal entropy generation rate for different nanofluid concentrations.

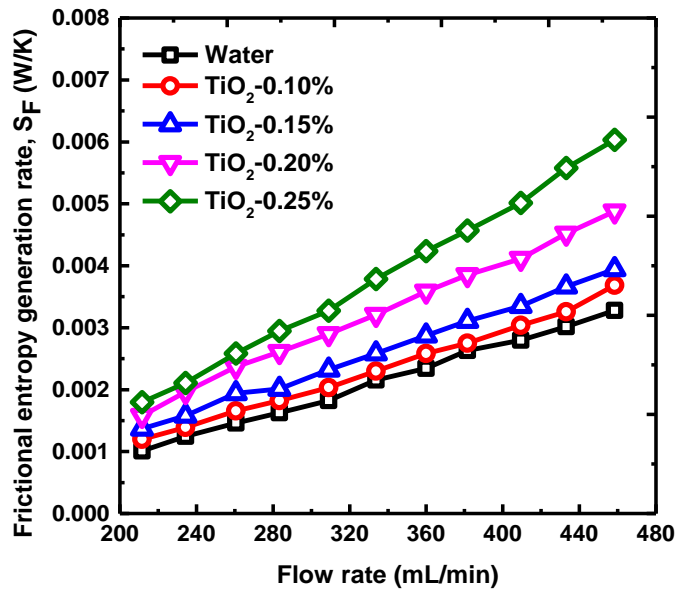


Figure 7.12 Frictional entropy generation rate for different nanofluid concentrations.

Figure 7.13 presents the Bejan number (Be) as a function of flow rate for different TiO_2 nanofluid concentrations. As observed, the effect of thermal entropy generation is higher than frictional entropy generated. Compared to the water, even with the use of very low volume fraction of TiO_2 -0.25%, increase in frictional entropy generation was

found. Additionally, at higher stability the viscosity of oxide based TiO_2 nanofluid is higher and leads to increased particle to particle and particle to surface interactions. This decreases the Bejan number for higher TiO_2 particle concentrations subjected to increased flow rates. The Bejan number is found more or less near the value ranging from 0.40 to 0.85.

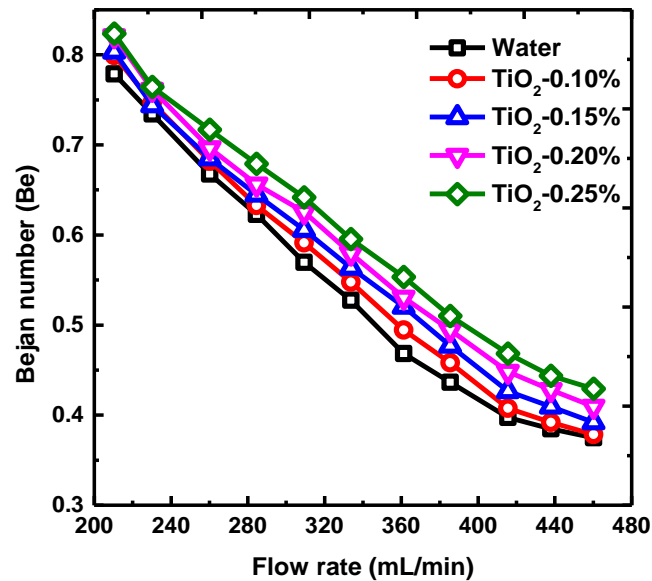
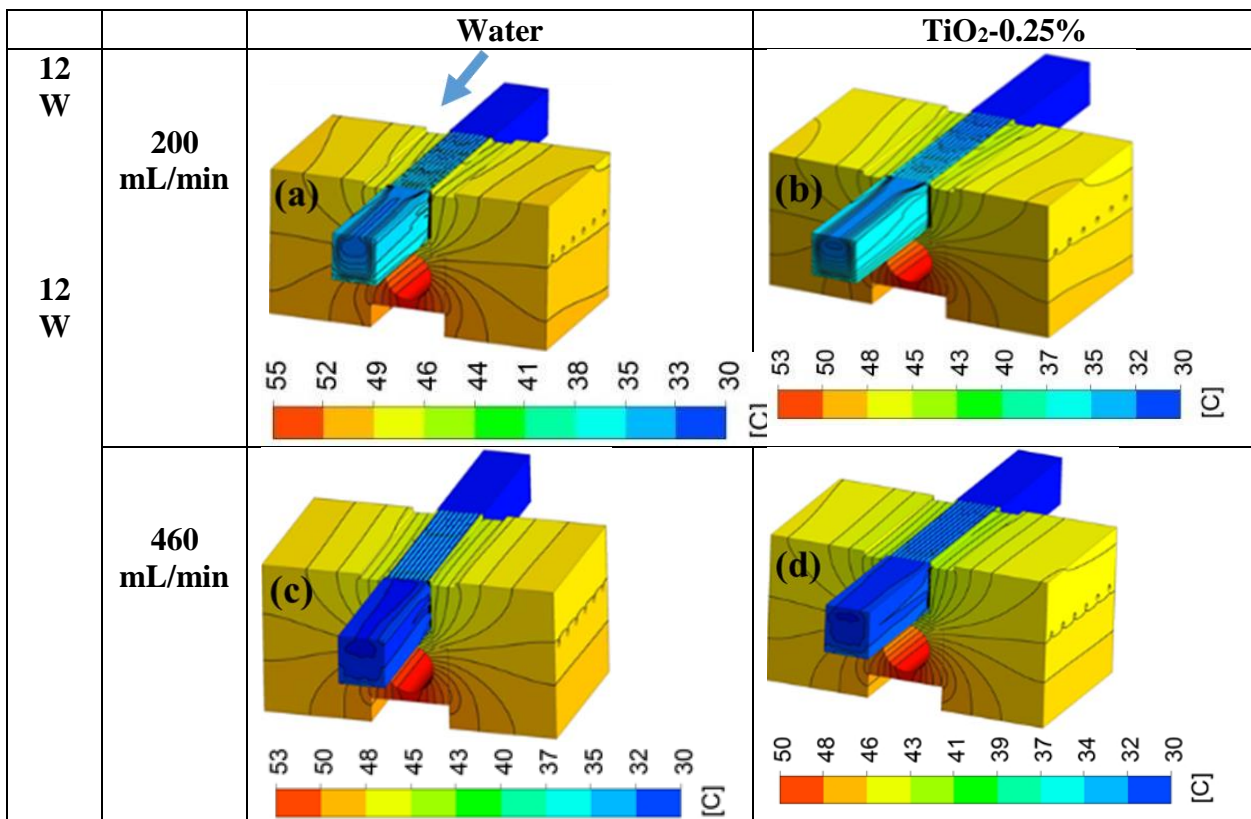


Figure 7.13 Bejan number variations as a function of flow rate for different TiO_2 nanofluid concentrations.

Figure 7.14 presents the effect of TiO_2 concentration on forced convection enhancement in the microchannel heat sink. It shows the temperature contours along the length of the flow in microchannel and the surrounding aluminium block. It is clear that the maximum temperature in all the simulated cases is located near the outlet region of the heat sink, and by using nanofluid peak temperature of the heat sink decreases. Figure 7.14(a) shows the temperature distribution for channel and aluminium block with water as working fluid for 12 W subjected to the flow rate of 200 mL/min. Maximum decrease in temperature is observed near the entrance region of the microchannel and accordingly the surrounding aluminium block temperature is also reduced. Highest temperature of 55°C is noticed near the heater. For the same flow rate by using 0.25%- TiO_2 nanofluid the maximum temperature is reduced to 53°C and outlet temperature increased to 38°C . Due to the increased thermal conductivity of the fluid

the axial thermal conduction effects of microchannel cooling is extended throughout the aluminium block, shown in Figure 7.14(b). On other hand the cooling effect in aluminium block is noticed highly parallel to microchannel for increased flow rate of 460 mL/min, shown in Figure 7.14(c). For the increased flow rate of 460 mL/min the cooling effects near the inlet as observed in the flow rate of 200 mL/min is not noticed due to reduced axial conduction. This reduces the conjugate cooling effects and provides the temperature contour distribution in aluminium block parallel to the channel flow. Similar trend is observed in TiO₂-0.25% nanofluid with reduced temperature near the channels shown in Figure 7.14(d).

Figures 7.14(e, f) shows the temperature distribution for the power of 18 W. For the flow rate of 200 mL/min maximum temperature of the sink reached up to 67°C shown in Figure 7.14(e). Outlet temperature for TiO₂-0.25% increased to 41°C shown in Figure 7.14(f). Additionally, the difference in temperature distribution trend for 460 mL/min is more or less identical when compared with 200 mL/min shown in Figures 7.14(g, h).



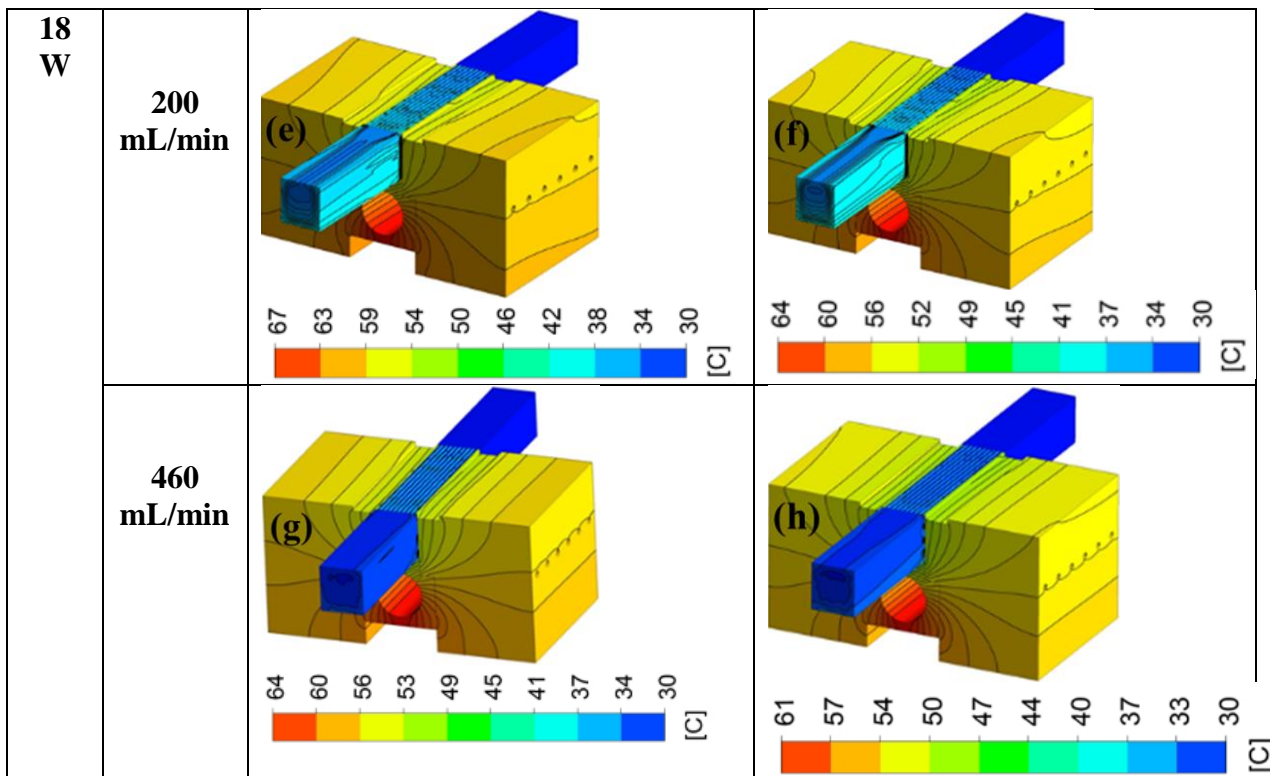


Figure 7.14 Temperature contours for different volume fractions, flow rate and power factor. 12 W power (a-d); 18 W power (e-h), (a) water at 200 mL/min, (b) TiO₂-0.25% at 200 mL/min, (c) water at 460 mL/min, (d) TiO₂-0.25% at 460 mL/min, (e) water at 200 mL/min, (f) TiO₂-0.25% at 200 mL/min, (g) water at 460 mL/min, (h) TiO₂-0.25% at 460 mL/min

Figure 7.15 depicts the temperature iso-surfaces at constant flow rate of 460 mL/min for different TiO₂ volume fractions. Figure 7.15(a) presents temperature iso-surfaces for water as working fluid. It is seen that maximum temperature of 46°C prevails near the channel floor. Above that second highest fluid temperature layer of 42°C is observed which is noticed from beginning of the microchannel. The predominant fluid temperature of 36°C is found above the second layer. Further, temperature iso-surfaces in aluminium block near the entrance region found parabolic due to the entrance effect and further along the length of the flow it moves inward to the channel wall. In this case, the effect of cooling is noticed in the aluminium near the vicinity of the microchannel which was not seen in other cases, shown in Figures 7.15(b-e). Figure 7.15(b) depicts the temperature iso-surfaces for TiO₂-0.10%, compared with the water the maximum outlet temperature of 46°C has increased and predominant fluid

temperature of 36°C reduced by 20%. Additionally, last channels of the heatsink develop the maximum outlet temperature which is seen throughout the channel height, shown in Figure 7.15(c).

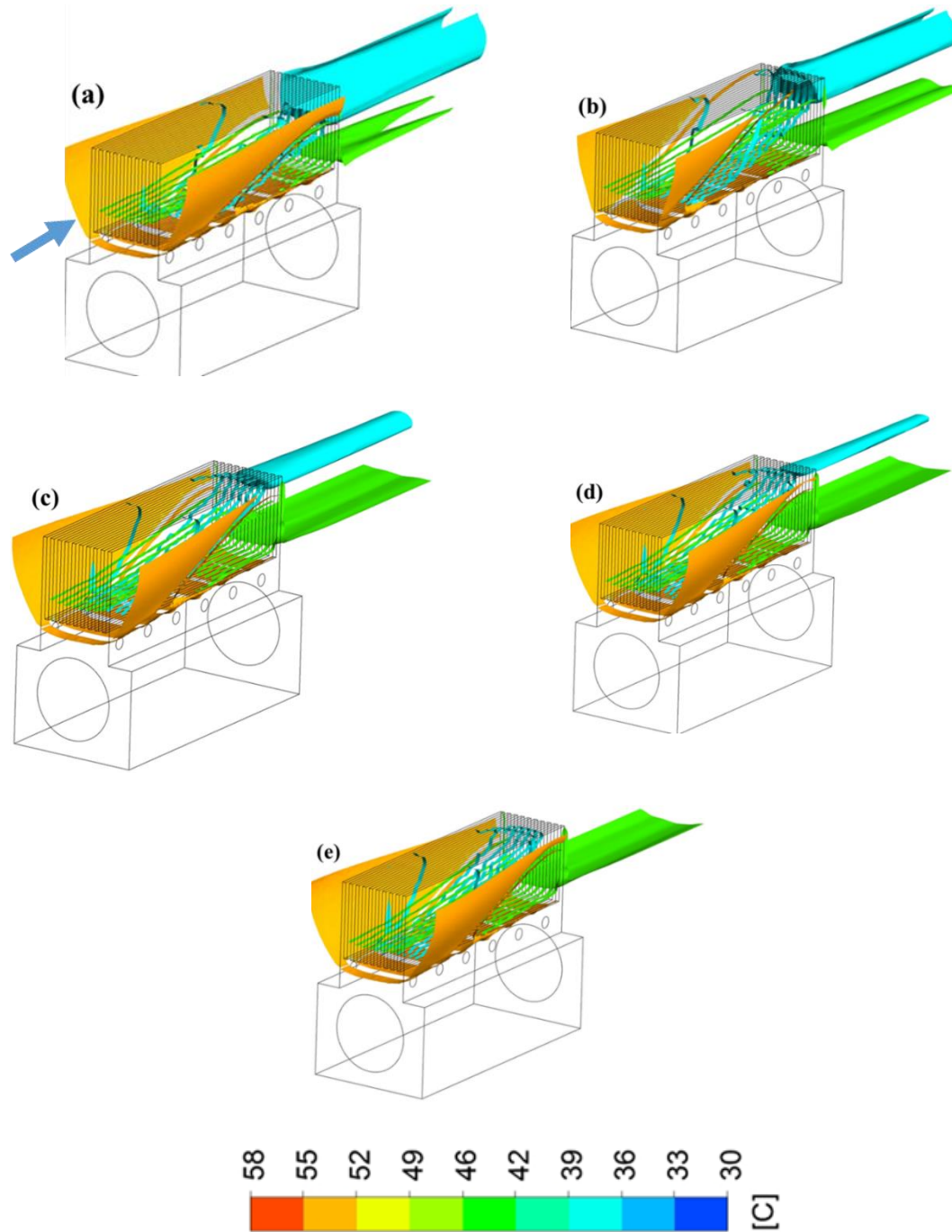


Figure 7.15 Temperature iso-surfaces for outlet fluid and aluminium block for different TiO_2 nanofluid at a constant flow rate of 460 mL/min with power factor of 18W. (a) water, (b) 0.1%, (c) 0.15%, (d) 0.20%, and (e) 0.25%.

Due to the increased thermal conductivity of the nanofluid the iso-surface for the 36°C decreased nearly half when compared with water. Furthermore, for working fluid TiO₂-0.20%, 36°C is reduced drastically and majority of the fluid is present at the top edge of central channels shown in Figure 7.15(d). Figure 7.15(e) depicts the completely disappeared temperature iso-surface of 36°C and completely filled 46°C temperature iso-surface near the outlet of the channel. This is highly attributed to the increased thermal conductivity of the working fluids.

7.7 CONCLUSIONS

In this study, the exergy, entropy generation, fluid hydrodynamics and heat transfer characteristics for a deep rectangular microchannel was investigated using TiO₂ nanofluid at different volume fractions. From the combined numerical and experimental studies the following key findings are listed:

- From the experiments, it has been observed during heating, the temperature difference between the copper and aluminium block approaches almost to 4°C but after sometime a steep decrease in temperature was observed while cooling in case of copper microchannel but the same was not noticed for aluminium block.
- Most importantly the entrance effect was not only observed in microchannel but also in the integrated regions of the microchannel. Also, when the flow rate is increased temperature isotherms were parallel in aluminium block.
- The nanofluid significantly reduces the temperature difference between the microchannel walls and the mean temperature of the fluid in the microchannel. More than the conjugate effects increase in volume fraction reduces the thermal resistance between the microchannel wall and fluid thereby elevating the outlet temperature to a great extent.
- The significant effects of axial thermal conduction at inlet and outlet of microchannels are mainly observed for TiO₂ nanofluid at lower flow rate. This axial conduction extends in aluminium block predominantly near inlet section and reduces for higher flow rates. For the maximum flow rate of 460 mL/min, the axial conduction becomes constant throughout the microchannel and effect of conjugate heat transfer is decreased.

- On analyzing the thermal and fluid hydrodynamics the conjugate effects were witnessed higher for TiO₂ nanofluid than water. The variation in conjugate effects among the TiO₂ nanofluid was found much similar. The increased flow rate influences the conjugate effect for both water and TiO₂ nanofluid.
- It was found that with the increase in flow rate, the outlet exergy increases for all the subjected TiO₂ nanofluid concentrations. The highest outlet exergy of 145 W was observed for the flow rate of 410 mL/min.
- Thermal entropy generation decreases for higher TiO₂ nanofluid concentration and flow rate. The frictional entropy generation increases for higher flow rate and nanofluid particle concentration.

7.8 CLOSURE

This chapter dealt with the irreversibility studies using heterogeneous integrated microchannel and the effect of the TiO₂ concentration at different flow rates. The next chapter deals with the use of parallel minichannel with rib structures to reduce the maldistribution based high temperature zones near the channel exit.

CHAPTER 8

INVESTIGATION ON INERTIAL MINICHANNELS TO MITIGATE FLOW MALDISTRIBUTION INDUCED HIGH TEMPERATURE ZONES

8.1 INTRODUCTION

Axial conduction in channels depends on inlet velocity and thermal conductivity of the working fluid. In the case of parallel channels, axial conduction depends on heat sink configuration and inlet velocity. That too at increased flow rates, the parallel channel generates flow maldistribution and develops localized high temperature zones in the heat sink. Effective use of heat sink configuration to mitigate axial conduction is found in literature; however, the axial conduction effects were not suppressed due to the flow maldistribution in the parallel channels. Henceforth, the present study provides an experimental and numerical insight to evaluate the potential of ribs and gravity based spillway channels to overcome the above mentioned issues in parallel channels. Especially, four different heat sink concept were designed using copper material. In which experiments are performed in normal straight channel and used as reference, while the remaining channel types are investigated numerically. The factors such as maldistribution, thermal resistance and pressure drop are considered to evaluate the impact of volume fraction and inlet velocity of the working fluid.

8.2 EXPERIMENTAL SETUP

The schematics of the exploded experimental setup is presented in Figure 8.1. It consists of heat generating processor chip, minichannel, transparent acrylic cover and bakelite headers for fluid flow. Figure 8.2 presents the schematics of the different channel configuration used for the investigation. The complete details of the setup is elaborately given in the Chapter 3.

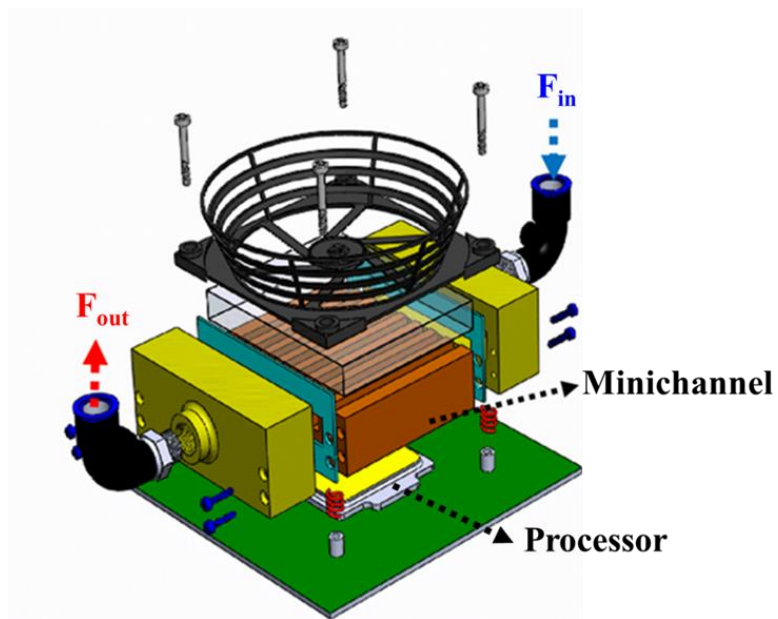


Figure 8.1 Exploded view of the experimental setup and channel flow structures used for the investigation.

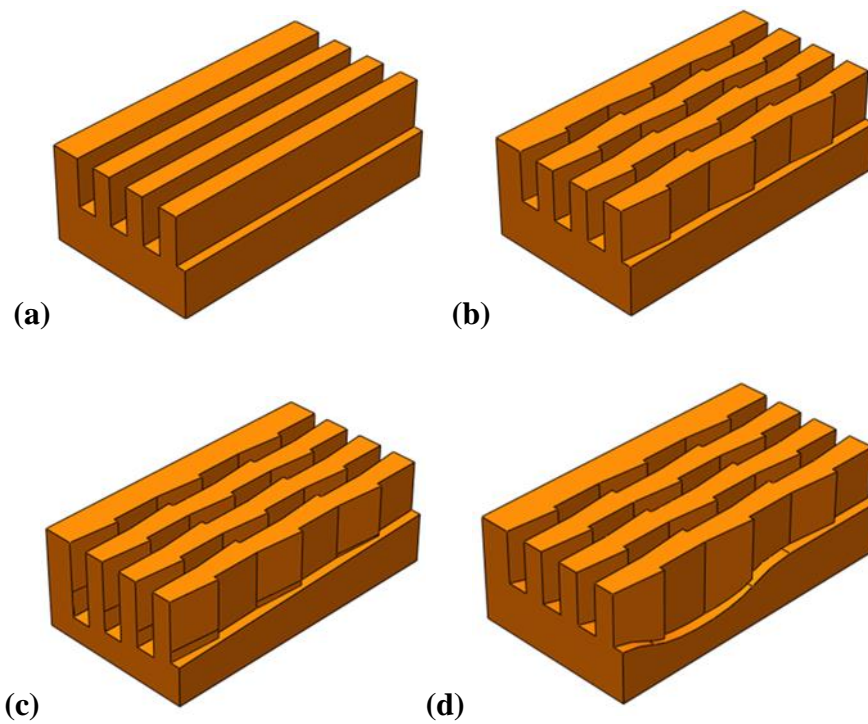


Figure 8.2 Schematics of the different channel configuration. (a) straight channel, (b) ribbed channel, (c) ribbed inclined, and (d) ribbed lifted.

8.3 NUMERICAL MODELLING

8.3.1 Boundary conditions

The schematics of the computational domain with boundary condition is shown in Figure 8.3.

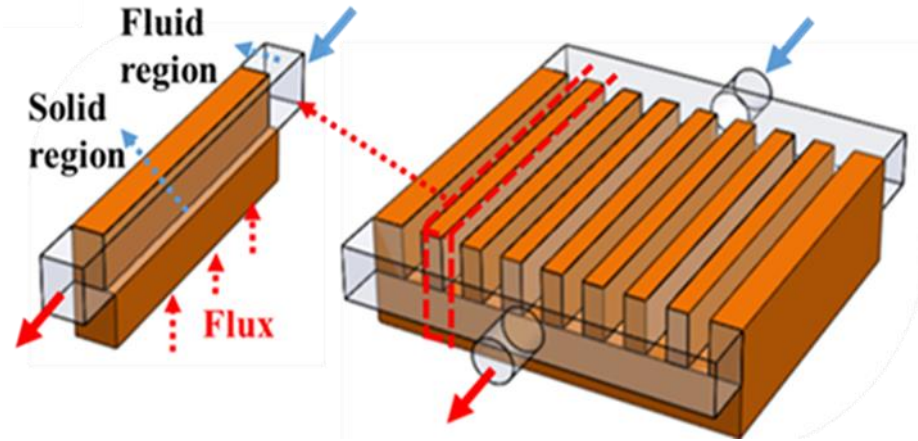


Figure 8.3 Schematics of the computational domain with boundary condition.

8.3.2 Governing equation

A single phase model is adopted for the conjugate studies of laminar forced convection heat transfer in a rectangular microchannel. This model involves solving conduction and convection heat transfer simultaneously. The governing equations pertaining to the analysis are given in Equations 8.1-8.6.

Continuity equation

$$\frac{\partial u}{\partial x} + \frac{\partial v}{\partial y} + \frac{\partial w}{\partial z} = 0 \quad (8.1)$$

X-momentum equation

$$u \frac{\partial u}{\partial x} + v \frac{\partial u}{\partial y} + w \frac{\partial u}{\partial z} = -\frac{1}{\rho} \frac{\partial p}{\partial x} + \nu \left(\frac{\partial^2 u}{\partial x^2} + \frac{\partial^2 u}{\partial y^2} + \frac{\partial^2 u}{\partial z^2} \right) \quad (8.2)$$

Y-momentum equation

$$u \frac{\partial v}{\partial x} + v \frac{\partial v}{\partial y} + w \frac{\partial v}{\partial z} = -\frac{1}{\rho} \frac{\partial p}{\partial y} + \nu \left(\frac{\partial^2 v}{\partial x^2} + \frac{\partial^2 v}{\partial y^2} + \frac{\partial^2 v}{\partial z^2} \right) \quad (8.3)$$

Z-momentum equation

$$u \frac{\partial w}{\partial x} + v \frac{\partial w}{\partial y} + w \frac{\partial w}{\partial z} = -\frac{1}{\rho} \frac{\partial p}{\partial z} + \nu \left(\frac{\partial^2 w}{\partial x^2} + \frac{\partial^2 w}{\partial y^2} + \frac{\partial^2 w}{\partial z^2} \right) \quad (8.4)$$

Energy equation of the fluid

$$\frac{\partial T}{\partial t} + u \frac{\partial T}{\partial x} + v \frac{\partial T}{\partial y} + w \frac{\partial T}{\partial z} = \alpha \left(\frac{\partial^2 T}{\partial x^2} + \frac{\partial^2 T}{\partial y^2} + \frac{\partial^2 T}{\partial z^2} \right) \quad (8.5)$$

Energy equation of the solid

$$\frac{\partial^2 T}{\partial x^2} + \frac{\partial^2 T}{\partial y^2} + \frac{\partial^2 T}{\partial z^2} = \frac{1}{\alpha} \frac{\partial T}{\partial t} \quad (8.6)$$

8.3.3 Grid independence study

The grid system employed in the numerical analysis has 600000 elements. The sensitivity of the numerical results is checked with different grid ranging from 15000 to 800000 as presented in Figure 8.4. There is no considerable change in the results beyond the grid size of 600000. Hence, the grid size of 600000 is used for further numerical simulations in order to minimize the computational time.

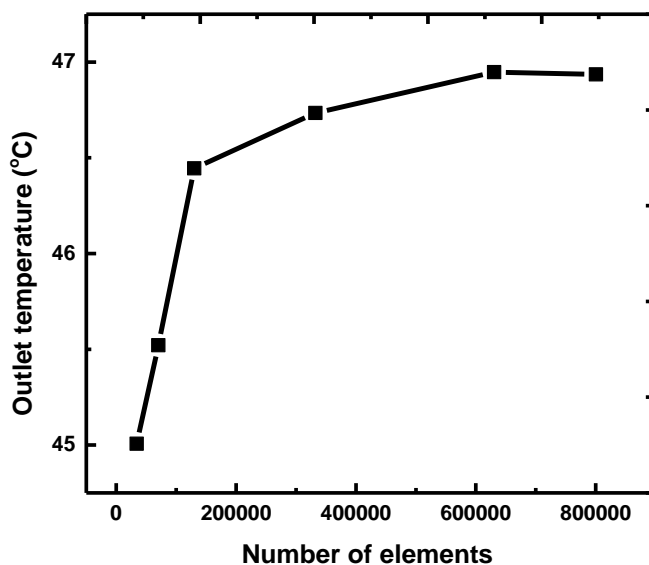
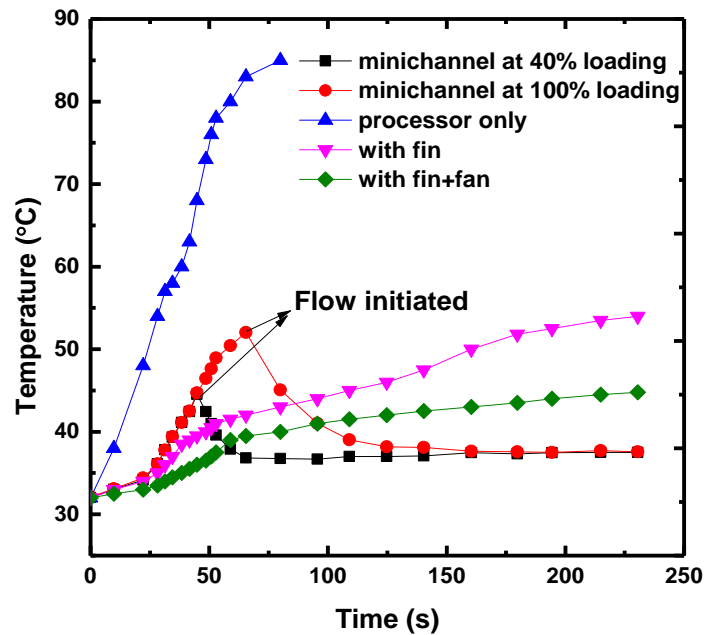


Figure 8.4 Grid independence study for the outlet temperature of fluid.

8.4 HEAT SINK MODULES COMPARISON

Figure 8.5 presents the comparison of cooling of minichannel with other existing cooling modules. Initially the system is allowed to operate without any cooling modules with the complete core being utilized.



Figures 8.5 Temperature distributions of the core under different cooling module conditions.

The core temperature reached 85°C around 50 s after that it almost maintained in the range, then the core die thermistor shuts off the processor. Similarly, the processor is subjected with fin, with fin +fan and minichannel. Except the case of minichannel all other cooling modules maintains the processor within the acceptable working limit. If we consider the module with fin +fan it almost maintains the module temperature near to 45°C. On the other hand minichannel maintained the sink temperature to 35°C.

8.5 TEMPERATURE DISTRIBUTION OF THE SOURCE AND MODULE

Figure 8.6 presents the IR images of the processor core at two loading conditions. The maximum temperature of 85.2°C in the core is with the case of 100% loading.

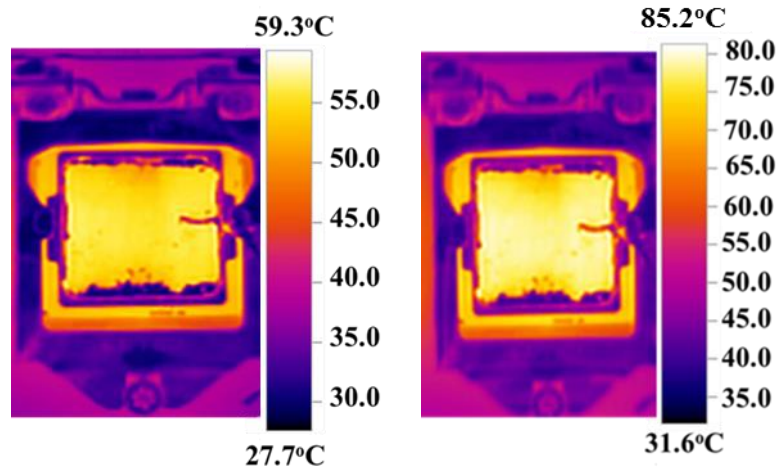
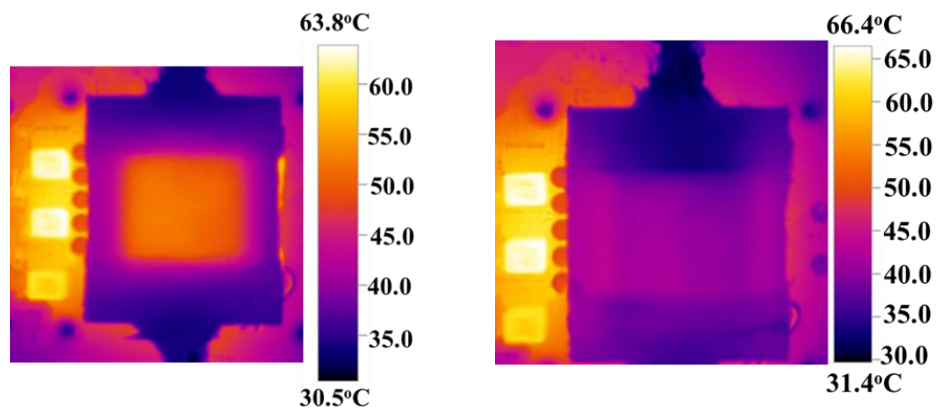


Figure 8.6 IR images of the processor core at two different loading. (a) 40% loading condition, and 100% loading condition.

Figure 8.7 presents the infrared photographs of the minichannel module at six progressive time interval using water as working fluid. Initially the temperature of the minichannel heatsink was about 55°C as shown in Figure 8.7(a). After the run time of 20 s the temperature of the sink reduced 10°C which is about 45°C as shown in Figure 8.7(b). On further progressive cooling, the sink temperature is maintained near 40°C as shown in Figures 8.7(c) and (d). Later a steady temperature of 37°C prevailed throughout the cooling period of the heat sink.



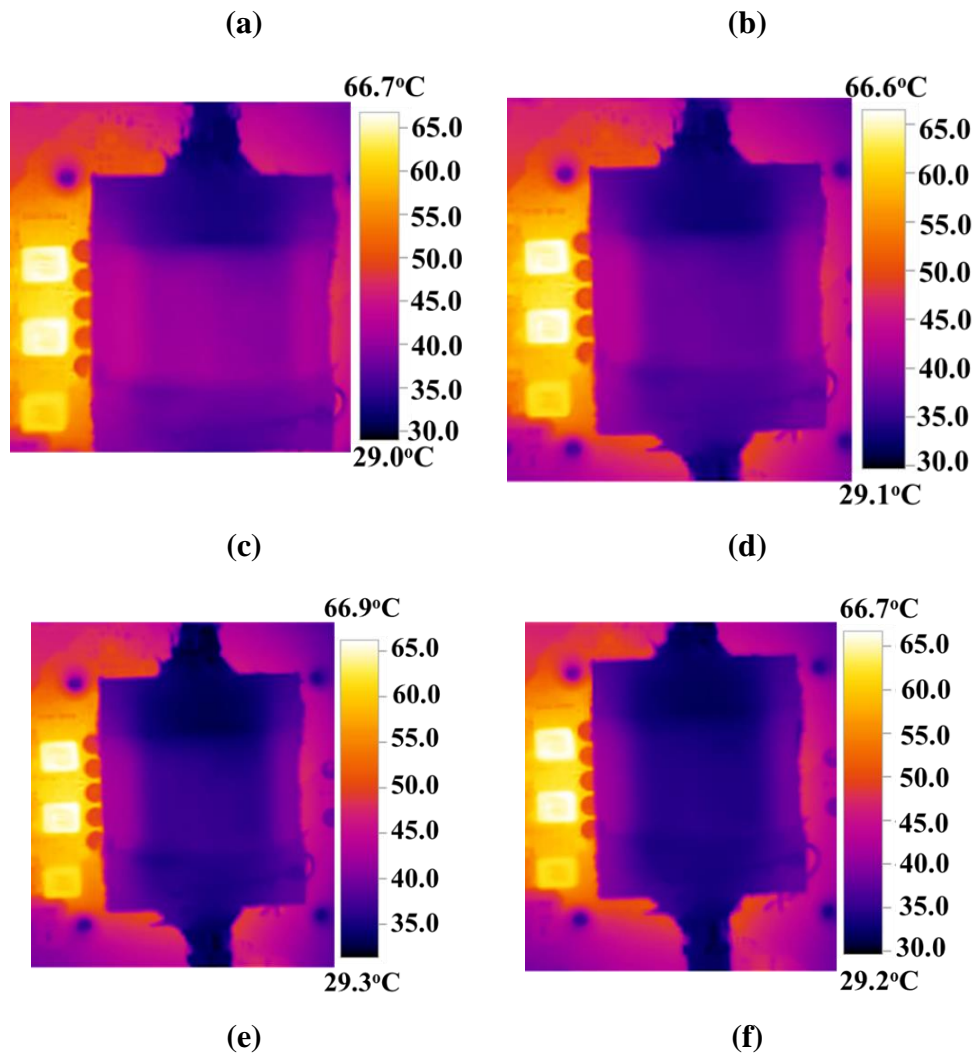


Figure 8.7 IR images of the processor core at progressive cooling different time periods.

(a) Time, $t=0$ s, (b) $t=20$ s, (c) $t=30$ s, (d) $t=50$ s, and (f) $t=60$ s.

8.6 RESULTS AND DISCUSSION

8.6.1 Validation study

Figure 8.8 depicts the comparison of experimental and numerical studies of transient temperature decrement at a flow rate of 210 mL/min. The numerical results match well with the experimental results with a deviation of 3%. The discrepancy in the numerical result is due to the factors of loss associated with radiation, thermal contact with the board and natural convection etc.

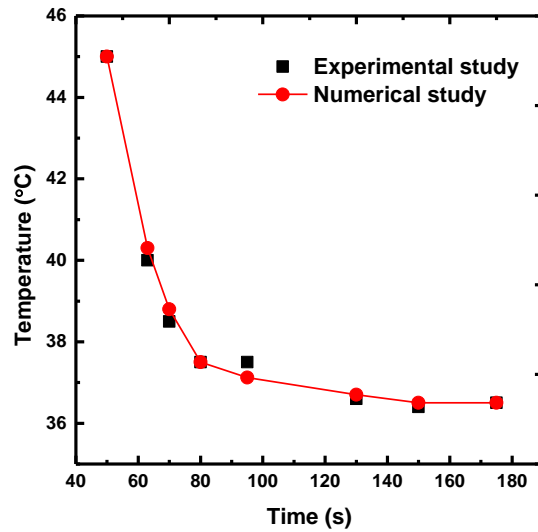


Figure 8.8 Experimental and numerical study comparison of temperature as a function of time.

The variation of pressure with Reynolds number for normal minichannel is shown in Figure 8.9. As shown the numerical model is agreeing well with the experimental results with slight deviation at higher Reynolds number. It is known that the pressure drop obtained from the experiments is high due to the surface roughness and flow line.

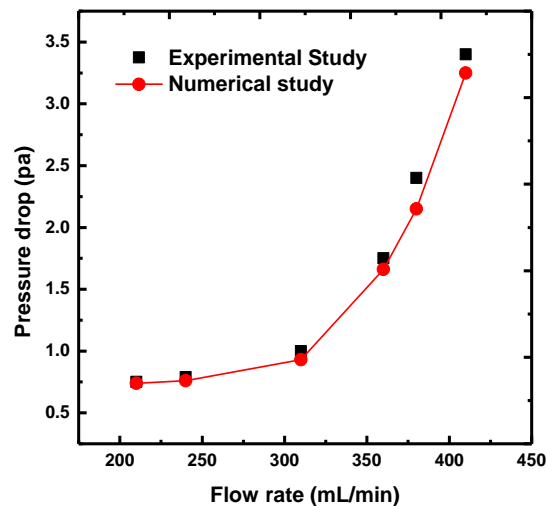


Figure 8.9 Experimental and numerical study comparison of pressure drop.

8.6.2 Thermo hydrodynamics study

The variation in channel temperature along the length of the minichannel for different channel structures is shown in Figure 8.10. It can be seen that for all the cases the fluid temperature tend to increase for the entire channel length and the maximum temperature increment in the ribbed minichannel is apparently higher than the normal minichannel. This increment is attributed as a result of mixing of fluids due to the ribs.

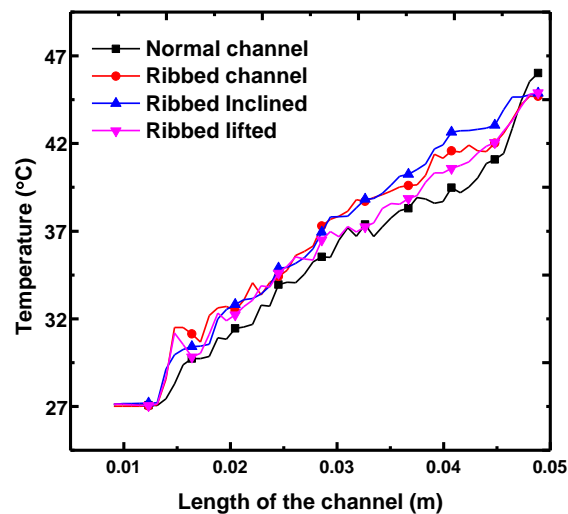


Figure 8.10 Temperature variation along length of the channel for different channels.

Figure 8.11 shows the results for velocity along the length of the channel with different channel structures. It is important that the normal channel has highly stable velocity throughout the channel length. But comparatively the velocity for ribbed channel is lower and more similar till the length of 0.025 m and gets deviated due to the channel design modifications. The lowest velocity in the channel is developed in ribbed inclined leading to large variations in velocities near the outlet region. In the case of chute spillway channels the velocity for center channels decreases to a maximum extent near the exit because the consecutively inclined channel spillways has increased the fluid velocities considerably. On other hand the exit velocity on ribbed lifted increased due to the development of hydraulic jump near the channel structure. The fluid accelerates and picks up momentum at drop structure, upon reaching base it experiences the submerged hydraulic jump where part of fluid with higher momentum leaves the

channel with increased velocity and remaining fluid, lost momentum due to hydraulic jump recirculated near the drop structure.

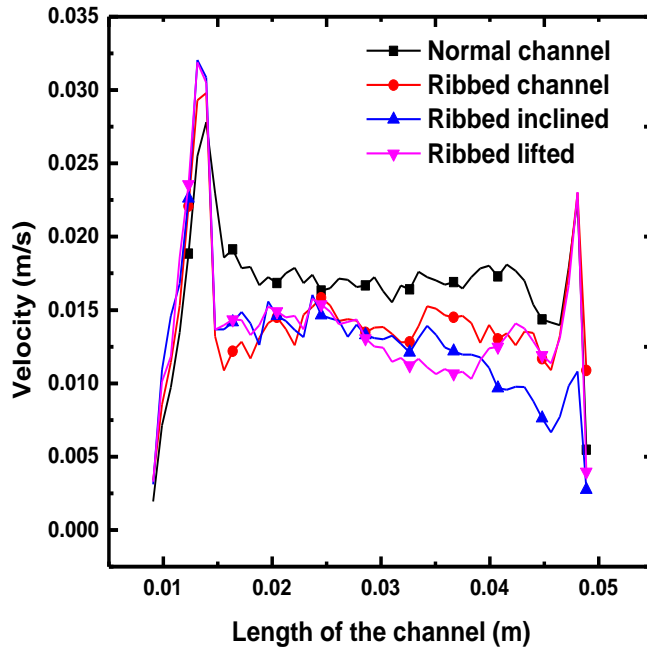


Figure 8.11 Velocity along length of the channel for different channels.

Figure 8.12 shows the pressure drop along the axial length of the channel for different ribbed channels. For all the numerical models the inlet velocity is based on the experimental flow rate. It can be seen that at initial distance of 0.015 m the pressure drop is maximum, but as it approach near the outlet at 0.045 m the pressure drop decreases. It is found that ribbed chute spill way channel develops lowest pressure drop than other three microchannel designs. The spillway channels carried enough fluid to reduce the pressure of the centerline channels. This effect is observed at initial pressure near inlet, a least pressure is generated for normal minichannel but along the axial length it peaks up to 4.4 Pa. Similarly, the maximum inlet pressure is for ribbed channels. Here again for hydraulic jump based channels the effect of pressure drop becomes more similar to that of normal channels. This is attributed to the partially increased velocity due to the submerged hydraulic jump spillway.

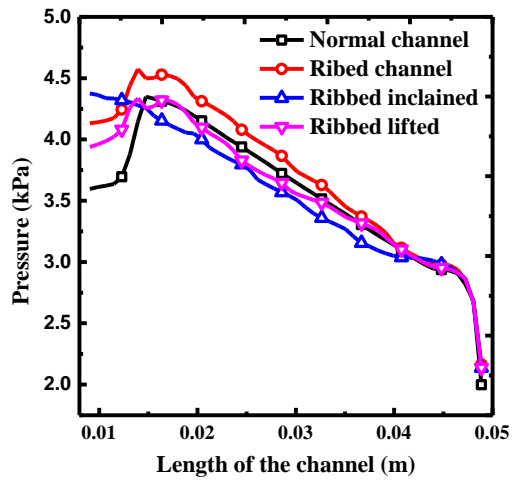


Figure 8.12 Pressure drop along length of the channel for different channels.

Figure 8.13 shows the temperature contours for different heat sink cross-section. The analysis of the thermal field distribution for different heat sink indicates that the higher temperature is seen near the outlet of the minichannel, but comparatively centerline channel has lower temperature. Figure 8.13(a) shows the temperature distribution for parallel minichannel where, it has lower T_{avg} than the remaining channel designs. Figure 8.13(b) shows the temperature distribution with added ribs, where by using ribs an alternating constrictions in fluid flow has been developed. This effect significantly enhances the fluid mixing and increases outlet fluid temperature with reduced heat sink temperature.

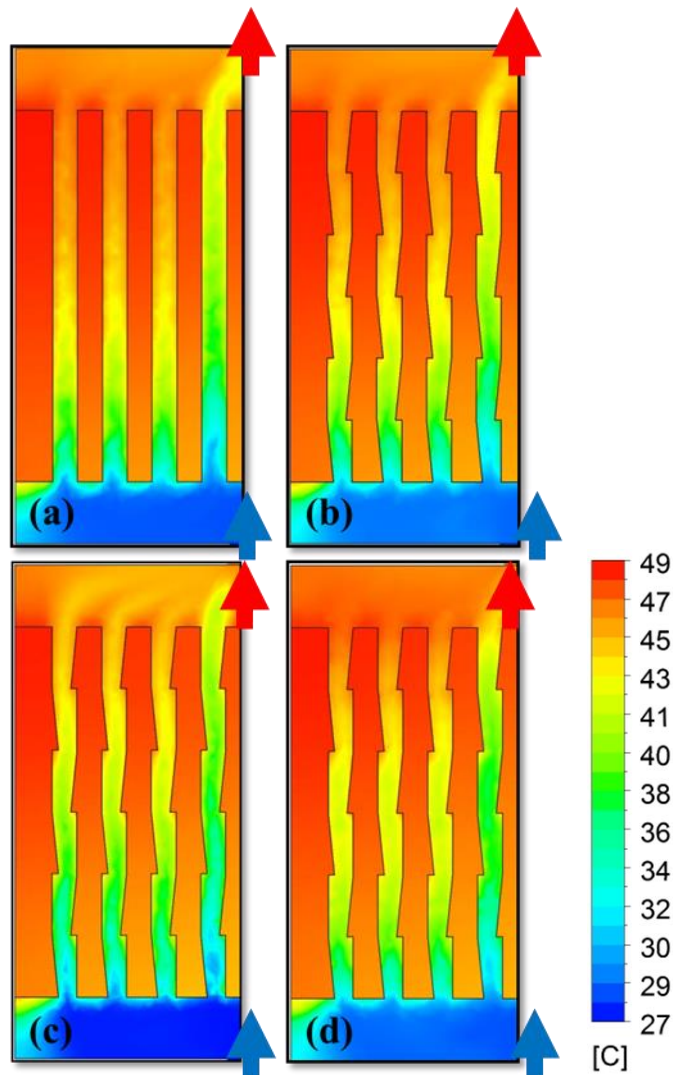


Figure 8.13 Temperature contours of minichannel for different channels (a) normal channel, (b) ribbed channel, (c) ribbed inclined, and (d) ribbed lifted.

The non-uniform temperature distribution among the channels is reduced to a great extent by the use of gravity based spillway design of channels as shown in Figure 8.13(c, d). Among these spill way design better uniform temperature is developed by chute type spillway as shown in Figure 8.13(c). This can be attributed to the increased fluid accelerations due to inclined spillways. Due to combined effect of ribs and acceleration gravity affects the peak temperature of the heat sink is reduced by 2°C. The temperature contour was found similar to that of normal channels which is shown in Figure 8.13(d).

Figure 8.14 shows the temperature contour near the exit of the minichannel in Y-Z plane. In first place, the effect of ribs result in decrease in temperature in all the three models followed by decrease in sink average temperature. Apart from the axial conduction effects, the cross-sectional temperature distribution is comparatively reduced with gravity spillways.

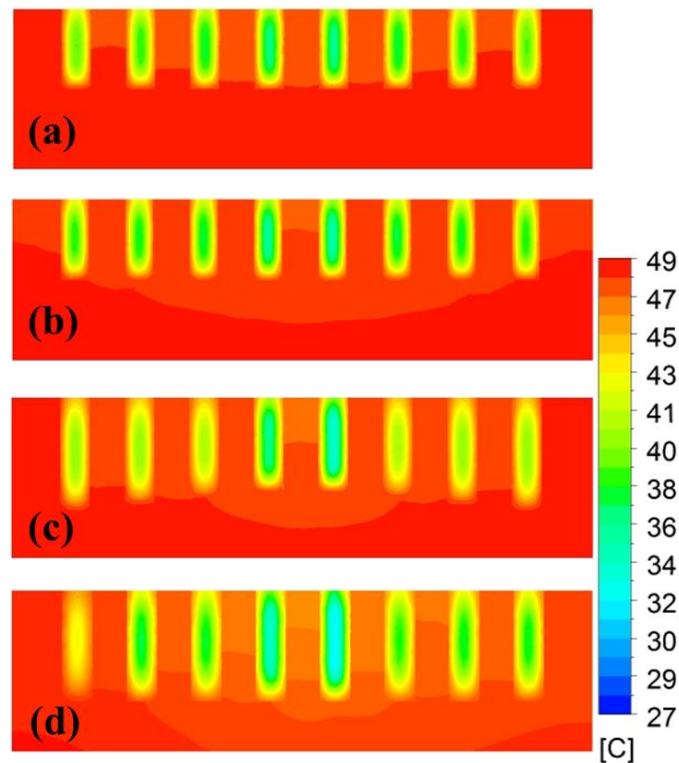


Figure 8.14 Y-Z plane temperature contours near the exit of the minichannel (a) Normal channel, (b) ribbed channel, (c) ribbed inclined, and (d) ribbed lifted.

Figure 8.14(a) shows the effect of cooling of parallel minichannel, the reduction in temperature is predominately observed near the channels and maximum temperature of the heat sink is not much influenced. Under the same channel the addition of ribs reduce the sink temperature, the maximum effect is seen at the central channel and extreme channels as shown in Figure 8.14 (b). In this case, temperature of the extreme channels has not decreased as that of central channels leaving extreme channels at higher temperature. It can be observed that the unique spillway configuration of minichannel reduced the extreme channels temperature to greater extent which is evident from Figure 8.14(c). Almost the entire channel region is maintained near 45°C and maximum temperature reduced for central channels. Figure 8.14(d) shows the temperature contour for submerged hydraulic jump spillway, with reduced temperature throughout the

cross-section including the base temperature. It should be noted that the temperature reduction at the central channels is nearly 43°C . Unlike the other channels, the submerged hydraulic jump develops recirculation in the drop section allowing the fluid to reduce the flow induced hotspot near the exit region of the minichannel.

Figure 8.15 shows that the temperature contour cross-section inside the minichannel. Figure 8.15(a) shows the normal parallel minichannel with increased thermal diffusion near the channel bed and not much variation is seen in fluid temperature along y direction.

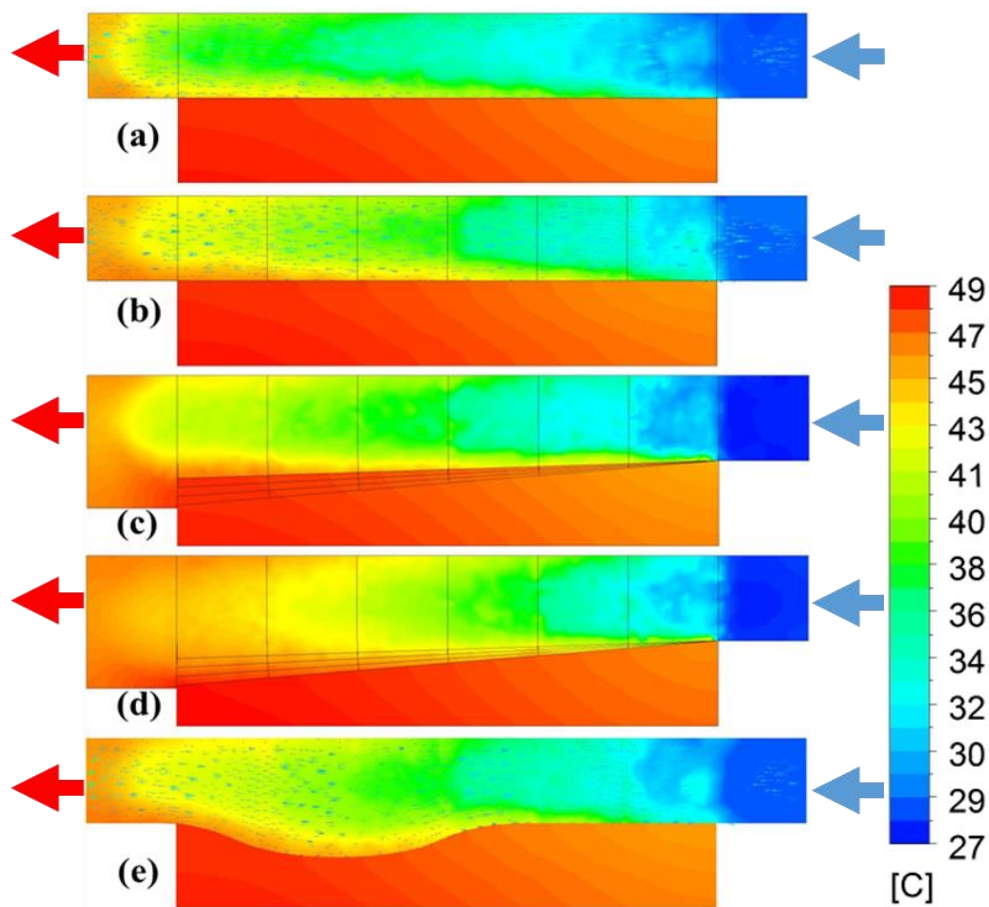


Figure 8.15 X-Z plane temperature contours for the entire length of minichannel (a) Normal channel, (b) Ribbed channel, (c) Ribbed inclined, (d) Ribbed inclined channel, and (e) Ribbed lifted.

Figure 8.15(b) shows the temperature contour for added ribs, which notably increases the mixing of fluid flow along the flow length. The ribs in the channels develops flow separation in main flow there by interrupting the thermal boundary layer. Figure 8.15(c, d) shows the temperature contour at central channels and at the extreme channels for a

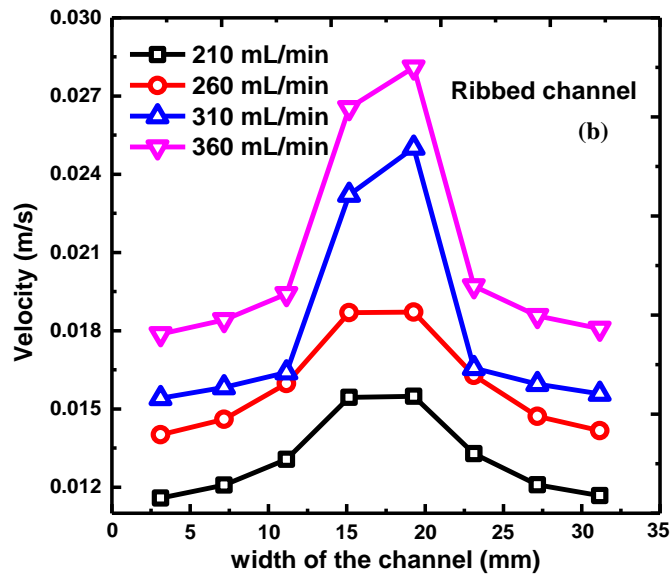
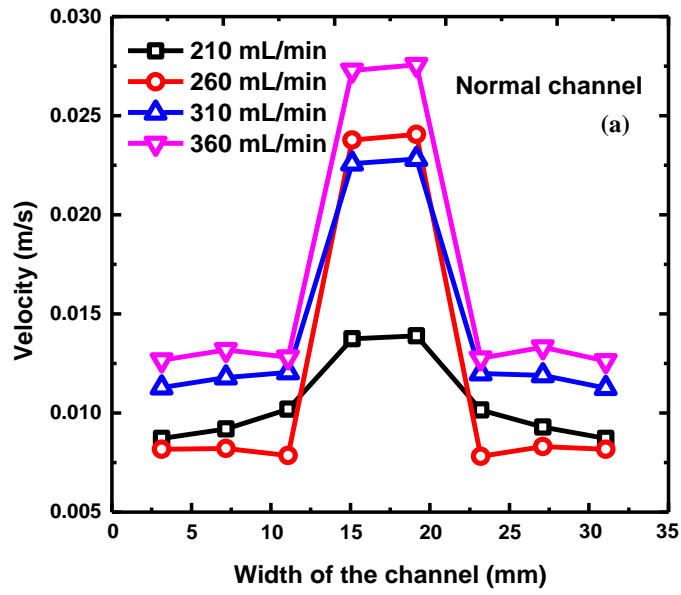
constant flow rate. From both the channels, it is observed that the extreme channels with 30° inclination carries higher outlet temperature with heat sink temperature decreasing as the angle of the spillway get increased.

Nevertheless in both the cases the chute spillways reduces the induced hotspots near the exit region, but the gravity enhanced fluid acceleration and interruption by fins increases the heat transfer. Figure 8.15(e) shows the temperature contour for submerged hydraulic jump model. The accelerated flow combined with recirculating currents towards the drop structure makes the submerged hydraulic model to carry maximum temperature from the sink.

8.6.3 Velocity study

For various channel designs, the comparisons of velocity distribution comparison among the minichannel for different flow rates is shown in Figure 8.16. The results indicate that for all the subjected models the maximum velocity is seen in the central channels and show more symmetrical distribution of velocity for all the flow rates. The maximum difference in velocity distribution is noticed for normal channels shown in Figure 8.16(a).

The velocity of the central channels reach up to 0.027 m/s for 360 mL/min, but the extreme channels have similar velocity nearing to 0.0125 m/s. This velocity deviation between central and extreme is found lesser for lower flow rate and much higher at increased flow rates. The addition of ribs in the channels considerably increased the velocity distribution in extreme channels shown, but the centerline channels has same velocity of 0.028m/s shown in Figure 8.16(b).



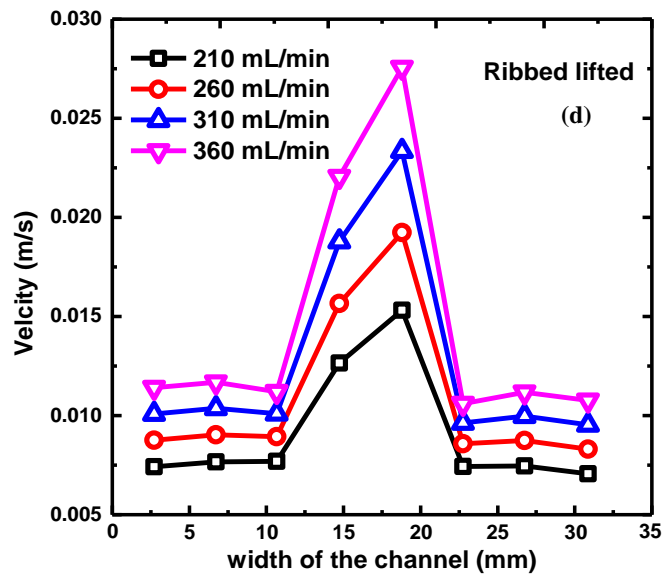
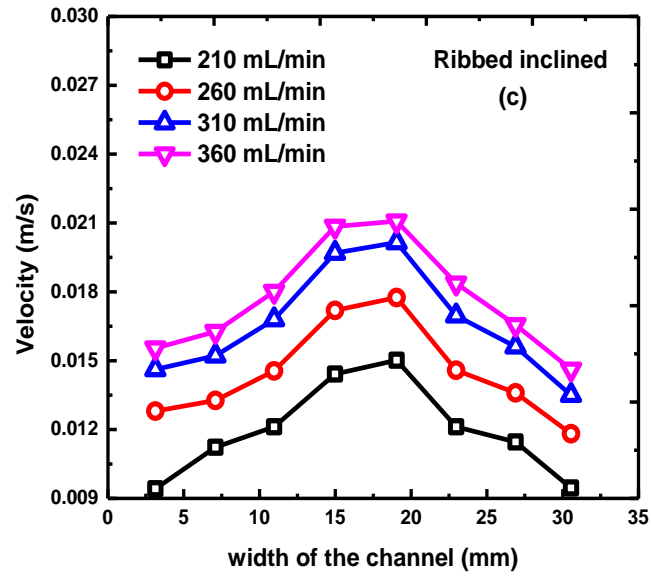


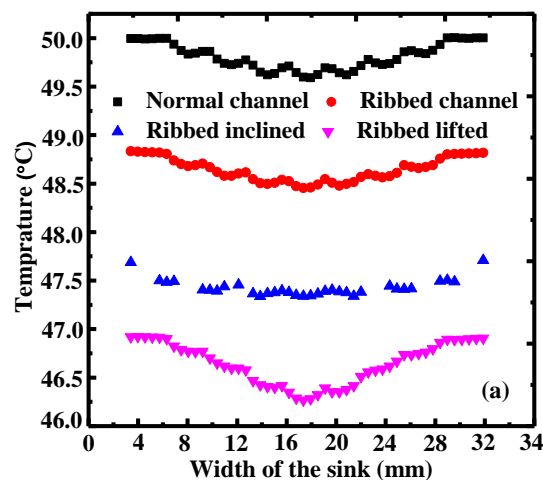
Figure 8.16 Velocity in minichannel for increased flow rate, (a) Normal channel, (b) ribbed channel, (c) ribbed inclined, and (d) ribbed lifted.

This is because the alternative ribs in the channels constrict the free flow of fluids in central channels, as a result the velocity in other channels has slightly increased. With the further addition of chute spillways, more significant distribution of velocity in channels are seen, presented in Figure 8.16(c). Moreover, the velocity of the centerline

channels reduced to a great extent by the combined effect of the flow ribs and fluid acceleration due to spillway channels. Similar results are not observed for hydraulic jump based spillway design, but instead a drastic difference in velocity distribution is seen among the channels. The reason is due to the huge momentum loss generated by the drop structure and additionally developed submerged hydraulic jump recirculation currents obstruct the normal flow velocities to a great extent. In the case of rib lifted the velocity distribution is same as that of the normal channels as shown in Figure 8.16(d).

8.6.4 Temperature distribution study

The temperature distribution in minichannel for different channel design near exit for different flow rates is presented in Figure 8.17. The measured temperature corresponds to the location reaching the entire width of the minichannel heat sink. This position is chosen to determine the maximum temperature distribution in width of the minichannel caused by flow maldistribution. Figure 8.17(a) shows the temperature distribution at a flow rate of 210 mL/min. the maximum temperature is seen for normal channel and the lowest for submerged hydraulic jump spillway case. The most uniform temperature distribution is observed for chute spillways. The entire width of the channel is prevailed with a temperature distribution of near 47°C, this trend is not seen in other designs. Similarly, decrease in temperatures were observed for all the subjected flow rates shown in Figures 8.17(b-d).



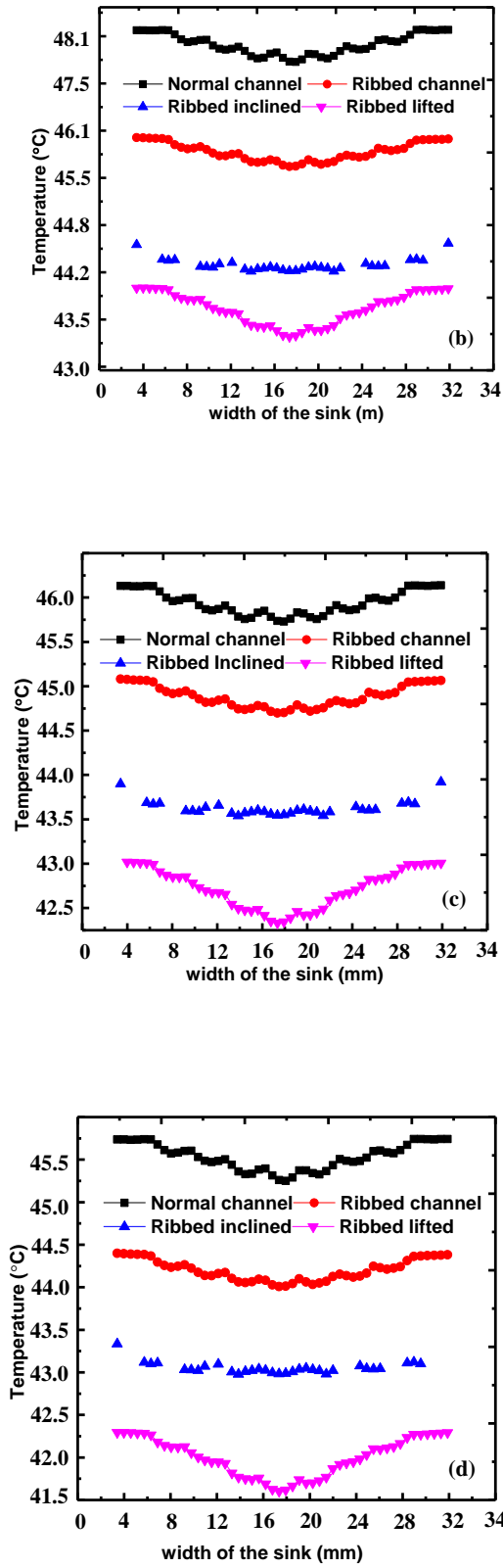


Figure 8.17 Temperature distribution in minichannel for different channel design near exit, (a) 210 mL/min, (b) 260 mL/min, (c) 310 mL/min, and (d) 360 mL/min.

It is very clear that comparatively the average temperature of the normal channels can be reduced with the spillway channels with the maximum peak temperature difference of 4°C.

Figure 8.18 shows the average microchannel temperature for all the different types of channel designs. The temperature at the central channels are comparatively lower than that of other channels. As discussed earlier the flow maldistribution effects develops the non-uniform temperature distribution in the minichannel. In all the cases the non-uniform temperature in channels is drastically lowered by using ribs, so that the temperature of the extreme channels reduces by 2°C. Further, decrease in temperature is provided by spillway channel design but the decrease in temperature is lower with comparison of that with added ribs.

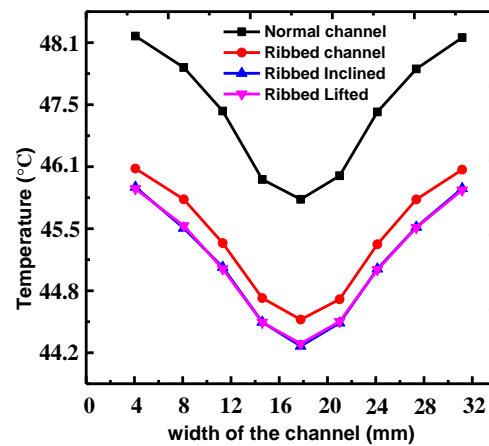


Figure 8.18 Temperature distribution along the width of the channel for different flow configurations.

Figure 8.19 presents the maximum base temperature as a function of flow rate for different channel configurations. The maximum base temperature was found for normal channels and on implementing ribs the sink base temperature reduced by 2°C. For the case of ribbed inclined and ribbed lifted the results were more or less same.

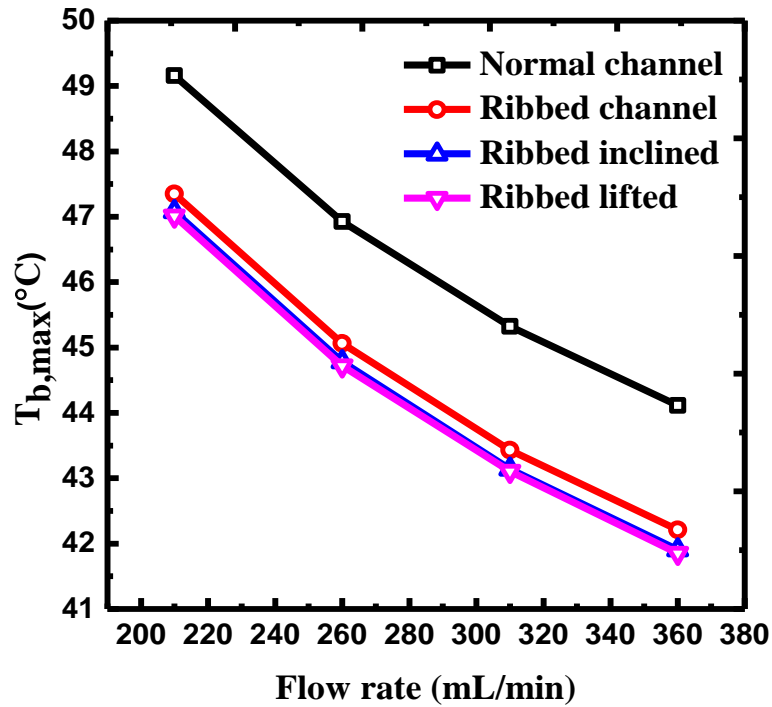


Figure 8.19 Maximum base temperature of the heat sink as a function of flow rate for different flow configuration.

8.7 CONCLUSIONS

In this study maldistribution characteristics of parallel minichannel heat sink is studied using water. The influence of ribs and flow structures in the parallel channel are elaborately discussed. From the combined experimental and numerical studies the following key findings are listed

- The inclined ribbed type based parallel channel developed reduced maldistribution. Compared to other inertial designs the velocity of the fluid at the extreme channels are high. Furthermore, the inclined channels reduced the maldistribution flow induced high temperature regions near the outlet.
- It was observed that the extreme channels with 30° inclination carries higher outlet temperature. The heat sink temperature kept on decreasing for higher angle of the spillway.

- On observing critically the effect of ribbed lifted type channels has more less similar flow distribution as that of normal channels. Better results were seen in the case of channel lifted type.
- The maldistribution influenced high temperature zones near the outlet of the channels was highly reduced for the case of inclined ribs channel that other flow modifications.

8.8 CLOSURE

This chapter dealt with the use of inertial minichannel heat sink for the reduction of maldistribution flow induced high temperature zones near the channel outlet. The parallel type minichannel is constructed experimentally and retained as a reference for the computationally modelled numerical flow structures. It was clear that the use of flow structures and inertial configuration has potential solution in reducing maldistribution based axial conduction with heat transfer enhancement.

CHAPTER 9

CONCLUSIONS

The thesis is directed towards establishing a successful method to treat the maldistribution induced high temperature zone developed in a parallel type channels. In this process several significant conjugate heat transfer characteristics were encountered and its nature is highly recurrent in many parallel type micro and macro channels. The microchannel part includes integrating thin copper heat spreader and a bulk heterogeneous aluminium block to investigate the influence of hotspot, interfacial material and nanofluid. The major achievement of this is the use of thin heat spreader to mitigate flow induced hotspot near the exit of the microchannel. In fact, heterogeneous integrated microchannel is used to observe the axial conduction based high temperature zones both numerically and experimentally. From this two integrated microchannel investigation it was clear that the flow induced high temperature zones in parallel channels are majorly due to maldistribution and axial conduction. To effectively tackle both the phenomenon parallel minichannel is experimented and used as a reference and 3D computational minichannel models with different inertial flow structures were used to reduce the maldistribution.

The thesis started with the introduction to the electronic cooling and microchannel. A brief introduction to the trade-offs in microchannel and its maldistribution flow effects were discussed in **Chapter 1**. The overview on the investigation of the integrated microchannel heat sink was explained with a sketch. Finally the organization of the thesis was presented. **Chapter 2** presented the literature review about the numerical and experimental techniques used in microchannel based electronic cooling and its observations. The experimental setup of the heat spreader integrated microchannel, heterogeneously integrated microchannel and minichannel heat sink were presented along with the various instruments used in **Chapter 3** with pictorial representation. **Chapter 4** discussed about the synthesis and characterization of the different nanofluid used in the experimental process.

Chapter 5 provided the approach of the heat spreader integrated microchannel used in the present work. The temperature distribution on the heat spreader was discussed from the point of hotspot and GO nanofluid. The heat transfer and friction factor investigations were highlighted. Hotspot migration in the heat spreader is explained for different nanofluid concentration and flow rates. It was found that the use of high thermal conductive fluids

reduces the parasitic heat loads to the neighboring components. The surrounding temperature prevailed near the heat sink reduces from 60°C to 42°C due to the microchannel heat sink and nanofluid. Further, the functionality of the heat spreader is highly effective at a low flow rates of 0.21-0.30 L/min, beyond which the presence of heat spreader is compromised. In **Chapter 6** investigation on temperature response effects in heat spreader integrated microchannel is presented. Theory and analysis of the temperature field propagation in the heat spreader is explained. A 3D computational model was considered to study the temperature superposition effects at different flow rates. Bulk diffusion study was proposed for high thermal conductivity nanofluid and its influence on heat spreader was qualitatively captured by experiments. Results clearly show that, the overall temperature of the heat sink increased by using higher volume fraction GO nanofluid. In case of higher Reynolds number the effect of increased heat sink temperature due to higher volume fraction has no notable effect. Apart from the fact that both microchannel and heat spreader is interfaced with silver, its effect is found negligible in the case of hotspot heat source.

Chapter 7 showed the numerical and experimental investigation of heterogeneous integrated microchannel to study the thermodynamic irreversibility and conjugate effects using TiO₂ nanofluid. A 3D computational domain is modelled and its credibility is proved with the repeated experimental results. The process began by validating the experimental setup with the benchmark heat transfer and friction factor equation of Shah and Hagen-Poiseuille. Later exergy and entropy analysis was considered to establish the relation between the thermal and frictional entropy generation using Bejan number. A numerical study based temperature contour for different nanofluid volume fraction was also provided. Most importantly the entrance effect was not only observed in the microchannel but also in the integrated region of the microchannel. Additionally, when the flow rate is increased temperature isotherms were parallel in aluminium block.

Finally, **Chapter 8** dealt with the investigation on inertial minichannel to mitigate flow maldistribution induced high temperature zones. An actual working workstation was used to perform experiments. The processor with different loading conditions were adopted for the investigation. Ribs were modelled in the parallel channels to enhance the mixing so that reduction in axial conduction is observed. Inertial type flow configurations were employed to reduce the uneven mass flux in the extreme channels. The combined effect of ribs and

inertial flow structures increase the average velocity of the fluid within the parallel channels. This inertial microchannel can be considered to be one of the significant flow configuration to reduce the maldistribution induced high temperature zones in parallel channels. The inclined ribbed type parallel channel developed reduced maldistribution. Compared to other inertial designs the velocity of the fluid at the extreme channels are high. Furthermore, the inclined channel reduced the maldistribution flow induced high temperature region near the outlet.

9.1 SCOPE FOR FUTURE WORK

1. The heat spreader integrated microchannel can be extended by incorporating micro heat pipes to dissipate heat from the heat spreader.
2. The influence of the heat spreader can be further enhanced by using the mini Phase change material at the circumference of the heat spreader.
3. Modelling the heterogeneous medium with several other thermal conductive materials to investigate the conjugate nature of the integrated domain.
4. The hotspot cores can be varied in accordance with the computational loads numerically and proportionally inlet flow can be modified to enhance the heat transfer.
5. Optimization studies in inertial minichannel can be performed by varying different rib structures and for high conductive nanofluid.

REFERENCES

- Abbassi, H., & Aghanajafi, C. (2006). "Evaluation of heat transfer augmentation in a nanofluid-cooled microchannel heat sink." *Journal of Fusion Energy*, 25(3-4), 187-196.
- Abdoli, A., Jimenez, G., & Dulikravich, G. S. (2015). "Thermo-fluid analysis of micro pin-fin array cooling configurations for high heat fluxes with a hot spot." *International Journal of Thermal Sciences*, 90, 290-297.
- Adewumi, O. O., Bello-Ochende, T., & Meyer, J. P. (2013). "Constructal design of combined microchannel and micro pin fins for electronic cooling." *International Journal of Heat and Mass Transfer*, 66, 315-323.
- Ahammed, N., Asirvatham, L. G., & Wongwises, S. (2016). "Entropy generation analysis of graphene–alumina hybrid nanofluid in multiport minichannel heat exchanger coupled with thermoelectric cooler". *International Journal of Heat and Mass Transfer*, 103, 1084-1097.
- Ahmed, H. E., Ahmed, M. I., Seder, I. M., & Salman, B. H. (2016). "Experimental investigation for sequential triangular double-layered microchannel heat sink with nanofluids." *International Communications in Heat and Mass Transfer*, 77, 104-115.
- Akbari, O. A., Khodabandeh, E., Kahbandeh, F., Toghraie, D., & Khalili, M. (2019). "Numerical investigation of heat transfer of nanofluid flow through a microchannel with heat sinks and sinusoidal cavities by using novel nozzle structure." *Journal of Thermal Analysis and Calorimetry*, 138(1), 737-752.
- Akbarinia, A., Abdolzadeh, M., & Laur, R. (2011). "Critical investigation of heat transfer enhancement using nanofluid in microchannels with slip and non-slip flow regimes." *Applied Thermal Engineering*, 31(4), 556-565.
- Alfarawi, S., Al-Dadah, R., & Mahmoud, S. (2017). "Transient investigation of mini-channel regenerative heat exchangers: Combined experimental and CFD approach." *Applied Thermal Engineering*, 125, 346-358.
- Al-Rashed, Abdullah AAA, Amin Shahsavar, Omid Rasooli, M. A. Moghimi, Arash Karimipour, and Minh Duc Tran. "Numerical assessment into the hydrothermal and entropy generation characteristics of biological water-silver nano-fluid in a wavy walled microchannel heat sink." *International Communications in Heat and Mass Transfer* 104 (2019): 118-126.
- Anoop, K., Sadr, R., Yu, J., Kang, S., Jeon, S., & Banerjee, D. (2012). "Experimental study of forced convective heat transfer of nanofluids in a microchannel." *International Communications in Heat and Mass Transfer*, 39(9), 1325-1330.
- Ansari, D., & Kim, K. Y. (2018). "Hotspot thermal management using a microchannel-pin fin hybrid heat sink." *International Journal of Thermal Sciences*, 134, 27-39.
- Antaki, Paul J. "New interpretation of non-Fourier heat conduction in processed meat." *J. Heat Transfer* 127, no. 2 (2005): 189-193.

- Baby, T. T., & Ramaprabhu, S. (2011). "Enhanced convective heat transfer using graphene dispersed nanofluids." *Nanoscale research letters*, 6(1), 289.
- Bahiraeei, Mehdi, and Saeed Heshmatian. "Application of a novel biological nanofluid in a liquid block heat sink for cooling of an electronic processor: thermal performance and irreversibility considerations." *Energy Conversion and Management* 149 (2017): 155-167.
- Bar-Cohen, A., & Wang, P. (2012). "Thermal management of on-chip hot spot." *Journal of Heat Transfer*, 134(5).
- Batchelor, G. K. (1977). "The effect of Brownian motion on the bulk stress in a suspension of spherical particles." *Journal of fluid mechanics*, 83(1), 97-117.
- Both, Soma, Balázs Czél, Tamás Fülöp, Gyula Gróf, Ákos Gyenis, Róbert Kovács, Peter Ván, and József Verhás. "Deviation from the Fourier law in room-temperature heat pulse experiments." *Journal of Non-Equilibrium Thermodynamics* 41, no. 1 (2016): 41-48.
- Brinda, R., Daniel, R. J., & Sumangala, K. (2012). "Ladder shape micro channels employed high performance micro cooling system for ULSI." *International Journal of Heat and Mass Transfer*, 55(13-14), 3400-3411.
- Brinkman, H. C. (1952). "The viscosity of concentrated suspensions and solutions." *The Journal of Chemical Physics*, 20(4), 571-571.
- Chai, L., Xia, G. D., & Wang, H. S. (2016). "Laminar flow and heat transfer characteristics of interrupted microchannel heat sink with ribs in the transverse micro chambers." *International Journal of Thermal Sciences*, 110, 1-11.
- Chai, L., Xia, G. D., & Wang, H. S. (2016). "Parametric study on thermal and hydraulic characteristics of laminar flow in microchannel heat sink with fan-shaped ribs on sidewalls—Part 2: Pressure drop." *International Journal of Heat and Mass Transfer*, 97, 1081-1090.
- Chai, L., Xia, G., Zhou, M., Li, J., & Qi, J. (2013). "Optimum thermal design of interrupted microchannel heat sink with rectangular ribs in the transverse micro chambers." *Applied Thermal Engineering*, 51(1-2), 880-889.
- Chen, J. K., Wang, T. S., & Zhou, X. (2017). "Full-chip thermal simulation of superconductor transition-edge sensor circuits". *IEEE Transactions on Applied Superconductivity*, 28(1), 1-11.
- Chen, Jun-Kang, Tian-Shun Wang, and Xingxiang Zhou. "Full-chip thermal simulation of superconductor transition-edge sensor circuits." *IEEE Transactions on Applied Superconductivity* 28, no. 1 (2017): 1-11.
- Chen, L., Yang, A., Xie, Z., & Sun, F. (2017). Constructal entropy generation rate minimization for cylindrical pin-fin heat sinks. *International Journal of Thermal Sciences*, 111, 168-174.
- Cheng, Xiao, and Huiying Wu. "Heat Transfer and Entropy Generation Analysis of Slit Pillar Array in Microchannels." *Journal of Heat Transfer* 142, no. 9 (2020): 092502.

Choi, S. U., & Eastman, J. A. (1995). "Enhancing thermal conductivity of fluids with nanoparticles (No. ANL/MSD/CP-84938; CONF-951135-29)." Argonne National Lab., IL (United States).

Conti, Alessandra, Giulio Lorenzini, and Yogesh Jaluria. "Transient conjugate heat transfer in straight microchannels." *International Journal of Heat and Mass Transfer* 55, no. 25-26 (2012): 7532-7543.

Datta, Aparesh, Dipankar Sanyal, Amit Agrawal, and Ajoy Kumar Das. (2019) "A review of liquid flow and heat transfer in microchannels with emphasis to electronic cooling." *Sādhanā* 44, no. 12: 1-32.

Drummond, K. P., Weibel, J. A., Garimella, S. V., Back, D., Janes, D. B., Sinanis, M. D., & Peroulis, D. (2016, May). "Evaporative intra chip hotspot cooling with a hierarchical manifold microchannel heat sink array." In 2016 15th IEEE Intersociety Conference on Thermal and Thermo mechanical Phenomena in Electronic Systems (ITherm) (pp. 307-315). IEEE.

Duangthongsuk, W., & Wongwises, S. (2009). "Measurement of temperature-dependent thermal conductivity and viscosity of TiO₂-water nanofluids." *Experimental thermal and fluid science*, 33(4), 706-714.

Duryodhan, V. S., Shiv Govind Singh, and Amit Agrawal. (2017) "Heat rate distribution in converging and diverging microchannel in presence of conjugate effect." *International Journal of Heat and Mass Transfer* 104: 1022-1033.

Ebrahimi, A., Rikhtegar, F., Sabaghan, A., & Roohi, E. (2016). "Heat transfer and entropy generation in a microchannel with longitudinal vortex generators using nanofluids." *Energy*, 101, 190-201.

Einstein, A. (1906). "A new determination of molecular dimensions." *Ann. Phys.*, 19, 289-306.

Faulkner, D. J., & Shekarriz, R. (2003, January). "Forced convective boiling in microchannels for kW/cm² electronics cooling." In ASME 2003 Heat Transfer Summer Conference (pp. 329-336). American Society of Mechanical Engineers Digital Collection.

Ghani, I. A., Kamaruzaman, N., & Sidik, N. A. C. (2017). "Heat transfer augmentation in a microchannel heat sink with sinusoidal cavities and rectangular ribs." *International Journal of Heat and Mass Transfer*, 108, 1969-1981.

Green, C., Fedorov, A. G., & Joshi, Y. K. (2009). "Fluid-to-fluid spot-to-spreader (F2/S2) hybrid heat sink for integrated chip-level and hot spot-level thermal management." *Journal of Electronic Packaging*, 131(2), 025002.

Hadad, Y., Ramakrishnan, B., Pejman, R., Rangarajan, S., Chiarot, P. R., Pattamatta, A., & Sammakia, B. (2019). "Three-objective shape optimization and parametric study of a micro-channel heat sink with discrete non-uniform heat flux boundary conditions." *Applied Thermal Engineering*, 150, 720-737.

- Hamilton, R. L., & Crosser, O. K. (1962). "Thermal conductivity of heterogeneous two-component systems." *Industrial & Engineering chemistry fundamentals*, 1(3), 187-191.
- Han, X., Fedorov, A., & Joshi, Y. (2016). "Flow boiling in microgaps for thermal management of high heat flux microsystems." *Journal of Electronic Packaging*, 138(4), 040801.
- Han, Y., Lau, B. L., Tang, G., & Zhang, X. (2015). "Thermal management of hotspots using diamond heat spreader on Si micro cooler for GaN devices." *IEEE Transactions on Components, Packaging and Manufacturing Technology*, 5(12), 1740-1746.
- He, Y., Jin, Y., Chen, H., Ding, Y., Cang, D., & Lu, H. (2007). "Heat transfer and flow behaviour of aqueous suspensions of TiO₂ nanoparticles (nanofluids) flowing upward through a vertical pipe." *International journal of heat and mass transfer*, 50(11-12), 2272-2281.
- Hekmatipour, F., Jalali, M., Hekmatipour, F., Akhavan-Behabadi, M. A., & Sajadi, B. (2019). "On the convection heat transfer and pressure drop of copper oxide-heat transfer oil Nanofluid in inclined micro fin pipe." *Heat and Mass Transfer*, 55(2), 433-444.
- Herwig, H., and K. Beckert. "Experimental evidence about the controversy concerning Fourier or non-Fourier heat conduction in materials with a nonhomogeneous inner structure." *Heat and Mass Transfer* 36, no. 5 (2000): 387-392.
- Heshmatian, S., & Bahiraei, M. (2017). "Numerical investigation of entropy generation to predict irreversibilities in nanofluid flow within a microchannel: effects of Brownian diffusion, shear rate and viscosity gradient." *Chemical Engineering Science*, 172, 52-65.
- Heshmatian, Saeed, Mehdi Bahiraei, and Mohammad Amani. "Modeling of irreversibility factors for nanofluid flow in different channels regarding nanoparticle arrangement." *Journal of Thermal Analysis and Calorimetry* 137, no. 2 (2019): 607-622.
- Hummers Jr, W. S., & Offeman, R. E. (1958). "Preparation of graphitic oxide. *Journal of the american chemical society*." 80(6), 1339-1339.
- Izadi, M., Behzadmehr, A., & Jalali-Vahida, D. (2009). "Numerical study of developing laminar forced convection of a nanofluid in an annulus." *International journal of thermal sciences*, 48(11), 2119-2129.
- Jung, J. Y., Oh, H. S., & Kwak, H. Y. (2009). "Forced convective heat transfer of nanofluids in microchannels." *International journal of heat and mass transfer*, 52(1-2), 466-472.
- Kalteh, M., Abbassi, A., Saffar-Avval, M., & Harting, J. (2011). "Eulerian–Eulerian two-phase numerical simulation of nanofluid laminar forced convection in a microchannel." *International journal of heat and fluid flow*, 32(1), 107-116.
- Kandlikar, S. G. (2005). "High flux heat removal with microchannels—a roadmap of challenges and opportunities." *Heat Transfer Engineering*, 26(8), 5-14.

- Karami, M., Shirani, E., & Avara, A. (2012). "Analysis of entropy generation, pumping power, and tube wall temperature in aqueous suspensions of alumina particles." *Heat Transfer Research*, 43(4).
- Kelly, B., Hayashi, Y., & Kim, Y. J. (2018). "Novel radial pulsating heat-pipe for high heat-flux thermal spreading." *International Journal of Heat and Mass Transfer*, 121, 97-106.
- Kewalramani, Gagan V., Gaurav Hedau, Sandip K. Saha, and Amit Agrawal. "Study of laminar single phase frictional factor and Nusselt number in In-line micro pin-fin heat sink for electronic cooling applications." *International Journal of Heat and Mass Transfer* 138 (2019): 796-808.
- Khoshvaght-Aliabadi, M., Hassani, S. M., & Mazloumi, S. H. (2017). "Enhancement of laminar forced convection cooling in wavy heat sink with rectangular ribs and Al₂O₃/water nanofluid." *Experimental Thermal and Fluid Science*, 89, 199-210.
- Khosravi, Raouf, Saeed Rabiei, Mehdi Bahiraei, and Ali Reza Teymourtash. "Predicting entropy generation of a hybrid nanofluid containing graphene-platinum nanoparticles through a microchannel liquid block using neural networks." *International Communications in Heat and Mass Transfer* 109 (2019): 104351.
- Koo, J., & Kleinstreuer, C. (2004). "A new thermal conductivity model for nanofluids." *Journal of Nanoparticle Research*, 6(6), 577-588.
- Kovács, Róbert, and Péter Ván. "Thermodynamical consistency of the dual-phase-lag heat conduction equation." *Continuum Mechanics and Thermodynamics* 30, no. 6 (2018): 1223-1230.
- Kumar, P. (2019). "Numerical investigation of fluid flow and heat transfer in trapezoidal microchannel with groove structure." *International Journal of Thermal Sciences*, 136, 33-43.
- Kundu, Balaram, Ranjan Das, Pramod A. Wankhade, and Kwan-Soo Lee. "Heat transfer improvement of a wet fin under transient response with a unique design arrangement aspect." *International Journal of Heat and Mass Transfer* 127 (2018): 1239-1251.
- Lee, D. H., Kim, S., Kim, H., & Lee, S. K. (2019). "Highly Efficient and Highly Conductive Phosphor-in-Glass Materials for Use in LD-Driven White-Light Lamp." *International Journal of Precision Engineering and Manufacturing-Green Technology*, 6(2), 293-303.
- Lee, Y. J., Lee, P. S., & Chou, S. K. (2012). "Enhanced thermal transport in microchannel using oblique fins." *Journal of Heat Transfer*, 134(10), 101901.
- Lee, Y. J., Singh, P. K., & Lee, P. S. (2015). "Fluid flow and heat transfer investigations on enhanced microchannel heat sink using oblique fins with parametric study." *International Journal of Heat and Mass Transfer*, 81, 325-336.
- Leong, K. Y., Saidur, R., Mahlia, T. M. I., & Yau, Y. H. (2012). "Entropy generation analysis of nanofluid flow in a circular tube subjected to constant wall temperature." *International Communications in Heat and Mass Transfer*, 39(8), 1169-1175.

- Li, F., Zhu, W., & He, H. (2019). "Numerical optimization on microchannel flow and heat transfer performance based on field synergy principle." *International Journal of Heat and Mass Transfer*, 130, 375-385.
- Li, J., & Kleinstreuer, C. (2008). "Thermal performance of nanofluid flow in microchannels." *International Journal of Heat and Fluid Flow*, 29(4), 1221-1232.
- Li, J., & Kleinstreuer, C. (2010). Entropy generation analysis for nanofluid flow in microchannels. *Journal of Heat Transfer*, 132(12).
- Li, Ping, Dingzhang Guo, and Xinyue Huang. "Heat transfer enhancement, entropy generation and temperature uniformity analyses of shark-skin bionic modified microchannel heat sink." *International Journal of Heat and Mass Transfer* 146 (2020): 118846.
- Li, Y., Zhang, F., Sunden, B., & Xie, G. (2014). "Laminar thermal performance of microchannel heat sinks with constructal vertical Y-shaped bifurcation plates." *Applied Thermal Engineering*, 73(1), 185-195.
- Li, Z., Tao, W. Q., & He, Y. L. (2005, January). "A numerical study of laminar convective heat transfer in microchannel with non-circular cross-section." In *ASME 3rd International Conference on Microchannels and Minichannels* (pp. 351-360). American Society of Mechanical Engineers.
- Lin, X., Mo, S., Jia, L., Yang, Z., Chen, Y., & Cheng, Z. (2019). "Experimental study and Taguchi analysis on LED cooling by thermoelectric cooler integrated with microchannel heat sink." *Applied Energy*, 242, 232-238.
- Liu, Lin, Liancun Zheng, Fawang Liu, and Xinxin Zhang. "An improved heat conduction model with Riesz fractional Cattaneo–Christov flux." *International Journal of Heat and Mass Transfer* 103 (2016): 1191-1197.
- Liu, M., Liu, D., Xu, S., & Chen, Y. (2011). "Experimental study on liquid flow and heat transfer in Micro Square pin fin heat sink." *International Journal of Heat and Mass Transfer*, 54(25-26), 5602-5611.
- Li, Z., Shahsavari, A., Niazi, K., Al-Rashed, A. A., & Rostami, S. (2020). Numerical assessment on the hydrothermal behavior and irreversibility of MgO-Ag/water hybrid nanofluid flow through a sinusoidal hairpin heat-exchanger. *International Communications in Heat and Mass Transfer*, 115, 104628.
- Lorenzini, D., & Joshi, Y. (2016, May). "CFD study of flow boiling in silicon micro gaps with staggered pin fins for the 3D-stacking of ICs." In *2016 15th IEEE Intersociety Conference on Thermal and Thermo mechanical Phenomena in Electronic Systems (ITherm)* (pp. 766-773). IEEE.
- Maganti, L. S., Dhar, P., Sundararajan, T., & Das, S. K. (2017). "Heat spreader with parallel microchannel configurations employing nanofluid for near-active cooling of MEMS." *International Journal of Heat and Mass Transfer*, 111, 570-581.

Mamand S. M., (2021). "Thermal conductivity calculation for nanoparticle embedded in a base fluid". *Applied Science*, 11(4), 1459.

Manay, E., & Sahin, B. (2017). "Heat transfer and pressure drop of nanofluids in a microchannel heat sink." *Heat Transfer Engineering*, 38(5), 510-522.

Manay, E., Akyürek, E. F., & Sahin, B. (2018). Entropy generation of nanofluid flow in a microchannel heat sink. *Results in Physics*, 9, 615-624.

Maranzana, G., Perry, I., & Maillet, D. (2004). "Mini-and micro-channels: influence of axial conduction in the walls." *International journal of heat and mass transfer*, 47(17-18), 3993-4004.

Mehta, B., & Khandekar, S. (2015). "Local experimental heat transfer of single-phase pulsating laminar flow in a square mini-channel." *International Journal of Thermal Sciences*, 91, 157-166.

Mirzaei, M., & Azimi, A. (2016). "Heat transfer and pressure drop characteristics of graphene oxide/water nanofluid in a circular tube fitted with wire coil insert." *Experimental heat transfer*, 29(2), 173-187.

Mitra, K., S. Kumar, A. Vedevarz, and M. K. Moallemi. "Experimental evidence of hyperbolic heat conduction in processed meat." (1995): 568-573.

Moghaddami, M., Mohammadzade, A., & Esfehiani, S. A. V. (2011). "Second law analysis of nanofluid flow." *Energy Conversion and Management*, 52(2), 1397-1405.

Mohammadian, S. K., & Zhang, Y. (2014). "Analysis of nanofluid effects on thermoelectric cooling by micro-pin-fin heat exchangers." *Applied Thermal Engineering*, 70(1), 282-290.

Moharana, M. K., Agarwal, G., & Khandekar, S. (2011). "Axial conduction in single-phase simultaneously developing flow in a rectangular mini-channel array." *International Journal of Thermal Sciences*, 50(6), 1001-1012.

Moraveji, M. K., Barzegarian, R., Bahiraei, M., Barzegarian, M., Aloueyan, A., & Wongwises, S. (2019). "Numerical evaluation on thermal-hydraulic characteristics of dilute heat-dissipating nanofluids flow in microchannels." *Journal of Thermal Analysis and Calorimetry*, 135(1), 671-683.

Narayanan, S., Fedorov, A. G., & Joshi, Y. K. (2010). "On-chip thermal management of hotspots using a perspiration nanopatch." *Journal of micromechanics and micro engineering*, 20(7), 075010.

Nimmagadda, R., & Venkatasubbaiah, K. (2015). "Conjugate heat transfer analysis of micro-channel using novel hybrid nanofluids ($Al_2O_3 + Ag/Water$)." *European Journal of Mechanics-B/Fluids*, 52, 19-27.

Ozguc, S., Pai, S., Pan, L., Geoghegan, P. J., & Weibel, J. A. (2019, May). "Experimental Demonstration of an Additively Manufactured Vapor Chamber Heat Spreader." In 2019 18th IEEE Intersociety Conference on Thermal and Thermo mechanical Phenomena in Electronic Systems (ITherm) (pp. 416-422). IEEE.

- Pak, B. C., & Cho, Y. I. (1998). "Hydrodynamic and heat transfer study of dispersed fluids with submicron metallic oxide particles." *Experimental Heat Transfer an International Journal*, 11(2), 151-170.
- Pak, B. C., & Cho, Y. I. (1998). "Hydrodynamic and heat transfer study of dispersed fluids with submicron metallic oxide particles." *Experimental Heat Transfer an International Journal*, 11(2), 151-170.
- Peng, X. F., & Peterson, G. P. (1996). "Convective heat transfer and flow friction for water flow in microchannel structures." *International journal of heat and mass transfer*, 39(12), 2599-2608.
- Peng, X. F., Wang, B. X., Peterson, G. P., & Ma, H. B. (1995). "Experimental investigation of heat transfer in flat plates with rectangular microchannels." *International Journal of Heat and Mass Transfer*, 38(1), 127-137.
- Peyghambarzadeh, S. M., Hashemabadi, S. H., Chabi, A. R., & Salimi, M. (2014). "Performance of water based CuO and Al₂O₃ nanofluids in a Cu-Be alloy heat sink with rectangular microchannels." *Energy conversion and management*, 86, 28-38.
- Pi, Y., Chen, J., Miao, M., Jin, Y., & Wang, W. (2018). "A fast and accurate temperature prediction method for microfluidic cooling with multiple distributed hotspots." *International Journal of Heat and Mass Transfer*, 127, 1223-1232.
- Qu, W., Mala, G. M., & Li, D. (2000). "Heat transfer for water flow in trapezoidal silicon microchannels." *International Journal of Heat and Mass Transfer*, 43(21), 3925-3936.
- Rimbault, B., Nguyen, C. T., & Galanis, N. (2014). "Experimental investigation of CuO-water nanofluid flow and heat transfer inside a microchannel heat sink." *International Journal of Thermal Sciences*, 84, 275-292.
- Roetzel, Wilfried, Nandy Putra, and Sarit K. Das. "Experiment and analysis for non-Fourier conduction in materials with non-homogeneous inner structure." *International Journal of Thermal Sciences* 42, no. 6 (2003): 541-552.
- Rowlette, Jeremy A., and Kenneth E. Goodson. "Fully coupled nonequilibrium electron-phonon transport in nanometer-scale silicon fets." *IEEE Transactions on Electron Devices* 55, no. 1 (2007): 220-232.
- Rubin, M. B. "Hyperbolic heat conduction and the second law." *International Journal of Engineering Science* 30, no. 11 (1992): 1665-1676.
- Sabaghan, A., Edalatpour, M., Moghadam, M. C., Roohi, E., & Niazmand, H. (2016). "Nanofluid flow and heat transfer in a microchannel with longitudinal vortex generators: two-phase numerical simulation." *Applied Thermal Engineering*, 100, 179-189.
- Said, Z., Sabiha, M. A., Saidur, R., Hepbasli, A., Rahim, N. A., Mekhilef, S., & Ward, T. A. (2015). "Performance enhancement of a flat plate solar collector using titanium dioxide nanofluid and polyethylene glycol dispersant." *Journal of Cleaner Production*, 92, 343-353.

Samal, Sangram Kumar, and Manoj Kumar Moharana. "Thermo-hydraulic and entropy generation analysis of recharging microchannel using water-based graphene–silver hybrid nanofluid." *Journal of Thermal Analysis and Calorimetry* 143, no. 6 (2021): 4131-4148.

Sarkar, S., Ganguly, S., & Dalal, A. (2012). "Analysis of entropy generation during mixed convective heat transfer of nanofluids past a square cylinder in vertically upward flow." *Journal of Heat Transfer*, 134(12), 122501.

Shafeie, H., Abouali, O., Jafarpur, K., & Ahmadi, G. (2013). "Numerical study of heat transfer performance of single-phase heat sinks with micro pin-fin structures." *Applied Thermal Engineering*, 58(1-2), 68-76.

Shah, R. K. (1975, December). "Thermal entry length solutions for the circular tube and parallel plates." In *Third national heat mass transfer conference*, Indian Institute of Technology, Bombay, India (Vol. 1, pp. 11-75).

Sharma, C. S., Tiwari, M. K., & Poulikakos, D. (2016). "A simplified approach to hotspot alleviation in microprocessors." *Applied Thermal Engineering*, 93, 1314-1323.

Sharma, H., Gaddam, A., Agrawal, A., Joshi, S. S., & Dimov, S. S. (2020). "Influence of texture shape and arrangement on thermo-hydraulic performance of the textured microchannels." *International Journal of Thermal Sciences*, 147, 106146.

Shen, H., Xie, G., & Wang, C. C. (2019). "The numerical simulation with staggered alternation locations and multi-flow directions on the thermal performance of double-layer microchannel heat sinks." *Applied Thermal Engineering*, 163, 114332.

Shen, Han, Gongnan Xie, and Chi-Chuan Wang. "Thermal performance and entropy generation of novel X-structured double layered microchannel heat sinks." *Journal of the Taiwan Institute of Chemical Engineers* 111 (2020): 90-104.

Siddique, Ayyaz, Bhaskar J. Medhi, Amit Agrawal, Anugrah Singh, and Sandip K. Saha. (2017) "Design of a collector shape for uniform flow distribution in microchannels." *Journal of Micromechanics and Micro engineering* 27, no. 7: 075026.

Sindhu, S., and B. J. Gireesha. "Entropy generation analysis of hybrid nanofluid in a microchannel with slip flow, convective boundary and nonlinear heat flux." *International Journal of Numerical Methods for Heat & Fluid Flow* (2020).

Singh, Shiv Govind, Amit Agrawal, and Siddhartha P. Duttagupta. (2011) "Reliable MOSFET operation using two-phase microfluidics in the presence of high heat flux transients." *Journal of Micromechanics and Micro engineering* 21, no. 10: 105002.

Singh, Shiv Govind, Siddhartha P. Duttagupta, and Amit Agrawal. (2009) "In situ impact analysis of very high heat flux transients on nonlinear pn diode characteristics and mitigation using on-chip single-and two-phase microfluidics." *Journal of Micro electromechanical Systems* 18, no. 6: 1208-1219.

Singh, P. K., Anoop, K. B., Sundararajan, T., & Das, S. K. (2010). Entropy generation due to flow and heat transfer in nanofluids. *International Journal of Heat and Mass Transfer*, 53(21-22), 4757-4767.

- Sirisha Maganti, L., Dhar, P., Sundararajan, T., & Das, S. K. (2017). "Selecting optimal parallel microchannel configuration (s) for active hot spot mitigation of multicore microprocessors in real time." *Journal of Heat Transfer*, 139(10).
- Sohel, M. R., Saidur, R., Hassan, N. H., Elias, M. M., Khaleduzzaman, S. S., & Mahbubul, I. M. (2013). Analysis of entropy generation using nanofluid flow through the circular microchannel and minichannel heat sink. *International Communications in Heat and Mass Transfer*, 46, 85-91.
- Snoussi, L., Ouerfelli, N., Sharma, K. V., Vrinceanu, N., Chamkha, A. J., & Guizani, A. (2018). "Numerical simulation of nanofluids for improved cooling efficiency in a 3D copper microchannel heat sink (MCHS)." *Physics and Chemistry of Liquids*, 56(3), 311-331.
- Soliman, A. M., & Hassan, H. (2019). "Effect of heat spreader size, microchannel configuration and nanoparticles on the performance of PV-heat spreader-microchannels system." *Solar Energy*, 182, 286-297.
- Soliman, A. M., Hassan, H., Ahmed, M., & Ookawara, S. (2020). "A 3d model of the effect of using heat spreader on the performance of photovoltaic panel (PV)." *Mathematics and Computers in Simulation*, 167, 78-91.
- Sreejesh, M., Dhanush, S., Rossignol, F., & Nagaraja, H. S. (2017). "Microwave assisted synthesis of rGO/ZnO composites for non-enzymatic glucose sensing and supercapacitor applications." *Ceramics International*, 43(6), 4895-4903.
- Sverdrup, P. G., S. Sinha, M. Asheghi, S. Uma, and K. E. Goodson. "Measurement of ballistic phonon conduction near hotspots in silicon." *Applied Physics Letters* 78, no. 21 (2001): 3331-3333.
- Tian, B., Yang, D., Ma, H., Xu, J., & Liang, D. (2019). "A manufacturing method of integrated ceramic heat spreaders embedded with interconnected microchannels." *Materials & Design*, 107969.
- Tokit, E. M., Mohammed, H. A., & Yusoff, M. Z. (2012). "Thermal performance of optimized interrupted microchannel heat sink (IMCHS) using nanofluid." *International Communications in Heat and Mass Transfer*, 39(10), 1595-1604.
- Tsai, T. H., & Chein, R. (2007). "Performance analysis of nanofluid-cooled microchannel heat sinks." *International Journal of Heat and Fluid Flow*, 28(5), 1013-1026.
- Tuckerman, D. B., & Pease, R. F. W. (1981). "High-performance heat sinking for VLSI." *IEEE Electron device letters*, 2(5), 126-129.
- Tullius, J. F., Vajtai, R., & Bayazitoglu, Y. (2011). "A review of cooling in microchannels." *Heat Transfer Engineering*, 32(7-8), 527-541.
- Vinodhan, V. L., & Rajan, K. S. (2014). "Computational analysis of new microchannel heat sink configurations." *Energy conversion and Management*, 86, 595-604.

- Vinoth, R., & Kumar, D. S. (2017). "Channel cross section effect on heat transfer performance of oblique finned microchannel heat sink." *International Communications in Heat and Mass Transfer*, 87, 270-276.
- Wang, B. X., & Peng, X. F. (1994). "Experimental investigation on liquid forced-convection heat transfer through microchannels." *International Journal of Heat and Mass Transfer*, 37, 73-82.
- Wang, P., Yang, B., & Bar-Cohen, A. (2009). "Mini-contact enhanced thermoelectric coolers for on-chip hot spot cooling." *Heat Transfer Engineering*, 30(9), 736-743.
- Wang, R. J., Wang, J. W., Lijin, B. Q., & Zhu, Z. F. (2018). "Parameterization investigation on the microchannel heat sink with slant rectangular ribs by numerical simulation." *Applied Thermal Engineering*, 133, 428-438.
- Wong, K. C., & Lee, J. H. (2015). "Investigation of thermal performance of microchannel heat sink with triangular ribs in the transverse micro chambers." *International Communications in Heat and Mass Transfer*, 65, 103-110.
- Xia, G. D., Liu, R., Wang, J., & Du, M. (2016). "The characteristics of convective heat transfer in microchannel heat sinks using Al₂O₃ and TiO₂ nanofluids." *International Communications in Heat and Mass Transfer*, 76, 256-264.
- Xie, G., Zhang, F., Sundén, B., & Zhang, W. (2014). "Constructal design and thermal analysis of microchannel heat sinks with multistage bifurcations in single-phase liquid flow." *Applied thermal engineering*, 62(2), 791-802.
- Xu, Jun, and Xinwei Wang. "Simulation of ballistic and non-Fourier thermal transport in ultra-fast laser heating." *Physica B: Condensed Matter* 351, no. 1-2 (2004): 213-226.
- Xuan, Y., & Roetzel, W. (2000). "Conceptions for heat transfer correlation of nanofluids." *International Journal of heat and Mass transfer*, 43(19), 3701-3707.
- Xie, Y., Zheng, L., Zhang, D., & Xie, G. (2016). "Entropy generation and heat transfer performances of Al₂O₃-water nanofluid transitional flow in rectangular channels with dimples and protrusions". *Entropy*, 18(4), 148.
- Yang, A., Chen, L., Xie, Z., Feng, H., & Sun, F. (2016). "Constructal heat transfer rate maximization for cylindrical pin-fin heat sinks." *Applied Thermal Engineering*, 108, 427-435.
- Yang, D., Jin, Z., Wang, Y., Ding, G., & Wang, G. (2017). "Heat removal capacity of laminar coolant flow in a micro channel heat sink with different pin fins." *International Journal of Heat and Mass Transfer*, 113, 366-372.
- Zhang, H., Shao, S., Xu, H., & Tian, C. (2013). "Heat transfer and flow features of Al₂O₃-water nanofluids flowing through a circular microchannel-Experimental results and correlations." *Applied Thermal Engineering*, 61(2), 86-92.

Zhang, Jingru, Tiantian Zhang, Shaurya Prakash, and Yogesh Jaluria. "Experimental and numerical study of transient electronic chip cooling by liquid flow in microchannel heat sinks." *Numerical Heat Transfer, Part A: Applications* 65, no. 7 (2014): 627-643.

Zhang, R., Hodes, M., Lower, N., & Wilcoxon, R. (2015). "Water-Based Microchannel and Galinstan-Based Minichannel Cooling beyond 1 kW/cm² Heat Flux." *IEEE Transactions on Components, Packaging and Manufacturing Technology*, 5(6), 762-770.

Zhao, J., Huang, S., Gong, L., & Huang, Z. (2016). "Numerical study and optimizing on micro square pin-fin heat sink for electronic cooling." *Applied Thermal Engineering*, 93, 1347-1359.

LIST OF PUBLICATIONS

INTERNATIONAL JOURNALS

1. **Narendran, G.**, Gnanasekaran, N., & Perumal, D. A. (2018). A review on recent advances in microchannel heat sink configurations. *Recent Patents on Mechanical Engineering*, 11(3), 190-215.
DOI: <https://doi.org/10.2174/2212797611666180726124047>. (Scopus)
2. **Narendran, G.**, Gnanasekaran, N., & Arumuga Perumal, D. (2019). Experimental Investigation on Heat Spreader Integrated Microchannel Using Graphene Oxide Nanofluid. *Heat Transfer Engineering*, 41(14). 1252-1274.
DOI: <https://doi.org/10.1080/01457632.2019.1637136>. (SCI, IF- 2.172)
3. **Narendran, G.**, Gnanasekaran, N., & Perumal, D. A. (2019). Thermodynamic irreversibility and conjugate effects of integrated microchannel cooling device using TiO₂ nanofluid. *Heat and Mass Transfer*, 56(2), 489-505.
DOI: <https://doi.org/10.1007/s00231-019-02704-z>. (SCI, IF-2.464)
4. **Narendran, G.**, Bhat, M. M., Akshay, L., & Perumal, D. A. (2018). Experimental analysis on exergy studies of flow through a minichannel using Tio₂/Water nanofluids. *Thermal Science and Engineering Progress*, 8, 93-104.
DOI: <https://doi.org/10.1016/j.tsep.2018.08.007>. (SCIE, IF- 4.946)
5. **Narendran, G.**, Gnanasekaran, N., & Perumal, D. A. A multiphysics approach for effective thermal management in a hetrogenous microchannel heat sink employing nanofluid. *Journal of heat transfer*, (Received comments). (SCI, IF-2.021)

INTERNATIONAL CONFERENCES

1. **Narendran, G.**, Gnanasekaran, N., & Perumal, D. A. (2019, March). Migration of flow inducted hotspot with heat spreader integrated microchannel subjected to asymmetric heat flux: A Multiphysics approach. In 2019 20th International Conference on Thermal, Mechanical and Multi-Physics Simulation and Experiments in Microelectronics and Microsystems (EuroSimE) (pp. 1-7). IEEE (Scopus).
2. **Narendran, G.**, Gnanasekaran, N., & Perumal, D. A. (2018). Flow induced hotspot migration studies with heat spreader integrated microchannels using reduced graphene oxide nanofluid. In 2018 19th International Conference on Thermal,

Mechanical and Multi-Physics Simulation and Experiments in Microelectronics and Microsystems (EuroSimE) (pp. 1-10). IEEE (Scopus).

3. **Narendran, G.**, Gnanasekaran, N., & Perumal, D. A. (2017). Numerical analysis of graphene nanofluid in microscale heat sink combined with heat spreader – a holistic approach for effective packaging. In 2017 6th Asian Symposium on Computational heat transfer and fluid flow, Dec 10- 13, Indian Institute of Technology, Madras, India.
4. **Narendran, G.**, Gnanasekaran, N., & Perumal, D. A. (2018) Experimental and numerical investigation on conjugate effects in deep parallel microchannels using TiO₂ nanofluid for electronic cooling. Fifth International Conference on Computational Methods for Thermal Problems (THERMACOMP 2018), July 09-11, 2018, IISc Bangalore, India (Scopus).
5. **Narendran, G.**, Gnanasekaran, N., & Perumal, D. A. (2019) Hydrodynamic Performance of Graphene Oxide Nanofluid in Heat Spreader Integrated Microchannel. In 12th, International Conference on thermal engineering: theory and applications, Feb 23-26, 2019, Gujarat, India.
6. Kumar, A., **Narendran, G.**, & Perumal, D. A. (2018, June). Entropy generation study of TiO₂ nanofluid in microchannel heat sink for Electronic cooling application. In IOP Conference Series: Materials Science and Engineering (Vol. 376, No. 1, p. 012013). IOP Publishing (Scopus).
7. Hegde, S. S., **Narendran, G.**, & Gnanasekaran, N. (2016, July). Conjugate heat transfer in a Hexagonal micro channel using hybrid nano fluids. In International Conference on Nanochannels, Microchannels, and Minichannels (Vol. 50343, p. V001T12A001). American Society of Mechanical Engineers (Scopus).
8. Hegde, S., **Narendran, G.**, & Ganasekaran, N. (2015). Conjugate heat transfer studies in a hexagonal micro channel. *Procedia Engineering*, 127, 719-726 (Scopus).
9. Kumar, A., **Narendran, G.**, & Perumal, D. A. (2019). Numerical Study of TiO₂ Nanofluid in Multistage-Bifurcated Microchannel Subjected to Hotspots. In *Advances in Fluid and Thermal Engineering* (pp. 793-801). Springer, Singapore (Scopus).

BIODATA

NAME: G NARENDRAN

DATE OF BIRTH: 24-09-1990

Mobile No.: +91 9894357198

Email:narendranganesan24@gmail.com



ADDRESS:

D.No:131, CLT&RI staff Quarters, Chengalpattu, Kancheepuram-603001,
Tamilnadu

QUALIFICATION:

Examination	Board/Institute	Year	Percentage/ CGPA
Ph.D (Thermal systems)	NITK, Surathkal	2019	7.0
M.des (System Design.)	IITDM, Kancheepuram	2014	7.6
B.E. (Mechanical Engg)	Anna University , Tiruchy	2012	7.1
HSLC	Tamilnadu state board	2008	90%
SSLC	Tamilnadu state board	2006	94%

PROJECT EXPERIENCE:

Sr. no	Name of the company	Project section	From	To
1	Ford India Ltd, Chennai	Body Shop	Jun, 2010	Jul, 2010
2	Winergy India Ltd, Chennai	Gear Transmission	Oct, 2010	Nov, 2010
3	Chennai Port Trust, Chennai	Engine Shop	Nov, 2010	Dec, 2010
4	Hyundai Motor India, Chennai	Aluminium Foundry	Feb, 2012	Apr, 2012
5	Indian Institute of Technology	Fluid System Laboratory	Jan, 2020	Nov, 2021

ACHIEVEMENTS:

1. District topper in SSLC science examination, 2006. Kancheepuram.
2. Recipient of BARC golden jubilee science symposium award, Kalpakkam 2006
3. Product of the year, appeared in the institute year book, IITDM, 2012.